

Acta Physica Hungarica

VOLUME 58, NUMBERS 1-2, 1985

EDITOR-IN-CHIEF

I. KOVÁCS

EDITORIAL BOARD

**Z. BAY, R. GÁSPÁR, N. KÜRTI, K. NAGY,
L. PÁL, A. SZALAY, I. TARJÁN, B. TELEGDI,
L. TISZA, E. WIGNER**



Akadémiai Kiadó, Budapest

ACTA PHYS. HUNG. APAHAQ 58 (1-2) 1-156 (1985) HU ISSN 0001-6706

ACTA PHYSICA HUNGARICA

A JOURNAL OF THE HUNGARIAN ACADEMY
OF SCIENCES

EDITED BY
I. KOVÁCS

Acta Physica publishes original papers on subjects in physics. Papers are accepted in English, French, German and Russian.

Acta Physica is published in two yearly volumes (4 issues each) by

AKADÉMIAI KIADÓ
Publishing House of the Hungarian Academy of Sciences
H-1054 Budapest, Alkotmány u. 21

Subscription information

Orders should be addressed to

KULTURA Foreign Trading Company
1389 Budapest P.O. Box 149

or to its representatives abroad.

Acta Physica is indexed in *Current Contents*, in *Physics Abstracts* and in *Current Papers in Physics*.

ACTA PHYSICA HUNGARICA

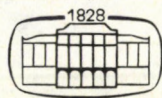
EDITORIAL BOARD

Z. BAY, R. GÁSPÁR, I. GYARMATI, N. KÜRTI, K. NAGY, L. PÁL,
A. SZALAY, P. SZÉPFALUSY, I. TARJÁN, B. TELEGDI, L. TISZA,
E. WIGNER

EDITOR-IN-CHIEF

I. KOVÁCS

VOLUME 58



AKADÉMIAI KIADÓ, BUDAPEST
1985

CONTENTS

Volume 58

Best wishes to Professor Sándor Szalay. <i>D. Berényi</i>	3
GENERAL PHYSICS	
Electrovac solutions with common shearing geodesic eigenrays. <i>B. Lukács</i>	149
Spherical functions of the Lorentz group on the hyperboloids. <i>M. Huszár</i>	175
ELEMENTARY PARTICLES AND FIELDS	
On the initial-value problem of linearized Einstein's equations. <i>A. Mészáros</i>	255
Schwinger model in temporal gauge. <i>J. Balog</i> and <i>P. Hráskó</i>	233
NUCLEAR PHYSICS	
High energy proton induced fission of light nuclei. <i>J. Németh</i> and <i>J. M. Irvine</i>	5
The effect of the properties of slowing media on nuclear lifetimes derived from DSA measurements. <i>M. M. Abdel Hady, Á. Z. Kiss, E. Koltay, B. Nyakó</i> and <i>M. Hautala</i>	11
Critical temperature of nuclear matter at the liquid-gas phase transition in a non-linear field theoretical model. <i>I. Lovas</i> and <i>Gy. Wolf</i>	23
Fine structure of the rms radius. <i>L. Végh</i>	29
The fate of relic neutrinos. <i>J. Balog</i> and <i>G. Marx</i>	35
Enhanced sensitivity of oxygen detection of 3.045 MeV (α, α) elastic scattering and its applications. <i>G. Mezey, E. Kótai, P. Révész, A. Manuaba, T. Lohner, J. Gyulai, M. Fried, Gy. Vizkeliethy,</i> <i>F. Pásztí, G. Battistig</i> and <i>M. Somogyi</i>	39
Investigations on fast neutron interactions with constructional materials. <i>L. Vasváry, F. Divós,</i> <i>G. Pető, J. Csikai</i> and <i>N. K. Mumba</i>	57
ATOMIC AND MOLECULAR PHYSICS	
Elastic scattering of electrons on He, Ne, Ar in the impact energy region from 1000 to 3000 eV. <i>J. Herbák, Á. Kövér, E. Szmola, D. Berényi</i> and <i>I. Cserny</i>	63
Investigation of L-subshell ionization of gold by low velocity proton bombardment. <i>K. Kiss,</i> <i>T. Papp, J. Pálincás, L. Sarkadi</i> and <i>B. Schlenk</i>	69
Second order calculations for L-shell ionization of gold by nitrogen ion impact. <i>L. Sarkadi</i> and <i>T. Papp</i>	75
Proposal for investigation of minor bodies of the solar system using remote sensing of electron beam induced X-ray fluorescence. <i>G. Hrehuss, T. I. Gombosi, I. Nádai, L. Pogány</i> and <i>K. Szegő</i>	83
Control of the trace element content of agricultural products by X-ray spectrometry. <i>L. Keszthelyi,</i> <i>I. Demeter, K. Hollós-Nagy</i> and <i>Z. Szőkefalvi-Nagy</i>	101

The $X\alpha$ method with ab initio exchange parameters, diamagnetic susceptibility and nuclear magnetic shielding constants for several atoms. <i>R. Gáspár and Á. Nagy</i>	107
Flavomononucleotide complex formation stabilized by polymer matrix. <i>R. Drabent and L. Szalay</i>	113
Dissociation energy of the SrH molecule. <i>V. G. Tulasigeri and V. M. Korwar</i>	157
The ground state of the Heisenberg Hamiltonian in four-spin systems with antiferromagnetic coupling. <i>S. Angelov and I. Mayer</i>	161
Dissociation energies for the electronic ground states of GaF, InF and TlF. <i>R. R. Reddy and T. V. R. Rao</i>	169
Molecular pseudopotential calculations VII. 1. <i>R. Gáspár and I. Tamássy-Lentei</i>	191
Molecular pseudopotential calculations VII. 2. <i>R. Gáspár, I. Tamássy-Lentei and Á. Derecskei-Kovács</i>	195
Molecular symmetry in ab initio calculations. I. <i>F. Bartha, E. Kapuy and C. Kozmutza</i>	219
Molecular symmetry in ab initio calculations. II. <i>F. Bartha and C. Kozmutza</i>	227
An integral representation of the $6j$ symbol. <i>S. Datta Majumdar</i>	265

CONDENSED MATTER

Investigations on colloid- and X_K -centres in coloured NaCl crystals. <i>L. Malicskó, R. Voszka and A. Watterich</i>	119
Geometrical structures of triatomic and tetraatomic clusters of Li, Na, K, Cu and Ag atoms. <i>I. László and A. Julg</i>	199
The influence of aggregation phenomena on the yield stress of NaCl(Ca) crystals. <i>J. Sárközi and E. Hartmann</i>	259
Surface of doped NaCl crystals annealed in air. <i>K. Orbán and J. Sárközi</i>	267

INTERDISCIPLINARY

Recent contributions to planning therapeutic irradiations. <i>L. Bozóky, G. József, Gy. Reischl and G. Varjas</i>	131
Problems of matching the fields in cobalt teletherapy. <i>Z. Dézsi, T. Borbély, L. Miltényi, E. Pintye, D. E. Groska and Gy. Vargha</i>	141

ASTROPHYSICS

Does Newton's world model revive? <i>A. Mészáros</i>	187
--	-----

BOOK REVIEWS

271

CONTENTS

Best wishes to Professor Sándor Szalay. <i>D. Berényi</i>	3
GENERAL PHYSICS	
Electrovac solutions with common shearing geodesic eigenrays. <i>B. Lukács</i>	149
NUCLEAR PHYSICS	
High energy proton induced fission of light nuclei. <i>J. Németh</i> and <i>J. M. Irvine</i>	5
The effect of the properties of slowing media on nuclear lifetimes derived from DSA measurements. <i>M. M. Abdel Hady, Á. Z. Kiss, E. Koltay, B. Nyakó</i> and <i>M. Hautala</i>	11
Critical temperature of nuclear matter at the liquid-gas phase transition in a non-linear field theoretical model. <i>I. Lovas</i> and <i>Gy. Wolf</i>	23
Fine structure of the rms radius. <i>L. Végh</i>	29
The fate of relic neutrinos. <i>J. Balog</i> and <i>G. Marx</i>	35
Enhanced sensitivity of oxygen detection of 3.045 MeV (α , α) elastic scattering and its applications. <i>G. Mezey, E. Kótai, P. Révész, A. Manuaba, T. Lohner, J. Gyulai, M. Fried, Gy. Vizkelethy,</i> <i>F. Pásztai, G. Battistig</i> and <i>M. Somogyi</i>	39
Investigations on fast neutron interactions with constructional materials. <i>L. Vasváry, F. Divós,</i> <i>G. Pető, J. Csikai</i> and <i>N. K. Mumba</i>	57
ATOMIC AND MOLECULAR PHYSICS	
Elastic scattering of electrons on He, Ne, Ar in the impact energy region from 1000 to 3000 eV. <i>J. Herbák, Á. Kövér, E. Szmola, D. Berényi</i> and <i>I. Cserny</i>	63
Investigation of L-subshell ionization of gold by low velocity proton bombardment. <i>K. Kiss, T. Papp,</i> <i>J. Pálinkás, L. Sarkadi</i> and <i>B. Schlenk</i>	69
Second order calculations for L-shell ionization of gold by nitrogen ion impact. <i>L. Sarkadi</i> and <i>T. Papp</i>	75
Proposal for investigation of minor bodies of the solar system using remote sensing of electron beam induced X-ray fluorescence. <i>G. Hrehuss, T. I. Gombosi, I. Náday, L. Pogány</i> and <i>K. Szegő</i>	83
Control of the trace element content of agricultural products by X-ray spectrometry. <i>L. Keszthelyi,</i> <i>I. Demeter, K. Hollós-Nagy</i> and <i>Z. Szókefalvi-Nagy</i>	101
The X α method with ab initio exchange parameters, diamagnetic susceptibility and nuclear magnetic shielding constants for several atoms. <i>R. Gáspár</i> and <i>Á. Nagy</i>	107
Flavomonucleotide complex formation stabilized by polymer matrix. <i>R. Drabent</i> and <i>L. Szalay</i>	113

CONDENSED MATTER

- Investigation on colloid- and X_k -centres in coloured NaCl crystals. *L. Malicskó, R. Voszka and A. Watterich* 119

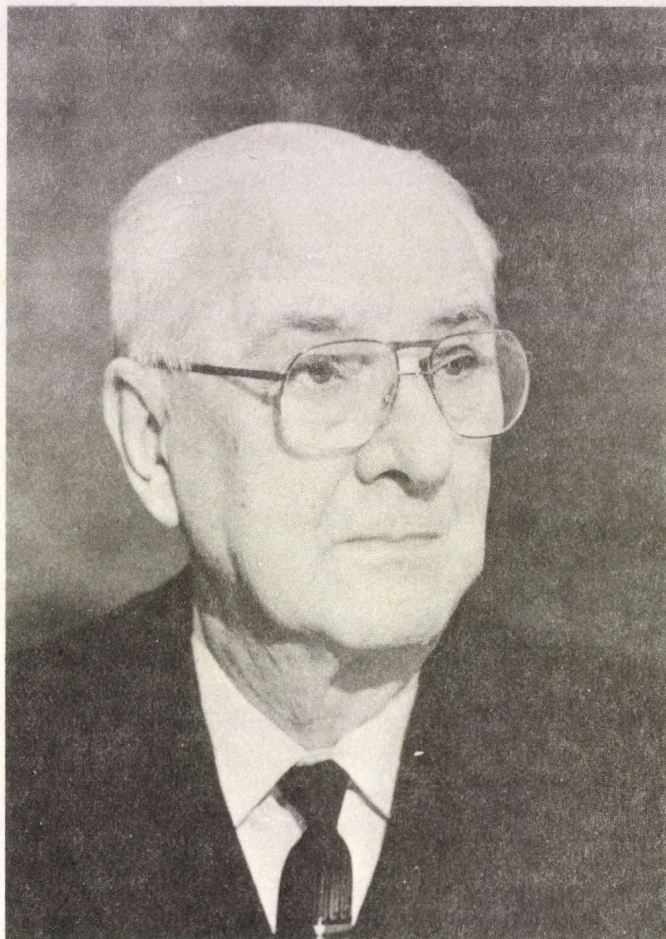
INTERDISCIPLINARY

- Recent contributions to planning therapeutic irradiations. *L. Bozóky, G. József, Gy. Reischl and G. Varjas* 131
- Problems of matching the fields in cobalt teletherapy. *Z. Dézsi, T. Borbély, L. Miltényi, E. Pintye, D. E. Groska and Gy. Vargha* 141

The final manuscript was received by the
Editorial Office on 15 January 1984

Manuscript received by Akadémiai Kiadó: 14 May 1984
Manuscript received by the Printers: 20 May 1984
Date of publication: 30 September 1985

PRINTED IN HUNGARY
Akadémiai Kiadó és Nyomda, Budapest



**BEST WISHES TO PROFESSOR SÁNDOR SZALAY
ON HIS 75th BIRTHDAY**

The life of Professor Sándor Szalay (A. Szalay) is very rich in achievements and results. He started his scientific career in Szeged, working together with Professor Szent-Györgyi and continued the research work in Budapest and Leipzig, but the decisive period for him was the half year he spent in Cambridge at the Cavendish Laboratory (headed at that time by Rutherford).

He came to Debrecen and started his teaching and research work here as a young scientist in 1936, and two years later, the University of Debrecen offered him a professorship. It was he who initiated nuclear physics research in Hungary. In the

meantime he had begun the careful selection of the best students and his close co-workers.

Professor Szalay — together with his co-workers — has produced a great number of new scientific results, not only in the field of nuclear reactions and structure but also in the broad field of the application of nuclear methods in biology and medicine, in geology and geochemistry, in environmental research, etc.

Despite the wealth of results, possibly the scientific school developed by Professor Szalay in Debrecen can be considered his main achievement.

The present Institute of Nuclear Research of the Hungarian Academy of Sciences (ATOMKI) and the Chair of Experimental Physics of Kossuth Lajos University are based on this school. The principal traditions of this school are, primarily, the experimental approach to the problems in physics and in applied research, the development and construction of new equipment, and the searching for new methods. Another characteristic of the school is the broad inter- and multidisciplinary interest in choosing the research topics as well as in carrying out investigations.

It is impossible to consider the achievements of Professor Szalay without appreciating his activities and successes centring on the practical applications of the scientific results. One might mention his role in the introduction of radioactive isotopes practice in Hungary, or in the discovery of the uranium deposit in this country, or in the field of microelement fertilization of plants and the microelement nutrition of animals.

On 4th October 1984 Professor Sándor Szalay, Member of the Hungarian Academy of Sciences, founder of the Institute of Nuclear Research, Debrecen, celebrated his 75th birthday. We wish him continued good health, and further successful work and creative activity in the future. It gives us immense pleasure to know that he is still full of new ideas and research plans.

Dénes Berényi

HIGH ENERGY PROTON INDUCED FISSION OF LIGHT NUCLEI*

J. NÉMETH

Nuclear Physical Institute KFA Julich, FRG

*Institute for Theoretical Physics, Roland Eötvös University
Budapest, Hungary*

and

J. M. IRVINE

*Department of Physics, University of Manchester
Manchester, U. K.*

Extended TDHF calculation is performed for light rotating nuclei to determine the dynamics of fission. If the model nucleus ^{144}Nb has 200 MeV excitation energy and $30 \hbar$ angular momentum, even such a light nucleus can fission. This circumstance can be the explanation of the facts observed in the case of high energy proton induced fission of light nuclei.

1. Introduction

According to experimental evidence high energy protons can induce fission of even relatively light ($A \sim 120\text{--}140$) nuclei [1, 2]. The fission process occurs in peripheral collisions, and the energy required is quite high. For example in the collisions with 200 MeV protons the fission probability is negligible, while in the case of 450 MeV protons it is already significant [2]. At the same time the fission barrier height of such nuclei is quite small, only ~ 60 MeV [3]. It is an interesting question, why this additional energy is needed. To understand the fission mechanism in such light nuclei, it is informative to investigate the time evolution of the process. A useful and mathematically tractable method for describing time-dependent processes is the time-dependent Hartree–Fock approximation. The TDHF method is a mean field approximation, the nucleons do not interact with each other directly, but only through a self-consistent, time-dependent one-body potential. It has the disadvantage that two-body collisions are neglected, although they play an important role in the case of fission. Nevertheless, it proved to be a very successful tool for the description of heavy-ion collisions, and this encourages us to try to find a modified version which takes into account two-body dissipation, and remains tractable.

The TDHF equations, determining the single-particle wave functions, are non-linear partial differential equations. To solve such equations we have to give the initial

* Dedicated to Prof. S. Szalay on his 75th birthday

conditions, that is to say the wave functions at time $t=0$. These initial conditions contain all the information about the physics of the process, how the nucleus is excited, etc. One usually starts from the ground state HF wave functions of the nucleus and modifies them in a systematic way to take into account excitation. For heavy-ion collisions the excitation has the form of translational kinetic energy of the target-projectile system. Other collective excitations are rotational or vibrational energy. The latter seems to be the most suitable for the inducement of fission. Giving increasing amounts of vibrational energy to a ground state nucleus one expects that the amplitudes for its deformation will grow and if it reaches the saddle point deformation, it will fission. However, in a mean field approximation, there is no way to change the single-particle level order: if a level was filled in the ground state, it remains filled during the whole evolution of the system. On the other hand in the real nucleus the occupation probabilities of the levels change as it gets more and more deformed due to the two-body collisions. To initiate this two-body dissipation, we assume that the n_i level occupation probabilities are time-dependent. This assumption is outside the validity of a mean field approximation, it cannot be based on a consistent theory, the time dependence of the n_i has to be given by some additional physical consideration.

In the second Section an extended version of the TDHF approximation is given. In the third Section we describe our calculational method for rotating nuclei and in the last Section the results are discussed.

2. Extended TDHF equations

The TDHF equations can be written as

$$i\hbar\psi_i = \hat{h}_{\text{HF}}\psi_i, \quad (2.1)$$

where \hat{h}_{HF} is a non-local single-particle Hamiltonian. Using the modified Skyrme force and retaining only the direct Coulomb and finite range Yukawa contributions \hat{h}_{HF} becomes local and can be written as

$$\hat{h}_{\text{HF}}^\alpha = -\frac{\hbar^2}{2m}\nabla^2 + U_S^\alpha + U_Y^\alpha + U_C^\alpha, \quad (2.2)$$

where U_S , U_Y and U_C are respectively the Skyrme, Yukawa and Coulomb force contributions to the single-particle potential. The label α distinguishes neutrons and protons. In the following spin-orbit and pairing forces are neglected.

It can be proven that in the TDHF approximation the total energy is a constant in time [4]. The energy and the mass number has to be a constant also in the modified TDHF approximation. This means that the time-dependent occupation probabilities have to fulfil the requirements

$$\frac{dN}{dt} = \sum_i \frac{dn_i}{dt} = 0, \quad (2.3)$$

$$\frac{dE}{dt} = \sum_i \varepsilon_i(t) \frac{dn_i}{dt} = 0, \quad (2.4)$$

where the ε_i are the time-dependent expectation values of the single particle Hamiltonian

$$\varepsilon_i(t) = (\psi_i, \hat{h}_{\text{HF}} \psi_i) \quad (2.5)$$

and in the deduction of Eq. (2.4) we have already used the TDHF equations (2.1).

Keeping the energy and the mass number constant, the n_i should change so that the entropy should be maximum. The maximum entropy can be got with an occupation probability corresponding to thermal equilibrium [5]

$$\bar{n}_i = \{1 + \exp [(\varepsilon_i(t) - \mu(t))/kT]\}^{-1}, \quad (2.6)$$

where $\mu(t)$ and $T(t)$ are determined from the mass number and the initial excitation energy. Assuming that the occupation probabilities are approaching with time the thermal equilibrium values (2.6), their time dependence can be expressed by the equation [6]

$$\frac{dn_i}{dt} = \frac{1}{\tau} (\bar{n}_i - n_i), \quad (2.7)$$

τ is a parameter which describes how fast thermal equilibrium [Eq. (2.7)] is reached. The time derivatives of the n_i clearly satisfy the Eqs (2.3) and (2.4).

Eqs (2.1) and (2.7) together with (2.6) are already suitable for the description of fission. In the case of high excitation energy the neglect of the pairing forces is probably justifiable. In the TDHF theory of fission even starting from a saddle point deformation, to get to the scission an exceptionally large (five times the realistic value) pairing force was needed [3]. In our opinion the pairing force in that case partly took on the role of Eq. (2.7): pairing is a very effective tool for changing the occupation probability of the levels. Using Eq. (2.7), however, removes the need for pairing in this regard.

3. Extended TDHF calculations for rotating nuclei

There is direct experimental evidence that high energy protons colliding peripherally with a nucleus can transfer large amounts of angular momentum [2].

To describe the fission of such nuclei one has to use TDHF equations with an angular momentum constraint [8]:

$$i\hbar\dot{\psi}_i = \hat{h}_{\text{HF}}\psi_i - \omega\hat{L}_y\psi_i, \quad (3.1)$$

where L_y is the y -component of the angular momentum operator.

In solving the Eqs (3.1) we restricted ourselves to axial symmetry. Using cylindrical polar coordinates (z, r, θ) we may write the wave functions as [9]

$$\psi_i(x, t) = \varphi_i(r, z, t) e^{im_i\theta} e^{ig(rzt)\cos\theta}, \quad (3.2)$$

where for the sake of simplicity we have chosen the g_i phase-functions to be the same in all states. The TDHF equations with angular momentum constraints can be written as [9]:

$$\begin{aligned}
 i\hbar\dot{\varphi}_i = & -\frac{\hbar^2}{2m}\left[\frac{\partial^2}{\partial r^2} + \frac{1}{r}\frac{\partial}{\partial r} + \frac{\partial^2}{\partial z^2} - \frac{m^2}{r^2}\right]\varphi_i + \\
 & + \hat{U}_{\text{HF}}\varphi_i + \frac{\hbar^2}{4m}\left[\left(\frac{\partial g}{\partial r}\right)^2 + \left(\frac{\partial g}{\partial z}\right)^2 + \left(\frac{g}{r}\right)^2\right]\varphi_i - \\
 & - \frac{1}{2}\hbar\omega\left[z\left(\frac{\partial g}{\partial r} + \frac{g}{r}\right) - r\frac{\partial g}{\partial z}\right]\varphi_i,
 \end{aligned} \tag{3.3}$$

where the phase function g is the solution of the equation

$$\begin{aligned}
 \frac{\partial\rho}{\partial r}\frac{\partial g}{\partial r} + \frac{\partial\rho}{\partial z}\frac{\partial g}{\partial z} + \rho\left[\frac{\partial^2 g}{\partial r^2} + \frac{1}{r}\frac{\partial g}{\partial r} + \frac{\partial^2 g}{\partial z^2} - \frac{1}{r^2}g\right] = \\
 = \frac{m\omega}{\hbar}\left(z\frac{\partial\rho}{\partial r} - r\frac{\partial\rho}{\partial z}\right).
 \end{aligned} \tag{3.4}$$

Eqs (3.3)–(3.4) depend on the occupation probabilities only through the density

$$\rho = \sum_i n_i |\psi_i|^2. \tag{3.5}$$

The solution of the extended TDHF equations can be obtained as follows. First we determine the static HF wave functions of the nucleus, and decide on the initial conditions. From the initial wave functions and density we can determine from Eq. (3.4) the g phase factor corresponding to the angular momentum constraint. Solving Eqs (3.3) we get the wave functions at the next time step. Calculating from Eq. (2.5) the time-dependent single-particle energies, using Eqs (2.6) and (2.7) the new occupation probabilities can be determined. Assuming that the wave functions do not depend too strongly on the changes of the n_i we can recalculate with the new density self-consistently the occupation probabilities. Repeating the procedure for the next time step we get the time evolution of the system.

4. Results

The initial conditions for the wave functions we try to choose so as to initialize the physical initial conditions leading to fission. Giving vibrational or rotational excitation energies, and starting from the ground state deformation in the unmodified TDHF approximation we did not get fission [10]. If we started from a strongly deformed state, with those levels filled up which lead to fission, vibrational excitation could already lead to fission. Using the extended TDHF equations we started from an

excited nucleus with 400 MeV, the excitation being partly vibrational and partly thermal, we still could not get any fission. Starting, however, from an excited nucleus with a high angular momentum ($30 \hbar$), already 200 MeV total excitation energy led to fission. On the basis of this calculation we have the following picture of high-energy proton-induced fission. The peripheral colliding high energy proton can transfer both energy and angular momentum to the nucleus. After the emission of a few high energy particles in direct reactions, the remaining nucleus is in an excited state. If the angular momentum of the nucleus is small, the shape of this compound system is almost spherical (the temperature tries to make the shape spherically symmetric), and even if part of the excitation energy is collective vibration, the nucleus decays by evaporation of particles. If, however, the compound nucleus is left with high angular momentum, the most favourable shape of the nucleus will be strongly deformed, even at a few MeV temperature [3]. At $30 \hbar$ angular momentum the nucleus is already close to the critical deformation. If we give to such nuclei a relatively small excitation energy, they can fission easily. The high energy of the protons is needed only to be able to transfer high enough angular momentum. To make the picture clearer further calculations are needed and are in progress.

Acknowledgement

One of the authors (JN) wants to express her thanks to Professors J. Speth and K. Goeke and the KFA Julich for their warm hospitality.

References

1. G. Andersson et al, *Z. Phys.*, *A293*, 241, 1979.
2. S. Kaufman and E. Steinberg, *Phys. Rev.*, *C22*, 167, 1980.
3. J. Nemeth, J. Okolowicz and J. M. Irvine, *Jour. Phys.*, *G9*, 1385, 1983.
4. A. Kermann and S. Koonin, *Ann. of Phys.*, *100*, 332, 1976.
5. M. Brack and P. Quentin, *Phys. Lett.*, *52B* 159, 1974.
6. W. Norenberg, *Nucl. Phys.*, *A. 409*, 191, 1983.
7. J. Negele et al, *Phys. Rev.*, *C17*, 1098, 1978.
8. H. Flocard et al, *Nucl. Phys.*, *A203* 433 1973; *A391*, 285, 1982.
9. H. Feldmeier, Oak Ridge Nat. Lab. Rep. ORUL/TH-6053, 1977.
10. J. Nemeth, S. Faedi and J. M. Irvine, in *Time-Dependent Hartree-Fock and Beyond* (Ed. K. Goeke and P. G. Reinhard) Lecture Notes in Physics 171, Springer-Verlag 1982.

THE EFFECT OF THE PROPERTIES OF SLOWING MEDIA ON NUCLEAR LIFETIMES DERIVED FROM DSA MEASUREMENTS*

M. M. ABDEL HADY,** Á. Z. KISS, E. KOLTAY and B. NYAKÓ

*Institute of Nuclear Research of the Hungarian Academy of Sciences
4001 Debrecen, Hungary*

and

M. HAUTALA

*Department of Physics, University of Helsinki
SF-00170 Helsinki 17, Finland*

Apparent lifetimes determined from Doppler Shift Attenuation (DSA) measurements are known to depend on the atomic number Z_2 of the stopping medium. It is shown here that inaccuracies in the data of the medium result in additional fluctuation as the function of Z_2 .

The determination of the actual conditions of the slowing medium helps in avoiding systematic errors in the evaluation. On the other hand, the use of experimentally determined range values for the proper selection of parameters f_e and f_n decreases the Z_2 dependence of apparent lifetimes. The above effects are investigated in the case of the 6.2 MeV excited state of ^{14}N excited in $^{13}\text{C}(p, \gamma)^{14}\text{N}$ nuclear reaction.

1. Introduction

In experiments aiming at the determination of the lifetimes of excited nuclear states by the Doppler shift attenuation method the proper selection of the stopping material is of special importance. As shown in a number of papers the measured lifetime is greatly affected by the properties of the substance in which the slowing down of the decaying recoil nucleus takes place.

Systematic investigations using a large number of different target backings as slowing layers were performed by Broude et al [1] as well as by Toulemonde and Haas [2] for recoil velocities $\beta = v/c \sim 1\%$ where electronic stopping plays a predominant role. In these works the measured lifetimes τ were found considerably fluctuating as the function of the atomic number Z_2 of the stopping medium. Toulemonde and Haas derived a linear dependence of τ on the electronic slowing down time α . In other works [3–5] attempts were made to correct the above mentioned Z_2 dependence by

* Dedicated to Prof. S. Szalay on his 75th birthday

** Permanent address: Ain Shams University, Cairo, Arab Republic of Egypt

introducing various correction formulae into the description of electronic stopping cross sections.

For lower recoil velocities ($\beta \sim 0.3\%$), where nuclear stopping dominates, the first systematic investigations were performed by Bister et al [6]. For this purpose they measured the mean lifetimes of three low lying ^{14}N states in the $^{13}\text{C}(p, \gamma)^{14}\text{N}$ reaction using targets prepared by separating ^{13}C ions onto or into backings made of eight different materials. The authors established the fact that the fluctuations of τ around the average value amount to $\pm 20\%$. The fluctuations were ascribed to the inaccuracies of the slowing theory, however, no systematic Z_2 dependence was stated by the authors.

In an earlier paper of some of the present authors [7] the measurements of Bister et al were repeated on ^{13}C targets deposited by vacuum evaporation on target backings of elements similar to those used by Bister et al. The evaluation of the measurements resulted in a well established Z_2 dependence of the experimental lifetimes. When arranging lifetimes according to their electronic slowing down times α a linear dependence was observable. The same can be stated for the data taken from Bister's work.

In the evaluation procedure aiming at the determination of $F(\tau)$ curve use is made of the actual values of the target thickness and the density of the target layer. These data are normally known at a low level of accuracy for evaporated layers. The chemical activity of the backing substances may cause further troubles. For implanted targets measured energy and dose of implanted ions permit an accurate determination of the above physical parameters. Consequently, the τ values obtained from measurements on implanted target layers are considered to be of higher accuracy.

In the energy region, where nuclear stopping dominates experimentally determined correction factors f_n and f_e are used by some authors [8] to correct the inaccuracy of the Lindhard-Scharff-Schiött (LSS) theory. However, no systematic studies have been made to compare the results of range and DSA measurements in various backings in this energy region.

The aim of the present work is to make a series of measurements in the case of the $^{13}\text{C}(p, \gamma)^{14}\text{N}$ nuclear reaction to investigate the influence of the above mentioned effects on the experimental lifetime of one of the excited levels of ^{14}N . The 6.2 MeV excited state of ^{14}N nucleus was found to be well suited for the investigation. Its lifetime $\tau = 187 \pm 14$ fs is well confirmed [8] and the $F(\tau)$ values for various backings vary from 0.3 to 0.6 and are well in the region where τ values most sensitively depend on $F(\tau)$ values. On the other hand, the ranges of ^{15}N ions have been measured in Ti, Ni, Cu, Mo, Ag, Ta, W and Au [9] in the energy interval 20–100 keV which contains the recoil energy of 80 keV of ^{14}N ions in the $^{13}\text{C}(p, \gamma)^{14}\text{N}$ reaction at the $E_p = 1.15$ MeV resonance. Both evaporation and implantation techniques were used in preparing the targets. In the experiments we completed the data of paper [7] by new results obtained from measurements on "slow" stopping substances (such as B, Mg, Sn, Zr, Pb), and a systematic comparison was made with range measurements available.

Some critical remarks concerning the above questions in DSA measurements are formulated, and the reliability of correcting the stopping values using experimental data for the ranges [9] is confirmed.

2. Experimental procedure and analysis

The measurements were performed with protons from the Van de Graaff accelerator of the Institute of Nuclear Research in Debrecen. The proton energy chosen corresponded to the right edge of the (p, γ) resonance at $E_p = 1.15$ MeV. The γ -rays were detected with a Harshaw 105 cm³ Ge(Li) detector (full width at half maximum = 3.6 keV for the 3.253 MeV ⁵⁶Co line) and analysed with a Nuclear Data 4096 channel pulse height analyser. The measurements were carried out at angles of 0, 60, 90 and 140° relative to the beam axis. The target-to-detector distance was 10.5 cm.

One part of the targets were fabricated by vacuum deposition of enriched (97.6%) ¹³C onto B, Mg, Ti, Zr, Sn and Pb backings. The thickness of the targets was 6 $\mu\text{g}/\text{cm}^2$. The thickness of the backings varied between 0.1–0.5 mm, while in the cases of B and Ti 150 $\mu\text{g}/\text{cm}^2$ ¹⁰B, and 250 $\mu\text{g}/\text{cm}^2$ ⁴⁸Ti were deposited onto 0.3 mm thick Cu plates, respectively. The targets were fabricated at CRN in Strasbourg. The other part of the targets were prepared by implanting a 20 mC/cm² fluence of 15 keV ¹³C⁺ ions into Ni, Mo and Ta in the isotope separator of the University of Helsinki. The target current was 1 μA .

Lifetimes were determined from the displacement of the centre of gravity of the 3891 keV γ -line. The functions $F(\tau)$ were calculated by a computer programme using the Blaugrund formalism, or by Monte Carlo calculation. In the Monte Carlo programme the scattering angles in collisions were calculated using the Thomas–Fermi potential as described in [10, 11]. One should notice that the nuclear stopping calculated in this way does not include the approximations of the Magic Formula that is used in the LSS theory. Differences between theory and experiment are thus due only to the potential itself.

Experimental $F(\tau)$ values measured on a number of targets with different backings and corresponding lifetimes of the 6.2 MeV ¹⁴N level obtained by Blaugrund and Monte Carlo calculations are presented in Table I. For generating these preliminary data the assumption $f_e = f_n = 1$ was used.

The spread of the τ values is considerable, furthermore, a systematic shift towards longer lifetimes is observable in the case of Monte Carlo results. The latter effect was found by other authors, too [12].

Considering the spread in the τ values in Table I arguments can be forwarded for the possible effects pertinent to the actual conditions of the slowing media composed of the target layer and backing. Some of the parameters describing the conditions of the physical system and playing an important role in the actual evaluation procedure are known in many cases on a low level of accuracy. Errors in the values for the thickness and density of the target layer as well as the presence of oxide on the surface may alter

the original Z_2 dependences caused by the atomic structure. Let us examine first the effect of the above conditions.

No principal argument was found for preferring either the Blaugrund or the Monte Carlo methods when investigating the variation of the lifetime as the function of Z_2 . Easier calculations and the availability of data published by other authors [6] made us to use the Blaugrund method.

Table I

Measured $F(\tau)$ values and derived lifetimes of the ^{14}N 6.2 MeV level with different stopping materials of atomic number Z_2 . (Error limits quoted are statistical only.)

Stopping medium	Z_2	Target thickness [$\mu\text{g}/\text{cm}^2$]	$F(\tau)$ %	τ_{BI} [fs]	τ_{MC} [fs]
B	5	2	60.0 ± 0.9	154 ± 6	154 ± 11
Mg	12	6	58.3 ± 0.7	225 ± 5	250 ± 8
Ti	22	2	43.6 ± 0.8	195 ± 6	254 ± 11
		6	$43.2 \pm 2.6^{\text{a)}$	$207 \pm 18^{\text{c)}$	—
Ni	28	6	$44.5 \pm 0.9^{\text{a)}$	116 ± 6	130 ± 9
		0 ^{b)}	32.5 ± 1.0	149 ± 7	182 ± 12
Cu	29	6	$42.0 \pm 0.9^{\text{a)}$	133 ± 6	145 ± 8
Zr	40	6	45.7 ± 1.0	159 ± 6	180 ± 9
Mo	42	2	$39.9 \pm 1.0^{\text{a)}$	134 ± 7	140 ± 11
		0 ^{b)}	32.5 ± 1.0	147 ± 8	170 ± 11
Ag	47	6	$40.8 \pm 0.8^{\text{a)}$	144 ± 5	160 ± 8
Sn	50	6	45.3 ± 1.0	162 ± 6	185 ± 8
Ta	73	6	$35.6 \pm 0.8^{\text{a)}$	146 ± 5	156 ± 8
		0 ^{b)}	26.8 ± 1.2	158 ± 9	184 ± 11
W	74	6	$39.0 \pm 1.0^{\text{a)}$	116 ± 8	120 ± 10
Au	79	6	$39.2 \pm 0.9^{\text{a)}$	118 ± 6	120 ± 9
Pb	82	6	46.9 ± 1.0	129 ± 7	130 ± 8

^{a)} Ref [7]

^{b)} implanted

^{c)} Ref. [7] recalculated

2.1. The thickness of the evaporated target layer

As stated in the work [6] the inaccuracy in the thickness of the carbon layer deposited onto heavy backings results in considerable error in the case of short lifetimes. This effect seems to be minimized here by having selected the level of the longest lifetime in ^{14}N for the purpose of this investigation. Even in this case, as clearly seen from the curves in Fig. 1 the 30% error of the target thickness leads to error ± 13 fs for heavy backings like tantalum (or gold). This value is quite high compared with the error ± 5 fs given by the statistical error in the experimental $F(\tau)$ value. The inaccuracy related to target thickness amounts to ± 10 fs for the backings Pb, Zr, Sn and Ni while for Mg it is less than ± 6 fs even if the target thickness is completely neglected (Fig. 1).

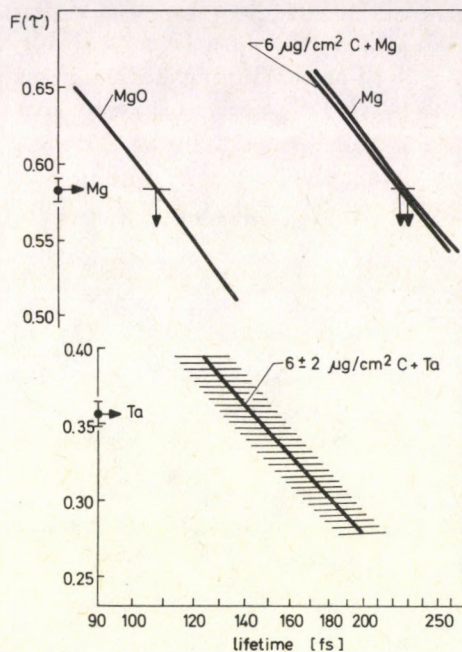


Fig. 1. Calculated $F(\tau)$ curves for Mg and Ta backings covered by an evaporated $6 \mu\text{g}/\text{cm}^2$ thick carbon target layer and for pure Mg and MgO backings without target layer

2.2. Density of the evaporated target and backing layers

The use of the bulk density values available in chemistry handbooks (e.g.: [13]) means an overestimation of the actual thin layer density by at least 10% [14]. Taking into consideration a 10% decrease in density for the evaporated C layer we obtain for heavier backings an insignificant 4 fs shift in the evaluated lifetime. For the case of evaporated backings of boron and titanium the shifts amounts to 15 and 20 fs, respectively.

2.3. Oxidation of the slowing layer

The oxidation of the slowing layer may appear mainly in the cases of Pb and Mg. As shown by a series of calculations even an unrealistic complete oxidation of the Pb backing would be ineffective on the calculated lifetimes. On the other hand, the experimental $F(\tau)$ value will result in drastically decreased lifetime if we suppose that the slowing process takes place in MgO instead of pure Mg. The actual values are 116 fs and 230 fs, respectively (Fig. 1). The same effect appears if the thickness of the MgO

layer amounts to $100 \mu\text{g}/\text{cm}^2$ equivalent to one quarter of the total range for the recoil ^{14}N ions. The situation is clearly shown by the curve in Fig. 2.

As shown by Rutherford backscattering measurements performed on our ^{13}C targets evaporated on Mg backing the surface oxidation gave an oxide layer of about $6\text{--}10 \mu\text{g}/\text{cm}^2$ which is somewhat thicker than the carbon target itself. Taking the presence of MgO into consideration (i.e. performing $F(\tau)$ calculations for a combination of $^{13}\text{C}\text{--MgO}\text{--Mg}$ system) we ended up with the lifetime 210 ± 10 fs.

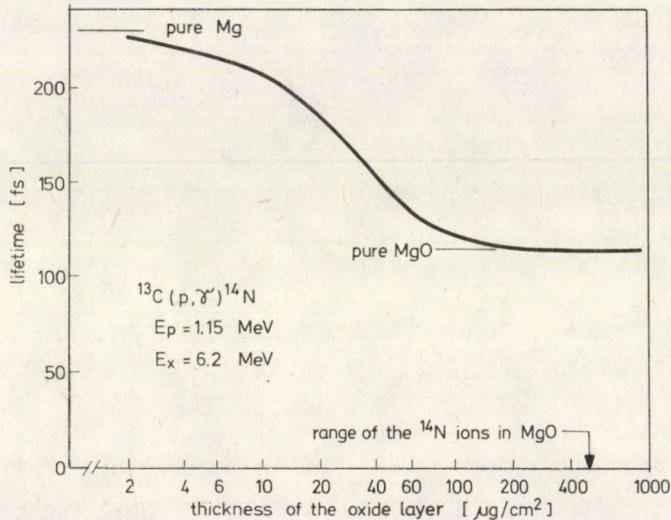


Fig. 2. The lifetime as a function of the thickness of a supposed oxide layer covering the Mg backing for an $F(\tau)=0.583$ value measured in the $^{13}\text{C}(p,\gamma)^{14}\text{N}$ reaction

3. Results and discussion

3.1. Z_2 dependence

The measured τ values and their errors are shown in Fig. 3. In the cases of B and Ti a correction has been made for the actual density [14] of the evaporated layer while the effect of oxidation has been taken into account for the Mg backing. The curve clearly shows up fluctuations reflecting the trend of the data in [1] and [2].

It was the case of Mg which drew our attention to the problem of chemically active stopping materials in DSA. The effect of the surface oxidation and possible build up of nitride layer is rather important for cases with high changes in layer densities. As shown in Table II composed on the basis of the data taken from [13] these drastic density changes are typical for alkali metals and alkaline-earths.

In order to demonstrate the effect of possible oxidation on determined lifetime we make use of the experimental $F(\tau)$ values obtained by Toulemonde and Haas [2] for the ^{22}Ne 3.34 MeV level in the $^{19}\text{F}(\alpha, p)^{22}\text{Ne}$ reaction. The τ data given in the last two columns of Table II are received from $F(\tau)$ calculations performed for elemental and compound media given in the first and third columns, respectively. For the majority of

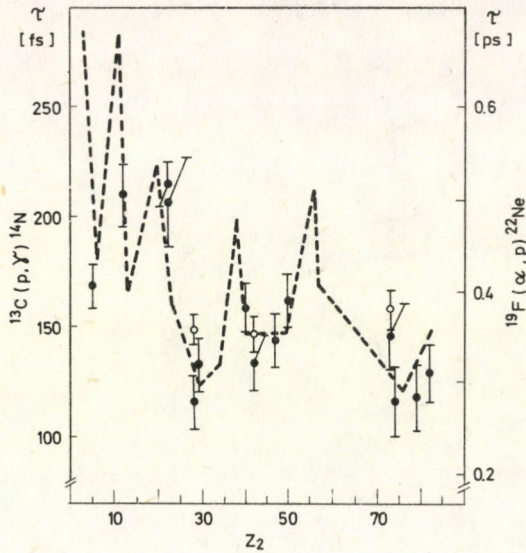


Fig. 3. Plot of meanlife of the 6.2 MeV level in ^{14}N v.s. atomic number Z_2 of the stopping material. The dotted curve is taken from [2] for the 3.34 MeV level in ^{22}Ne and fitted to the present values. The full dots and open circles represent lifetimes for evaporated and implanted targets, respectively

Table II

The effect of possible change in the chemical form of backing material on lifetimes calculated from experimental $F(\tau)$ data of [2]

Stopping element	Density [g/cm ³]	Stopping compound	Density [g/cm ³]	$F(\tau)_{\text{exp}}$	τ [fs] for stopping	
					element	compound
Li	0.534	Li ₂ O	2.013	0.72	690	190
Na	0.97	Na ₂ O ₂	2.805	0.65	690	260
Mg	1.74	MgO	3.58	0.65	430	200
Ca	1.54	CaO	3.25	0.64	560	280
		Ca ₃ N ₂	2.63			350
Sr	2.6	SrO ₂	4.56	0.65	480	280
Ba	3.51	BaO ₂	4.96	0.62	500	350
		Ba ₃ N ₂	4.783			380
Pb	11.34	PbO	9.53	0.46	360	390

the cases the pairs of τ values differ considerably. These differences call one's attention to the importance of the exact knowledge on the actual chemical conditions of the slowing material. Calculated lifetimes as the function of the thickness of oxide or nitride layers composed on some backing substances are shown in Fig. 4 for the case of the above mentioned reaction (when neglecting target thickness). As it is clearly seen, even the presence of a thin 30–50 $\mu\text{g}/\text{cm}^2$ oxide layer decreases the lifetimes considerably, especially in the cases of Li (or Na) and Ca.

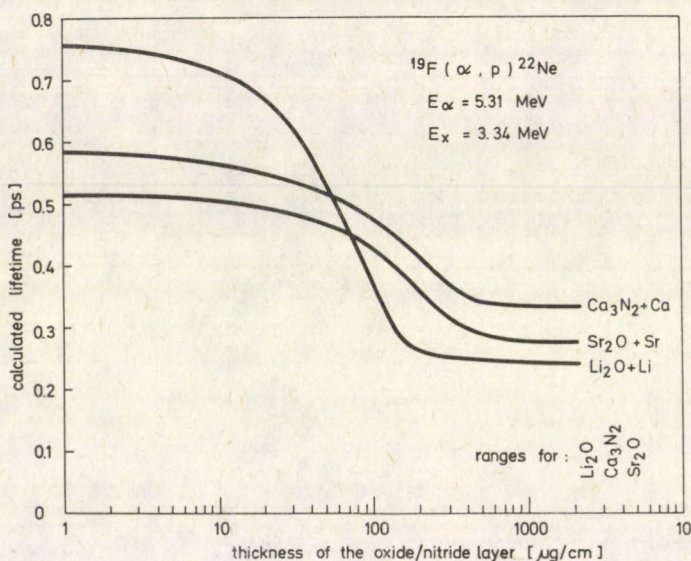


Fig. 4. As Fig. 2 for experimental $F(\tau)$ values shown in Table II and measured in the $^{19}\text{F}(\alpha, p)^{22}\text{Ne}$ reaction [2]

It is important to mention that part of the slowing materials presented in Table II corresponds to Z_2 values with extreme long lifetimes published in [1] and [2]. It was admitted even by the authors of [15] that the data of Broude et al [1] for the highly active materials calcium and barium were affected by chemical changes due to exposure to air. As shown by the results of [15] where an attempt was made to avoid the compound formation on the surface the overall range of the Z_2 dependence appears to be significantly smaller than that given in their earlier publication.

The effect of the oxidation and nitride formation can be kept at low level if special measures are taken to keep the target away from the air [1, 2, 15]. Nevertheless, it seems to be practical to make DSA measurements and charged particle backscattering analysis simultaneously in order to get data on the actual target condition for a more correct lifetime evaluation.

3.2. The elimination of the Z_2 dependence

Our aim is now to remove the variations in the apparent τ -values by using measured range data given by Luomajärvi et al [9]. This is possible if only nuclear stopping is important and the error in the electronic stopping does not seriously affect the results. When the electronic stopping is less important, its inaccuracy can partly be removed by the assumption of $f_e = f_n$, i.e. by correcting the electronic and nuclear stopping to the same amount. This is justified by the fact that both of them are related to the electron shell structure.

We studied the influence of nuclear and electronic stopping both on range determination and DSA analysis. First we calculated ranges by the Monte Carlo method. We varied $f_e = f_n$ and found the ranges to change as $R = R_0/f_n (=f_e)$, where R_0 denotes the range at $f_e = f_n = 1$. Thus the correction factors may be taken directly from the range measurements. The ranges were further calculated by using the LSS transport theory in the second order approximation [16] varying the correction factors separately. The results are shown in Table III for Ta, Cu and B. It can be seen that nuclear stopping is the dominating factor for all the backings treated.

Table III

The comparison of 80 keV N ranges $R(f_e, f_n)$ for various f_e, f_n -values.

Backing	$R(1.2, 1)$	$R(0.8, 1)$	$R(1, 1.2)$	$R(1, 0.8)$
	$R(1, 1)$	$R(1, 1)$	$R(1, 1)$	$R(1, 1)$
Ta	0.96	1.05	0.87	1.19
Cu	0.94	1.08	0.89	1.15
B	0.91	1.12	0.92	1.11

In a second set of calculations, we determined the τ value using different correction factors, for Ti backing. Ti was the lightest backing investigated in the measurements of Luomajärvi et al [9]. For $f_n = f_e = 1$, τ amounts to 253 fs. For $f_n = 1$, $f_e = 1.16$ and $f_n = f_e = 1.16$ τ values are 230 fs and 188 fs, respectively. So we may conclude that even for the lightest backing, f_e is less important.

It is quite well justified in our case to calculate the $f_n = f_e$ value from the data of range measurements, and to use them in the determination of lifetimes.

In [9] the ranges are calculated in the approximation of the LSS theory. To find the correction factors for our $F(\tau)$ calculations, we first had to calculate the ranges of 80 keV N ions in Ti, Ni, Cu, Mo, Ag, Ta, W and Au. The calculated ranges were on an average 1.05 ± 0.02 times higher than those calculated with the Monte Carlo program using the LSS theory. The final $f_n = f_e$ values thus received are 1.16, 0.90, 0.88, 1.00, 0.96, 1.00, 0.88 and 0.83 for Ti, Ni, Cu, Mo, Ag, Ta, W and Au, respectively.

The final corrected and uncorrected τ -values are presented in Fig. 5 for implanted and evaporated targets. From a comparison of the respective curves the

following results can be obtained. First, the average of the uncorrected τ values in evaporated targets is 154 ± 47 fs while the corrected mean value amounts to 165 ± 15 fs and the variations are clearly reduced. Secondly, τ -values for the evaporated targets are about 20 fs shorter than those measured on implanted layers. This is probably due to the inaccuracies in the data characterising the evaporated layer. It is worth-while to

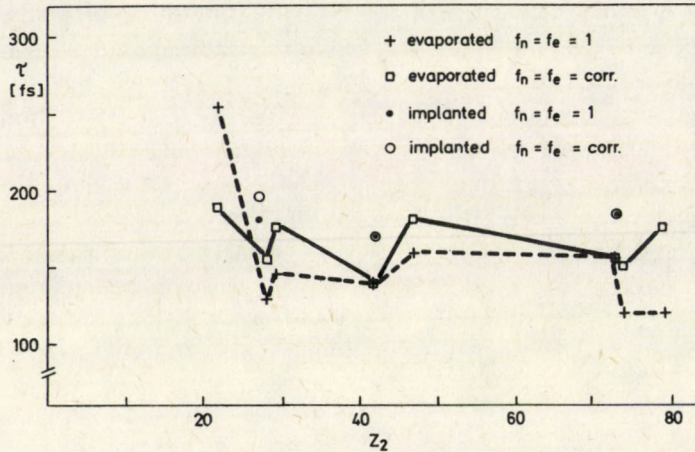


Fig. 5. Comparison of the corrected and uncorrected τ values

point out that this difference can be decreased when the neglected effect of the smaller density of evaporated carbon layer (Section 2.2) is taken into consideration. From the actual figures one can conclude that evaporation results in thin layers with densities even lower than expected above.

As a conclusion we may say that the variation in the τ values in the low recoil velocity region can be removed by using the data of the range measurements. However, the use of evaporated targets may cause a number of error sources and uncertainties. Therefore, the use of implanted targets is preferable whenever possible.

Acknowledgement

The participation of M. S. Antony in the early stage of this work is kindly acknowledged.

References

1. C. Broude, P. Engelstein, M. Popp and P. N. Tandon, *Phys. Lett.*, *39B*, 184, 1972.
2. M. Toulemonde and F. Haas, *Phys. Rev.*, *C15*, 49, 1977.
3. B. M. Latta and P. J. Scanlon, *Phys. Rev.*, *A13*, 1370, 1976.
4. W. Pietsch, U. Hauser and W. Neuwirth, *Nucl. Inst. and Meth.*, *132*, 79, 1976.
5. B. C. Robertson, *Phys. Lett.*, *68B*, 424, 1977.
6. M. Bister, A. Anttila, M. Piiparinen and M. Viitasalo, *Phys. Rev.*, *C3*, 1972, 1971.
7. M. S. Antony, A. Z. Kiss, E. Koltay, B. Nyakó and Gy. Szabó, *Izv. Akad. Nauk SSSR, Ser. Fiz.*, *44*, 1031, 1980.
8. M. Bister, A. Anttila and J. Keinonen, *Phys. Rev.*, *C16*, 1303, 1977.
9. M. Luomajärvi, J. Keinonen, M. Bister and A. Antilla, *Phys. Rev.*, *B18*, 4657, 1978.
10. M. Bister, M. Hautala and M. Jäntti, *Rad. Effects*, *42*, 201, 1979.
11. M. Hautala, *Rad. Effects*, *51*, 35, 1980.
12. B. W. Sargent, W. G. Hanson, P. A. Puhach and D. Sinclair, *Nucl. Instr. and Meth.*, *124*, 265, 1975.
13. *Handbook of chemistry and physics*, (53rd ed.), Ed. by R. C. Weast, The Chemical Rubber Co., Cleveland, Ohio, 1972-73.
14. A. Anttila, private communication.
15. C. Broude, F. A. Beck and P. Engelstein, *Nucl. Phys.*, *A216*, 603, 1973.
16. J. Lindhard, M. Scharff and H. E. Schiøtt, *K. Dan. Vidensk. Selsk. Mat.-Fys. Medd.*, *33*, No. 14, 1963.

CRITICAL TEMPERATURE OF NUCLEAR MATTER AT THE LIQUID-GAS PHASE TRANSITION IN A NONLINEAR FIELD THEORETICAL MODEL*

I. LOVAS and GY. WOLF

*Central Research Institute for Physics
1525 Budapest, Hungary*

In Walecka's mean field theoretical model complemented with nonlinear terms, we search for the value of the critical temperature of nuclear matter compatible with the experimental data, i.e. with the observed binding energy, density, and compressibility of nuclear matter at zero temperature. Our result is in the region of the other theoretical estimates [5]...[9], but is much higher than the result obtained from experimental data [4].

A great deal of effort has been devoted to studying nuclear matter with the help of extremely high energetic particles and heavy ions. Two recent important results of this work were the determination of the compressibility and the critical temperature of nuclear matter.

The compressibility (K) was obtained with the help of heavy ion reactions [1]. Negative pion multiplicities were measured and calculated in the cascade model as a function of the laboratory energy. At a given energy the calculated yield was higher than the measured one so the calculation attributes lower energy to a given yield compared with the measurement. This energy difference is considered to be the compressional energy (not contained in the cascade model). In addition to the compressional energy the compression was also calculated at each laboratory energy. In this way the compressional energy could be obtained as a function of the compression. A quadratic function of the compression was fitted to the compressional energy. The result of the fitting was $K = 240$ MeV which is very close to the earlier results ($K \approx 200$ MeV).

In the other experiment [2] the mass distribution of the fragments ($6 \leq A_f \leq 30$) produced in high energy proton-nucleus collisions was measured. The isobaric yield was found to be proportional with $A_f^{-\tau}$ where A_f is the fragment mass number and $\tau = 2.6$. This is a very interesting observation because the critical point of the liquid-gas phase transition was studied theoretically in [3] where a similar power law was obtained for the distribution of the liquid droplets near the critical point with $2 < \tau < 3$ (for van der Waals system $\tau = 2.33$...). The similarity of the experimental and theoretical distributions was interpreted as a phase transition near the critical

* Dedicated to Prof. S. Szalay on his 75th birthday

point. With this assumption for evaluating the measurements, they obtained the $T_c = 3.3$ MeV for the critical temperature [4].

However, this interpretation of the measurements is by no means obvious: on the one hand the earlier theoretical estimates for this critical temperature gave much higher values, viz. between 15 MeV and 22 MeV [5–9]; on the other hand, the mass distribution is a power function of A_f only in the vicinity of the critical point. It is not obvious what kind of mechanism brings the expanding nuclear system near to the critical point, nor is it obvious what kind of mechanism stabilizes it there. These questions are due to be discussed in a future paper and here we confine ourselves to the critical temperature.

To analyse the critical temperature we use a relativistic field theoretical model introduced by Walecka. Originally it was devised as a means of studying infinite, dense nuclear or neutron matter (e.g. neutron stars), but it has also been applied for finite nuclei [10], and the results were in reasonable agreement with the experimental data.

In Walecka's original model [11–13] the Lagrangian density is given by

$$\begin{aligned} \mathcal{L}_0 = & -\hbar c \left[\bar{\psi} \left(\gamma_\lambda \frac{\partial}{\partial x_\lambda} + \frac{m_b c}{\hbar} \right) \psi \right] - \frac{c^2}{2} \left[\left(\frac{\partial \varphi}{\partial x_\lambda} \right)^2 + \frac{m_s^2 c^2}{\hbar^2} \varphi^2 \right] - \\ & - \frac{1}{4} F_{\lambda\rho} F_{\lambda\rho} - \frac{m_v^2 c^2}{2\hbar^2} V_\lambda V_\lambda + i g_v \bar{\psi} \gamma_\lambda \psi V_\lambda + g_s \bar{\psi} \psi \varphi, \end{aligned} \quad (1)$$

where

$$F_{\lambda\rho} = \frac{\partial V_\rho}{\partial x_\lambda} - \frac{\partial V_\lambda}{\partial x_\rho}. \quad (2)$$

Here ψ is the nucleon field of mass m_b ; φ is a neutral scalar meson field of mass m_s ; and V_λ is a neutral vector meson field of mass m_v . The scalar meson field gives the attraction and the vector meson field gives the short range repulsion between the nucleons.

The field equations obtained as the Euler–Lagrange equations from the Lagrangian density are given by

$$\left(\gamma_\mu \frac{\partial}{\partial x_\mu} - i \frac{g_v}{\hbar c} \gamma_\mu V_\mu + \frac{m_b c}{\hbar} - \frac{g_s}{\hbar c} \varphi \right) \psi = 0, \quad (3a)$$

$$\left(\square - \frac{m_s^2 c^2}{\hbar^2} \right) \varphi = - \frac{g_s}{c^2} \bar{\psi} \psi, \quad (3b)$$

$$\frac{\partial}{\partial x_\rho} F_{\lambda\rho} + \frac{m_v^2 c^2}{\hbar^2} V_\lambda = i g_v \bar{\psi} \gamma_\lambda \psi. \quad (3c)$$

In these equations we substitute the meson fields, and the baryon currents by their constant macrocanonical expectation values:

$$\bar{\varphi} = \varphi_0, \quad (4a)$$

$$\bar{V}_\lambda = i\delta_{\lambda 4} V_0, \quad (4b)$$

$$\bar{\bar{\psi}\psi} = \rho_s, \quad (4c)$$

$$\bar{\psi^+\psi} = \rho_B. \quad (4d)$$

The "mean field" equations are:

$$\left[\gamma_\mu \frac{\partial}{\partial x_\mu} + \left(m_b - \frac{g_s}{c^2} \varphi_0 \right) \frac{c}{\hbar} + \frac{g_v}{\hbar c} \gamma_0 V_0 \right] \psi = 0, \quad (5a)$$

$$\frac{m_s^2 c^2}{\hbar^2} \varphi_0 = \frac{g_s}{c^2} \rho_s, \quad (5b)$$

$$\frac{m_v^2 c^2}{\hbar^2} V_0 = g_v \rho_B. \quad (5c)$$

These "mean field" equations can be obtained directly from the "mean field" Lagrangian density:

$$\begin{aligned} \mathcal{L}_0^{MF} = & -\hbar c \left[\bar{\psi} \left(\gamma_\lambda \frac{\partial}{\partial x_\lambda} + \frac{g_v}{\hbar c} \gamma_0 V_0 + \left(m_b - \frac{g_s}{c^2} \varphi_0 \right) \frac{c}{\hbar} \right) \psi \right] - \\ & - \frac{m_s^2 c^4}{2\hbar^2} \varphi_0^2 + \frac{m_v^2 c^2}{2\hbar^2} V_0^2. \end{aligned} \quad (6)$$

In this model there are two free parameters: $C_v = g_v^2 / (\hbar c) m_b^2 / m_v^2$ and $C_s = g_s^2 / (\hbar c^3) m_b^2 / m_s^2$ which were fitted to the binding energy (BE), and the density of nuclear matter at zero temperature (ρ_0). In this model the calculated compressibility $K = 550$ MeV is too large compared with the experimental value, $K = 240$ MeV. This model should therefore be modified to describe the compressibility too.

The most general renormalizable Lagrangian density for these fields, given by

$$\mathcal{L} = \mathcal{L}_0 - U(\varphi), \quad (7)$$

where

$$U(\varphi) = \frac{a}{3} g_s^3 \varphi^3 + \frac{b}{4} g_s^4 \varphi^4 \quad (8)$$

was suggested to study the nuclear matter [14], [15]. In the mean field approximation we introduce a further simplifying assumption:

$$\frac{\partial \bar{U}}{\partial \varphi}(\varphi) = \frac{\partial U}{\partial \varphi}(\varphi_0). \quad (9)$$

So

$$\mathcal{L}^{MF} = \mathcal{L}_0^{MF} - U(\varphi_0). \quad (10)$$

From the Lagrangian density the energy-momentum tensor can be derived in a standard way. The diagonal elements of the energy-momentum tensor, viz. pressure (P), and energy density (E), can be expressed as follows:

$$e = E \cdot \frac{\hbar^3}{m_b^4 c^5} = \frac{\gamma}{2\pi^2} \int dt [\sqrt{t^2 + \chi^2} t^2 (n(t) + \bar{n}(t))] + \frac{1}{2} C_v \rho_B^2 \frac{\hbar^6}{m_b^2 c^6} + \frac{1}{2C_s} (1-\chi)^2 + \frac{A}{3} (1-\chi)^3 + \frac{B}{4} (1-\chi)^4 \quad (11)$$

$$p = P \cdot \frac{\hbar^3}{m_b^4 c^5} = \frac{1}{3} \frac{\gamma}{2\pi^2} \int dt \left[\frac{t^4}{\sqrt{t^2 + \chi^2}} (n(t) + \bar{n}(t)) \right] + \frac{1}{2} C_v \rho_B^2 \frac{\hbar^6}{m_b^2 c^6} - \frac{1}{2C_s} (1-\chi)^2 - \frac{A}{3} (1-\chi)^3 - \frac{B}{4} (1-\chi)^4, \quad (12)$$

where γ is the spin-isospin degeneracy factor ($\gamma=2$ for neutron matter, and $\gamma=4$ for nuclear matter), χ is the effective mass ($\chi=(m_b - g_s/c^2\varphi_0)/m_b$). The baryon density is given by:

$$\rho = \rho_B \frac{\hbar^3}{m_b^3 C^3} = \frac{\gamma}{2\pi^2} \int dt [t^2 (n(t) - \bar{n}(t))]. \quad (13)$$

The fermion distribution functions are given by:

$$n(t) = (\exp \{[\sqrt{t^2 + \chi^2} - v]/\Theta\} + 1)^{-1}, \quad (14a)$$

$$\bar{n}(t) = (\exp \{[\sqrt{t^2 + \chi^2} + v]/\Theta\} + 1)^{-1}. \quad (14b)$$

The dimensionless temperature is defined by $\Theta = kT/(m_b c^2)$, and the dimensionless chemical potential by $\mu/(m_b c^2) = v + C_v \rho_B$. The effective mass must be determined self-consistently from Eq. (5b):

$$\chi \frac{\gamma}{2\pi^2} \int dt \left[\frac{t^2}{\sqrt{t^2 + \chi^2}} (n(t) + \bar{n}(t)) \right] = \frac{1}{C_s} (1-\chi) + A(1-\chi)^2 + B(1-\chi)^3. \quad (15)$$

In this model there are four free parameters: $C_v = g_v^2/(\hbar c)m_b^2/m_v^2$, $C_s = g_s^2/(\hbar c^3)m_b^2/m_s^2$, $A = (\hbar^3 c^3/m_b)a$, and $B = \hbar^3 c^5 b$, which should be fixed by fitting to measured quantities. We have only three measured parameters of the nuclear matter: BE, ρ_0 , and K , so we must still look for an additional one. Since there are some estimates for the coupling constant of the vector meson g_v , derived from phase-shift analysis of nucleon-nucleon scattering data, and the mass of the vector meson is also measured, C_v can be considered as a measured quantity. In that all of these measured values have some uncertainties, we extend our examination to an interval around the

estimated values. We make the C_v step, and at each C_v we fix the other three free parameters by fitting to BE, ρ_0 , and K . After the fitting we can determine the critical temperature drawing the isotherms of the system. A typical calculated phase-diagram is sketched in Fig. 1. According to our calculations this can be done except for an interval of C_v . The results of our calculations can be found in Table I. In this model T_c must be between 11.3 MeV and 17.6 MeV, considering the experimental limits for C_v : $160 \leq C_v \leq 220$; even this interval is limited to a narrower one, viz. 13.3–15.9 MeV. Our results are in the region of the earlier estimates but much higher than the value $T_c = 3.3$ MeV obtained in [4]. Various possibilities are available for explaining this large discrepancy: either the exchange energy neglected by the mean field approximation becomes important at such temperatures; or the interpretation of the experiment and/or the evaluation of the data in [4] should be changed. These open questions require further examination.

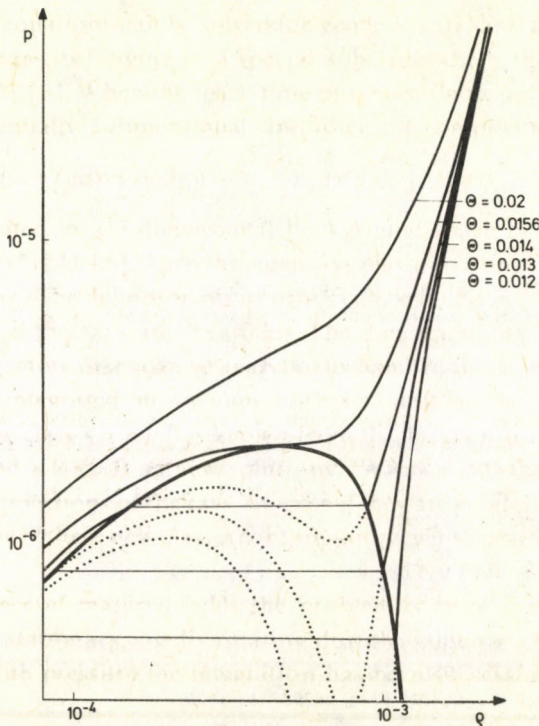


Fig. 1. Dimensionless pressure $p [= Ph^3/(m_b^4 c^5)]$ of nuclear matter as a function of dimensionless nuclear density $\rho_0 [= \rho_B h^3/(m_b^3 c^3)]$ for the parameters $C_v = 200$, $C_s = 309.8$, $A = 0.002806$, and $B = -0.003872$. The corresponding binding energy, normal density, compressibility, and critical temperature are given by BE = -16 MeV, $\rho_0 = 0.1725$ fermi $^{-3}$, $K = 240$ MeV, and $T_c = 14.6$ MeV. The isotherms are labelled by the dimensionless temperature $\Theta [= kT/(m_b c^2)]$.

Table I

Critical temperature $\Theta_c [\theta_c = kT_c/(m_\pi c^2)]$ as a function of $C_v [C_v = g_v^2/(\hbar c)m_b^2/m_v^2]$ at compressibility $K = 240$ MeV and various values of the binding energy (BE), and the normal density (ρ_0). The incompatibility of the values of C_v , BE, ρ_0 and K is indicated in the Table by a dash (-).

BE[MeV]	-17	-17	-15	-15
$C_v \rho_0$ [fermi ⁻³]	0.145	0.202	0.145	0.202
60	-	-	-	-
80	-	-	18.5	18.1
100	-	-	18.1	17.7
120	17.0	16.5	17.7	17.3
140	16.7	16.2	17.4	16.9
160	16.5	16.0	17.0	16.5
180	16.2	15.7	16.4	15.8
200	16.0	15.4	15.8	15.1
220	15.7	15.1	15.0	14.2
240	15.3	14.7	14.2	13.3
260	14.9	14.3	13.6	-
280	14.5	13.8	-	-
300	14.0	13.3	-	-
350	12.8	12.0	-	-
360	-	-	-	-

References

1. R. Stock, R. Book, R. Brockman, J. W. Harris, A. Sandoval, H. Stroebele, K. L. Wolf, H. G. Pugh, L. S. Schroeder, M. Maier, R. E. Renfordt, A. Dacal and M. E. Ortiz, Phys. Rev. Lett., 49, 1236, 1982.
2. J. E. Finn, S. Agarwal, A. Bujak, I. Chuang, L. J. Gutay, A. S. Hirsch, R. W. Minich, N. T. Porile, R. P. Scharenberg, B. C. Stringfellow and F. Turkot, Phys. Rev. Lett., 49, 1321, 1982.
3. M. Fisher, Physics, 3, 255, 1967.
4. R. W. Minich, S. Agarwal, A. Bujak, J. Chuang, J. E. Finn, L. J. Gutay, A. S. Hirsch, N. T. Porile, R. P. Scharenberg, B. C. Stringfellow and F. Turkot, Phys. Lett., 118B, 458, 1982.
5. M. W. Curtin, H. Toki and D. K. Scott, Phys. Lett., 123B, 289, 1983.
6. D. Q. Lamb, J. M. Lattimer, C. J. Pethick and O. G. Ravenhall, Nucl. Phys., A360, 459, 1981.
7. B. Friedman and V. R. Pandharipande, Nucl. Phys., A361, 502, 1981.
8. G. Röpke, L. Münchow and H. Schulz, Phys. Lett., 110B, 21, 1982.
9. M. Barranco and J. R. Buchler, Phys. Rev., C22, 1729, 1980.
10. F. E. Serr and J. D. Walecka, Phys. Lett., 79B, 10, 1978.
11. J. D. Walecka, Ann. Phys., 83, 1974.
12. J. D. Walecka, Phys. Lett., 59B, 109, 1975.
13. I. Lovas, Nucl. Phys., A367, 509, 1981.
14. J. Boguta and A. R. Bodmer, Nucl. Phys., A292, 413, 1977.
15. J. Boguta and S. A. Moszkowski, Nucl. Phys., A403, 445, 1983.

FINE STRUCTURE OF THE RMS RADIUS*

L. VÉGH

*Institute of Nuclear Research of the Hungarian Academy of Sciences
4001 Debrecen, Hungary*

The fine structure of nuclear rms charge radii found in experimental data for isotopic and isotonic sequences is discussed within a phenomenological treatment. It is demonstrated that the polarization effect responsible for the fine structure can be described by the degree of occupation of the valence shell.

The mass number dependence of the measured rms charge radii can be approximately expressed by the empirical formula [1]:

$$r_{st} = \sqrt{3/5}(1.15 + 1.80A^{-2/3} - 1.2A^{-4/3})A^{1/3} \text{ fm}, \quad (1)$$

which holds for nuclei with the number of nucleons A near the valley of stability.

For the isotopes of a given element, however, the increase of the experimentally determined rms radius of the charge distribution r_c with the neutron number N is systematically less than expected from the average trend (1) [2-4]. In addition, the presence of shell effects in isotope shift data has been also suggested [5] and a more pronounced shell effect has been shown in work [6].

A comprehensive study of experimental rms charge radii has been carried out by Angeli and Csatlós [7, 8]. This systematics shows that the deviations from the average A dependence given in formula (1) follow simple trends. For an isotopic sequence of an element, the normalised rms charge radii v_c formed as

$$v_c = r_c/r_{st} \quad (2)$$

and plotted as a function of N lie on or close to straight lines. The slopes of these lines denoted by a_z vary systematically as a function of atomic number Z . The products $\bar{A}_z a_z$, where \bar{A}_z is the average mass number for the respective element, show a characteristic sawtooth structure [7]. There are discontinuities in the values of the slopes for elements that contain $N = 8, 20, 28, 50, 82, 88, 90$ and 126 neutrons. The slopes for the normalised rms charge radii for isotonic sequences show similar behaviour and the discontinuities can be found at sequences that contain $Z = 10, 20, 28, 50, 82$ protons [8].

The Hartree-Fock BCS calculations using the energy density formalism and including a BCS treatment of pairing correlations have reproduced only $\sim 20\%$ of the

* Dedicated to Prof. S. Szalay on his 75th birthday

observed shell effects in isotopic and isotonic sequences [9]. The calculations have been performed by assuming spherical shapes. The calculated shell effect is attributed to the electromagnetic spinorbit effect [10], the contribution to r_c of the moving magnetic moments.

On the other hand the calculations have reproduced the average trend of rms radius with an error $< 1\%$ over the entire periodic table. They reproduce the average behaviour of $\bar{A}_z a_z$ having an approximate $A^{1/5}$ dependence for r_c as estimated in [4]. On the grounds of the calculated Hartree-Fock charge densities, a simple parametrization of the two parameter Fermi function

$$\rho_q(r) = \rho_0 (1 + \exp(r - R_q)/a_q)^{-1} \quad (3)$$

has been suggested where the parameters R_q and a_q have the following form [9]:

$$R_q(N, Z) = -0.5401 + 1.249 A^{1/3} - 0.9532 (N - Z)/A \text{ fm}, \quad (4)$$

$$a_q(N, Z) = 0.4899 - 0.1236 (N - Z)/A \text{ fm}. \quad (5)$$

Recently all available information on the charge distribution of even-even nuclei has been analysed systematically by Friedrich and Voegler [11]. They have discussed several definitions of the surface thickness and their analysis shows that the observed shell effect of the rms charge radii is completely contained in the skin thickness of charge distributions. This argument implies that the role of the volume shell effects is negligible.

The existence of the "shell effect" within the droplet model has been demonstrated by Myers and Schmidt [12]. The "shell effect" can be attributed to the deformations and the change of the neutron skin defined as the difference of the neutron and proton droplet model effective sharp radii. For the calculation of the rms charge radii the deformations have been extracted from the tabulated values of the Q_2 and Q_4 multipole moments calculated with the microscopic-macroscopic approach of Möller and Nix [13]. The calculated rms charge radii, except the range of the light nuclei to $N, Z < 28$, show a satisfactory agreement with the trend of Angeli and Csatlós [7].

The simple character of the trend offers the possibility to draw up a general picture on the change of the surface thickness and that of the deformation and neutron skin for the whole range of nuclei. As the trend does not depend on the specific value of Z , it depends only on the values of N , the valence neutrons must polarize the proton distribution in such a way that the polarization is unrelated to the shell structure of protons. Taking into account the simplicity of the trend the description of polarization may be quite easy. We suppose that for a nucleus with neutron number N the polarization depends only on the ratio

$$R_N = \frac{N - N_{md}}{N_{mu} - N_{md}}, \quad (6)$$

where N_{mu} and N_{md} are the magic neutron number closest to N , $N_{md} \leq N \leq N_{mu}$.

In order to check this hypothesis we have constructed a simple model based on the two parameter Fermi distribution as given in [3-5]. The R_N dependence of the charge distribution caused by the polarization is described by the redefinition of the surface parameter $a_q(N, Z)$. In formula (5) $a_q(N, Z)$ is replaced by $a_q^*(N, Z, R_N)$ where

$$a_q^*(N, Z, R_N) = a_q(N, Z) + \delta(R_N). \quad (7)$$

For nuclei with magic neutron numbers ($R_N=0, 1$) $\delta(R_N)$ should take its minimum value as the magic nuclei have the stiffest surface. $\delta(R_N)$ should have its maximum value at $R_N=0.5$ according to the larger deformation in the middle of the valence shell. If we assume a smooth R_N dependence for $\delta(R_N)$ the above conditions can be satisfied in the simplest form by a sinusoidal function of R_N :

$$\delta(R_N) = d \cdot \sin R_N \pi. \quad (8)$$

The quantity d has length dimension and we have taken it proportional to the thickness of the filled valence neutron shell defined as

$$d = d_0 [R_n(N_{mu}, Z) - R_n(N_{md}, Z)], \quad (9)$$

where d_0 is a free parameter and $R_n(N, Z)$ is the radius of the neutron distributions.

Neglecting the electromagnetic spin-orbit term, giving only 20% of the observed shell effects, and other small terms [14] giving very small corrections to r_c , the calculated ratio v_c^{th} has the following form:

$$v_c^{\text{th}} = \left(\int_0^\infty \rho_q(r) r^4 dr \right)^{1/2} / r_{st}, \quad (10)$$

where $\rho_q(r)$ is normalised to unity.

If d is small compared to a_q then the values of v_c^{th} for isotopic sequences in a limited range of nuclei lie approximately on straight lines in accordance with the experiments. For the first shells which contain only a few particles there exist data only for two or three neighbouring isotopes so the deviations from the straight line cannot be discussed. The only exception is the sequence of Ca isotopes from $N=20$ to $N=28$, but here a systematic deviation from the straight line can be observed experimentally. Our calculated values of v_c^{th} show similar behaviour (see Fig. 1).

Choosing the value of $d_0 = -0.07$ for $Z < 20$ and $d_0 = 0.07$ for $Z \geq 20$ we can reproduce the sawtooth structure over the whole region of Z , (see Fig. 2). In the range of the strongly deformed nuclei we can reproduce only the average decrease of the $\bar{A}_z a_z$ values. Small discontinuities in the calculated values can be explained by the investigated ranges of the given isotopes. The shell correction parameter d is quite small, its value is about 5-15% of a_q over the whole Z range.

To see if the above parametrization describes a general tendency the study of isotonic sequences is an effective method. If such an effect exists then we have to

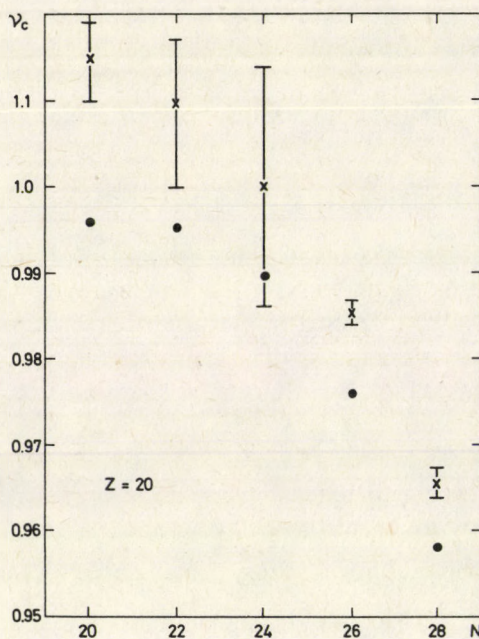


Fig. 1. The rms charge radii normalised by formula (1) for Ca isotopes. The experimental data are taken from [8], the calculated ones are denoted by dots

reproduce the similar trends in the isotonic sequences. If $N = \text{const}$ then like in formula (7, 8) we can write

$$a_q^*(N, Z, R_z) = a_q(N, Z) + d \sin R_z \pi, \quad (11)$$

with

$$R_z = \frac{Z - Z_{md}}{Z_{mu} - Z_{md}} \quad (12)$$

and

$$d = d_0 [R_q(N, Z_{mu}) - R_q(N, Z_{md})], \quad (13)$$

where Z_{mu} and Z_{md} are the magic numbers closest to Z , $Z_{mu} \geq Z \geq Z_{md}$. With the same values of parameter d_0 as used above, that is $d_0 = -0.07$ for $N < 20$ and $d_0 = 0.07$ for $N \geq 20$, we have calculated the $\bar{A}_N a_N$ values, where a_N is the slope, \bar{A}_N is the average mass number for the isotonic sequence of neutron number N . The results are presented in Fig. 3. As the Figure shows there is a satisfactory agreement between the calculated values and the experimental trend.

Fig. 2 and Fig. 3 show that the theoretical values of v_c for isotopic and isotonic sequences exhibit a small oscillating tendency around the experimental straight lines. This behaviour of the calculated values is due to the simple sinusoidal form of $\delta(R_N)$ in (8) and $\delta(R_Z)$ in (11). An accurate fit to the experimental trends could be given by a more sophisticated function of R_N or R_Z .

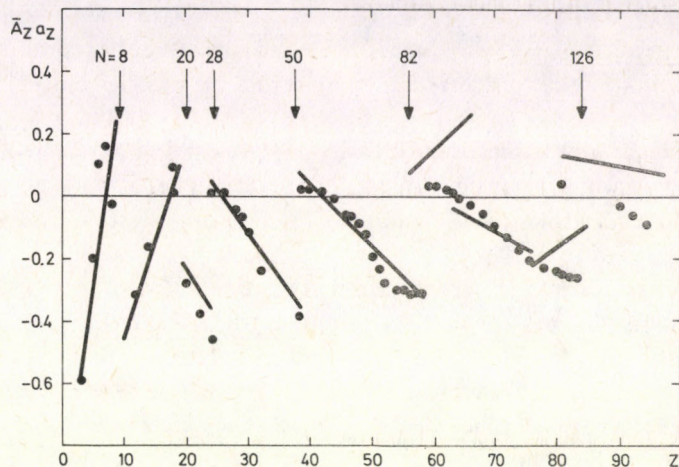


Fig. 2. The slopes a_z of normalized rms radii for isotopic sequences multiplied by the average mass numbers \bar{A}_z as a function of atomic numbers. The solid lines show the result of a weighted least-squares fit to $\bar{A}_z a_z$ values derived from experimental data [7]. Dots denote the calculated values

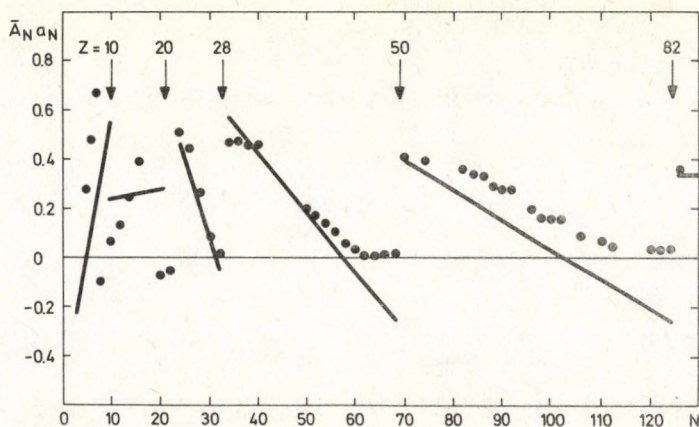


Fig. 3. The slopes a_N of normalized rms radii for isotonic sequences multiplied by the average mass numbers \bar{A}_N as a function of neutron numbers. The solid lines show the result of a weighted least squares fit to $\bar{A}_N a_N$ values derived from experimental data [8]. Dots denote the calculated values

The results suggest that the starting hypothesis is correct: the polarization effect responsible for the shell structure of the rms charge radii can be described by R_N for isotopic, by R_Z for isotonic sequences.

In the range of $20 < N, Z < 82$ there is a good agreement between the calculated and measured trends. This suggests that in this range the deformation and neutron skin effects have a stable character, they do not show "phase transitions".

In the range of the $N = 82 - 126$ shell there are two sudden changes in the experimental trend, at $N = 88 - 90$ and $N = 114$, which cannot be reproduced with our simple assumption. These discontinuities can reflect the drastic change in the type of the deformation.

Light nuclei ($A < 40$) present an interesting problem. In this region ($2 < N, Z < 20$) the slopes show an opposite behaviour as at heavier nuclei as they increase with the increase of atomic number (neutron number) for isotopic (isotonic) sequences.

The success of this simple phenomenological description calls for microscopic explanation. The microscopic interpretation of the $d_0 = 0.07$ shell correction parameter would give an insight into some of the essential properties of finite nuclei.

It is possible that deformed Hartree-Fock calculations can give explanation for the "shell effect". But we have to note that although the spherical Hartree-Fock BCS calculations [9] contain the neutron skin effects they do not show essential "shell effect". As besides the deformation the neutron skin plays a central role in the half-empirical explanation of the effect [12] we may have doubts about the success of the deformed Hartree-Fock calculations. It cannot be excluded that the understanding of the "shell effect" requires models beyond the Hartree-Fock method.

Acknowledgement

The author is indebted to Dr. I. Angeli and Dr. B. Gyarmati for valuable comments on the manuscript.

References

1. H. R. Collard, L. R. B. Elton and R. Hofstadter, Nuclear radii, in Landolt-Börnstein, group I. Vol. 2. edited by H. Schopper, Springer, Berlin, 1967.
2. L. R. B. Elton, Phys. Rev., *158*, 970, 1967.
3. F. G. Perey and J. P. Schiffer, Phys. Rev. Lett., *17*, 324, 1966.
4. J. P. Schiffer, J. A. Nolen and N. Williams, Phys. Lett., *29B*, 399, 1969.
5. D. N. Stacey, Rep. Prog. Phys., *29*, 171, 1966.
6. E. B. Spera, E. T. Ritter, R. B. Perkins, G. A. Rinker, L. K. Wagner, H. D. Wohlfahrt, G. Fricke and R. M. Steffen, Phys. Rev., *C 14*, 731, 1976.
7. I. Angeli and M. Csatlós, Nucl. Phys., *A 288*, 480, 1977.
8. I. Angeli and M. Csatlós, ATOMKI Közlemények, *20*, 1, 1978.
9. I. Angeli, M. Beiner, R. J. Lombard and D. Mas, J. Phys., *G 6*, 303, 1980.
10. W. Bertozzi, J. L. Friar, J. Heisenberg and J. W. Negele, Phys. Lett., *41B*, 408, 1972.
11. J. Friedrich and N. Voegler, Nucl. Phys., *A 373*, 192, 1982.
12. W. D. Myers and K.-H. Schmidt, Proc. 4th Int. Conf. on Nuclei Far from Stability, Helsingor, 1981 (CERN 81-09, Geneva 1981), p. 90
13. P. Möller and J. R. Nix, Nucl. Phys., *A 361*, 117, 1981.
14. J. L. Friar, J. W. Negele, Adv. Nucl. Phys., *8*, 219, 1975.

THE FATE OF RELIC NEUTRINOS*

J. BALOG and G. MARX

Department of Atomic Physics, Roland Eötvös University
Budapest, Hungary

Big Bang cosmology has concluded that there are about 150 neutrinos and antineutrinos of each family in a ccm of the present universe. The "missing mass" phenomena in the astrophysics of galaxies can be explained if at least one type of these neutrinos may be massive and stable. Pair annihilation will be the final fate of these neutrinos.

The present universe contains a relic electromagnetic radiation of the temperature $T_\gamma = 2.7$ K, corresponding to $N_\gamma = 550$ photons per ccm. In the first second after Big Bang, neutrinos were in thermal equilibrium with photons. This enables us to estimate the present number of neutrinos:

$$N = \frac{3}{4} \times \frac{4}{11} \times N_\gamma = 150 \quad \nu \text{ and } \bar{\nu} \text{ per ccm}$$

for each neutrino family [1]. If the stable relic neutrinos are all massless, their temperature is expected to be $T_\nu = (4/11)^{1/3} T_\gamma = 2.0$ K. There are, however, some indications that at least one sort of neutrinos is massive ($m_\nu \neq 0$). In this case E is proportional to p^2 instead of p , which means a different scaling and cooling behaviour and results in a much lower effective neutrino temperature:

$$T_\nu \simeq \left(\frac{4}{11}\right)^{2/3} \frac{kT_\gamma^2}{2m_\nu c^2}.$$

$kT_\gamma = 2.7$ meV is certainly much smaller than the fashionable neutrino rest energy $m_\nu c^2 = 30 \pm 15$ eV, so the present nonrelativistic neutrino gas may be supercold ($T_\nu \simeq 10^{-4}$ K), which makes it highly unstable against gravitational concentrations [2]. In superclusters of galaxies the neutrino mass density may exceed the mass density of nucleons, in case of large spiral galaxies it may reach even the average galactic mass density [3]. These massive neutrinos are supposed to be stable in themselves, but they may suffer pair annihilation, either into massless neutrinos via conventional weak interactions, or into photons via their electromagnetic form factor.

If massive neutrinos and massless neutrinos exist as well and if they are both stable, because each lepton generation obeys a different exact conservation theorem,

* Dedicated to Prof. S. Szalay on his 75th birthday

then pairs of massive neutrinos annihilate into massless neutrino pairs via simple first order weak interaction with a cross section

$$\sigma \simeq g^2 m_\nu^2 \beta^{-1},$$

where g is the Fermi coupling constant of weak interactions, $v = c\beta$ is the velocity in C. M. system and m_ν is the rest mass of the massive neutrino. This gives numerically

$$\sigma \simeq 10^{-52} \text{ cm}^2 \left(\frac{m_\nu}{30 \text{ eV}} \right)^2 \beta^{-1}$$

corresponding to an annihilation probability $N\sigma v \simeq 10^{-33} \text{ year}^{-1}$ in a universe, which is filled homogeneously by neutrinos. In this case the actual lifetime of the massive neutrinos against annihilation would be comparable to that of protons.

If even the lightest neutrino has a nonvanishing rest mass, this can annihilate only into photons. In this case the dominating annihilation diagrams are shown in Figs 1 and 2. The annihilation matrix elements are by orders of magnitudes smaller

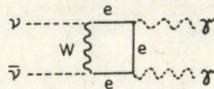


Fig. 1

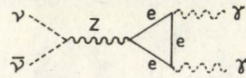


Fig. 2

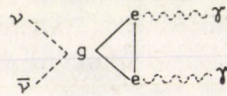


Fig. 3

than expected on dimensional grounds. In low energy limit the leading term $\sim \alpha g m_\nu$ cancels due to Bose symmetry of the emitted photons and due to electric current conservation, so the largest term is of order $\alpha g m_\nu^3 / m_e^2$. Luckily the matrix element of Fig. 1 is just (-2) times that of Fig. 2 at low energies. So one may restrict himself to Fig. 2, which can be substituted by Fig. 3 in low energy limit:

$$\begin{aligned} M_{\mu\nu} = & \frac{\alpha g}{10\pi\sqrt{2}m_e^2} \mathcal{F}\gamma^\rho(1-\gamma_5)u \cdot \left\{ \frac{1}{2} \varepsilon_{\mu\nu\sigma\pi} k_2^\sigma (k_{1\rho} + k_{2\rho}) - \right. \\ & - \frac{1}{3} \varepsilon_{\mu\sigma\rho\pi} k_1^\sigma k_2^\pi k_{1\nu} - \frac{1}{3} \varepsilon_{\sigma\nu\rho\pi} k_1^\sigma k_2^\pi k_{2\mu} - \frac{1}{3} \varepsilon_{\mu\nu\rho\sigma} k_{1\tau} k_{2\tau} (k_1^\sigma - k_2^\sigma) - \\ & \left. - \frac{7}{6} \varepsilon_{\mu\sigma\rho\pi} k_1^\sigma k_2^\pi k_{2\nu} - \frac{7}{6} \varepsilon_{\sigma\nu\rho\pi} k_1^\sigma k_2^\pi k_{1\mu} \right\} + O(\alpha g m_\nu^5 m_e^{-4}). \end{aligned}$$

corresponding to a cross section

$$\sigma = \frac{\alpha^2}{144\pi} g^2 m_\nu^2 \left(\frac{m_\nu}{m_e}\right)^3 \beta^{-1}$$

for the $\nu + \bar{\nu} \rightarrow \gamma + \gamma$ annihilation. (Here α is the electric fine structure constant.) $\sigma \rightarrow 0$ for $m_\nu \rightarrow 0$ and it is very small for light neutrinos. Numerically,

$$\sigma = 10^{-78} \text{ cm}^2 \cdot (m_\nu c^2 / 30 \text{ eV})^6 \beta^{-1}.$$

The neutrino annihilation would give a very monochromatic U.V. spectrum ($h\nu = m_\nu c^2$), but its intensity is unobservable, due to the very low annihilation probability $N\sigma v \simeq 10^{-58} \text{ year}^{-1}$ for a homogeneous neutrino distribution of $N_\nu = 150 \nu$ and $\bar{\nu}$ per ccm^4 .

In an expanding universe the neutrino density decreases as

$$\dot{N} = -3HN - v\sigma N^2,$$

where the Hubble parameter H may be taken from the Einstein equation

$$H^2 = \frac{8\pi G}{3} \rho.$$

Here G is the Newtonian constant of gravity and ρ is the mass density. In the late universe (after the supposed decay of protons) massive neutrinos will be the dominating source of gravity, $\rho = Nm_\nu$, consequently

$$\dot{N} = -(24\pi G m_\nu)^{1/2} N^{3/2} - \sigma v N^2.$$

The expansion will decrease the neutrino density more considerably than annihilation.

Within stable neutrino concentrations, however, N is large and constant (it may reach $N \simeq 10^8 \nu$ and $\bar{\nu}$ per ccm and it may remain so). In case of weak annihilation ($\nu_m + \bar{\nu}_m \rightarrow \nu_0 + \bar{\nu}_0$) the neutrino superstars may disappear simultaneously or even earlier than stars, within 10^{-30} years. In case of electromagnetic annihilation ($\nu_m + \bar{\nu}_m \rightarrow \gamma + \gamma$), however, neutrino superstars may have a life time $> 10^{50}$ years. Neutrino superstars were the first macroscopic things (created at about $t = 10^3$ years after Big Bang [2]) and they will be the last ones ($t > 10^{50}$ years). They survive the stars disappearing earlier due to the finite proton life time (after $t \simeq 10^{30}$ years) and due to black hole decay [5]. Lone massive neutrinos will live even longer in the expanding intergalactic space. The universe will return to its maximum entropy state only after the annihilation of the last massive neutrinos.

Acknowledgement

One of the authors is very much indebted to Dr. N. Cabibbo, Dr. P. Feldman and Dr. A. S. Szalay for valuable discussions.

References

1. Ya. B. Zeldovich and S. S. Gerstein, *JETP-USSR Letters*, *4*, 176, 1966.
2. A. S. Szalay and G. Marx, *Astronomy and Astrophysics*, *49*, 437, 1976; G. Marx, *Proc. DESY Workshop*, 1982; J. Silk, A. S. Szalay and Ya. B. Zeldovich, *Scientific American*, *83*, No. 11, 1983.
3. G. Marx, L. Fodor and S. Kövesy-Domokos, *Acta Phys. Hung.*, *17*, 171, 1964; G. Marx, *Proc. Neutrino 76*, Aachen 643, 1976.
4. A. de Rujula and S. Glashow, *Phys. Rev. Letters*, *45*, 942, 1980; F. W. Stecker, *Phys. Rev. Letters*, *45*, 1460, 1980.
5. De Witt, *Phys. Rep.*, *19C*, 295, 1975.

ENHANCED SENSITIVITY OF OXYGEN DETECTION OF 3.045 MeV (α , α) ELASTIC SCATTERING AND ITS APPLICATIONS*

G. MEZEY, E. KÓTAI, P. RÉVÉSZ, A. MANUABA, T. LOHNER,
J. GYULAI, M. FRIED, GY. VIZKELETHY, F. PÁSZTI and G. BATTISTIG

*Central Research Institute for Physics
1525 Budapest, Hungary*

and

M. SOMOGYI

*Research Institute for Technical Physics of the Hungarian Academy of Sciences
1325 Budapest, Hungary*

Based on a simple theoretical background, numerous applications of the $^{16}\text{O}(\alpha, \alpha)^{16}\text{O}$ reaction are reviewed. The reaction lowers the detection limit of the conventional RBS by a factor of 17. The advantages of the method for several applications will be discussed.

Introduction

Analysis of oxygen content and oxidation properties is of considerable importance in solid state physics and chemistry. Nuclear techniques provide a useful means of lowering the limits for detecting this element.

For medium energy projectiles (100 keV–5.5 MeV) four methods have been proposed till now, viz. the nuclear reaction techniques (d, p) and (p, α) [1, 2]; conventional backscattering [3, 4]; the resonant proton scattering at 4 MeV (p, p) [5, 6]; and the (α , α) compound reaction at 3.045 MeV. Based on Cameron's work [7], the last of these methods was demonstrated in early measurements of our group in 1972 [8] and was also mentioned in a review paper by Chu et al [9].

Here we review the application of this resonance showing examples, where the technique has definite advantages. The main points will be SiO_2 studies [10], native oxide on GaP [11, 12, 13], oxide on metal films [10, 12], buried oxides and implanted oxygen [14], oxide crystals [15] and the improvement of depth resolution [16]. It is also applied in a complex study to investigate crystals grown under microgravity conditions [17].

* Dedicated to Prof. S. Szalay on his 75th birthday

Method and experimental

A detailed study of the $^{16}\text{O}(\alpha, \alpha)^{16}\text{O}$ reaction in a gaseous target, from the viewpoint of nuclear physics, was published in 1953. The resonance is centred around $E_R = 3.045$ MeV with a cross-section maximum of $\sigma_R = 5.5 \cdot 10^{-25} \text{ cm}^{-2}$, a factor of 17 over an extrapolated regular Rutherford cross-section. The half-width of resonance $\Gamma = 10$ keV was found. A sharp dependence on detection angle was established, the reaction can be detected only for backscattering geometries.

There is still some dispute concerning the value 17; Wang et al [18] concluded upon a somewhat lower number.

The cross section, unfortunately, varies even for a moderately thin target (comparable with the half-width, i.e. approximately 50 nm, in SiO_2). This variation, however, obeys the Breit–Wigner dispersion relation, except for some tail regions. Therefore, a simple analytical calculation helps in calibrating the scale factors [9]. It can be shown that for thin target approximation, the result reduces to the normal backscattering relation with an increased cross-section (σ_R).

Experiments were made on the 5 MeV Van de Graaff accelerator of our laboratory using a goniometer, and a standard backscattering detector and electronics. The vacuum was kept at 10^{-5} Pa during the experiments.

Results and discussion

a) Silicon oxide studies

Dry thermal oxides on silicon were used to measure the resonance parameters. Figure 1 shows the resonance character of the nuclear reaction; Fig. 2 shows excitation functions for different projectile energies and oxide thicknesses. The measured points represent the integrated number of counts within the resonance peak after background subtraction. The position of maximum yield is shifted with increasing oxide thickness in accordance with

$$E = E_R + \frac{\beta}{2} = E_R + N t^{\text{SiO}_2} \epsilon^{\text{SiO}_2} / 2, \quad (1)$$

where β is the thickness of the oxide in eV-s; N^{SiO_2} the density of the oxide; and ϵ^{SiO_2} the stopping cross-section of the incident beam at E_R in $\text{eV cm}^2/\text{atom} \cdot 10^{15}$. In the region of the thin target approximation, the maximum values increase linearly with target thickness [10] (curves Nos. 1 to 5).

The energy calibration was carried out on native silicon oxide where the silicon scattering yield at the oxygen energy was reduced by channelling.

The density and the stopping cross-section can be calculated either on an atomic or a molecular basis. Table I summarizes the basic values for SiO_2 , SiO and pure silicon.

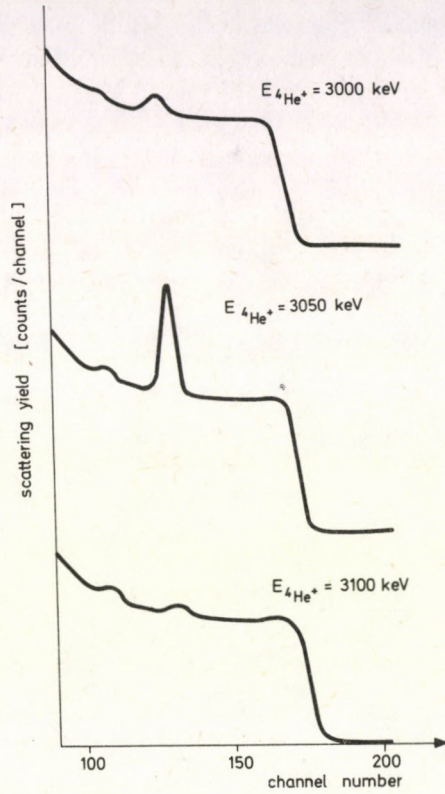


Fig. 1. Resonance character of the reaction. The bombarding energies are 3000, 3050, 3100 keV

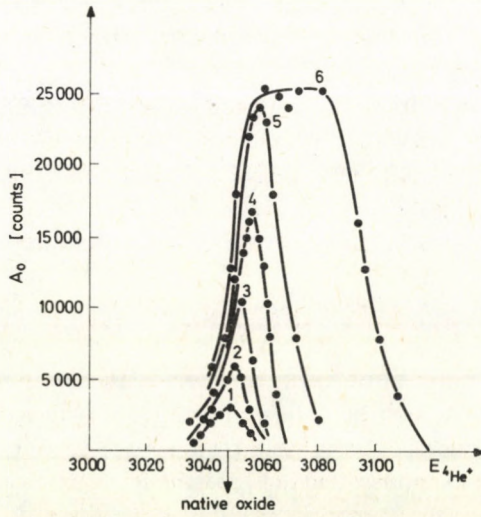


Fig. 2. Excitation function for oxides of different thicknesses

Here α_0 is the stoichiometric parameter. Both $N^{\text{SiO}\alpha_0}$ and $\sigma^{\text{SiO}\alpha_0}$ can be expressed by the number of silicon and oxygen atoms which are present in the surface layer:

$$\varepsilon^{\text{SiO}\alpha_0} = \varepsilon_{\text{Si}} + \alpha_0 \varepsilon_0 \quad (2)$$

on a molecular basis.

Table I

Elementary	
Stopping cross-sections at $E_R = 3045$ keV	
	$\varepsilon_{\text{Si}} = 39.9 \cdot 10^{-15}$ eV cm ²
	$\varepsilon_0 = 28.4 \cdot 10^{-15}$ eV cm ²
On molecular basis:	$\varepsilon^{\text{SiO}_2} = \varepsilon_{\text{Si}} + 2\varepsilon_0 = 96.7 \cdot 10^{-15}$ eV cm ²
	$\varepsilon^{\text{SiO}} = \varepsilon_{\text{Si}} + \varepsilon_0 = 68.3 \cdot 10^{-15}$ eV cm ²
Densities:	
	$n^{\text{SiO}_2} = 2.24 \cdot 10^{22}$ SiO ₂ /cm ³
	$n^{\text{SiO}} = 2.9 \cdot 10^{22}$ SiO/cm ³
	$n^{\text{Si}} = 4.99 \cdot 10^{22}$ Si/cm ³
Stopping powers	
	$S^{\text{SiO}_2} = 2.1$ eV/nm so 1 keV is equivalent to 4.6 nm
	$S^{\text{SiO}} = 1.98$ eV/nm so 1 keV is equivalent to 5.0 nm
	$S^{\text{Si}} = 2.0$ eV/nm 1 keV is equivalent to 5.0 nm

If $\alpha_0 = 2$ the oxide is SiO₂, if $\alpha_0 = 1$ the oxide is SiO. For other α_0 values the oxide is non-stoichiometric. Thus, thin oxides can be characterized by their maximum scattering yield $A(A_0^{\text{MAX}})$ and the corresponding energy shift. From these measured values the oxide thickness and the α_0 stoichiometric parameter can be evaluated.

Figure 3 shows the normalized A_0^{MAX} as a function of β for SiO₂ and SiO systems. Here δE means the energy width of the detection system in KeV/channel units and H_{Si} is the random height at the silicon edge. The clear separation between oxides of different composites comes from the difference in the stopping cross-section (Table I). Curves Nos. 5 and 6 of Fig. 2 show saturation, and the Breit-Wiegner approximation is no longer valid. For such thick layers where the yield saturates, the half of the excitation function increases as

$$\Gamma = (\Gamma^2 + \beta^2)^{1/2} \quad (3)$$

and, depending on the composition, A_0^{MAX} also varies. From the saturation values of A_0^{MAX} and Γ , β and α_0 can also be obtained. For thick oxides, however, the other method such as simple backscattering yield results more easily.

The limiting-case is demonstrated in Fig. 4; the spectrum was taken on a 113 nm thick SiO₂/Si structure as the β energy thickness is less than 3Γ , the Breit-Wiegner approximation is still valid.

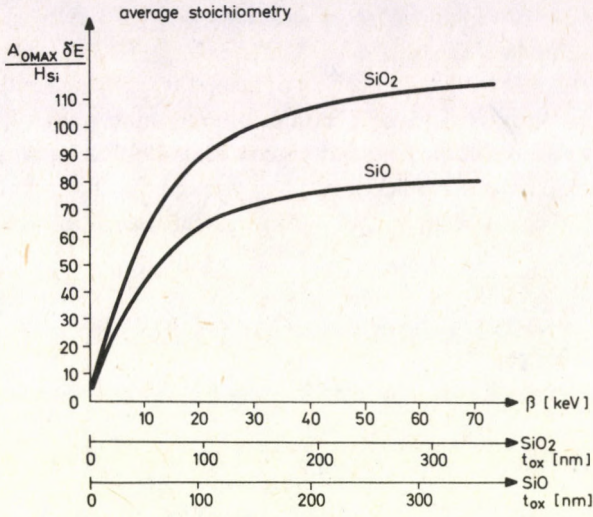


Fig. 3. Normalized oxygen peak as a function of the oxide thickness for SiO_2 and SiO

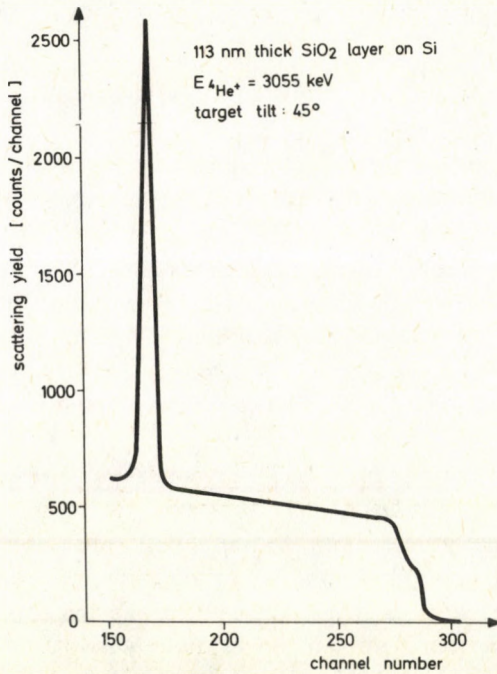


Fig. 4. RBS spectrum of a 113 nm thick oxide

b) Native oxides

The most straightforward application of resonant scattering is the measurement of stoichiometry on native oxides of silicon and compound semiconductors.

The simplest case is silicon. Chu and his coworkers [4] systematically studied the composition of silicon oxides vs thickness. They pointed out that the thinner the oxide the more surplus silicon was found; in addition, the orientation dependence of the native oxide was described. For wafers of $\langle 111 \rangle$ orientation, the quantity of oxygen and silicon was $4 \times 10^{15} \text{ cm}^{-2}$ and $1 \times 10^{16} \text{ cm}^{-2}$, respectively. For $\langle 100 \rangle$ silicon, the quantity of oxygen was below the detection limit of the 2 MeV $^4\text{He}^+$ backscattering technique, i.e. $1 \times 10^{15} \text{ cm}^{-2}$.

Using the (α, α) nuclear reaction, native oxide at both orientations can easily be measured.

Table II summarizes the results together with the surface processing.

Table II

Orientation of silicon	Processing and analysis	Quantity of oxygen [$\times 10^{15} \text{ cm}^{-2}$]
$\langle 111 \rangle$	20 min after HF etching	3.8 (0.9)
$\langle 111 \rangle$	6 months after HF etching	4.2 (0.5)
$\langle 100 \rangle$	2 min after HF etching	0.7 (0.3)
$\langle 100 \rangle$	6 months after HF etching	0.9 (0.3)

This (α, α) scattering is useful to determine the composition of very thin surface films (1.5–5 nm) on GaP subjected to the chemical treatments used in Schottky barrier technology. The composition of anodic oxide films grown on GaP were reported by Poate et al [19]. Fully oxidized native oxide layers have a Ga : P : O composition of 1 : 1.1 : 4.5 and oxygen deficiency was found for thinner layers [20].

We used typical Schottky barrier technology for the polishing, etching and vacuum evaporation. Three sets of samples were used to provide a variation of chemical process:

- i) samples etched with aqua regia, and rinsed with water;
- ii) samples etched with aqua regia, rinsed with water and then with methanol;
- iii) samples etched with aqua regia, rinsed with water, then etched with 5 wt % bromine in methanol and finally rinsed with methanol (full procedure).

The substrates were Te doped and cut in the $\langle 100 \rangle$ orientation from a liquid-encapsulated Czochralski-grown ingot. The sample was heated in vacuum, prior to metal evaporation, to the relatively high temperatures of 260 °C for 20 min. In general, thin surface oxide layers form on semiconductors immediately after etching and their thickness increases logarithmically with time under atmospheric conditions [21].

Our intention was to produce Schottky barriers on samples with the same surface conditions as those analysed by resonant backscattering. Thick gold layers would have made channelling measurements impossible; the metal deposition was performed only for the purpose of the electrical measurements; for comparability, the same timing was necessary. The actual layer thicknesses were measured by ellipsometry and they were 2.8 ± 0.15 and 3.3 ± 0.15 nm for samples i), ii) and iii) (Table III).

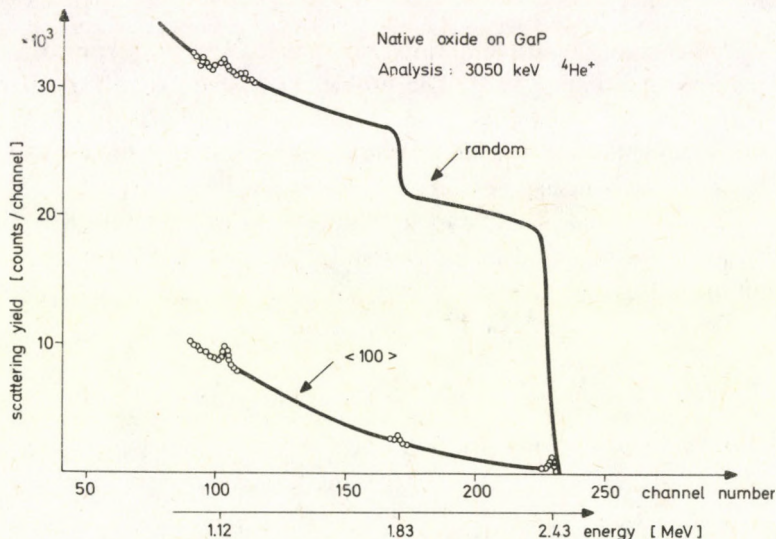


Fig. 5. Native oxide investigation on $\langle 100 \rangle$ GaP crystal

Figure 5 shows an example illustrating the sensitivity for detecting spontaneous oxide on GaP. The step height in the random spectrum at 2433 keV corresponds to the concentration of Ga atoms in the crystal, the superimposed step at 1830 keV is the contribution of phosphorus. The energy of α particles scattered on oxygen atoms corresponds to 1116 keV. The lower curve was taken in the $\langle 100 \rangle$ direction of the crystal; the peaks at the above mentioned energies correspond to the quantities of Ga and P and O atoms in the surface oxide layer.

Table III summarizes the ratios of Ga : P : O obtained from the backscattering measurements and the absolute number of oxygen atoms. The highest oxygen content was found with the bromine treatment, but in all cases oxygen deficiency was established.

Table III

Sample	Ratios of Ga : P : O	Number of O atoms cm^{-2}
i)	1 : 1.4 : 1.3	$1.66 \cdot 10^{16}$
ii)	1 : 1.5 : 1.2	$2.1 \cdot 10^{16}$
iii)	1 : 1.47 : 1.77	$1.82 \cdot 10^{16}$

From forward current-voltage measurements the n values which are sensitive to interface effects, were 1.5, 1.45 and 1.25, respectively. Similar tendency was observed for the Schottky barrier heights: 1.9, 1.85 and 1.65 eV. Thus the electrical characteristics are best for the bromine-treated sample.

c) Oxidation studies

The influence of ion-implantation on the oxidation properties of silicon and metals was an early finding [22]. The problem, however, is still of great interest especially in cases where implantation is used as a predeposition step and heat treatment is assumed to drive atoms to the proper depth and this heat treatment is performed under an oxidizing ambient.

On the other hand, if ion implantation can cause passivation of the silicon surface without causing any deterioration in its characteristics, new ideas in device fabrication may also arise.

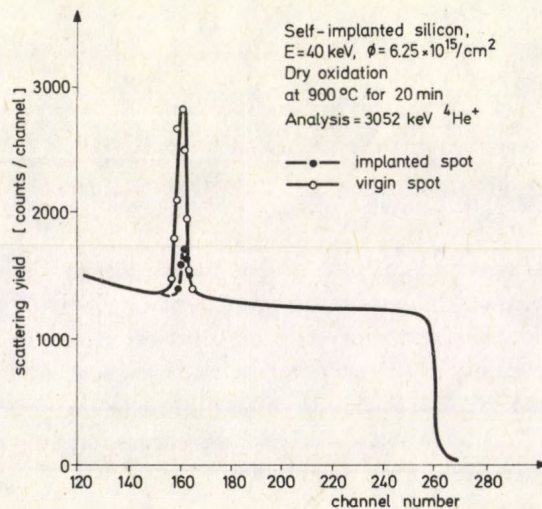


Fig. 6. Passivation studies: silicon self-implantation causes a passivation of 90%

The application of ($^4\text{He}^{++}$, $^4\text{He}^{++}$) resonance for such investigations allows us to study the earlier stage of the oxidation process where oxides are thin and no additional complications arise from stress.

Elements of groups III, IV and V were implanted into Si of $\langle 111 \rangle$ and $\langle 100 \rangle$ orientation in the energy range of 40–80 keV with doses between 1×10^{14} to

$6 \times 10^{15} \text{ cm}^{-2}$ [23]. Most of the oxidation took place in a dry O_2 atmosphere at 900°C . Special care was taken with regard to the reference samples: all samples were partly masked against the implantation beam and the implanted and non-implanted parts were not separated throughout.

If preanneals were made, usually at 550°C , 3 h was chosen in dry N_2 to achieve full regrowth [24].

To investigate the effect of crystal orientation and radiation damage on the oxidation speed, we performed silicon self-implantation in wafers of both orientations and Ge^+ implantation into $\langle 111 \rangle$ silicon at room temperature. Surprisingly both for Si^+ and Ge^+ implants efficient passivation was observed for 20 to 40 min oxidation time.

Figure 6 shows the two spectra taken on $\langle 111 \rangle$ oriented silicon: one on the implanted, the other on the virgin part of the sample. Here the passivation is more than 90%, i.e. a slowing down of the oxidation rate of more than an order of magnitude.

On samples with $\langle 100 \rangle$ orientation, the silicon self-implantation produced enhancement compared with the virgin silicon. These results suggest that the oxidation rate is orientation dependent for implanted samples and the oxidation speeds fulfil the following relation:

$$V_{\text{imp}} \langle 100 \rangle > V_{\text{virgin}} > V_{\text{imp}} \langle 111 \rangle$$

Implantation of dopant species in Si resulted in a dose dependent effect on the oxide growth rate. The effect of Sb on $\langle 100 \rangle$ Si is shown in Table IV.

Table IV

Effect of 40 keV antimony implantation on dry oxidation of $\langle 100 \rangle$ Si (relative oxide thickness for 900°C , 20 min)

Dose [cm^{-2}]	Ni/No
1×10^{13}	0.97
3×10^{14}	1.1
6×10^{14}	0.92
1×10^{15}	0.61
2×10^{15}	0.83
3.9×10^{15}	1.4
6.2×10^{15}	3.1

The impurity was investigated on $\langle 111 \rangle$ oriented Si; most impurities resulted in enhancement except for the oxidation rate of Ga. The most outstanding effect was found for antimony and arsenic. These results are summarized in Table V.

Table V

Effect of 40 keV implantation on dry oxidation of $\langle 111 \rangle$ Si (relative oxide thickness for 900 °C, 20 min)
Ni/No

Dose [cm^{-2}]	B	Al	Ga	P	As	Sb
1×10^{14}	—	—	—	—	1.51	2.5
1×10^{15}	1.71	1.25	0.74	1.52	1.65	1.2
3×10^{15}	—	1.91	—	—	2.3	3.8
6×10^{15}	1.25	—	0.37	1.61	2.3	3.1

It is clear that

- implantation of group IV elements has a great influence on oxidation (passivation);
- substrate orientation plays a substantial role;
- most implants have a strong dose effect, nevertheless, they cause enhancement.

The strict correlation between oxide growth and lattice reordering suggests that lattice disorder effects dominate or at least compensate a simple chemistry rule [6].

d) Buried oxides and comparison with other techniques [12]

In our endeavours to outline the applicability and detection limits, we prepared 5 sets of samples. In the first two sets, beneath 100 nm thick polycrystalline silicon were an 80 nm and a native oxide on $\langle 100 \rangle$ wafer, respectively. The others were implanted with O^+ ($E = 50 \text{ keV}$, 5×10^{14} , 1.5×10^{15} and 5×10^{15}). This energy corresponds to $R_p = 114 \text{ nm}$ with $\Delta R_p = 43 \text{ nm}$.

The analysis of the buried native oxide is shown in Fig. 7. At the resonant energy the surface oxygen is detected. If one increases the energy of the He^+ beam, the resonance conditions are met deeper and deeper. Between 3050–2064 keV, the oxygen content of the poly-Si is detected. At 3068 keV, the interfacial native oxide is measured by the resonance.

These measurements were compared with 2 MeV $^4\text{He}^+$ backscattering and AES and SIMS. The latter techniques were carried out at the University of Illinois, USA.

The conclusions can be summarized as follows:

- In some way or other all the techniques are able to detect oxygen.
- Conventional RBS cannot be utilized to measure buried oxygen.
- The (α, α) resonant scattering proved to be more sensitive. The 8 nm and the native oxide and the two higher dose implants can easily be measured; only the lowest dose was below the detection limit.
- Both AES and SIMS were able to detect oxygen. The most sensitive technique was

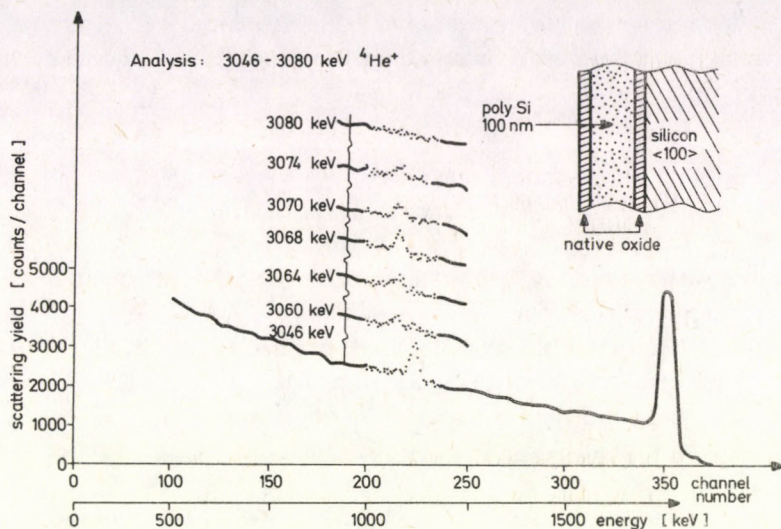


Fig. 7. Buried native oxide measurement on <100> silicon

SIMS. The limiting factor for AES was the noise in the electron detection system, for SIMS the residual gas of the chamber. Both of these contributions can be minimized: by using computer noise reduction, or by better vacuum, respectively. The detection limits for the buried oxides are shown in Table VI.

Table VI

Method	Detection limits	
	[atom %]	[atom · cm ⁻³]
2 MeV RBS	10	5×10^{21}
3.045 MeV resonance	0.5 - 1	5×10^{20}
AES	0.1	5×10^{19}
SIMS (1.10^{-5} Pa)	0.001	5×10^{17}
(1.10^{-8} Pa)	0.00002	1×10^{16}

- We would mention that for surface oxygen the detection limit of RBS and the resonant scattering decreases by a factor of two and matches AES.
- All the techniques exhibit some unique properties. For example, SIMS and the $^{16}\text{O}(\alpha, \alpha)^{16}\text{O}$ scattering are sensitive to the oxygen isotopes.
- Both ion scattering techniques can be combined with channelling; consequently, additional information can be obtained such as the orientation of polycrystallites, the radiation disorder in the case of implanted samples, and lattice location of oxygen for high concentrations.
- Both ion scattering techniques are absolute; the total amount of oxygen and the

direct depth scales can easily be obtained. For SIMS and AES, the use of standards and many corrections are necessary to quantify the measurements; but even so their quantification is still questionable.

e) Improved sensitivity and depth resolution combining resonance scattering and tilted target methods

Till now we used $\Gamma = 10$ keV which corresponds, approximately, to 50 nm in silicon and a lowered detection limit by a factor of 17.

On the other hand, the glancing angle geometry is generally used to improve both the depth resolution and sensitivity of the RBS technique [25]. Combination of the two methodological innovations gives more promising parameters, i.e. 5–10 nm depth resolution with an even lower detection limit for oxygen. For these experiments special sandwich sample configurations were prepared. Si single crystals were thermally oxidized in dry oxygen atmosphere at 800 °C. The thickness of oxide of 16 nm was determined by ellipsometry. Aluminium overlayers of 50 and 100 nm were evaporated onto the oxide. On the Al surface thin native oxide was formed. In all cases the excitation curves were measured.

Figures 8 a and b show the excitation curves measured on 100 nm thick Al overlayer by normal incidence and by applying a 81.5° target tilt. In the first case oxygen peaks from the top native oxide and the buried one are barely separated. On the tilted sample the peak-to-peak distance is 150 keV, for further calculations one has to take into account the energy thickness of the buried oxide. As was found at 21 keV (with no metal) the β value is, according to Eq. (3), 18.5 keV.

For the buried film the beam straggling has a significant contribution, too. For evaluation the formula

$$\text{FWHM} = (\beta^2 + \Gamma^2 + \delta(\Delta E)^2)^{1/2}$$

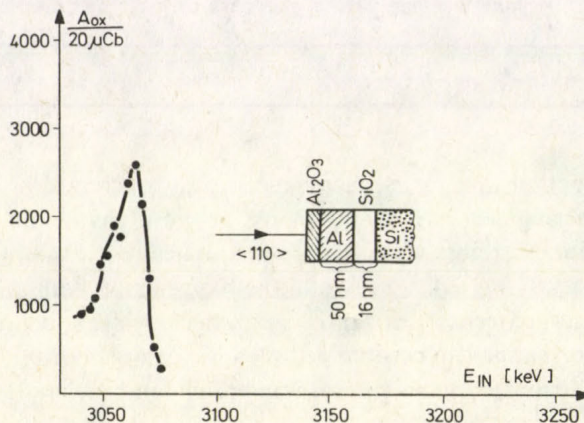


Fig. 8a. Excitation curves for surface native oxide and buried one for normal incidence

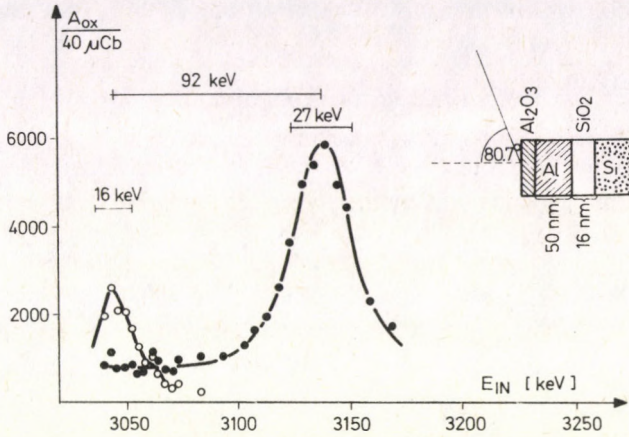


Fig. 8b. Energy scan of sandwich structure for 81.5° tilt. (magnification 6.75)

should be applied instead of Eq. (3). From the data of Fig. 8 the magnification is 6.75.

If one defines the depth resolution as a clear separation of excitation curves for two infinitely thin oxides at a given depth and the FWHM is increased only by straggling, one obtains the variation of the FWHM of the oxygen peak (the depth resolution) as a function of depth as shown in Fig. 9.

The glancing incidence gives an additional increase in the sensitivity. The variation of the signal-to-background ratio was investigated as a function of tilt angle. Figure 10 shows the ratio of the area of the oxygen peak to the silicon background in backscattering spectra taken on a 7 nm SiO₂/Si sample with different tilt angles. All spectra were measured in random directions. The sensitivity increased to a maximum of 3.5 at 83°.

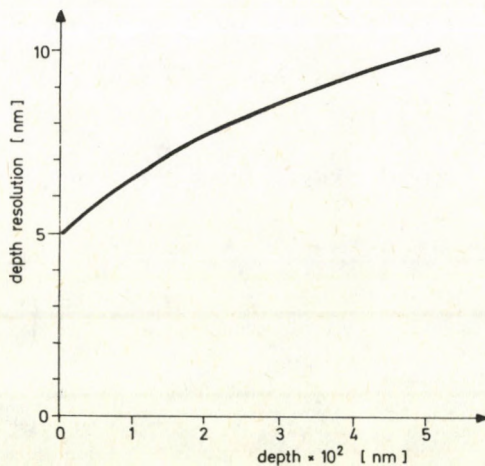


Fig. 9. Calculated depth resolution for oxygen resonance as a function of depth for buried oxides

So the ultimate sensitivity increases by a factor of 20.5. This value matches with data obtained with AES.

f) Oxygen on thin metal films

On self supporting thin layers where no scattering occurs, at the energy of oxygen the detection limit depends only on the accelerator time. An example for a 1 μm thick Al layer is shown in Fig. 11.

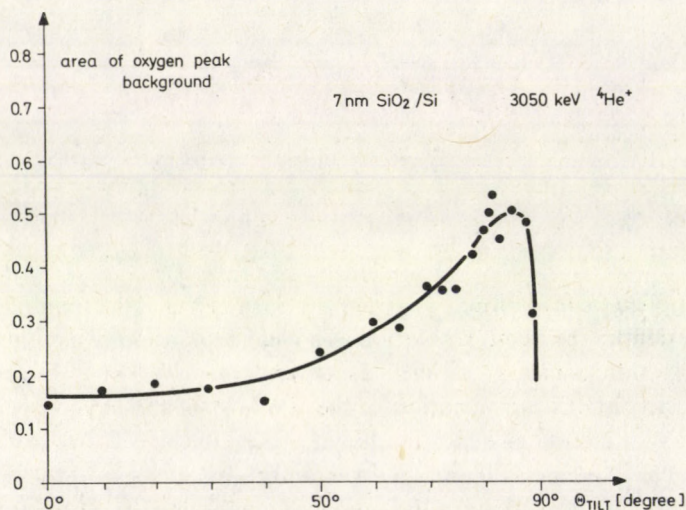


Fig. 10. Change of sensitivity for 7 nm SiO_2/Si as a function of tilt angle

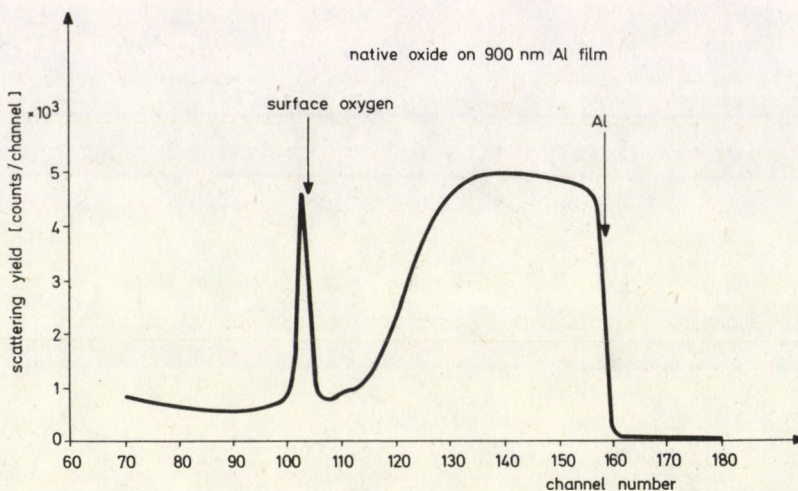


Fig. 11. Native oxide analysis on self-supporting Al film

There are some important metal sandwiches where this technique yields a very complex analysis of the structure. The spectra give both the enhanced sensitivity for absorbed or bound oxygen and the composition analysis achievable by normal backscattering.

For example in a Gd-Co system the oxygen influences the magnetic properties in several ways. It can be pointed out that the oxygen take up for Gd is much higher than for Co.

Figure 12 illustrates the power of the method, where both the amount of absorbed oxygen and composition of the sandwich were analysed.

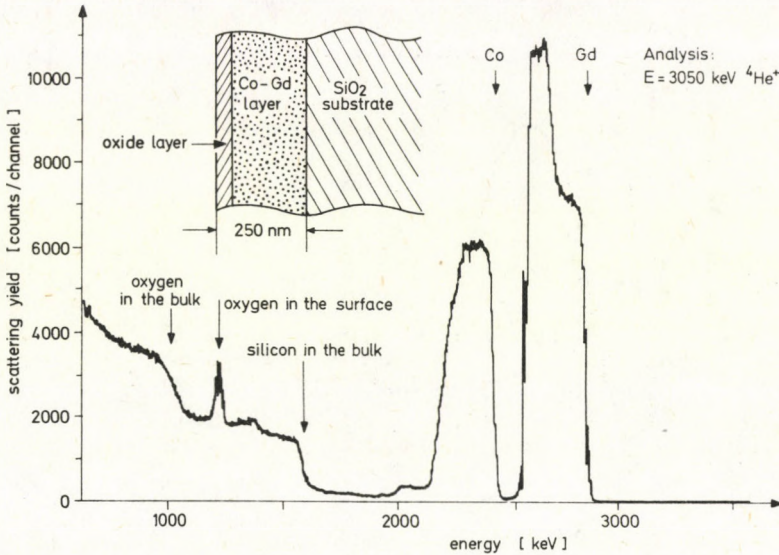


Fig. 12. Analysis of Gd-Co structure. Both surface and bulk oxygen are clearly distinguishable

g) Oxide crystals

The method offers another unique possibility when combined with channelling effect in oxygen containing crystalline materials, first of all, in oxide crystals.

Let us consider the crystal lattice of an oxide. If the single crystal is oriented with the incoming analysis beam with an axis or plane, where atomic ions contain both metal and oxygen atoms, the shadow cones of the former will mask the oxygen atoms. In a perfect crystal, therefore, normal minimum yields will be measured.

If the crystal contains damage, e.g. if it has been bombarded with particles (implanted), then atoms move out of lattice positions, thus increasing the minimum yield of channelling.

The (α, α) reaction offers now an unparalleled method to detect dislocated oxygen atoms simply by gradually increasing the bombarding energy from 3.045 MeV. If the

particles are monoenergetic to a factor of $10^{-5} - 10^{-4}$, a width of $\approx 10 - 20$ nm resolution will result from deconvolution of the oxygen signal.

Figure 13 shows an example where the oxygen damage distribution is displayed for a 80 keV neon bombarded $Y_{1.4}Sm_{0.3}Lu_{0.4}Ca_{0.9}Ge_{0.9}Fe_{4.1}O_{12}$ epitaxial layer on gallium gadolinium garnet. (The bombarding dose was 6×10^{14} atoms/cm²).

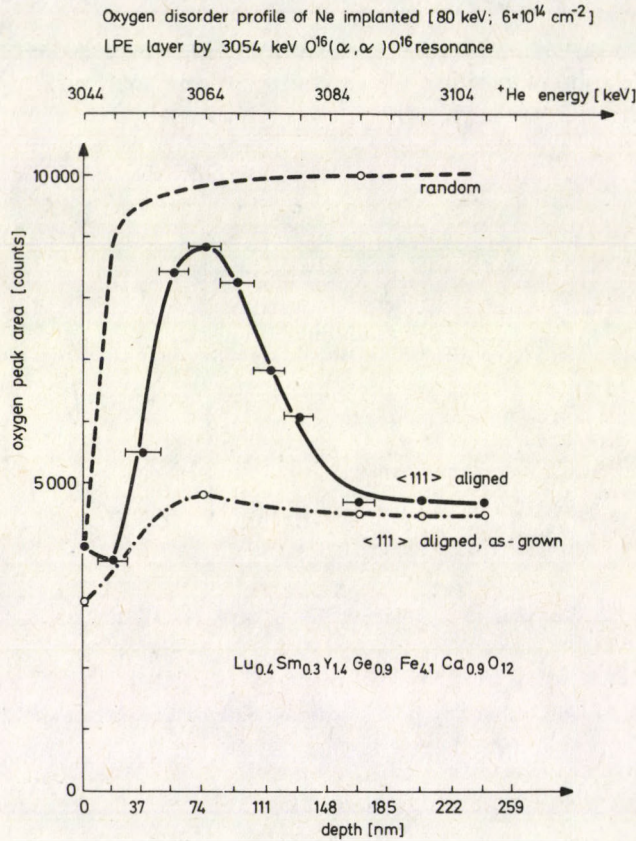


Fig. 13. Oxygen damage distribution for an 80 keV neon bombarded $Y_{1.4}Sm_{0.3}Lu_{0.4}Ca_{0.9}Ge_{0.9}Fe_{4.1}O_{12}$ with dose of 6×10^{14}

Conclusion

Comparison of the method with other ion-beam oxygen detection procedures shows that there are cases where the 3.045 MeV resonance turns out to be the most favourable.

The background sensitivity is similar to that of normal backscattering of the (p, p) reaction. Alignment of the substrate helps. For the (p, p) reaction the resonances

from the matrix may also disturb. Detection limits are not extremely low: an order of magnitude worse than AES (or the same with the tilted target method) but the absolute depth scale may compensate for this inconvenience. Nuclear reactions are also somewhat more sensitive than the (α, α) reaction, but for a natural mixture of isotopes, the (α, α) case for thin films is more favourable because of better energy resolution.

The method is capable of giving normal backscattering spectra (with the same electronics) together with enhanced sensitivity of oxygen detection. In view of this, the analysis of a film covered, say, by a native oxide is probably the most suitable problem for the method described.

References

1. G. Amsel, J. P. Nadai, E. D. Artemare, D. David and J. Moulin, *Nucl. Instr. Meth.*, **92**, 481, 1971.
2. S. T. Picraux, G. Amsel and L. C. Feldman, *Ion Beam Handbook for Material Analysis*, Eds. J. W. Mayer and E. Rimini, Academic Press, New York, 1977.
3. O. Meyer, J. Gyulai and J. W. Mayer, *Surf. Sci.*, **22**, 263, 1970.
4. W. K. Chu, E. Lugujo, J. W. Mayer and T. W. Sigmon, *Thin Solid Films*, **19**, 329, 1973.
5. G. Dearnaley, P. D. Goode, W. S. Miller and J. F. Turner, *Ion Implantation in Semiconductors and Other Materials*, Ed. B. L. Crowder, Plenum Press, New York, 1973, p. 405.
6. G. Dearnaley, J. M. Freeman, R. S. Nelson and J. Stephen, *Ion Implantation*, North Holland, Amsterdam, 1973, p. 734.
7. J. Cameron, *Phys. Rev.*, **90**, 839, 1953.
8. L. Keszthelyi, I. Demeter, G. Mezey, Z. Szőkefalvi-Nagy and L. Varga, *Proc. Int. Meeting on Ion Implantation in Semiconductors*, Rossendorf, GDR, ZfK-236, 1972, p. 111.
9. W. K. Chu, J. W. Mayer, M.-A. Nicolet, G. Amsel, T. Buck and F. Eisen, *Thin Solid Films*, **17**, 1, 1973.
10. G. Mezey, J. Gyulai, T. Nagy, E. Kótai and A. Manuaba, *Ion-Beam Surface Layer Analysis*, Eds. O. Meyer, G. Linker, F. Käppeler, Plenum Press, New York, 1976, p. 303.
11. G. Mezey, T. Nagy, J. Gyulai, E. Kótai, T. Lohner and M. Somogyi, *Thin Solid Films*, **43**, L23, 1977.
12. G. Mezey, T. Nagy, J. Gyulai, E. Kótai, T. Lohner, M. Somogyi and C. A. Evans, *Proc. 7th International Vac. Congr. and 3rd Int. Conf. on Solid Surfaces*, Vienna, 1977 p. 571.
13. M. Somogyi, M. Farkas, G. Mezey and J. Gyulai, *Thin Solid Films*, **60**, 377, 1979.
14. G. Mezey, E. Kótai, T. Nagy, L. Lohner, A. Manuaba, J. Gyulai, V. R. Deline, C. A. Evans and R. J. Blattner, *Nucl. Instr. Meth.*, **167**, 279, 1979.
15. G. Battistig, P. Révész, E. Kennedy and J. Gyulai, to be published.
16. E. Kótai, G. Mezey, T. Lohner, A. Manuaba, F. Pászti and J. Gyulai, *Nucl. Instr. Meth.*, **180**, 619, 1981.
17. I. Gyuro, E. Lendvay, T. Görög, T. Lohner, M. Hársy, I. Pozsgai, K. Somogyi, J. Gyulai, M. Ránki, L. Varga, R. Koltai, J. Giber, L. Bori, L. L. Regel, N. A. Kulchitskiy and V. T. Khryapov, to be published in *Proc. XXXIV Congress of the International Astronautical Federation*.
18. Z. L. Yang, J. F. M. Westendorp and F. W. Saris, *Nucl. Instr. Methods*, **211**, 193, 1983.
19. J. M. Poate, T. M. Buck and B. Schwartz, *J. Chem. Solids*, **34**, 779, 1973.
20. J. M. Poate, P. J. Silverman and J. Yehalan, *J. Electrochem. Soc.*, **120**, 844, 1973.
21. F. Kukes, *Surf. Sci.*, **30**, 91, 1972.
22. O. Meyer and J. W. Mayer, *Rad. Effects*, **3**, 139, 1970.
23. G. Mezey, T. Nagy, J. Gyulai, E. Kótai, A. Manuaba, T. Lohner and J. W. Mayer, *Ion Implantation in Semiconductors*, 1976. Eds. F. Chernow, J. A. Borders and D. K. Brice, Plenum Press, New York, 1977, p. 49.
24. H. Muller, W. K. Chu, J. Gyulai, J. W. Mayer, T. W. Sigmon and T. R. Cass, *Appl. Phys. Lett.*, **26**, 292, 1975.
25. J. S. Williams and W. Möller, *Nucl. Instr. Meth.*, **157**, 213, 1978.

INVESTIGATIONS ON FAST NEUTRON INTERACTIONS WITH CONSTRUCTIONAL MATERIALS*, **

L. VASVÁRY, F. DIVÓS,*** G. PETŐ, J. CSIKAI and N. K. MUMBA****

*Institute of Experimental Physics
4001 Debrecen, Hungary*

On the basis of flight-time difference the direct and scattered neutrons as well as gammas produced in the target head and samples were separated. Using this method the attenuation of primary neutrons and gammas originating from the target head has been studied in addition to the measurements on the thickness dependence of the secondary gamma yield from extended samples of Al, Fe, Pb, paraffin and reinforced concrete. Results indicate a geometry dependence of the removal cross sections.

The removal cross section of brick, gravel, sand, river sand, reinforced concrete and water has also been measured by activation threshold detector technique.

1. Introduction

The removal cross section can be used for a rapid estimation of the necessary shielding for fast neutron sources [1]. Removal cross sections have been measured [1, 2, 6, 7] for various elements and construction materials by activation threshold detectors. The time of flight spectrometry seems to be a suitable technique to determine the removal cross sections in a more rapid way and, additionally, it gives the possibility to study the induced secondary radiations having an important role in the accurate determination of dose rates.

The aim of the present work is to provide more data for the calculation of shielding around neutron generators as well as to study the applicability of the time of flights (T.O.F) technique.

2. Experimental technique

The time of flight spectrometer [8] based on nanosecond pulsed neutron generator [4, 5] has been used for the measurements. Neutrons were produced in D + T reaction with a pulse width of 2 ns and an average current of 5 μ A with a repetition rate of 1.25 Mcps. The NE-218 type neutron detector was placed inside a shielding having a 44 cm deep cylindrical collimator with a diameter of 11 cm, at 90° to the direction of the

* Dedicated to Prof. S. Szalay on the occasion of his 75th birthday with the compliments of his former students.

** This work was supported in part by IAEA

*** Present address: Nuclear Power Station, Paks, Hungary

**** Permanent address: National Council for Scientific Research, Lusaka, Zambia.

ion beam. The source-detector and the source-sample distances are 283 cm and 29.5 cm, respectively. The sample sizes are given in Table I. As can be seen in Fig. 1 the gammas from the target head and from the samples as well as the primary neutrons can easily be separated on the basis of flight times at the present resolution of 3.4 ns.

Table I

Removal cross sections for construction materials measured by activation threshold detector technique

Material	Density [g/cm ³]	Sample size [cm]	Σ [cm ⁻¹]
Brick	1.63	75 × 35	0.0478 ± 0.0019
Gravel	1.83	50 × 50	0.0517 ± 0.0021
Dried sand	1.49	50 × 50	0.0461 ± 0.0018
Dried river sand	1.60	50 × 50	0.0465 ± 0.0019
Reinforced concrete	2.39	20 × 20	0.0761 ± 0.0023
		50 × 50	0.0777 ± 0.0019
Water	0.999	50 × 50	0.0819 ± 0.0033

A stylyene crystal was used for monitoring at 90° to the beam direction. The primary neutrons were also selected on the basis of flight times. A more detailed description of the measuring system is given in [8].

The same threshold detector activation technique was used as in our previous measurement [2] completing it with an aluminium container for sand and water samples.

3. Results and discussion

The results of the activation threshold detector measurements are summarised in Table I. These materials were used in the building constructed for the high current neutron generator of the Institute. No deviation was observed for sands of different origin. The change in the sample size causes also a negligible influence on the removal cross section in the case of concrete.

Using the time of flight technique the primary neutron peaks obtained at different sample thicknesses for a given monitor counts were evaluated choosing different energy regions. This method renders it possible to compare the results for the removal cross sections obtained by activation and T.O.F. techniques. The primary neutron intensities as a function of sample thickness for different materials are plotted in Fig. 2. The removal cross sections determined by least square fits are listed in Table II. Strong threshold dependence of the removal cross sections was obtained only for lead due to the contribution of inelastic scattering. The gamma intensities from the target head as well as from the samples in function of sample thickness are given for different materials in Figs 3 and 4

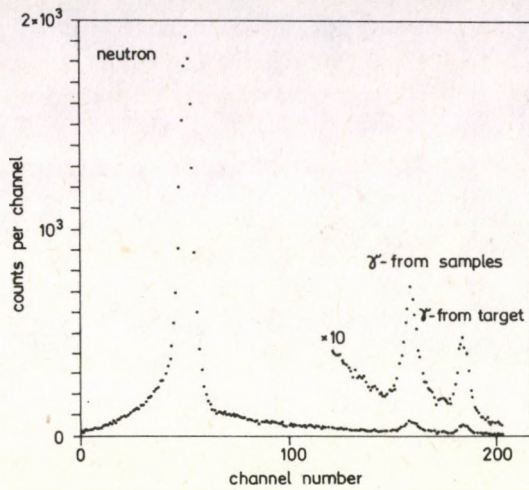


Fig. 1. Time distribution of pulses by neutrons and gammas

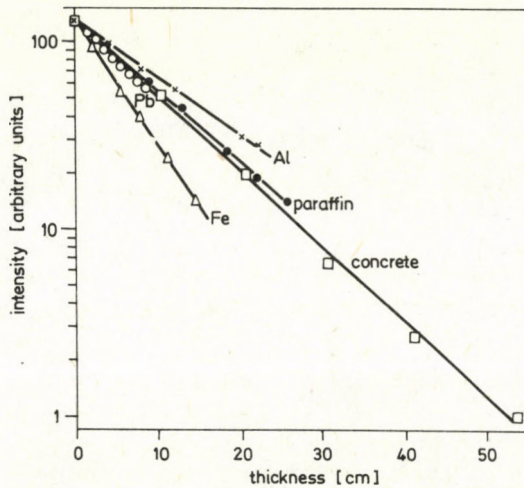


Fig. 2. Attenuation of primary neutrons in different materials

The energy spectrum of gammas has not been determined in this experiment. However, on the basis of the gamma attenuation coefficient of 0.5 cm^{-1} obtained for lead, the average energy of the gammas from the target head was found to be about 2.5 MeV. The spectrum of secondary gammas from the samples is very complex, therefore, an average energy cannot be deduced from the results. The gamma yield curves show a maximum at thicknesses of about 5 cm, 7 cm and 15 cm for lead, iron and concrete, respectively (see Figs 3 and 4).

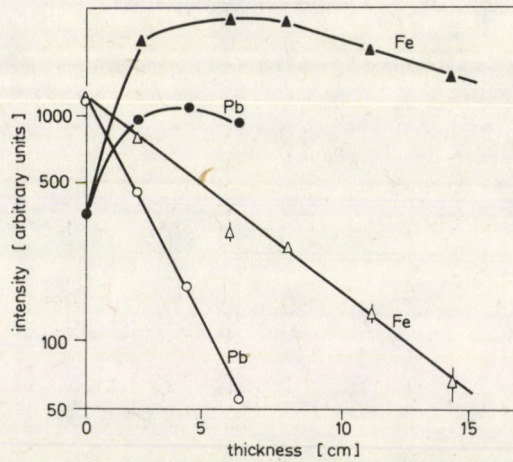


Fig. 3. Attenuation of gamma radiation from the target head in steel (triangles) and in lead (circles) as well as the secondary gamma-ray yield from steel (full triangles) and lead (full circles) samples

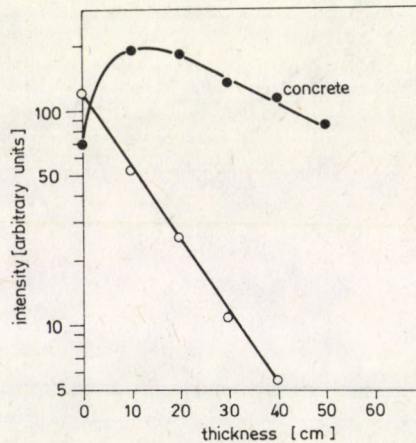


Fig. 4. Attenuation of gamma radiation from the target head in concrete (circles) as well as the secondary gamma yield (full circles) from this sample

According to the data listed in Table II the removal cross sections have no strong dependence on the change of detection threshold, therefore, the deviation of about 20% between the present results and the earlier data obtained by activation technique can only be explained by the geometry difference of the measurements. This was also proved by the Monte Carlo calculations [3] indicated in Fig. 5. The removal cross

Table II

Removal cross sections measured by time of flight technique using different thresholds

Sample	Size [cm]	Σ [cm^{-1}]		
		$E_{\text{thr}} = 11 \text{ MeV}$	$E_{\text{thr}} = 13 \text{ MeV}$	$E_{\text{thr}} = 14 \text{ MeV}$
Steel	disks, $\varnothing 30$	—	0.1483 ± 0.0017	0.1519 ± 0.0018
Aluminium	slabs, 30×30	—	0.0708 ± 0.0022	0.0708 ± 0.0012
Lead	slabs, 30×30	0.1156 ± 0.0049	0.1099 ± 0.0028	0.0899 ± 0.0054
Paraffin	disks, $\varnothing 30$	0.0816 ± 0.0019	0.0856 ± 0.0013	0.0929 ± 0.0018

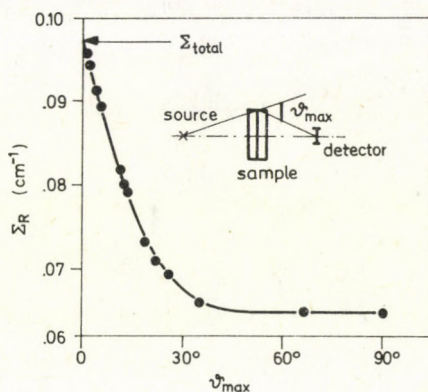


Fig. 5. The removal cross section of paraffin as a function of maximum scattering angle calculated (3) by the Monte Carlo method

section for paraffin was calculated as a function of maximum scattering angle defined by the geometry as shown in Fig. 5. The relative good agreement between the previous removal cross section measurements [1, 2, 6, 7] performed at different geometrical conditions can be explained only if one supposes that the maximum scattering angle was higher than about 45° . In the present measurements the maximum scattering angle was about 30° due to the large sample-detector distance needed for the time of flight technique, resulting in larger removal cross sections than those obtained by the foil activation method. These results confirm that the removal cross section concept might give only a rough estimate in the shielding designs.

Using the present experimental arrangement with an additional gamma spectrometer gated according to the flight time of gammas from the samples, more detailed data should be obtained for shielding calculations.

References

1. S. S. Nargolwalla and E. P. Przybylowicz, *Activation Analysis with Neutron Generators*, J. Wiley and Sons, New York/London/Sydney/Toronto, 1973.
2. A. Boufraquech, G. Pető and J. Csikai, *Acta Phys. Hung.*, 55, 33, 1984.
3. F. Divós, *ATOMKI Report*, X/4, 1983.
4. T. Sztaricskai, L. Vasváry and G. Pető, *Proceedings of the Vth International Symposium on Interactions of Fast Neutrons with Nuclei, Organised by the Technical University, Dresden, Nov. 17-21, 1975, Gaussig, GDR. ZfK-324*, p. 218, 1976.
5. L. Vasváry, T. Sztaricskai, G. Pető and B. V. Devkin, *ZfK-476*, p. 88, 1982.
6. P. N. Cooper and S. M. Kabir, *J. of Nucl. Energy*, 26, 569, 1972.
7. O. Bozyap and L. R. Day, *Health Physics*, Pergamon Press, 28, 101, 1975.
8. A. V. Anriashin, B. V. Devkin, A. A. Lychagin, J. V. Minjko, A. N. Mironov, V. S. Nesterenko and T. Sztaricskai, G. Pető, L. Vasváry to be published.

ELASTIC SCATTERING OF ELECTRONS ON He, Ne, Ar IN THE IMPACT ENERGY REGION FROM 1000 TO 3000 eV*

J. HERBÁK**, Á. KÖVÉR, E. SZMOLA***, D. BERÉNYI and I. CSERNY

*Institute of Nuclear Research of the Hungarian Academy of Sciences
4001 Debrecen, Hungary*

Elastic electron scattering cross sections for He, Ne and Ar targets were determined at 1000, 2000 and 3000 eV impact energy in the angular region from 49.6° to 130° by using a special double cylindrical mirror electron spectrometer, an electron gun and a gas beam target array. At 200, 500 and 800 eV, respectively, measurements were carried out also for normalization and/or checking.

Introduction

In the last few years a great number of papers were published on the elastic scattering of electrons (see e.g. a recent survey in [1]). Measurements of the differential cross sections, however, were carried out over a wide angular range (especially at higher angles) only at relatively smaller impact energies.

As regards the target species, in the case of He, Williams and Willis published cross section data for incident electron energies from 20 to 400 eV over the angular range from 20° to 150° [2]. Kurepa and Vuskovic measured the cross section for impact energies of 100, 150, 200 eV in the angular range between 5° and 150° [3]. Shyn [4] and Register et al [5] determined the elastic cross section for the impact energy range of 2 to 400 eV and 5 to 200 eV, respectively, in the angular region from 6° to 156° and from 10° to 140° , respectively. The last case, however, was measured as a proposed calibration standard with an estimated accuracy of the data within 5 to 9%, depending on the impact energy.

For Ne gas as the target, DuBois and Rudd [6] published results in the energy range 50–800 eV between 2° and 150° , and Williams and Crowe have results in the range 20–400 eV between 20° and 150° [7]. Elastic scattering cross sections for Ar, however, were determined by DuBois and Rudd [6] and by Srivastava et al [8], in the energy range from 20 to 800 eV and from 3 to 100 eV, respectively; the angular range covered was from 2° to 150° [6] and from 20° to 135° [8], respectively.

* Dedicated to Prof. S. Szalay on his 75th birthday

** Permanent address: Medicor Works, Debrecen, Hungary

*** Permanent address: Department of Physics, Technical University for Heavy Industry, Miskolc,

Hungary

The only paper where the elastic scattering of electrons was studied in the relatively higher impact energy region, namely from 100 to 3000 eV, was published by Jansen et al [9] but at the same time, they have data only at the scattering angles between 5° and 55° .

In the present paper our purpose was to study the elastic scattering of electrons in the impact energy range from 1000 to 3000 eV on He, Ne and Ar at scattering angles between 49.6° and 130.0° , where the experimental data are completely lacking. For normalization and checking purposes, several measurements were carried out at some other impact energies too (200, 500, 800 eV).

As regards the theoretical interpretation many calculations on the elastic scattering of electrons have been published, especially on the differential cross section for elastic electron scattering (recently e.g. [10–12]; see a short survey in [1]). However, the number of calculations at the higher impact energy region, where measurements were carried out, is very small. The theoretical values of McCarthy et al [13] seem to be the most suitable for comparison with the present experimental results. These calculations were performed on the basis of an optical model for a number of target gases (He, Ne, Ar, Kr, Xe) in a wide impact energy and scattering angle region (from 20 to 3000 eV; from 5° to 170°) and the calculated values are given in very detailed tabulations.

Experimental

The measurements were carried out by means of a new double, distorted field cylindrical mirror electron spectrometer (ESA-13) with second order focusing, constructed at this Institute [14]. The entrance angle of the analyser was 43.5° relative to the axis of the cylinders. The schematic diagram of the spectrometer and the experimental arrangement are given in Fig. 1.

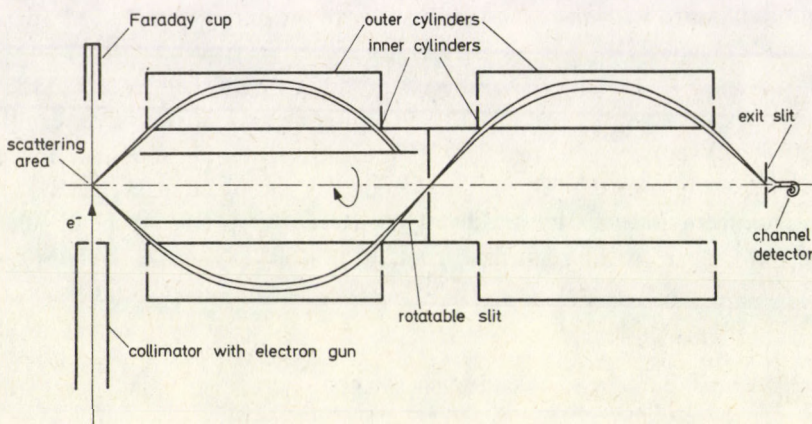


Fig. 1. Schematic diagram of the experimental arrangement

A slit on the surface of a cylinder inside the spectrometer cylinders was turned around during the measurements to make it possible to set the required angle, relative to the direction of the electron beam, for the scattered electrons to be detected (see "rotatable slit" in Fig. 1).

The magnetic field inside the spectrometer was reduced to less than 10 nT (1 mG) by using two coaxial mu-metal shielding cylinders. The relative energy resolution of the spectrometer was 0.3%. The direction of the electron beam was perpendicular to the spectrometer axis. In order to form the electron beam and to define its direction, a collimator system was used with 3 diaphragms ($\varnothing 1$, $\varnothing 1$, $\varnothing 1.7$ mm).

The direction of the gas beam target was perpendicular to the plane defined by the axis of the spectrometer and the direction of the electron beam from the electron gun. The nozzle was a $\varnothing 0.5 \times 5$ mm tube. A piece of a channel plate was fixed to the exit of the tube in order to create a multi-hole nozzle. In this case the profile of the gas beam was far better than a single tube array. The nozzle was just above the electron beam where the electrons scattered from the surface of the nozzle were certainly not detectable in the spectrometer (about 1 mm). The pressure of the gas buffer (in front of the nozzle) was stabilized with the help of an electromagnetic membrane valve and a Pirani gauge. The typical pressure in the buffer was 5 mbar. The overall pressure in the collision chamber was about 1.10^{-6} Pa without, and about 2.10^{-5} Pa with the operation of the beam-target, respectively.

The electron gun was fixed to the collimator. It was a Pierce type, with an indirectly heated oxide cathode. The heating current of the cathode was stabilized.

Measurement control and data acquisition were carried out by a TPA-i small computer. The other electronic units (CAMAC control units, power supplies) were similar to those used earlier [15, 16]. The electrons were detected by a channel electron multiplier: type B419 BL/01.

The present measurements produce only relative differential elastic cross sections. These cross sections are put on an absolute scale as follows. In the case of Ar and Ne our data were normalized to the absolute data of DuBois and Rudd [6] for every angle at 800 eV electron impact energy by dividing their cross section values by our corresponding intensity data:

$$\frac{\sigma(800, \theta)}{I(800, \theta)} = a(\theta) \quad \theta = 49.6^\circ, \dots, 130^\circ. \quad (1)$$

For an He target a similar procedure was carried out by using the data of Register et al [5] at 200 eV.

To use the $a(\theta)$ factors, it is not sufficient for one to have absolute cross section values in the present experimental arrangement. Thus at the different impact energies our data are normalized to those of Jansen et al [9] for every target (He, Ne, Ar) at 50° scattering angle (after interpolation to 49.6°):

$$\frac{\sigma(E, 50^\circ)}{I(E, 50^\circ)} = b(E, 50^\circ). \quad (2)$$

The absolute differential cross section will be determined according to

$$\sigma(E, \theta) = a(\theta) \cdot b(E, 50^\circ) \cdot J(E, \theta). \quad (3)$$

Figure 2 shows the comparison of our data with those of DuBois and Rudd at 500 eV impact energy for Ne and Ar.

To estimate the errors in the present measurements, the contributions from the errors of the data of DuBois and Rudd as well as those of Register et al were taken into consideration in addition to the statistical error. These errors are below 20% in every case.

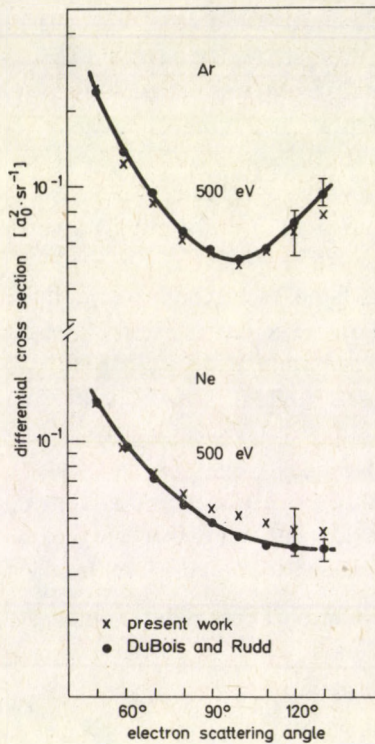


Fig. 2. Comparison of our experimental data with the corresponding ones published by DuBois and Rudd [6]

The actual values of the errors are indicated in some cases in Fig. 3. It should be mentioned, however, that the real errors may be somewhat higher than these values, as is also true for other published differential cross section data. This is shown by the deviations of the corresponding values of different authors.

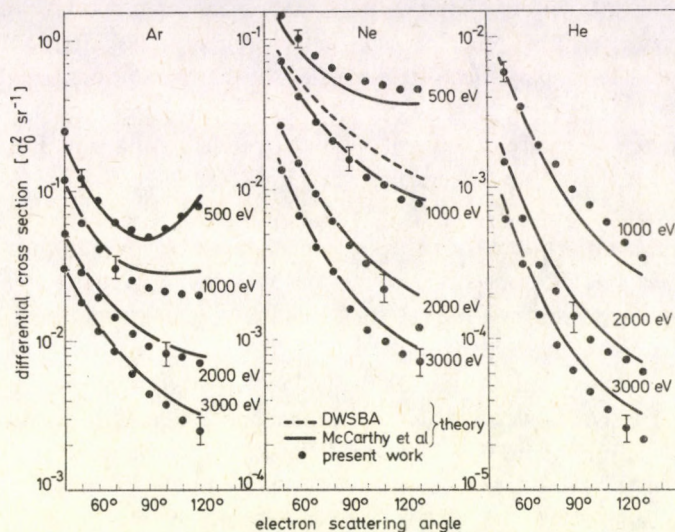


Fig. 3. Differential elastic cross sections determined in the present study in comparison with the theoretical values of McCarthy et al [13]. In one case of Ne (1000 eV) the results of Dewangan and Walters' calculations (DWSBA) [10] are also indicated

Results and discussion

The results obtained in the present measurements for the differential elastic cross sections in the case of He, Ne and Ar are given in Table I at 1000, 2000 and 3000 eV impact energy.

Table I

Differential cross sections for elastically scattered electrons (in units of $a_0^2 \cdot sr^{-1}$)

θ	He			Ne			Ar		
	1000	2000	3000	1000	2000	3000	1000	2000	3000
49.6°	5.72(-3)*	1.46(-3)	6.09(-4)	7.00(-2)	2.60(-2)	1.36(-2)	1.13(-1)	5.32(-2)	3.09(-2)
60.8°	3.44(-3)	6.10(-4)	3.10(-4)	4.26(-2)	1.47(-2)	6.85(-3)	6.11(-2)	2.88(-2)	1.83(-2)
69.8°	1.90(-2)	3.02(-4)	1.40(-4)	2.77(-2)	9.18(-3)	4.16(-3)	4.16(-2)	1.98(-2)	1.17(-2)
79.7°	1.40(-3)	2.10(-4)	9.02(-5)	2.12(-2)	6.02(-3)	2.86(-3)	3.01(-2)	1.43(-2)	8.66(-3)
90.0°	9.58(-4)	1.38(-4)	6.00(-5)	1.57(-2)	4.15(-3)	1.59(-3)	2.56(-2)	1.13(-2)	6.02(-3)
100.2°	7.66(-4)	9.86(-5)	4.36(-5)	1.17(-2)	3.18(-3)	1.17(-3)	2.28(-2)	9.22(-3)	4.44(-3)
110.1°	5.88(-4)	7.98(-5)	3.29(-5)	1.05(-2)	2.16(-3)	9.87(-4)	2.18(-2)	8.38(-3)	3.77(-3)
119.1°	4.25(-4)	7.00(-5)	2.48(-5)	8.35(-3)	1.62(-3)	8.08(-4)	2.03(-2)	7.89(-3)	2.99(-3)
130.0°	3.33(-4)	5.86(-5)	2.08(-5)	7.88(-3)	1.20(-3)	7.25(-4)	2.00(-2)	7.01(-3)	2.48(-3)

(*5.72(-3)=0.00572)

In Fig. 3 our data are compared with the theoretical calculations of McCarthy et al [13]. In one case the theoretical values of Dewangan and Walters [10] are also indicated. In the latter paper, however, the results of the calculations are not given in tabulations only in diagrams, so their reading out is rather inaccurate.

The present values are compared with the published data in Fig. 2. To our knowledge, no other data have been published for 1000, 2000 and 3000 eV electron impact energy.

As regards comparison of our results with theory, the conclusion is as follows. The agreement at smaller angles is better in general. It is a tendency which can be observed in other cases too when experiment and theory are compared.

In some cases the agreement is particularly good, e.g. for Ne at 49.6, 60.8 and 69.8° if the impact energy is 1000 and 2000 eV. The overall disagreement is the largest for He. For as Ar target, however, at 500 eV impact energy the agreement is very good at every angular value, where we determined the experimental cross sections in this study.

Acknowledgement

The authors are indebted to Mr. L. Gulyás for his technical assistance during the measurements.

References

1. E. Szmola and J. Herbák, *ATOMKI Közl.*, to be published.
2. J. F. Williams and B. A. Willis, *J. Phys. B: Atom. Molec. Phys.*, **8**, 1670, 1975.
3. M. V. Kurepa and L. Vuskovic, *J. Phys. B: Atom. Molec. Phys.*, **8**, 2067, 1975.
4. T. W. Shyn, *Phys. Rev. A*, **22**, 916, 1980.
5. D. F. Register, S. Trajmar and S. K. Srivastava, *Phys. Rev. A*, **21**, 1134, 1980.
6. R. D. DuBois and M. E. Rudd, *J. Phys. B: Atom. Molec. Phys.*, **9**, 2657, 1976.
7. J. F. Williams and A. Crowe, *J. Phys. B: Atom. Molec. Phys.*, **8**, 2233, 1975.
8. S. K. Srivastava, H. Tanaka, A. Chutjian and S. Trajmar, *Phys. Rev. A*, **23**, 2156, 1981.
9. R. H. J. Jansen, F. J. de Heer, H. J. Juyken, B. van Wingerden and J. J. Blaamur, *J. Phys. B: Atom. Molec. Phys.*, **9**, 185, 1976.
10. D. P. Dewangan and H. R. J. Walters, *J. Phys. B: Atom. Molec. Phys.*, **10**, 637, 1977.
11. W. C. Fon, K. A. Berrington and A. Hibbert, *J. Phys. B: Atom. Molec. Phys.*, **14**, 307, 1981.
12. W. C. Fon and K. A. Berrington, *J. Phys. B: Atom. Molec. Phys.*, **14**, 323, 1981.
13. I. E. McCarthy, C. J. Noble, B. A. Phillips and A. D. Turnbull, *Phys. Rev. A*, **15**, 2173, 1977.
14. D. Varga, A. Kövér, L. Kövér, R. Redler, J. Herbák, E. Szmola, I. Cserny, Gy. Móri, *Nucl. Instrum. Meth.* in print.
15. I. Kádár, B. Sulik, I. Cserny, T. Lakatos and J. Végh, *ATOMKI Közl.* **23**, 42, 1981.
16. I. Cserny, Doctoral thesis, *ATOMKI*, Debrecen, 1982.

INVESTIGATION OF L-SUBSHELL IONIZATION OF GOLD BY LOW VELOCITY PROTON BOMBARDMENT*

K. KISS, T. PAPP, J. PÁLINKÁS, L. SARKADI and B. SCHLENK

*Institute of Nuclear Research of the Hungarian Academy of Sciences
4001 Debrecen, Hungary*

Proton induced X-ray emission was used to measure absolute L-subshell and total L-shell ionization cross sections of gold in the energy range 0.2–0.6 MeV. The experimental results were compared with the predictions of two versions (RPWBA-BC, CPSSR) of the plane wave Born approximation.

1. Introduction

In the past few years many investigations were carried out by bombarding solid targets with different ions and detecting the emitted X-rays as a means of studying the characteristics of the inner shell ionization processes. Most of these studies focused on K-shell ionization, and attention has only recently been called to L-shell ionization [1–16]. Inner-shell ionization cross sections are not only of practical interest (e.g. for material analysis, etc.) but in addition they make it possible to test the different collision theories. Among these theories considerable efforts were made to extend the region of validity of the PWBA (plane wave Born approximation) to make it suitable to describe the K- and the L-shell ionization of medium and heavy elements at light ion impact in a broad energy range [7–11]. Corrections have been developed for the phenomena of the so-called “increased binding energy” and “Coulomb deflection and retardation”, and the importance of the electronic relativistic effects in the target atomic states has also been recognized. The CPSSR [7] and the RPWBA-BC [11] theories came into being in these ways and they gave, generally, good agreement with the experimental data in the case of light ion impact on heavier target elements at higher energies [1, 8, 12, 13]. At low energies however, if the atomic number of the bombarding particle (Z_1) is larger than one, the experimental results show large deviations from the CPSSR theory [14]. These deviations are, for example, greater than one order of magnitude in the low projectile velocity region at $Z_1 = 7$ [14]. To clarify the reason for this discrepancy, in an earlier work we studied the atomic number dependence of the L-subshell ionization cross sections by bombarding Sm, Er, Au targets with $^2\text{H}^+$, $^4\text{He}^+$, $^{12}\text{C}^+$, $^{14}\text{N}^+$ projectiles [15]. The measured cross sections were normalized to the deuteron data and

* Dedicated to Prof. S. Szalay on his 75th birthday.

the largest deviations from the CPSSR theory were found at $Z_1 = 6,7$. These deviations could be reduced when some kind of second order effects were taken into account [15, 16, 17]. On the basis of the existing data, the agreement between the CPSSR values and the experimental L-subshell ionization cross sections seems to be good for protons and deuterons of low energy. The measured absolute L-subshell ionization cross sections below 0.8 MeV bombarding energies are, however, incomplete or not accurate enough to draw an unambiguous conclusion.

In view of this we set out to measure absolute L-subshell ionization cross sections of gold by proton bombardment in the energy range 0.2–0.6 MeV, and to compare these data with the CPSSR and RPWBA-BC theories.

2. Experimental procedure

The description of the experimental arrangement can be found in [14, 15]. About $80 \mu\text{g}/\text{cm}^2$ thin targets were evaporated onto $20 \mu\text{g}/\text{cm}^2$ carbon backings and irradiated with a well collimated proton beam from the 800 kV Cockroft–Walton generator of the institute. The emitted X-rays were detected by a KeVeX Si(Li) detector at an angle of 55 degrees. The scattered projectiles were also detected by means of a silicon surface barrier detector. The energy loss of the protons in the target was taken into careful consideration in the same way as in [15].

The measured X-ray spectra were evaluated by using an iterative Gaussian fitting program, and the L_{α} , $L_{\gamma 1}$, $L_{\gamma 2, 3, 6}$ peak areas were extracted. The scattered particle spectra were analysed by using a simple background subtraction procedure. From the ratios of the X-ray yields to the yield of the scattered protons we determined the X-ray production cross sections with the aid of calculated Rutherford scattering cross sections. In these calculations we used a shell-shielded Coulomb potential [18] to calculate the Rutherford scattering cross sections. To spare the efficiency calibration of the X-ray detector and the determination of the solid angles of both detectors, we normalized our present cross section values to those obtained in an earlier measurement [5], viz. to the total L-shell X-ray production cross section at 0.5 MeV proton energy ($(0.530 \pm 0.08) \times 10^{-24} \text{ cm}^2$). The L-subshell ionization cross sections were determined from the L_{α} , $L_{\gamma 1}$, $L_{\gamma 2, 3, 6}$ X-ray production cross sections according to the method proposed by Datz et al [1]. In this conversion the fluorescence yields and the Coster–Kronig transition probabilities of Krause [19], as well as radiative transition widths of Scofield [20] were used.

In this low energy region the subshell ionization cross sections depend very strongly on the bombarding energy (proportional to E^7). This implies that the determination of the energy loss correction introduces considerable uncertainties to the cross section values. Due to this and to the uncertainties of the applied atomic parameters, the accuracy of the obtained cross section values is estimated to be 20%.

3. Results and discussion

The measured L-subshell and total L-shell ionization cross sections are given in Table I and are shown in Figs 1–4. In order to compare our data with those of other authors the L-shell ionization cross-sections are also plotted in Figs 1–4. The predictions of the CPSSR and RPWBA-BC theories are also shown for comparison.

Table I

Measured L-subshell ionization cross sections for proton impact on gold
(in units of 10^{-24} cm²)

Bombarding energy [MeV]	L_1	L_2	L_3	L_{tot}
0.2	0.002	0.0002	0.002	0.0042
0.4	0.19	0.062	0.33	0.57
0.5	0.41	0.21	0.98	1.6
0.6	0.65	0.46	2.1	3.2

(errors in the tabulated values are 20%)

In the Figures the ionization cross sections are shown as functions of the bombarding energy. The full curves are the results of the RPWBA-BC, the broken curves are associated with the CPSSR theory. The earlier experimental results are marked with triangles [1] and open circles [2]. The filled circles represent the results of our measurements.

As can be seen from Figs 1–4, the RPWBA-BC and the CPSSR theories describe the measured L-subshell and total L-shell ionization cross sections within the error limits, when the bombarding energy is larger than 0.3 MeV. Deviations exceeding the error limits occur only at 0.2 MeV energy. The data at the lowest energies are not accurate enough to see the region of validity of both theories. Further accurate measurements are necessary to clarify the low velocity limit of these theories.

Acknowledgement

Thanks are due to Mr. F. L. Gáll for his excellent technical assistance.

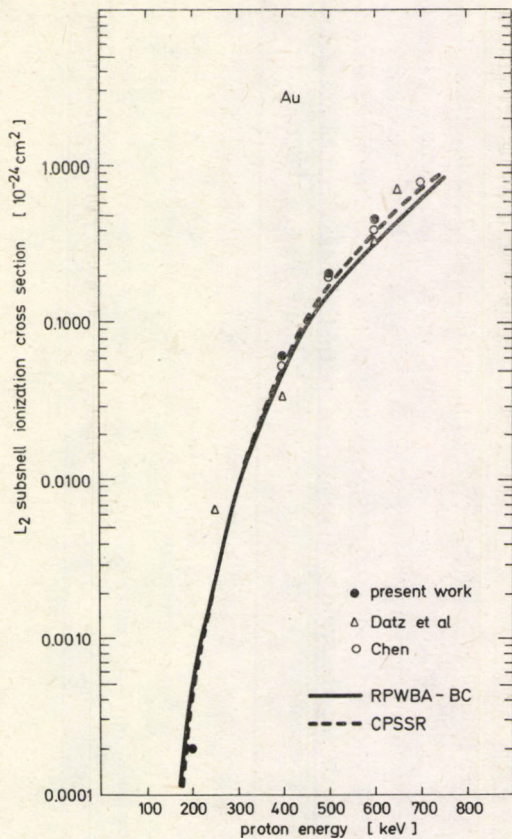


Fig. 1. L_2 -subshell ionization cross sections for proton impact on Au. Experimental data: ● present work, △ ref. [1], ○ ref. [2]. Theory: — RPWBA-BC [11], - - - CPSSR [7]

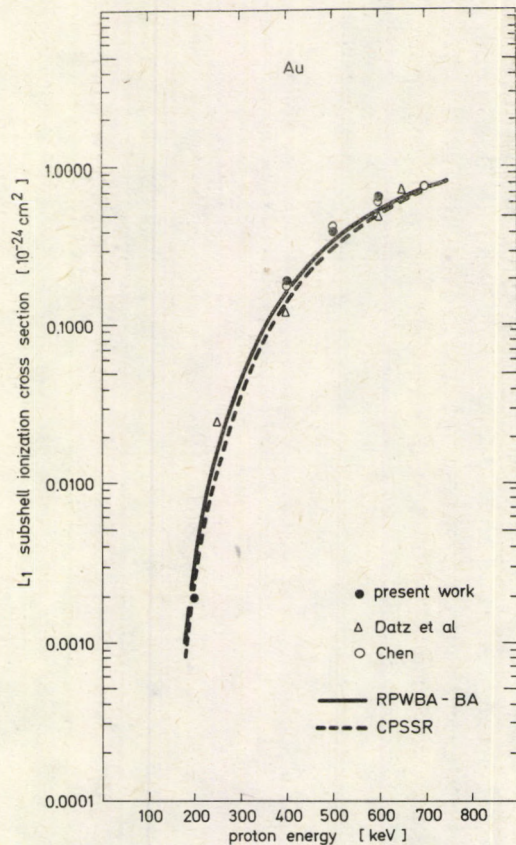


Fig. 2. As for Fig. 1, but for the L_1 subshell

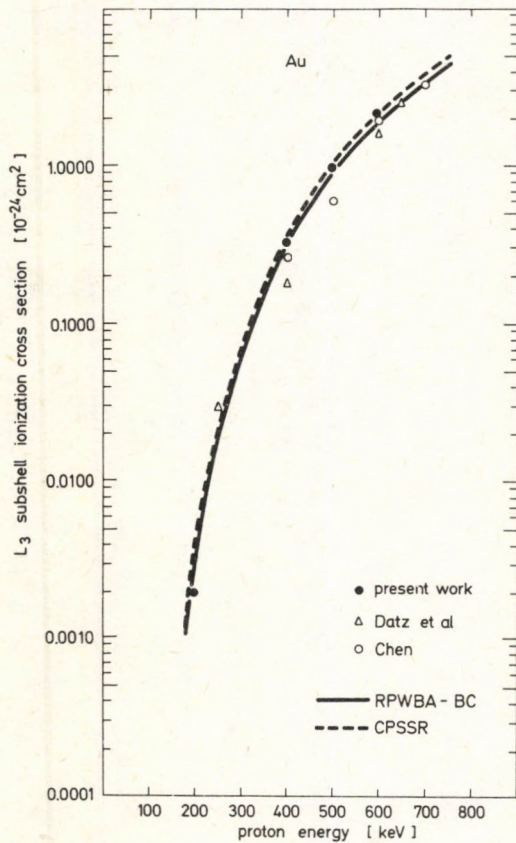


Fig. 3. As for Fig. 1. but for the L_3 subshell

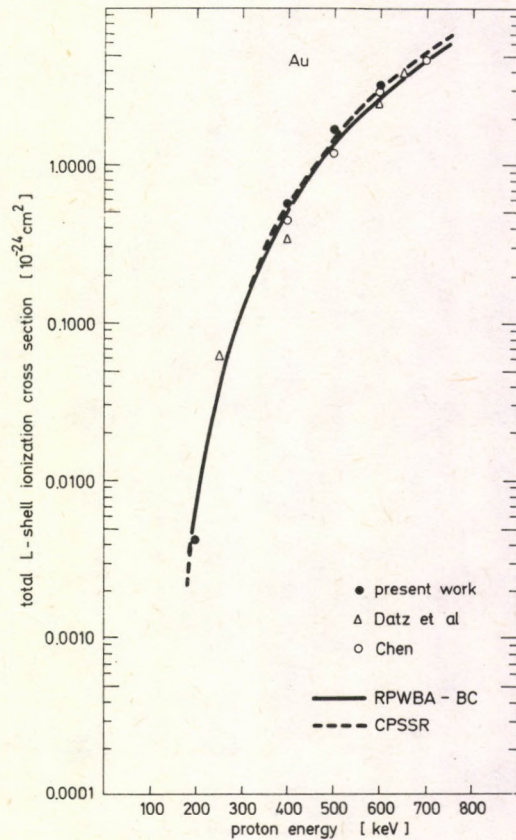


Fig. 4. As for Fig. 1, but for the total L shell

References

1. S. Datz, J. L. Duggan, L. C. Feldmann, E. Laegsgaard and J. U. Andersen, *Phys. Rev.*, *A9*, 192, 1974.
2. J. R. Chen, *Nucl. Instr. and Meth.*, *142*, 19, 1977.
3. J. F. Morgan, C. N. Chang and S. L. Blatt, *Phys. Rev.*, *A12*, 1731, 1975.
4. T. K. Li, D. L. Clark and G. W. Greenless, *Phys. Rev. Lett.*, *37*, 1205, 1976.
5. L. Sarkadi and T. Mukoyama, *J. Phys. B: Atom. Molec. Phys.*, *13*, 2255, 1980.
6. W. Jitschin, A. Kashuba, R. Hippler and H. O. Lutz, *J. Phys. B: Atom. Molec. Phys.*, *15*, 763, 1982.
7. W. Brandt and G. Lapicki, *Phys. Rev.*, *A10*, 474, 1974.
8. W. Brandt and G. Lapicki, *Phys. Rev.*, *A20*, 465, 1979.
9. P. A. Amundsen, *J. Phys. B: Atom. Molec. Phys.*, *10*, 1079, 1979.
10. L. Kocbach, *J. Phys. B: Atom. Molec. Phys.*, *9*, 2269, 1976.
11. T. Mukoyama and L. Sarkadi, *Bull. Inst. Chem. Res. Kyoto Univ.*, *57*, 33, 1979.
12. C. V. Barros Leite, N. V. de Castro Faria and A. G. de Pinho, *Phys. Rev.*, *A15*, 943, 1977.
13. D. Bhattacharya, S. K. Bhattacharjee and S. K. Mitra, *J. Phys. B: Atom. Molec. Phys.*, *13*, 967, 1980.
14. J. Pálinkás, L. Sarkadi, B. Schlenk, I. Török, Gy. Kálmán, C. Bauer, K. Brankoff, D. Grambole, C. Heiser, W. Rudolph and H. J. Thomas, *IEEE Trans. Nucl. Sci.*, *NS-30*, 970, 1983.
15. T. Papp, J. Pálinkás, L. Sarkadi, B. Schlenk, I. Török and K. Kiss, *Nucl. Instr. and Meth.*, *B4*, 311, 1984.
16. L. Sarkadi and T. Mukoyama, *Nucl. Instr. and Meth.*, *B4*, 296, 1984.
17. L. Sarkadi and T. Papp, this issue p. 75.
18. A. Van Wijngaarden, E. J. Brimmer and W. E. Baylis, *Can. J. Phys.*, *48*, 1835, 1970.
19. M. O. Krause, *J. Phys Chem. Ref. Data*, *8*, 307, 1979.
20. J. H. Scofield, *Atom. Data Nucl. Data Tables*, *14*, 121, 1974.

SECOND ORDER CALCULATIONS FOR L-SHELL IONIZATION OF GOLD BY NITROGEN ION IMPACT*

L. SARKADI**

*Faculty of Physics, University of Bielefeld, D-4800 Bielefeld
Federal Republic of Germany*

and

T. PAPP

*Institute of Nuclear Research of the Hungarian Academy of Sciences
4001 Debrecen, Hungary*

We give a comparison between the predictions of the recent second order theory of Sarkadi and Mukoyama and experimental cross sections of L-subshell ionization of gold by nitrogen ions in the energy range 2.4-18.2 MeV. Considerable improvement has been observed compared to the previous two-step model which neglects the possible interference effects between first- and second order ionization amplitudes.

1. Introduction

In the field of the physics of atomic collisions a considerable and increasing amount of work is devoted to study the ionization of the inner shells of atoms by energetic heavy charged particles. These studies are motivated partly by the fundamental demand to understand more deeply the collision and ionization phenomena as well as the atomic (ionic) structure, and partly by practical applications. In some cases the investigations search for the limits of the present description of our physical world by basic theories. For example, considerable efforts are made to check the predictions of the quantum electrodynamics measuring the Lamb shift in a highly ionized heavy atom [1], or to get information about the behaviour of the matter in a "superstrong" electric field by observation of spontaneously emitted positrons from violent collisions of the heaviest atoms [2]. As fields of practical applications we can mention the material analysis and the thermonuclear fusion research.

In this Institute a series of experiments and theoretical investigations has been carried out in the past few years for the L-shell ionization of heavier atoms by light and heavy ions [3-13]. One of the aims of these studies was to establish the dependence of the L-subshell ionization cross sections on the projectile atomic number, thereby to

* Dedicated to Prof. S. Szalay on his 75th birthday

** Permanent address: Institute of Nuclear Research of the Hungarian Academy of Sciences (ATOMKI), Debrecen, Hungary H-4001, Pf. 51.

trace the ionization phenomena as a function of the strength of the interaction between the colliding objects. From the theoretical point of view this provides a check of the validity of a given perturbation theory applied to the description of the ionization (excitation) process. The first Born approximation turned out to be a satisfactory description for the ionization of the L subshells by *protons* in a remarkable range of the collision velocity and target elements. For helium and even heavier projectiles, however, large deviations occur between the experimental and (first order) theoretical cross section values. The deviations, which are particularly large for the L_2 subshell, increase with increasing projectile nuclear charge and decreasing velocity. For an ion as heavy as oxygen the departure from the direct theory can exceed the one order of magnitude. But this failure of the first order theory is not surprising if we regard the perturbation series expansion parameter

$$\lambda = \frac{Z_1 e^2}{h v},$$

which, for example, for a bombardment by helium ions at 100 keV/amu energy is equal to one. Here Z_1 is the atomic number of the projectile and v is the collision velocity. Therefore, the second or higher order terms of the Born series may not be negligible. Indeed, we have shown [6, 11, 12] that for heavy-ion impact the ionization of an electron from a given subshell may take place with large probability via two- (multiple-) step processes involving other L substates as intermediate states. For a first glance the virtual excitations of the L substates (fully filled with electrons) as a part of the ionization process seem to violate the Pauli exclusion principle, but this is not the case. Actually, the states which are populated by the electrons during the collision are far from being atomic states due to the strong perturbation represented by the time varying Coulomb force of the projectile. Therefore, the perturbed states are those which must obey the Pauli principle, and the *atomic* L states can safely be used as intermediate states.

It is known, however, that to make second or even higher order calculations is an incomparably more difficult task than to calculate first order cross sections. In spite of the difficulties we have made attempts at a quantitative description on the basis of simple physical considerations and applying several approximations. These attempts resulted first in the more or less classical "two-step model" [6] and recently in a more exact quantum mechanical treatment referred to as "second order SCA (Semi-Classical Approximation) calculations" [12]. In [12, 13] we have made a detailed comparison between the predictions of the latter model and the experiments. However, these comparisons involved only L-subshell ionization cross section *ratios* and cross sections measured *relative* to deuteron bombardment. The aim of the present work was to extend the comparisons for absolute cross sections.

2. The two-step model and the second order SCA description

The common feature of the two models is that both calculate second order contributions to cross sections calculated in a first order ionization theory. The first order theory which we use is the CPSSR model [14]. This model gives an excellent description of the ionization of inner shells by light-ion impact in a large range of the relative collision velocity (for K shell see e.g. [15]), and it is widely used for the calculation of cross sections. The CPSSR theory is essentially a plane-wave Born approximation with the inclusion of several corrections for low-velocity effects: The deflection and retardation of the projectile in the Coulomb field of the target nucleus, the increase of the binding energy of the target electrons due to the adiabaticity of the collision, and a correction to account for the relativistic effects in the target atomic states which are neglected in the PWBA. The ionization cross sections in the two-step model (denoted by $\sigma_{n_L}^{TS}$) are expressed by the following equations

$$\begin{aligned} \sigma_{n_L}^{TS} = & 2\pi \int_0^{\infty} P_{n_L}^i(b) \left[1 - \sum_{n'_L (\neq n_L)} P(n_L, n'_L, b) \right] b db \\ & + \sum_{n'_L (\neq n_L)} 2\pi \int_0^{\infty} P_{n'_L}^i(b) P(n'_L, n_L, b) b db. \end{aligned} \quad (1)$$

Here n_L is a short notation of the quantum numbers (l, j, m_j) of the eight L substates (including also the degenerate states), b is the impact parameter, $P_{n_L}^i(b)$ is the probability of the direct ionization of an electron from the state $|n_L\rangle$, and $P(n_L, n'_L, b)$ is the probability that a vacancy transfers from the state $|n_L\rangle$ to the state $|n'_L\rangle$ due to a second interaction of the projectile with the L-shell electrons. It can be shown easily that

$$\sum_{n_L} \sigma_{n_L}^{TS} = \sum_{n_L} 2\pi \int_0^{\infty} P_{n_L}^i(b) b db \quad (2)$$

that is the total L-shell ionization cross section remains unchanged. This also reflects the physical meaning of Eq. (1), namely that the vacancies created by the direct ionization mechanism are redistributed among the subshells in a second step of the same collision.

Eq. (1) is largely simplified applying the following approximation. The $P(n_L, n'_L, b)$ "intrashell" transition probabilities are slowly varying functions of the impact parameter [16] in that range where the direct ionization has a dominant contribution to the total (integrated) cross section. Therefore we can replace them by constants

$$P(n_L, n'_L, b) \approx P(n_L, n'_L, \bar{b}_{n_L}), \quad (3)$$

where the average impact parameters \bar{b}_{n_L} are given by [17]

$$\bar{b}_{n_L} = c_{n_L} \frac{\hbar v}{E_{n_L}}, \quad c_{n_L} = \begin{cases} 1.5 & \text{for the } L_1 \text{ subshell} \\ 2.0 & \text{for the } L_2 \text{ and } L_3 \text{ subshells.} \end{cases} \quad (4)$$

In Eq. (4) E_{n_L} is the binding energy of the L substate. Inserting Eq. (3) into Eq. (1) we get

$$\begin{aligned} \sigma_{n_L}^{TS} = & \sigma_{n_L}^{CPSSR} \left[1 - \sum_{n'_L (\neq n_L)} P(n_L, n'_L, \bar{b}_{n_L}) \right] \\ & + \sum_{n'_L (\neq n_L)} \sigma_{n'_L}^{CPSSR} P(n'_L, n_L, \bar{b}_{n'_L}). \end{aligned} \quad (5)$$

The CPSSR cross sections enter into this equation through the well-known equivalence of the integrated (over the impact parameter) SCA cross sections and the cross sections calculated in the plane-wave Born approximation [18]

$$2\pi \int_0^\infty P_{n_L}^i(b) b db = \sigma_{n_L}^{CPSSR}. \quad (6)$$

The two-step model, however, cannot be traced back to the equations of the perturbation theories. It is based only on a simple physical picture, namely on the idea of the vacancy redistribution process. From Eq. (1) one can see that the coupling of the L substates is described by transition probabilities instead of transition amplitudes, which means that the possible interference effects are neglected. Furthermore, the intrashell transition probabilities cannot be determined unambiguously due to the fact that the time of the event of the primary vacancy creation is not known. It is only the quantum mechanical treatment which can overcome these difficulties. In the following we give a short review of a more exact model based on second order perturbation theory. A more detailed formulation of this model can be found in [12].

Similarly to the two-step model, our second order theory is also formulated in the semi-classical approximation, that is the projectile is assumed moving on a classical path. This means that the excitation of the target electrons is treated in the framework of the time-dependent perturbation theory. To a good approximation we can apply independent-particle model. Within this model, if we are interested only in the production of a vacancy in a given shell without specification of the final state, the problem is enormously reduced [19]. One has to solve "only" the one-electron equations for amplitudes describing excitations to the unoccupied (bound and unbound) states of the target atom. Including only L substates as intermediate (virtual) states, these equations lead to the following second order amplitude for the transition $|i\rangle \rightarrow |f\rangle$ (in atomic units)

$$\begin{aligned} a_f^{(2)} = & -i \int_{-\infty}^{\infty} dt \left[U_{fi} \exp\left(-i \int_{-\infty}^t dt' U_{ii}\right) \right. \\ & \left. + \sum_{n_L (\neq i)} U_{fn_L}(-i) \int_{-\infty}^t dt' U_{n_L i} \exp\left(-i \int_{-\infty}^{t'} dt'' U_{ii}\right) \right], \end{aligned} \quad (7)$$

with the notations

$$\begin{aligned}
 U_{mk}(t) &= V_{mk}(t) \exp(i\omega_{mk}t), \\
 V_{mk}(t) &= \int d\vec{r} \psi_m^* V(t) \psi_k, \\
 \omega_{mk} &= E_m - E_k.
 \end{aligned}
 \tag{8}$$

Here $V(t)$ is the perturbing potential due to the Coulomb interaction between the projectile nucleus and the target electron, ψ_m and ψ_k are one-electron eigenstates, and E_m and E_k are the corresponding energy eigenvalues of the unperturbed atom. In Eq. (7) the first term describes the direct ionization, the second term gives the contribution from the two-step processes. The exponential functions with the diagonal matrix elements are related to the phenomenon of the "increased binding energy".

In the present phase of our work we could calculate the amplitudes given by Eq. (7) only by introducing several approximations. We have derived a second order *correction factor* to first order cross sections instead of calculating absolute cross sections. This factor is a ratio of second to first order transition probabilities, for which we have chosen the most representative ones: We have made the calculations at average impact parameters (see Eq. (4)), and we have considered only transitions with the minimum energy transfer, which are known to give the dominant contribution to the total cross section at low collision velocities. Furthermore, the angular momentum of the final states has been restricted to $l=0$ and 1. In the multiple expansion of the perturbing potential the monopole, dipole, and quadrupole terms have been evaluated.

Making a comparison between the experimental data and the predictions of this model for *absolute* cross sections, the neglect of the binding effect is not justified in contrast to the case of the subshell ionization cross section *ratios* [12]. The exact calculation of this effect according to Eq. (7) is not possible by our present computer code, therefore we have approximated it using the so-called "united atom" approach. This replaces the atomic number and the binding energy of the target atom by those of the target-projectile composite system. This approximation is justified if the average impact parameter is much smaller than the radius of the L subshell. The collisions studied in the present paper meet this requirement.

3. Comparison with experimental data

The number of experiments on absolute cross sections of L-shell ionization by heavy-ion impact is very small. Mainly L X-ray production cross sections have been reported in the literature, and we can compare our theoretical results only with our own L-subshell ionization cross section data for nitrogen impact ionization of gold in the energy range 2.4–18.2 MeV [9, 10]. In Figs 1–3 the experimental data are plotted together with curves belonging to theories: CPSSR (full line), two-step model (dashed line), and second order SCA with the united atom approximation (dotted line). It can be

seen that for L_1 and L_3 subshells the CPSSR and second order SCA give approximately the same description of the experimental data, and we can speak about a reasonable agreement. In the case of the L_2 subshell, however, the CPSSR theory considerably underestimates the experimental cross sections. A significant improvement has been achieved by the two-step model at lower energies, but still a deviation of a factor of five

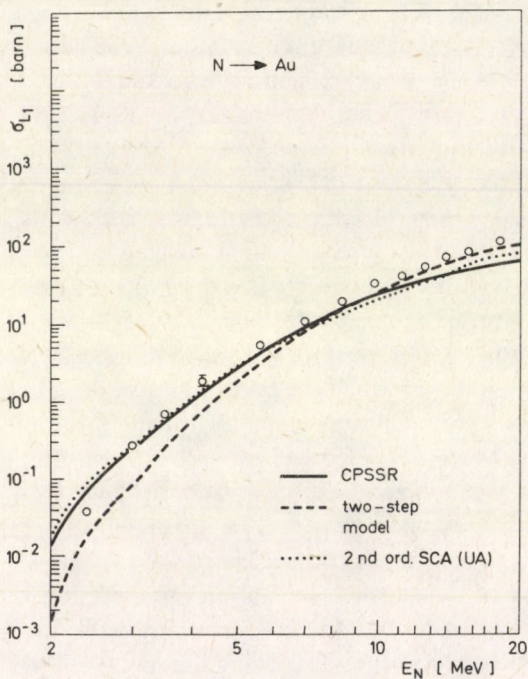


Fig. 1. Experimental [9, 10] and theoretical [14, 6, 12] L_1 -subshell ionization cross sections of gold at nitrogen ion impact

remained at intermediate energies. This discrepancy is probably due to the neglect of the interference effects between the first- and second order ionization amplitudes. Indeed, the more exact second order SCA calculations have reduced further the deviations, the dotted curve goes very nicely almost parallel with the experimental data in a broad energy range.

4. Conclusion

The present comparison between experimental and theoretical cross sections gives a further evidence that second order effects play an important role in the ionization of the L subshells of heavier atoms by heavy-ion bombardment. For the

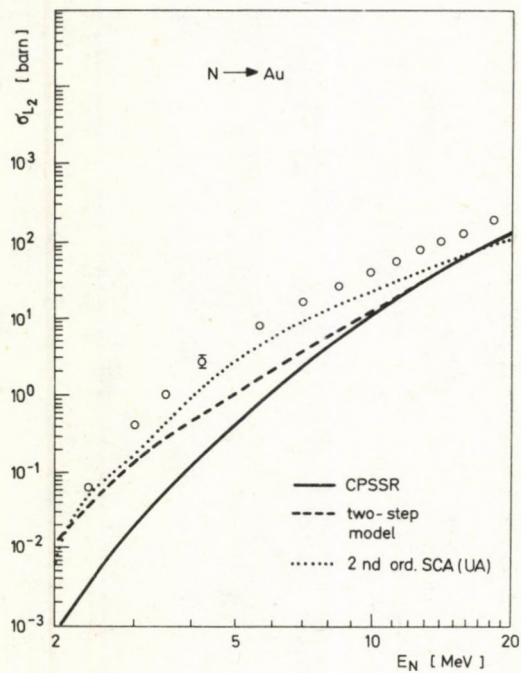


Fig. 2. The same as Fig. 1 but for the L_2 subshell

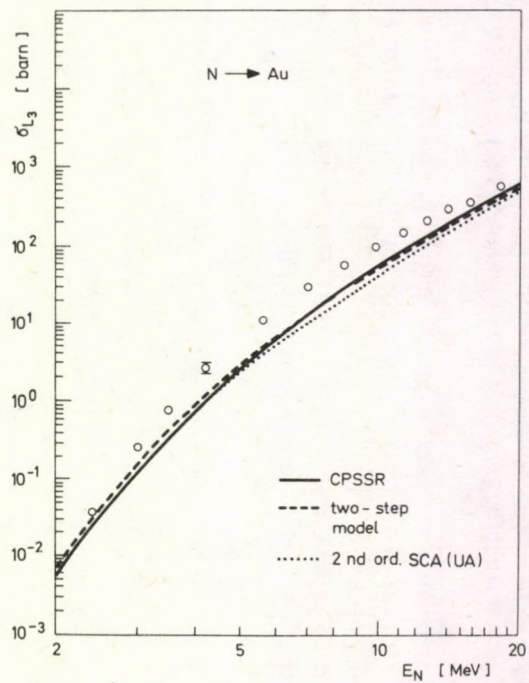


Fig. 3. The same as Fig. 1 but for the L_3 subshell

collision of a nitrogen ion with a gold atom we have found a reasonable agreement between the experimental data and the predictions of the second order SCA calculations. We remark that the agreement is not within the experimental errors, but this cannot be expected from such a crude model with lot of approximations. The next steps towards a more realistic model would be performing the integration over the impact parameter instead of regarding average values, as well as including the binding effect in the calculations exactly. From the other hand, further cross section measurements are needed for other projectiles and target elements in order to make a more detailed comparison between experiment and theory.

Acknowledgement

This project was financially supported partly by the Deutsche Forschungsgemeinschaft.

References

1. H. Gould and R. Marrus, *Phys. Rev.*, A 28, 2001, 1983.
2. U. Müller, G. Soff, T. de Reus, J. Reinhardt, B. Müller and W. Greiner, *Z. Phys.*, A 313, 263, 1983.
3. L. Sarkadi and T. Mukoyama, *J. Phys. B: Atom. Molec. Phys.*, 13, 2255, 1980.
4. J. Pálincás, L. Sarkadi and B. Schlenk, *J. Phys. B: Atom. Molec. Phys.*, 13, 3829, 1980.
5. J. Pálincás, B. Schlenk and A. Valek, *J. Phys. B: Atom. Molec. Phys.*, 14, 1157, 1981.
6. L. Sarkadi and T. Mukoyama, *J. Phys. B: Atom. Molec. Phys.*, 14, L255, 1981.
7. T. Mukoyama and L. Sarkadi, *Phys. Rev.*, A 25, 1411, 1982.
8. J. Pálincás, L. Sarkadi, B. Schlenk, I. Török and Gy. Kálmán, *J. Phys. B: Atom. Molec. Phys.*, 15, L451, 1982.
9. J. Pálincás, L. Sarkadi, B. Schlenk, I. Török, Gy. Kálmán, C. Bauer, K. Brankoff, D. Grambole, C. Heiser, W. Rudolph and H. J. Thomas, *IEEE Trans. Nucl. Sci.*, Vol. NS-30, 970, 1983.
10. J. Pálincás, L. Sarkadi, B. Schlenk, I. Török, Gy. Kálmán, C. Bauer, K. Brankoff, D. Grambole, C. Heiser, W. Rudolph and H. J. Thomas, *J. Phys. B: Atom. Molec. Phys.*, 17, 131, 1983.
11. L. Sarkadi, *Nucl. Instr. and Meth.*, 214, 43, 1983.
12. L. Sarkadi and T. Mukoyama, *Nucl. Instr. and Meth.*, B4, 296, 1984.
13. T. Papp, J. Pálincás, L. Sarkadi, B. Schlenk, I. Török and K. Kiss, *Nucl. Instr. and Meth.*, B4, 311, 1984.
14. W. Brandt and G. Lapicki, *Phys. Rev.*, A 20, 465, 1979.
15. H. Paul and W. Obermann, *Nucl. Instr. and Meth.*, 214, 15, 1983.
16. J. H. McGuire, D. J. Land, J. G. Brennan and G. Basbas, *Phys. Rev.*, A 19, 2180, 1979.
17. G. Lapicki and W. Losonsky, *Phys. Rev.*, A 20, 481, 1979.
18. J. Bang and J. M. Hansteen, *K. Danske Vidensk. Selsk., Mat.—Fys. Medd.*, 31, No. 13, 1, 1959.
19. J. F. Reading, *Phys. Rev.*, A 8, 3262, 1973.

PROPOSAL FOR INVESTIGATION OF MINOR BODIES OF THE SOLAR SYSTEM USING REMOTE SENSING OF ELECTRON BEAM INDUCED X-RAY FLUORESCENCE*

G. HREHUSS, T. I. GOMBOSI, I. NÁDAY, L. POGÁNY and K. SZEGŐ

*Central Research Institute for Physics
1525 Budapest, Hungary*

The composition of the surface material of minor bodies in the solar system can be measured using a semiconductor soft X-ray spectrometer mounted on the space probe. The characteristic X-rays are to be excited by a 20 kV-low current electron beam of an on-board electron gun. The main features of the method are described. Estimations on its sensitivity, supported by a model experiment, are also given. The minimum fly-by distance to apply this method can be estimated as a few kilometers.

Summary

X-ray spectra excited in the surface material of a celestial body depend on the composition of the surface material. They provide information on the concentration of elements in the top few hundred micrometers of the surface. On a rendezvous mission to an asteroid or to another minor body the detection of X-ray fluorescence spectra enables a large number of elements to be analysed, including most of those of prime scientific interest.

The proposed experiment has the following main features:

- Using a spacecraft-mounted electron gun producing e.g. 1 mA current of 20 keV particles, atoms in the surface layer of a minor celestial body with no intrinsic magnetic field and atmosphere can be excited and will emit characteristic X-ray radiation. The fluorescent X-ray spectrum is detected on board by a cooled Si(Li) semiconductor detector with an energy resolution of about 0.2 keV.
- On the basis of the characteristic X-ray spectrum the concentrations of elements from Na to Ni can be determined. Moreover, by using higher electron energies this range can be extended towards higher atomic numbers as well.
- Various technical solutions are recommended for investigating local changes in surface composition.

The proposed method is suitable for studying the surface composition of asteroids, minor celestial bodies and of planetary satellites having no atmosphere and

* Dedicated to Prof. S. Szalay on his 75th birthday

intrinsic magnetic field, provided that the miss distance is less than a few km and that at least 100 s is available for the measurements.

The method has the advantage that it can be applied at large heliocentric distances, where solar radiation induced X-ray fluorescence intensities are insufficient for composition tests. Its other advantage is that the exciting source is precisely known and that the intensity of the electron source can be varied as a function of the approach distance.

An estimation of the expected accuracy of measurement of the characteristic X-ray spectrum is given in the proposal and our ideas concerning some subsystems, especially the power supply unit of the electron gun and the spectrometer electronics, are outlined. An estimate is given for the amount of data to be transmitted by the telecommunication system of the space probe. The possibility of data reduction by an on-board microprocessor based data-processing system is also discussed.

Table I

Size, mass and power consumption of the equipment

	[dm ³]	[kg]	[W]
Electron gun with shielding	2	3	—
Detector system	1	1.5	—
Cooling system	~3	~5	10
Analogue electronic unit	2	2.5	6
Digital electronic unit	1	1.0	3
Power supplies	3	5.0	30
Total	12	18.0	49

1. Scientific objectives

Asteroids seem to constitute an ordered assemblage of primitive planetesimals and their fragments in which important information is preserved about the structure of the protoplanetary nebula and the processes that produced the planetary bodies of the solar system.

One of the primary scientific purposes of investigating asteroids is to determine their composition. X-ray fluorescence measurements can provide information on the concentration of elements in the top few hundred micrometers of a surface.

Asteroids are bombarded continuously by particles, including protons from the solar wind, from solar flares and from the galactic cosmic rays. The footprint of these long-term bombardments is preserved in the surface through enrichment of volatile material, activation of radioactive species, ionization damage, and loss of constituents as a result of sputtering as well as outgassing. Consequently, the surface composition

carries a mixture of information about the ambient structure of the celestial body and external astrophysical effects.

The remote sensing X-ray fluorescence method [1] was used to investigate the geochemical composition of the lunar surface in the experiments carried out on spacecraft Apollo-15 and Apollo-16. In this case the characteristic lines of the elements forming the surface were excited by the primary X-ray emission from the solar corona.

In order to detect the fluorescence radiation three proportional chambers were used but as the energy resolution of these detectors was not suitable for resolving the characteristic lines of the surface elements, one detector was equipped with a thin Al filter, another with a thin Mg filter. In these cases the Al/Si and Mg/Si concentration ratios of the surface could be determined in the vicinity of Mare Tranquillitatis. Though the area surveyed by the detectors was about $100 \times 100 \text{ km}^2$ using differential scanning techniques, the above ratios were determined with a resolution of about $15 \times 15 \text{ km}^2$.

Based on a similar principle another project is known in which a gas-proportional-scintillation detector with a large sensitive area and with considerably better energy resolution has been proposed to replace the proportional detectors [2]. This gas-proportional-scintillation detector safely resolves the K_{α} -lines of Si and Al in the case of low solar activity, while with flare activity it makes possible to detect the K_{α} -lines of Mg, Al, Si, Ca and Fe though the separation of the K_{α} -lines of Fe, Co and Ni is uncertain. The advantage of this type of detector is the large sensitive area; it has, however, the disadvantage of a relatively large mass ($1 - 2 \times 20 \text{ kg}$).

The common disadvantage of solar radiation excited fluorescence spectrum measurements is that the intensity of the characteristic lines strongly depends on the instantaneous structure of the X-ray spectrum of the solar corona, and this structure significantly changes from time to time, particularly in the case of flare activity. Thus it is necessary to measure simultaneously the solar spectrum, consequently it may become necessary to double the number of spectrometers. In Fig. 1, on the basis of data

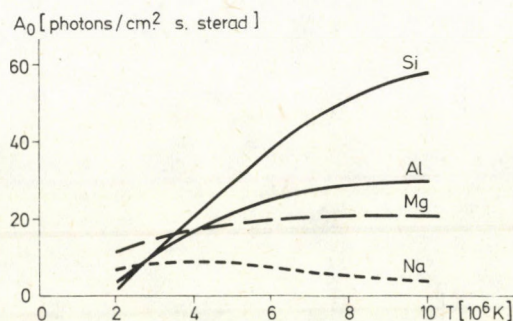


Fig. 1. The specific fluorescent intensity of the K_{α} -lines of some elements in basalt as a function of the coronal temperature, at the Earth's distance (after [2])

of [2], the values of intensity of the K_{α} -lines of Si, Al, Mg and the Na content of basalt are shown as a function of solar coronal temperature. It is obvious that the intensity ratio of these characteristic lines of highest importance can significantly change even during low solar activity (see the curves below the coronal temperature of 4×10^6 K). At the same time the method has the advantage that the measured intensity of the fluorescence radiation does not depend on the distance between the space probe and the celestial body as long as the surface fully occupies the field of view of the spectrometer.

2. Description of the method

In our proposal the following situation is considered

1. the approach distance of the celestial body to be examined is in the order of 1–10 km and the duration of the approach is larger than 100 s;
2. the celestial body has no significant atmosphere and intrinsic magnetic field;
3. the magnetic field strength between the celestial body and space probe is small.

When these conditions are met it is possible to excite the atoms of the material forming the surface by the electron beam of a 15–30 kV electron gun mounted on the space probe and to record the spectrum of the generated characteristic radiation by means of a spectrometer with a total surface of a few cm^2 , built of planar Si(Li) semiconductor detectors with an energy resolution of about 200 eV. The required exciting current is of the order of 1–10 mA. There is no special requirement with regard to the focusing of the electron beam except that the region of incidence of the electron beam is to be found within the surface region marked out by the field of view of the spectrometer (Fig. 2). It is also assumed that the solar corona is not within the field of view of the detectors. Thus the radiation detected by the spectrometer arises almost exclusively from the surface of the celestial body under examination. The main components of the radiation consist of the fluorescence radiation excited by the solar X-ray emission and the X-ray emission excited by the electrons.

The spectrometer detects the radiation quanta separately, the amplitude of the output voltage pulses being proportional to the quantum energy. The spectrum can be

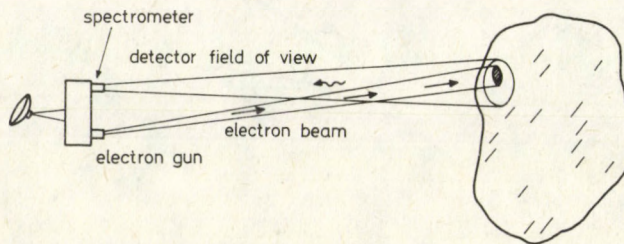


Fig. 2. Illustration of the method

measured by using, for example, a multi-channel analyser. Because of the Be-window to be used in order to protect the detectors and to eliminate the visible and ultra-violet radiation the spectrometer is sensitive to energies higher than 1 keV.

For a measurement of geochemical significance it is necessary that

1. the characteristic lines of the most important elements could be resolved,
2. the measured intensity of those lines should be statistically significant.

The energy values of the K_{α} characteristic lines of the most important elements are shown in Table II.

Table II

The K_{α} -energy of some important elements. Because of the Be-window, only those elements having $E_{K_{\alpha}}$ higher than 1 keV have been listed. For elements having lower atomic number the detector has an efficiency $\ll 100\%$

Element	$E_{K_{\alpha}}$ [keV]	Element	$E_{K_{\alpha}}$ [keV]	Element	$E_{K_{\alpha}}$ [keV]
Na	1.04	Cl	2.62	Cr	5.41
Mg	1.25	K	3.31	Mn	5.90
Al	1.49	Ca	3.69	Fe	6.40
Si	1.74	Ti	4.51	Co	6.92
S	2.31	V	4.95	Ni	7.47

It can be seen from the data in Table II that the first requirement given above can be fulfilled if the energy resolution is not worse than about 0.2 keV. The second requirement needs more detailed examination.

Let us consider a given element of the surface. Let η (sterad $^{-1}$) be the probability that one electron generates one K_{α} -quantum in unit angle directed towards the detector. During a measurement of period t the number of quanta within the K_{α} -line in question is given by

$$N_e = 6.24 \times 10^{18} \eta I t f / R^2, \quad (1)$$

where I [A] is the current emitted from the gun, f [m 2] is the effective surface of the detector system and R [m] is the distance of the space probe from the surface of the celestial body.

In Fig. 3 the probability η as a function of electron energy is shown for the thick targets indicated there. As η turns out to be in the order of 10^{-4} for the electron energies considered, one can substitute in Eq. (1) $\eta \approx 10^{-6} \rho$, where ρ stands for the percentage abundance of the element being examined in the surface material. Assuming $\rho = 10\%$, $I = 1$ mA, $f = 10^{-3}$ m 2 , $R = 10^3$ m and a measuring period of 100 s, we obtain $N_e \approx 6200$, with a relative statistical error $N_e^{-1/2} = 1.3\%$. A more accurate estimation of η based on a model experiment will be discussed in Section 4.

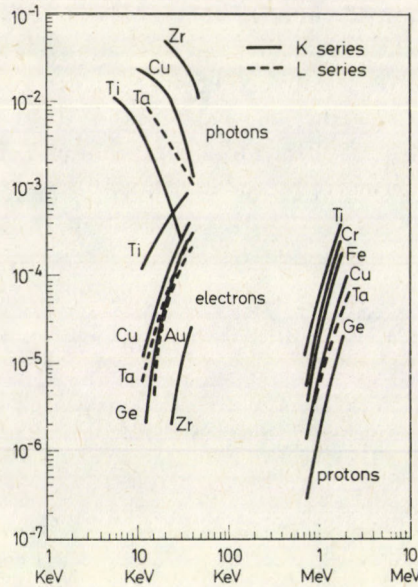


Fig. 3. The excitation probability per unit solid angle of characteristic X-ray lines as a function of the energy of some exciting particles, for different targets as indicated ([3])

The same characteristic line is excited by the radiation of the Sun as well. The number of those photons detected can be written as

$$N_f = A_0 \left(\frac{r_0}{r} \right)^2 \Delta\Omega f t, \quad (2)$$

where r_0 and r stand for the distances of the Earth and the celestial body investigated, respectively, from the Sun; $\Delta\Omega$ [sterad] is the solid angle subtended by the detector field of view; A_0 [$\text{m}^{-2} \cdot \text{sterad}^{-1} \cdot \text{s}^{-1}$] is the intensity of the characteristic photons radiated back in unit solid angle and in unit surface area at the Earth's distance. For the values of coefficient A_0 , data can be found in [2], some of them are shown in Fig. 1. Assuming $A_0 = 10^5$ photon $\cdot \text{m}^{-2} \cdot \text{sterad}^{-1} \cdot \text{s}^{-1}$ as an estimation, $\Delta\Omega = 10^{-2}$ sterad (a conical field of view with 6° aperture) $f = 10^{-3} \text{ m}^2$ and a measuring period of $t = 100$ s we find that for a celestial body at the distance of Mars, for example, we have $N_f = 40$ with a relative statistical error of 16%. At an approach distance of $R = 10$ km the electron excitation contribution obtained is of the same order as that of the fluorescent one. Bearing in mind this possibility it seems to be of practical benefit to interrupt the operation of the electron gun from time to time in order to measure the fluorescence component as a background.

In the measured spectrum the characteristic lines are superimposed on a continuous background, the major part of which is the bremsstrahlung with intensity

depending on the average atomic number of the material as well as on the electron energy. The background correction to each characteristic line does not exceed some per cent for most of the materials in question; the total continuous background however is to be taken into account as a detector loading rate.

As has been proven by the spectra measured by electron excitation the intensity of total bremsstrahlung background forms about 25% of the intensity of all characteristic radiations except for targets composed of elements of higher atomic number, in which case the intensity of the bremsstrahlung is of the same order or higher than that of the line radiation. A further background with continuous energy distribution is generated by the solar radiation scattered back from the surface and by the cosmic radiation penetrating the detectors. The corresponding intensities can be estimated (see [2]) as 4×10^3 and 1×10^3 particles \cdot m⁻² \cdot s⁻¹ keV, respectively.

Considering $R = 1$ km, $f = 10^{-3}$ m², $I = 1$ mA and a region of energy ranging from 1 keV to 10 keV, for estimating the detected intensity it is assumed that the essential part of the characteristic spectrum lies in this region ($\eta = 10^{-4}$). In this case the detected photon intensities are as follows:

Table III
Detected photon intensities

Characteristic radiation		Continuous background radiation	
Source	Detected photon/s	Source	Detected photon/s
electron excitation	600	bremsstrahlung	150
fluorescence excitation* for quiet Sun condition	20	photons scattered back from solar radiation*	40
for flare activity	100	cosmic radiation	10
Total max.	700	Total	200

* Data from Ref. [2] calculated, for example, to a celestial body found at a Mars' distance.

The counting rate to be processed by the detector system is of the order of 10^3 pulses/s, for other distances R it varies approximately as R^{-2} with respect to the data given above. At a beam current of $I = 1$ mA and distances of $R \geq 5$ km the intensity of characteristic lines excited by electrons is of the same order or lower than the continuous background due to the cosmic radiation. The region in which the proposed method can be applied can be characterized by the parameter $\alpha = If/R^2$.

Its lower limit is determined by the dominance of the fluorescence contribution and the continuous background correction; the upper limit being connected with the

maximum counting rate of the detectors and the corresponding electronics. The region of applicability is estimated as

$$10^{-13} \text{ A} \leq \alpha \leq 10^{-11} \text{ A} . \quad (3)$$

If the approach distance R is extremely large or small such that α does not lie in the above region, the electron current should be changed.

The outlined measuring method, in its simplest version, is suitable for determining the average composition of a surface lying in the field of view of the spectrometer, provided that it is fully covered by the electron beam. Due to the relative motions of the celestial body and the space probe (unless this motion is too rapid) there is a possibility to measure the local change in the composition: during the passing-by more spectra are measured in subsequent periods. If one scans periodically with a properly focused electron beam within the field of view by means of a deflector system one obtains fairly good spatial resolution. The amplitude, the identifier and the time of arrival of each detector signal are to be stored as a single event. In this case the phase of scanning should be precisely synchronized and the actual distance R should always be known (for higher distances R the total flight time of electrons and photons may influence the phase conditions of scanning on the surface). This procedure corresponds to the X-ray microanalytical method widely used in scanning electron microscopes.

A simple solution providing space resolution of medium quality is to equip the detector elements with collimators, each covering a possibly connected but non-overlapping region of the total field of view (Fig. 4). This method has the disadvantage that the detected intensity decreases as the space resolution increases, which can be compensated only by the measuring period or the beam current.

It is necessary that the electron beam should travel between the space probe and the celestial body without any essential change of direction otherwise the spectrometer has to be directed in accordance with the deflection of the electron beam. The condition

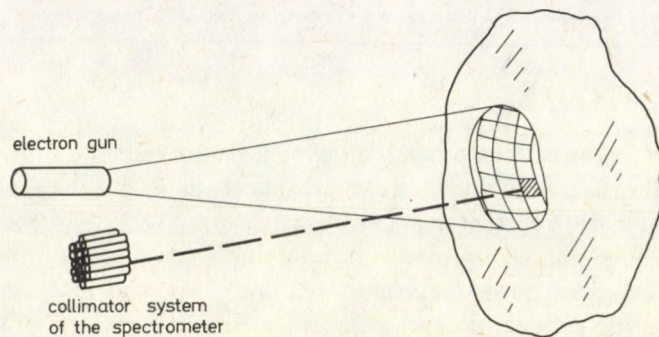


Fig. 4. A possible improvement of the space resolution by making use of a collimator system

is that the Larmor radius of the electron path should essentially exceed the approach distance R , i.e.

$$p/eB \gg R \quad (4)$$

in Si units, where e stands for the charge, p for the momentum of the electron and B for the magnetic field. For electrons of 20 keV energy the requirement $BR \ll 5 \times 10^{-4} T \cdot m = 500 \text{ gauss} \cdot \text{cm}$ is obtained. It is also required that the surface of the examined celestial body should be free of local magnetic fields. The limit given by Eq. (4) holds for the strength and dimensions of this type of magnetic fields too.

The above estimations indicate that by means of electron excitation, X-ray spectra of adequate accuracy can be measured to determine the concentration of the most important elements forming the surface. Despite the fact that there is a possibility for some on-board data reduction of spectra (i.e. for performing the background corrections, identifying the characteristic lines and determining their intensities), the complete evaluation falls predominantly on the ground dataprocessing centre. The quantitative processing of X-ray spectra is a complex task of reference measurement and computation. First it is necessary to select standard rocks and soil samples with surface and internal structures such that a spectrum similar to the measured one is obtained, then the concentration values in question can be computed by means of a program system comparing the spectra measured at the standard sample and the celestial body. Several program systems of this kind have been elaborated for microanalysis using electron beam probes and a program system of this type can be adapted for the given purpose. Measuring equipment for laboratory use in which standard materials can be excited and measured in accordance with the experiments in space is required for the purpose of evaluation performed on the ground. In standard microanalytical measuring arrangements using an electron beam, the angle between the momentum of the exciting electrons and that of the back-radiated photons is different from what can be realized in space, therefore facilities can be used only with certain modifications.

3. Description of the instrument

3.1. Construction of the spectrometer

As stated in Section 2, the spectrometer is to have an energy resolution $\Delta E \approx 0.2 \text{ keV}$ in the energy region $1 \text{ keV} \leq E \leq 10 \text{ keV}$ to be examined. This condition is met by commercially available 3–5 mm thick planar Si(Li), Ge(Li), or intrinsic-Ge semiconductor detectors of good quality and of 1–2 cm² surface, provided these detectors and the FET-input stage of the pre-amplifier can be maintained at the temperature of liquid nitrogen (77 K). Under these conditions the typical value of

resolution at $E=5.9$ keV is $\Delta E=0.2$ keV [3]. The known expression of the ΔE linewidth (FWHM) for Si and Ge based semiconductor detectors is

$$\Delta E [\text{eV}] = \sqrt{Z^2 + 2.15 E [\text{eV}]},$$

where the value of noise component Z should be less than 200 eV. At temperatures $T > 100$ K, in the soft X-ray region the noise component dominates with the typical value of Z being 20 keV for $T=300$ K.* Of the three listed detectors, the application of Si(Li) detectors is recommended from the practical point of view. The Ge(Li) detectors are to be kept at liquid nitrogen temperature continuously in order to prevent the redistribution of Li. The Si(Li) and intrinsic-Ge detectors are to be cooled down only for the period of the measurement. The Ge-based detectors have the common disadvantage that the probability of the escape of the Ge K_α radiation is by about 2 orders of magnitude higher than that of the Si [3], therefore a great number of disturbing escape lines can fall into the energy region under investigation.

Thus the spectrometer should consist of a number of Si(Li) detector elements, corresponding to the required detection surface. These detector elements with the FET-inputs of their pre-amplifiers can be mounted on a common cooling block. The technical feasibility of cooling is not dealt with here.

The detectors must always be kept in a good vacuum ($< 10^{-2}$ Pa). In order to provide this and to eliminate the visible and ultra-violet radiations a 10 μm thick, iron-free, vacuum-tight Be-window should be used in front of the detector.

Correct operation and the energy calibration of the detector system must be checked periodically. This checking can be performed in practice by means of a weak Fe^{55} radiation source (Mn K_α , $E=5.9$ keV), which can be moved by remote control.

The detector system includes a carefully engineered collimator or collimator system. Strong permanent magnets are to be used at the inlet of the collimator to keep out the electrons scattered back from the surface.

3.2. Electronics

A cooled Si(Li) detector assembled from 5–10 detector elements serves for measuring the radiation. A separate amplifier is connected to each detector element. Using this method, for collimated detectors it becomes possible to identify the detector signals, or to exclude the faulty detector elements.

The simplified block diagram of the electronics is shown in Fig. 5. Each detector element comprises a preamplifier, a shaping amplifier and a delaying circuit. In order to achieve a lower noise level ($Z \approx 200$ eV) the input FET transistors of the pre-amplifiers

* The detector noise is connected with the concentration of charge carriers in the conduction band, this concentration being proportional to $T^{3/2} \exp(-\epsilon/2kT)$ where ϵ is the width of the gap and T is the temperature. In addition to the detector noise the noise of the pre-amplifier, which can be reduced to 150–200 eV at a temperature of $T=77$ K, should also be taken into account.

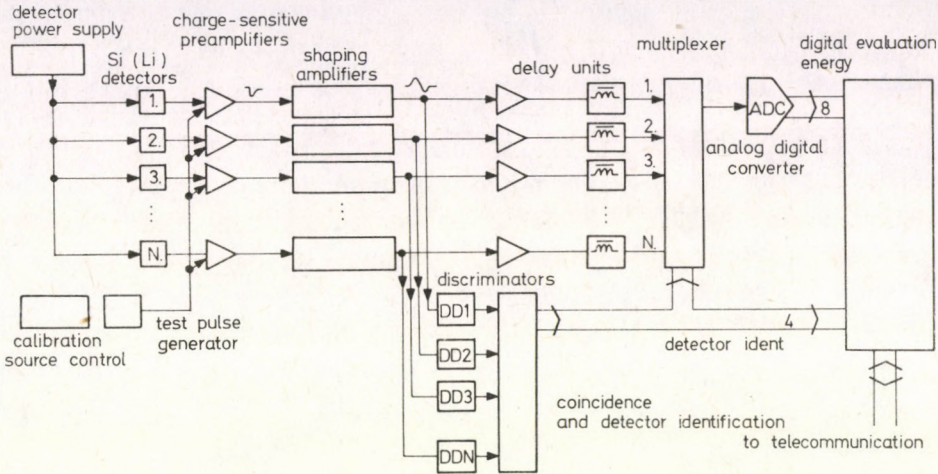


Fig. 5. A simplified diagram of the detector electronics

together with the detectors are cooled. It is advisable to perform double differentiation, pole-zero compensation and triple integration in the shaping amplifiers. The output of the amplifier is connected to a discriminator system whose signal gets to a special coincidence circuit. This circuit, in addition to the suppression of pile-up, creates the address of the operated detector and also controls the analogue multiplexer connected to the input of the ADC circuit. The analogue-digital converter (ADC) can be an 8-bit fast Wilkinson type ADC (≈ 30 eV per channel). The address of the detector element and the digitized value of amplitude proportional to the energy reaches the digital signal processing unit.

This reading method can be applied with a relative low loss ($\approx 3\%$ loss, by using a 100 MHz ADC) even with the maximum count rate of 10^4 pulses/s.

The task and structure of digital signal processing electronic equipment depends, to a large extent, on the nature of the measurement, on the features, and on the data rate of the telemetric channel. The output data rate values are shown in Table IV using different data compressing methods at 10^4 pulses/s data rate and 10 detector elements.

Table IV
Output data rate values

	Data rate
Event storage	20 kByte/s
Spectrum storage	500 Byte/s
Storage of the number of elements and trace elements	50 Byte/s
Storage of the number of major elements (8 pcs)	20 Byte/s

The tasks of an intelligent data processing unit are as follows: to calibrate the detectors and amplifier channels, to exclude the occasionally faulty channels from the measurement, to evaluate the auxiliary data (e.g. temperature of detectors, etc.), to perform background correction, to evaluate the measured spectra, to arrange the data formats and to perform the transitional storage of the data.

This unit is also responsible for controlling and testing the operation of the electron gun.

3.3. Considerations relating to the electron gun

The electron-optics issues of the construction of the electron gun are not dealt with here but it must be emphasized that the already accelerated beam should not scatter on the metal parts of the gun (not even a fraction of the current) and proper protection of the detector system against radiation should be provided. If the distance R between the space probe and the celestial body is not too small, it is beneficial to mount the electron gun and the spectrometer on the space probe as far as possible from each other.

The extent to which the long electron beam is made divergent by its internal electromagnetic forces is to be examined. It is also to be carefully studied to what potential the space probe is charged with respect to the target due to the emission of the electron beam and whether or not this prevents the emission. Consideration has also to be given as to whether it is practical to use an auxiliary, low-power ion source of the same current operating simultaneously in order to avoid charging up.

The discontinuous operation of the electron gun is required for measuring fluorescence radiation components and for background measurements (for example, 10 s of continuous operation followed by a pause of the same duration, in repeated cycles).

3.4. Power supply unit of the electron gun

The electron gun requires a power supply of 20 kV and 1–10 mA. The power supply unit also provides the heating of the electron gun. It is useful to design the high-voltage supply units to have two stages: the first stage would generate a medium voltage (≈ 300 V); the second stage would generate the 20 kV voltage level.

3.5. Mass, volume and output requirements

The estimated values relate to a detector system assembled from 10 detector elements, to the electronics and to an electron gun of 20 kV/1 mA. The large capacity data memory is not included in the digital signal processing electronic equipment. The power requirement is to be understood as primary power (at an on-board voltage of 27 V). The weight and volume of the electronic units include their supply units.

Table V

Weight, volume and power requirement of the system

	Mass [kg]	Volume [dm ³]	Power [W]
Electron gun + shielding	3	2	—
Power supply unit	5	3	30*
Cooling system (approximately)	5	3	10
Detectors + collimators + cleaning magnet	1.5	1	—
Detector electronics (for 10 detectors)			
Amplifiers, multiplexer, ADC, coincidence	2.5	2	6.0
Digital signal processing electronic device	1.0	1	3.0

* Assuming a duty cycle of 50%

4. Model experiments on meteorite samples

The yield parameter η of characteristic radiations excited by fast electrons plays a decisive role in the proposal. The measurability of a given characteristic line depends primarily on the order of magnitude of the corresponding η which, of course, is a function of the concentration of the element in question. In Section 2 it has been shown that at an exciting current of 1 mA and assuming a detector surface of $1 \times 10^{-3} \text{ m}^2$, an approach distance of 1 km and a measuring period of 100 s, $10^3 - 10^4$ photons can be detected in one characteristic line if the corresponding η is in the order of 10^{-5} (photon/electron · steradian). This value of η is based on an approximate estimation and should be confirmed either empirically or by calculations on more exact grounds.

For targets of plain surface and consisting of a single element it is possible to determine η by simple calculation [4] with a result which, however, does not exceed the level of estimation due to some factors whose values are not precisely known. The difficulties are even more severe in the case of rocks and other materials consisting of more than one element and having a natural rough surface. Under these circumstances an empirical determination of the yield parameter η has been preferred by using meteorite samples as targets.

In our experiments three meteorite samples have been investigated, the material of rock meteorites "Kunashak" (dust-like sample) and "Saratov" (grain samples), and small rough pieces from the iron meteorite "Sihote Alin". First the samples were examined by X-ray excitation. The exciting radiation source was shielded Cd-109 (22.1 keV, nominal activity 25 mCi) or Fe-55 (5.9 keV, nominal activity 100 mCi) in annular source configuration. The spectrometer was a 30 mm²/3 mm Si(Li) Canberra semiconductor detector, including an "X-ray Amplifier", "Spectrum Enhancer" and MCA 8100 multichannel analyser. The purpose of this measurement was merely to get a qualitative picture on the rough structure of the spectrum above 2 keV quantum

energies. That is why we did not attempt to minimize the absorbents (air gap, sample supporting sheet) between the sample and the detector. The measured spectra are shown in Figs 6, 7 and 8. The inserts correspond to excitation with 5.9 keV, with perpendicular axis in linear scale. The K_{α} -line of Ar arises from the air gap between the sample and the detector. Beside showing the most dominant elements this measurement demonstrates the extent to which the spectra depend on the energy of the exciting photons.

The actual model-experiment was performed by using the scanning electron microscope JSM-35 (JEOL, Japan). This electron microscope is equipped with a spectrometer suitable for measuring X-ray radiation excited by the electron beam. It is a Si(Li) semiconductor detector with a 7.5 μm thick Be-window and an effective surface of $f = 12.4 \text{ mm}^2$ manufactured by Princeton Gamma-Tech., who also provided a computer-based system for spectrum analysis and display. The distance of the detector from the irradiated point of the sample is $R = 89 \text{ mm}$, thus the detection solid-angle is $\Delta\Omega = 1.55 \times 10^{-3}$ steradian. The second area was always restricted to the surface of the samples. Two samples of each meteorite were examined. The samples were fixed in the standard way by means of graphite suspension. The electron beam had an energy of 20.0 keV and the current was $I = 480 \text{ pA}$. The period of each measurement was 100 s (live time), with a deadtime correction of about 2%. The value of the parameter α introduced in this proposal is $\alpha = 7.4 \times 10^{-13} \text{ A}$, which falls into the interval of applicability (see Eq. (3)). The only essential deviation of the model experiment from the arrangement given in the proposal is that the angle ϑ between the momenta of the electrons and measured photons (see Fig. 9) was 64° (instead of $\vartheta = 0$), due to technical reasons.

The spectra measured on meteorite samples are shown in Figs 10, 11 and 12. For clarity, one of the spectrum pairs is displaced along the vertical axis. In separate Tables the number of counts below the more typical characteristic peaks (corrected for background) are also shown. As the measured intensities to a rough approximation vary with the cosine of angle ϑ , the number of counts given in the Tables can be considered as a reliable lower limit, from the point of view of the experiment in space. Spectra similar in quantity and quality can be expected when measuring celestial bodies having surface and structure similar to those of the examined meteorites.

It is obvious from the Figures that even in the case of the iron meteorite, the continuous background due to bremsstrahlung is of relatively low intensity such that the P, S and Ni components occurring in a small part can also be detected. The discrepancies between the measurements on the same meteorite can be explained both by the microscopic differences in the concentration distribution, and by the possibility that the emission of photons took place on a surface segment of different roughness. In the proposed space experiment all microscopic differences, both in concentration and in surface structure, are expected to be averaged out so that the measured spectrum reflects the average composition of the irradiated part of the surface.

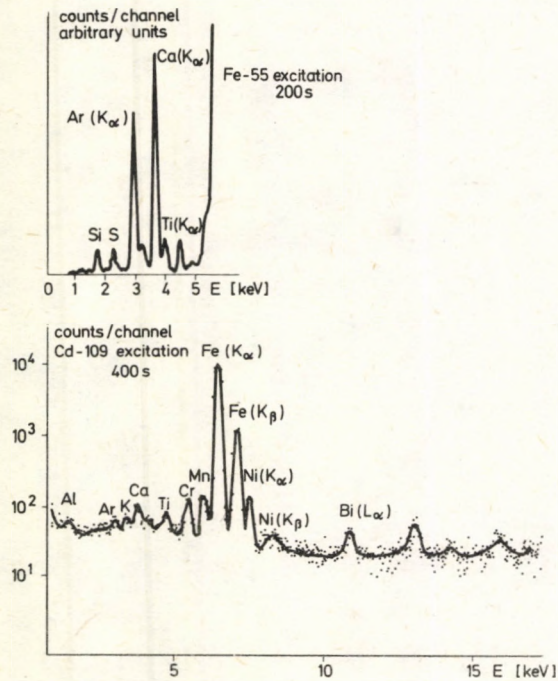


Fig. 6. The X-ray fluorescent spectra of a sample from the rock meteorite "Kunashak" as excited by the 22.1 keV X-rays of a Cd-109 source and by the 5.9 keV X-rays of a Fe-55 source (see insert), respectively. The intensity of the latter spectrum is on linear scale

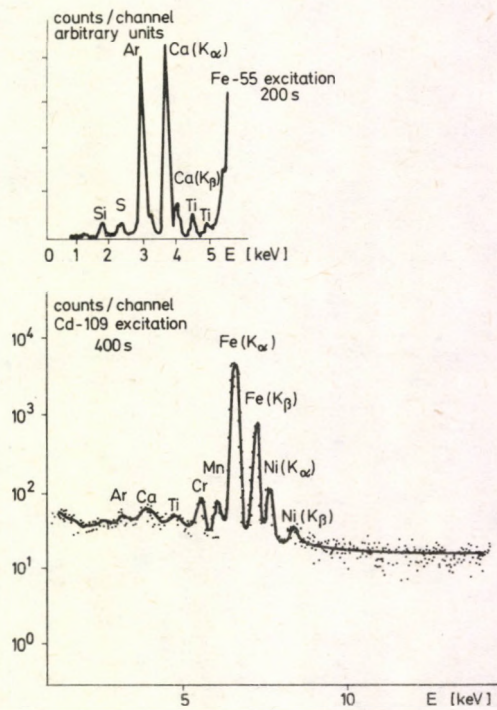


Fig. 7. The X-ray fluorescent spectra of a sample from the rock meteorite "Saratov" with excitations as in Fig. 6

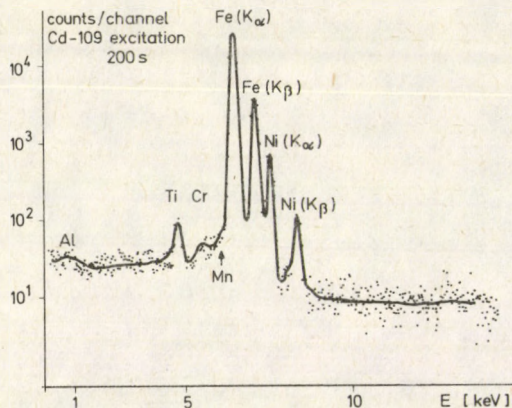


Fig. 8. The X-ray fluorescent spectra of a sample from the iron meteorite "Sihote Alin" as excited by the 22.1 keV X-rays of a Cd-109 source

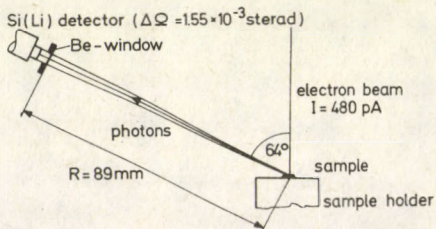


Fig. 9. The schematic layout of the model experiment

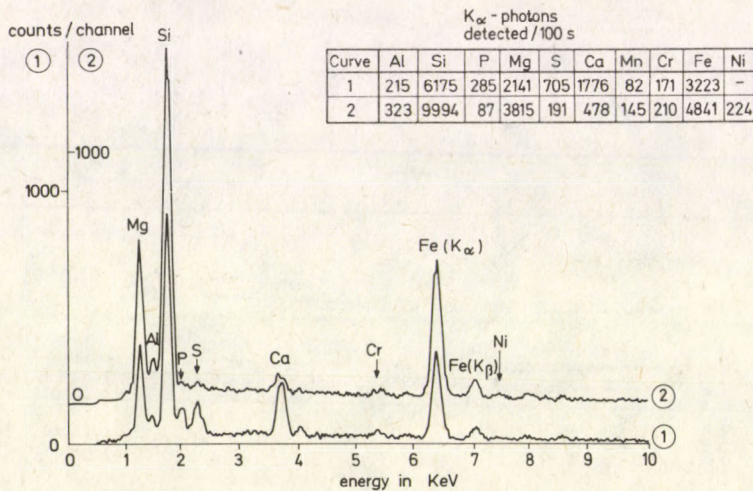


Fig. 10. The X-ray spectra of two samples from the rock meteorite "Saratov" as excited by a 20 keV electron beam. Spectrum No 2 is shifted upwards. Insert shows the number of counts in the K_{α} -lines of the elements indicated

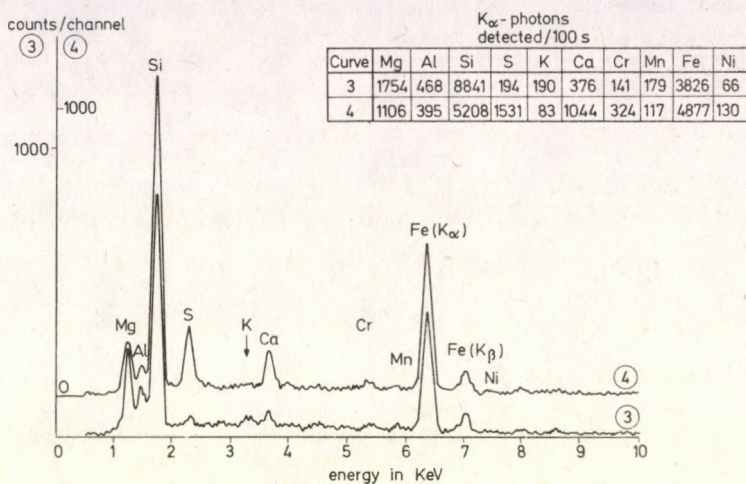


Fig. 11. The X-ray spectra of two samples from the rock meteorite "Kunashak" as excited by a 20 keV electron beam. Spectrum No 4 is shifted upwards. Insert shows the number of counts in the K_α-lines of the elements indicated

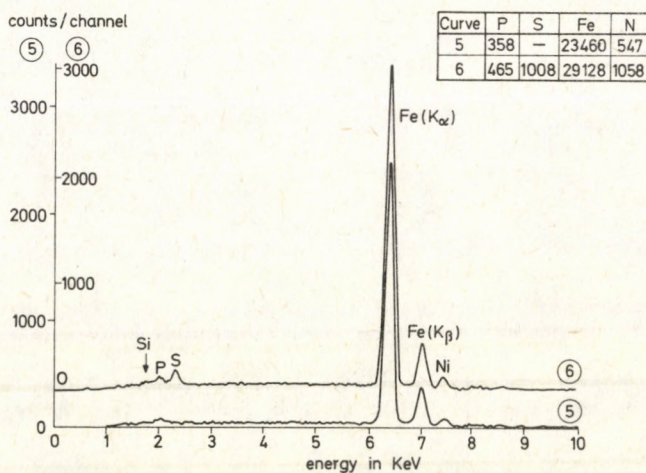


Fig. 12. The X-ray spectra of two samples from the iron meteorite "Sihote Alin" as excited by a 20 keV electron beam. Spectrum No 6 is shifted upwards. Insert shows the number of counts in the K_α-lines of the elements indicated

Finally, the values of the yield parameter η for each element found in the meteorite samples are summarized in Table VI. These are calculated by

$$\eta = \frac{n}{t \cdot I \cdot \Delta\Omega \cdot \cos \vartheta} = 4.8 \times 10^{-9} n,$$

where n is the average of the counts of the two measurements. The data in Table VI correspond to $\vartheta = 0^\circ$ and are given in units of 10^{-5} photons/electron · steradian.

Table VI

The yield parameter η in units of 10^{-5} photons/electron · steradian for different elements in the case of meteorites as indicated

Element	"Saratov"	"Kunashak"	"Sihote Alin"
Mg	1.43	0.69	—
Al	0.13	0.21	—
Si	3.88	3.37	—
P	0.089	—	0.20
S	0.22	0.41	0.24
K	—	0.066	—
Ca	0.54	0.34	—
Cr	0.091	0.11	—
Mn	0.054	0.071	—
Fe	1.94	2.09	12.62
Ni	0.054	0.047	0.39

5. Acknowledgement

The authors wish to express their thanks to Dr. Mária Csajka, and to Dr. Z. Szőkefalvi-Nagy for their help in performing the model experiments, and to Dr. Ágnes Csanády for helpful discussions.

References

1. C. G. André, M. I. Bielefeld, E. Eliason, L. Soderblom, I. Adler, J. A. Philpotts, *Science*, 197, 986, 1977.
2. A. Peacock, M. Sims and B. G. Taylor, A Geochemical Survey of the Lunar Surface Using a Remote Sensing X-ray Fluorescent Spectrometer, Space Science Department, European Space Agency, January, 1983.
3. Ralf Woldseth, X-ray Energy Spectrometry, Publ. KEVEX Corporation, Burlingame, California, 1973.
4. S. J. B. Reed, Electron Microprobe Analysis, Cambridge University Press, 1975.

CONTROL OF THE TRACE ELEMENT CONTENT OF AGRICULTURAL PRODUCTS BY X-RAY SPECTROMETRY*

L. KESZTHELYI, I. DEMETER, K. HOLLÓS-NAGY** and Z. SZŐKEFALVI-NAGY

*Central Research Institute for Physics
1525 Budapest, Hungary*

Pelletized premix samples were analysed by XRF; deviations were observed in their trace element contents. PIXE measurements were performed on chicken muscle and chicken liver samples prepared by freeze-drying and ashing but the elemental contents did not reveal evaluable correlations.

1. Introduction

Biological organisms are mainly composed of H, C, N, O, P, S, but certain elements like Na, Mg, Cl, K, Ca are also present in significant amounts. In addition to these macroconstituents a considerable number of so-called micro- or trace elements are also essential for life. For higher animals the dietary essentials are Cr, Mn, Fe, Co, Cu, Zn, Mo (all transition elements) and Se, I and Sn, while F, V, Ni, As, Br, Cd and Ba form the group of probably essential elements [1, 2].

The concentrations of these essential trace elements are in the ppm range. In order to preserve the functional and structural integrity of animal tissues the values of these elements must be maintained within relatively narrow limits. Because most of the trace elements are supplied by food, to prevent dietary deficiency or toxicity animals must be given a diet containing the required elements in adequate amounts, in proper proportions, and in available forms. Nowadays the micro element necessities of animals in stock breeding are provided by adding so called "premixes" to the food. The reliable control of the elemental compositions of these premixes is equally important both for the factories producing the premixes and for the farms. Premixes tend to be expensive: if too much is given, this means an unnecessary increase in the cost of meat production whereas deficiencies may give rise to problems in the growth and health of animals. This paper describes X-ray fluorescence (XRF) measurements of the elemental composition of different premix samples and the preliminary efforts to monitor trace element levels of different animal tissues by particle induced X-ray emission (PIXE).

* Dedicated to Prof. S. Szalay on his 75th birthday

** Biological Research Centre, 6701 Szeged, Hungary

2. Principles of XRF and PIXE methods

The sample of interest is irradiated by monochromatic X- or γ -rays of an appropriate radioactive source in the case of XRF [3] or a proton beam of 2–4 MeV energy for PIXE [4]. These irradiations induce the characteristic X-rays of the constituent atoms of the sample. Since the energies of these radiations are characteristic of the atomic number of the elements, simple qualitative elemental analysis can be performed by precise measurements of the X-ray spectra. The intensities of the different characteristic X-rays, on the other hand, are strongly correlated with the concentrations of the elements of interest thereby allowing quantitative analyses. In the simplest case when the sample is so thin that its disturbing effects on the X-rays and the energetic protons are negligible this correlation is a direct proportionality. The analysis of thicker samples, however, requires more complicated calculations [5, 6], or comparison with standard samples of similar but well known composition.

3. XRF measurements of different premixes

About 1 g from each of the premix samples provided by the "Vörös Csillag" Agricultural Co-operative, Füzesgyarmat, Hungary, was simply pressed into pellets of 12 mm in diameter, applying 15 t/cm² pressure using a hydraulic press. The pellets were put on a 2.5 μ m thin Mylar foil (Somar Laboratories, Inc.) stretched over the source holder containing a ¹⁰⁹Cd radioisotope ring source of 925 MBq activity for X-ray excitation (New England Nuclear Co.). The characteristic X-rays were detected with a vertically mounted Si(Li) detector (Model 7333E) coupled to X-ray processing electronics (Models 1713 and 1764) manufactured by Canberra Inc. The analog signals were converted and stored by a Canberra multichannel analyser (Model 8100). Net peak areas in the spectra were calculated from the integrals under the peaks of interest and that of suitable background regions, using a HP-29 programmable pocket calculator. To obtain the elemental concentrations the peak intensities were compared with those obtained by irradiating a set of reference pellets pressed from Bowen's kale [7] containing 0, 0.1 and 1% additional Fe and Zn. The results of the 8000 s long measurements are summarized in Table I. The experimental errors are not indicated at each particular concentration, the overall precision in the 1000 μ g/g range is estimated to be 10%, and 20% elsewhere.

Two main conclusions can be drawn from the Table. Firstly, it is immediately clear that premixes Nos 1 and 2 differ drastically from the others. Figure 1 also demonstrates this difference and suggests that probably these samples are final food mixtures and not the premixes themselves. Namely, simultaneously with the characteristic X-ray peaks the intensity ratio of incoherently to the coherently scattered exciting photon intensities is also very different. Because this ratio increases with the average atomic number of the sample, "premix" No. 1 (and No. 2 also) must contain

Table I

Trace element content of different premixes [$\mu\text{g/g}$]

No	Mn	Fe	Ni	Cu	Zn	Rb	Sr
1	—	280	40	47	85	14	39
2	—	130	—	12	35	6	—
3	1100	5300	200	1800	5600	2	54
4	800	1700	200	2100	1500	2	48
5	500	2600	100	1700	2600	—	51
6	2500	2800	—	300	3000	4	65
7	1900	2500	—	300	550	2	60

much more of the light component (composed of H, C, O and N) compared with the others.

Secondly, the elemental contents of the real premixes also show serious deviations. The Fe and Zn contents of premixes Nos 3 and 4, for instance, differ by a factor greater than three, but the Cu contents in samples Nos 4 and 6 are even more divergent. These results prove that regular control of the elemental composition of the premixes is strongly recommended in order to maintain the quality of feed at a desirable level.

4. PIXE analysis of chicken muscle and chicken liver tissues

Soft animal-tissue samples have a very low mineral content in their bulk composed from low atomic number elements even after complete dehydration. This is highly inconvenient for XRF analysis because of the large background resulting from the incoherently scattered exciting radiation. To reduce this background, the elimination of the organic bulk is desirable. Of the various destructive methods [8] dry ashing was chosen. From 1 g raw tissue, however, only about 1.5 mg ash remains, which is too small for easy XRF measurements. On the other hand, this quantity is far enough for the PIXE method, so this latter was chosen for the elemental analysis.

Tissue samples of about 1 g were quickly frozen in liquid nitrogen and lyophilized in a glass vacuum desiccator which was pumped overnight through a cold trap. The freeze dried tissues were powdered in agate mortar and placed in platinum or quartz crucibles. The samples were ashed at 700 °C for 4–5 hours in a muffle oven. The ash was dissolved in 1 ml of 6N HNO₃ (Carlo Erba) with a Y concentration of 500 ppm as an internal standard. A 5 μl aliquot of this solution was placed on the 2.5 μm Mylar foil mounted on the pure aluminium target holder and allowed to dry at room temperature in a glass desiccator.

The samples were irradiated with 2.5 MeV protons from the 5 MeV Van de Graaff accelerator of our Institute. The X-rays produced passed through the 4 μm thick

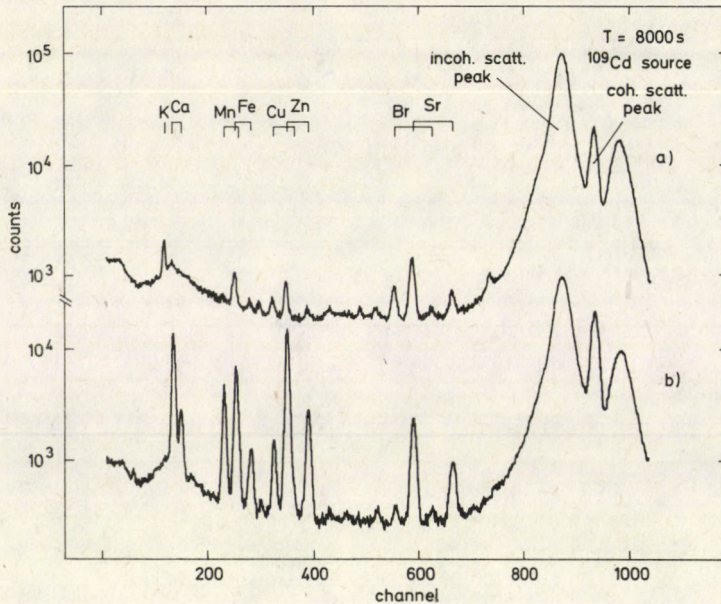


Fig. 1. XRF spectra of premixes No 1 (a) and No. 4 (b)

Mylar window of the target chamber and 17.5 mm air before entering the X-ray detector (the same as was used in the XRF measurements) positioned at 90° to the beam.

In order to find a correlation between the trace element content of certain animal tissues and that of the food supplied earlier to the animals, many chicken muscle and chicken liver samples were prepared and analysed. (Samples were taken from chickens fed by premix-containing food and also from controls which received a different diet.) Figure 2 shows a typical PIXE spectrum from the analysis of chicken liver. The conclusions of these measurements can be summarized as follows.

The results of repeated measurements on the same target agreed with each other within the experimental error. Measurements on parallel samples prepared from the same solution also gave consistent results. These facts confirm the reliability of both the PIXE method and the target preparation process and exclude observable radiation damage on the targets. On the other hand the trace element content of different parts from the same organ exhibited variations of similar magnitude as those obtained from analyses of samples from different individuals. Muscle turned out to be more heterogeneous in this sense than liver. Because of this large scatter in the experimental data the expected correlation could not be observed. In order to find a representative sampling method, more systematic investigations are needed.

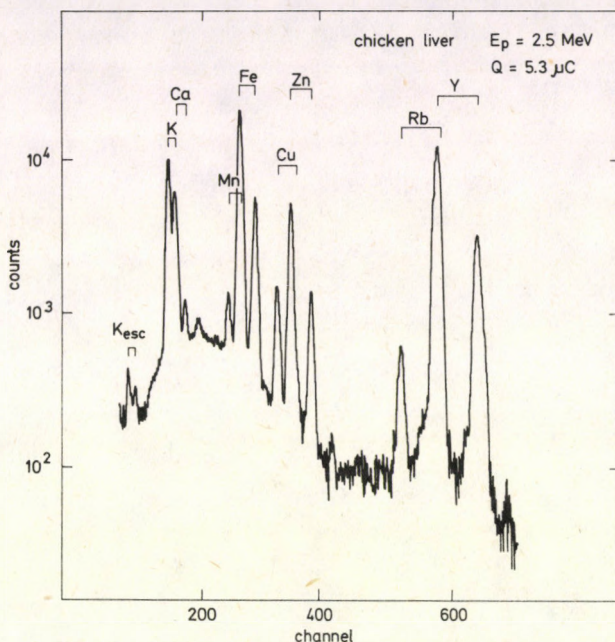


Fig. 2. PIXE spectrum of chicken liver sample

Acknowledgement

The authors are grateful to Dr. L. Prohászka, who initiated the tissue analysis and also provided the samples, for his kind cooperation and for fruitful discussion.

References

1. E. J. Underwood, Trace Elements in Human and Animal Nutrition, Academic Press, New York, 1971.
2. V. Valkovic, Trace Element Analysis, Taylor and Francis, London, 1975.
3. Sz. Török and Z. Szőkefalvi-Nagy, J. Radioanal. Chem. 78, 117, 1983.
4. L. Keszthelyi, L. Varga, I. Demeter, K. Hollós-Nagy and Z. Szőkefalvi-Nagy, Anal. Biochem. 139, 418, 1984.
5. R. Tertian and F. Claisse, Principles of Quantitative X-Ray Fluorescence Analysis, Heyden, London, 1982.
6. W. Reuter, A. Lurio, F. Cardone and J. F. Ziegler, J. Appl. Phys., 46 3194, 1975.
7. G. Demortier, Radiochem. Radioanal. Letters, 20 197, 1974.
8. T. T. Gorsuch, The Destruction of Organic Matter, Pergamon Press, Oxford, 1970.

THE $X\alpha$ METHOD WITH AB INITIO EXCHANGE PARAMETERS, DIAMAGNETIC SUSCEPTIBILITY AND NUCLEAR MAGNETIC SHIELDING CONSTANTS FOR SEVERAL ATOMS*

R. GÁSPÁR and Á. NAGY

*Institute of Theoretical Physics, Kossuth Lajos University
4010 Debrecen, Hungary*

Since the appearance of the $X\alpha$ method there have been several attempts to make it an ab initio theory introducing an ab initio exchange parameter α into the $X\alpha$ method. In his previous papers one of the authors suggested a self-consistent way of calculating exchange parameter α in the $X\alpha$ method. The diamagnetic susceptibility and the nuclear magnetic shielding constants are presented for atoms with the atomic numbers $Z = 3 - 36$. The $X\alpha_{\text{SCF}}$ values are close to the Hartree-Fock results. It is shown that the $X\alpha$ spin orbitals approximate the Hartree-Fock ones near the nucleus better than far from the nucleus. In the values calculated by the $X\alpha$ method for the diamagnetic susceptibility the shell structure of atoms is reflected. The nuclear magnetic shielding constants do not have a similar feature.

Introduction

In the past three decades considerable progress has been made in the theory of exchange. The $X\alpha$ method has been suggested and developed by Slater [1] since 1951. Another way of introducing the $X\alpha$ method has been proposed by one of the authors [2]. Since that time the $X\alpha$ method has been widely used in various fields of research.

One of the fascinating current problems in the $X\alpha$ method is to derive theoretical exchange parameters. Gopinathan, Whitehead and Bogdanovič [3] introduced theoretical exchange parameters, but they applied an adjusting parameter in their formula.

One of the authors proposed an ab initio method for the determination of the self-consistent exchange parameters in the $X\alpha$ method [4]. Recently, the authors made a comparison of the orbitals of Neon, Argon and Krypton calculated by the Hartree-Fock and the $X\alpha$ method with several values of α including the self-consistent exchange parameter α [5].

Several years ago one of the authors [6] derived an analytical formula for the nuclear shielding factor from general principles of the quantum theory. Now the diamagnetic susceptibility and the nuclear magnetic shielding constants for several

* Dedicated to Prof. S. Szalay on his 75th birthday

atoms have been calculated by the $X\alpha$ method with SCF exchange parameters. Our results are only slightly different from the Hartree-Fock data with a substantial saving in the computations.

The method

Our method proceeds from the free-electron gas model. The exchange potential of a free electron having spin up is given by the expression

$$V_{x\uparrow}(1) = -8F(\eta) \left[\frac{3}{4\pi} \rho_{\uparrow}(1) \right], \quad (1)$$

where

$$F(\eta) = \frac{1}{2} + \frac{1}{4\eta} (1 - \eta^2) \ln \left| \frac{1 + \eta}{1 - \eta} \right| \quad (2)$$

and

$$\eta = \frac{k}{k_F} \quad (3)$$

is the reduced momentum of the electron considered. ρ_{\uparrow} is the total density with spin up.

$$E_{F\uparrow} = k_{F\uparrow}^2 \quad (4)$$

is the Fermi energy. Energy is in Rydbergs, other quantities are in atomic units. It is possible to average the exchange potential (1) in the momentum space

$$V_{x\uparrow}(1) = -8 \left[\frac{3}{4\pi} \rho_{\uparrow}(1) \right]^{1/3} \frac{\int_{\eta_1}^{\eta_2} F(\eta) \eta^2 d\eta}{\int_{\eta_1}^{\eta_2} \eta^2 d\eta}. \quad (5)$$

So an $X\alpha$ exchange potential

$$V_{x\alpha\uparrow}(1) = -6\alpha_{\uparrow} \left[\frac{3}{4\pi} \rho_{\uparrow}(1) \right]^{1/3} \quad (6)$$

is obtained with the parameter

$$\alpha_{\uparrow} = \frac{\left\{ \frac{1}{2} (\eta^3 + \eta) - \frac{1}{4} (\eta^2 - 1)^2 \ln \left| \frac{1 + \eta}{1 - \eta} \right| \right\}_{\eta_1}^{\eta_2}}{\left\{ \eta^3 \right\}_{\eta_1}^{\eta_2}}. \quad (7)$$

If the averaging process is done over all the occupied states (i.e. $\eta_1 = 0$ and $\eta_2 = 1$), the value of the exchange parameter is 1, the parameter that was proposed by Slater. If

we average over a thin shell near the Fermi surface (i.e. $\eta_1 = \frac{k_{F\uparrow} - \varepsilon}{k_{F\uparrow}}$ and $\eta_2 = 1$ and $\varepsilon \rightarrow 0$)

$\alpha = \frac{2}{3}$ is obtained. It is the exchange parameter suggested by Gáspár. In his earlier

papers one of the authors [4] introduced the following averaging process. The average is done over a thin shell near the Fermi surface for a layer having v_{\uparrow} electrons in the unit volume (i.e. $\eta_1 = \eta = \left(1 - \frac{v_{\uparrow}}{\rho_{\uparrow}}\right)^{1/3}$, $\eta_2 = 1$) and so the exchange parameter is given by

$$\alpha_{\text{shell}\uparrow}(1) = \frac{\rho_{\uparrow}}{v_{\uparrow}} \left\{ 1 - \frac{1}{2} \eta^3 - \frac{1}{2} \eta + \frac{1}{4} (\eta^2 - 1)^2 \ln \left| \frac{1 + \eta}{1 - \eta} \right| \right\}, \quad (8)$$

where

$$v_{\uparrow}(1) = u_i^*(1) u_i(1) \quad (9)$$

is the density of the electron in question. As the exchange parameter (8) is different for different shells, another averaging can be carried out

$$\alpha_{\uparrow}(1) = \frac{\sum_j n_j \alpha_{\text{shell}\uparrow}(1)}{\sum_j n_j}, \quad (10)$$

where n_j denotes the number of the electrons in the shell j . Though this exchange parameter is the same for the electrons having the same spin, it is still a function of the position of the electron. A constant parameter α_{\uparrow} can be introduced so that the mean squared deviation of $V_{X\alpha\uparrow}(1)$ and $V_{X\alpha\uparrow(1)}(1)$ is minimized. Here $V_{X\alpha\uparrow}(1)$ is the usual X α potential with the constant exchange parameter α_{\uparrow}

$$V_{X\alpha\uparrow}(1) = -6\alpha_{\uparrow} \left[\frac{3}{4\pi} \rho_{\uparrow}(1) \right]^{1/3} \quad (11)$$

and $V_{X\alpha\uparrow(1)}(1)$ is a modified X α exchange potential with the exchange parameter (10) which is not a constant

$$V_{X\alpha\uparrow(1)}(1) = -6\alpha_{\uparrow}(1) \left[\frac{3}{4\pi} \rho_{\uparrow}(1) \right]^{1/3}. \quad (12)$$

The α_{\uparrow} exchange parameter has to be determined self-consistently.

This way of calculating the exchange parameter α can be considered an ab initio one as it contains no adjustable parameter (in contrast with the original X α method)

Results and discussion

The diamagnetic susceptibility is given by [7]

$$\chi_d = -\frac{1}{6} N \alpha^2 a_0 \sum_i \langle r_i \rangle, \quad (13)$$

where N , a_0 and α are Avogadro's number, the Bohr radius and the fine structure constant, respectively. The summation is extended over the electrons in the system. r_i is the distance of the electron i from the nucleus.

In a homogeneous external magnetic field H_0 , the effective magnetic field acting on the nucleus is

$$H = H_0 - \sigma H_0, \quad (14)$$

where σ is the nuclear magnetic shielding constant. The diamagnetic nuclear shielding factor has been calculated by Lamb [8]

$$\sigma_d = \frac{1}{3} \alpha^2 \sum_i \left\langle \frac{1}{r_i} \right\rangle. \quad (15)$$

Table I

Diamagnetic susceptibility and nuclear magnetic shielding constants calculated for several atoms by the $X\alpha_{\text{SCF}}$ method and the Hartree-Fock theory [9].

Atomic number	Diamagnetic susceptibility [$10^{-11} \text{ m}^3 \text{ mol}^{-1}$]		Magnetic shielding constants [10^{-5}]	
	$X\alpha_{\text{SCF}}$	HF	$X\alpha_{\text{SCF}}$	HF
3	1.66	1.48	9.99	10.2
4	1.39	1.37	14.81	15.0
5	1.76	1.26	20.27	20.2
6	1.12	1.09	26.15	26.1
7	1.00	0.96	32.58	32.6
8	0.91	0.89	39.58	39.5
9	0.82	0.81	47.17	47.1
10	0.76	0.74	55.32	55.2
11	2.21	2.15	62.79	62.9
12	2.24	2.35	70.90	70.9
13	2.69	2.65	78.96	79.0
14	2.61	2.56	87.41	87.4
15	2.43	2.40	96.10	96.1
16	2.34	2.31	105.05	105.0
17	2.20	2.19	114.28	114.3
18	2.08	2.06	123.78	123.8
19	4.01	4.06	132.84	132.9
20	4.29	4.48	142.22	142.3
21	4.03	4.21	152.12	152.1
22	3.80	3.98	162.23	162.3
23	3.60	3.77	172.60	172.7
24	3.42	3.01	183.21	183.7
25	3.25	3.41	194.07	194.2
26	3.12	3.26	205.19	205.3
27	2.99	3.12	216.54	216.6
28	3.13	3.00	228.13	228.2
29	2.77	2.63	239.97	240.5
30	2.67	2.77	252.05	252.2
31	2.69	3.24	267.01	263.9
32	3.38	3.30	279.93	275.7
33	3.35	3.25	287.60	287.7
34	3.31	3.26	299.74	299.8
35	3.24	3.21	312.03	312.1
36	3.16	3.13	324.48	324.6

The results gained for the diamagnetic susceptibility and the diamagnetic nuclear shielding constant seem to be good criteria for the correctness of the wave functions.

Table I contains the diamagnetic susceptibility and the nuclear magnetic shielding constants for several atoms. Table I includes not only the results of the $X\alpha$ calculations with ab initio exchange parameters but those of the Hartree-Fock theory [9], too. The $X\alpha$ results for the nuclear magnetic shielding constants are closer to the Hartree-Fock values than for the diamagnetic susceptibilities. The expectation values $\left\langle \frac{1}{r} \right\rangle$, i.e. the nuclear magnetic shielding constants show how adequate the spin orbitals are near the nucleus. The correctness of the wave functions far from the nucleus can be detected by the expectation values $\langle r^2 \rangle$ i.e. the diamagnetic susceptibility. It means that the $X\alpha$ orbitals are closer to the Hartree-Fock ones near the nucleus than far from the nucleus.

Looking at the diamagnetic susceptibilities the shell structure of atoms can be easily followed. The $X\alpha$ method enables calculations for the average-energy-of-the-configuration. It means that for closed shells the $X\alpha$ results are closer to the exact ones than for open shells. Moreover, for open shells the spin-polarized $X\alpha$ method is to be applied. Here results of a non-spin-polarized calculation are presented. This approximation is especially problematic for odd atomic numbers. The greatest deviations between the diamagnetic susceptibilities calculated by the $X\alpha$ and Hartree-Fock methods can be seen in these cases. Generally, the worst $X\alpha$ results are gained for the open shells having only one or only a few electrons. If the number of electrons in the open shell is larger, the diamagnetic susceptibilities calculated by the $X\alpha$ method are closer to those of the Hartree-Fock theory. Of course, only the diamagnetic susceptibility is sensitive to the shell structure of the atom. The nuclear magnetic shielding constant does not reflect the shell structure, as the expectation values $\left\langle \frac{1}{r} \right\rangle$ chiefly depend on the behaviour of the spin orbitals near the nucleus.

References

1. J. C. Slater, *Phys. Rev.*, *81*, 385, 1951.
2. R. Gáspár, *Acta Phys. Hung.*, *3*, 263, 1954.
3. M. S. Gopinathan, M. A. Whitehead and R. Bogdanovič, *Phys. Rev.*, *A14*, 1, 1976.
4. R. Gáspár, *Acta Phys. Hung.*, *35*, 213, 1974; *Acta Phys. et Chim. Debr.*, *19*, 7, 1974; *Acta Phys. et Chim. Szeged.*, *20*, 321, 1974.
5. R. Gáspár and Á. Nagy, *Acta Phys. Hung.*, *53*, 247, 1982.
6. R. Gáspár, *Acta Phys. Hung.*, *28*, 71, 1970; *Acta Phys. et Chim. Debr.*, *16*, 7, 1971.
7. J. H. Van Vleck, *Theory of Magnetic Susceptibilities*, Oxford Univ. Press, London, 1932.
8. W. E. Lamb, Jr., *Phys. Rev.*, *60*, 817, 1941.
9. G. Malli and S. Fraga, *Theoret. Chim. Acta (Berl.)*, *5*, 275, 1966.

FLAVOMONONUCLEOTIDE COMPLEX FORMATION STABILIZED BY POLYMER MATRIX*

REGINA DRABENT

*Department of Physics, Institute of Physics and Food Chemistry
Academy of Agriculture and Technology, Olsztyn, Poland*

and

L. SZALAY

*Department of Biophysics, József Attila University
Szeged, Hungary*

The molecular complex formation of flavomononucleotide (FMN) stabilized by a poly(vinyl alcohol) (PVA) matrix has been studied using absorption, fluorescence and polarized fluorescence spectroscopy. FMN forms monomers and excimers with fluorescence maxima at about 510 and 540 nm, respectively. The FMN excimers are stabilized by a PVA matrix and form an energetically well-isolated molecular complex suitable for modelling in vivo reaction system in which electronically excited states participate.

1. Introduction

The functions of biological molecules are generally expressed through specific interactions with other molecules. These interactions are important in enzymatic processes and may be treated as molecular complex formation [5, 8].

Flavin coenzymes form various intermolecular complexes with proteins and different organic compounds. In addition, they can form dimers, higher multimers or several oxidized and reduced flavins. Flavin complex formation is known to depend strongly on the physical and chemical properties of the dispersion phase [3, 5, 7, 8, 10].

The structure of flavin intermolecular complexes and the mechanism of complex formation have not been clearly explained. Many authors have shown that the interaction causes the molecules to stack on each other vertically, the complexes being stabilized by a weak interaction such as hydrogen-bonding, charge-transfer interaction or other non-bonding forces. Flavins can also form exciplexes with several organic molecules. The molecular complexes of flavins can be fluorescent or non-fluorescent [5, 7–10].

The results of many experiments performed under different physical and chemical conditions suggest that the microenvironment and steric factors of the interacting molecules play important roles in the complex formation. On the other

* Dedicated to Prof. S. Szalay on his 75th birthday

hand, in biological systems interaction occurs especially between flavin molecules stabilized by proteins: between flavins and flavoproteins or/and between flavoproteins.

In this paper an investigation of the flavomononucleotide (FMN) complex formation stabilized by synthetic macromolecules is presented. The macromolecule used in our case was poly(vinyl alcohol) (PVA). The PVA chains interact with the flavins and induce a change in the charge distribution in the flavin molecules [1]. Thus, PVA films are in many ways similar to liposome systems, micellar systems, surfactants, etc. [2, 9].

2. Experimental

FMN ($C_{17}H_{20}N_4NaO_9P$) from Fluka AG and coarse-grained PVA powder from Loba-Chemie Wien-Fischamend were used for the experiments. FMN was dissolved in an aqueous solution of PVA and isotropic films were obtained by water evaporation [4]. The FMN concentrations were given in gram FMN per gram PVA and in mole FMN per mole PVA monomer (Table I). The PVA macromolecules are built up from two types of monomers; vinyl alcohol $CH_2=CHOH$ (M_1) and vinyl acetate $CH_2=CHOOCCH_3$ (M_2). The PVA used in our experiment contained much M_2 , but not more than 50% [4]. The average molar mass of the PVA monomers is therefore not higher than $(44 + 86) \cdot \frac{1}{2} = 65$. The number of PVA monomers per FMN molecule is given in Table I.

The *absorption spectra* were measured with a Specord UV-Vis Zeiss spectrophotometer and with another one of higher precision (the optical density error is ± 0.0003) built in our laboratory in Olsztyn. The thickness of the films at low concentrations was about 0.2 mm, while that of the films with high concentrations used to measure the absorption spectra was one order of magnitude less.

Table I

Fluorescence and emission anisotropy of FMN in a PVA matrix and the ratios of PVA monomers to FMN molecules at different concentrations

C	Concentrations		Location of fluorescence maximum [nm]	Emission anisotropy $\lambda_{exc} = 470$ nm $\lambda_{fluor} = 490 - 620$ nm	Number of PVA monomers per FMN
	FMN in g/g PVA	FMN in $\frac{M}{M_a}$ PVA			
C ₁	$8 \cdot 10^{-5}$	$1.1 \cdot 10^{-5}$	519	—	$9.2 \cdot 10^4$
C ₂	$4 \cdot 10^{-4}$	$5.4 \cdot 10^{-5}$	520	0.305	$1.8 \cdot 10^4$
C ₃	$2 \cdot 10^{-3}$	$2.7 \cdot 10^{-4}$	522	0.300	$3.7 \cdot 10^3$
C ₄	$4 \cdot 10^{-3}$	$5.4 \cdot 10^{-4}$	532	0.210	$1.8 \cdot 10^3$
C ₅	$1.2 \cdot 10^{-2}$	$1.6 \cdot 10^{-3}$	543	0.080 0.175*	$6.1 \cdot 10^2$

* for $\lambda_{fluor} \geq 540$ nm

M = number of FMN moles, M_a = number of PVA moles for the average monomer mass

The fluorescence spectra were measured with a Perkin-Elmer MPF 44A spectrofluorimeter. Linear polarized exciting light was used. We measured fluorescence

$$F(\lambda_{em}) = (F + bF)k_1(\lambda_{em})$$

and emission anisotropy spectra

$$r(\lambda_{em}) = \frac{F - bF}{F + 2bF},$$

where $k_1(\lambda_{em})$ = quantum correction coefficient with correction for reabsorption, and b = polarization coefficient. All measurements were carried out at room temperature.

3. Results

a) Absorption spectra

The long-wave absorption band of FMN in PVA was measured for all concentrations. The maximum of the band is at about 445 nm; its location and shape do not change with the concentration (Fig. 1, dotted line).

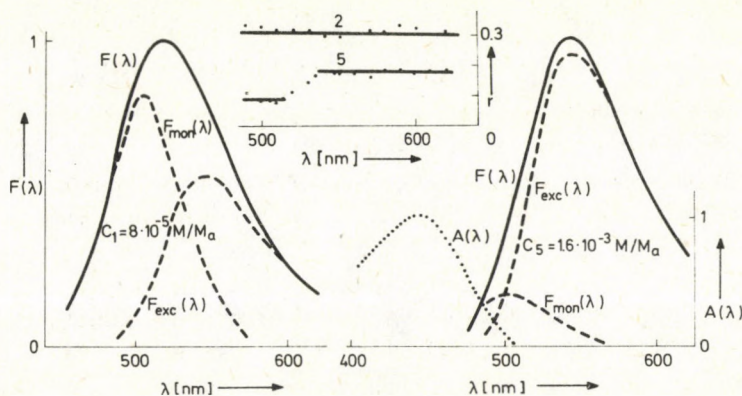


Fig. 1. Relative fluorescence spectra of FMN, $F(\lambda)$, in PVA matrix (solid lines), and those of the monomers, $F(\lambda)_{mon}$, and excimers, $F(\lambda)_{exc}$ (broken lines) at different concentrations. Relative absorption spectrum of FMN, $A(\lambda)$, in PVA matrix. Emission anisotropy spectra (inset) for 4.10^{-4} (2) and $1.2.10^{-2}$ (5) g/g concentrations, respectively

b) Fluorescence and emission anisotropy spectra

The emission spectra of FMN were measured for excitations with 470 and 420 nm, within the long-wave absorption band. The spectra for the two excitations were similar. Figure 1 (solid lines) and Table I show that the fluorescence spectra are

shifted towards longer waves with the increase of the FMN concentration. For low concentrations of FMN the anisotropy of emission, r , is constant over the whole emission spectrum (Fig. 1, inset curve 2). The r values at the highest concentration C_5 have two regions: r is constant for λ_{em} 540 nm and decreases towards shorter waves (Fig. 1, inset, curve 5).

4. Discussion

Since the absorption spectra do not depend on the concentration from C_1 to C_5 , there are only monomeric FMN molecules present in the whole range of these concentrations. The shift of the fluorescence spectra toward longer waves, however, indicates the presence of at least two fluorescent species with different fluorescence spectra, which contribute to the total fluorescence according to their relative amounts. This is corroborated by the emission anisotropy spectrum, which is constant for C_1 but suddenly increases towards the longer waves, revealing the appearance of a new fluorescent species. The new species should be a fluorescent dimer, commonly called an excimer.

In order to find the relative fluorescence spectra of the monomer and excimer species, the total fluorescence, F , can be considered to be a linear combination of the monomer and excimer fluorescences, F_{mon} and F_{exc} , respectively. Therefore, the experimentally obtained $F(\lambda) = k_1 F_{mon}(\lambda) + k_2 F_{exc}(\lambda)$. If we suppose that $F(\lambda) = k_2 F_{exc}(\lambda)$ for C_5 , $F_{exc}(\lambda)$ can be calculated for all concentrations at zero approximation, and similarly, if $F(\lambda) = k_1 F_{mon}(\lambda)$ for C_1 , we have $F_{mon}(\lambda)$. Thereafter we can determine the approximate relative fluorescence spectra $F_{mon}(\lambda)$ and $F_{exc}(\lambda)$ at a second approximation (Fig. 1, broken lines). After this procedure we have the component spectra for C_1 and C_5 , the sum of which results in the total spectrum. The maximum of $F_{mon}(\lambda)$ and $F_{exc}(\lambda)$ is at about 506 and 544 nm, respectively. At a concentration of C_1 , monomer and excimer fluorescence contribute to the total fluorescence in almost equal proportions, while at the higher concentration C_5 the monomer contribution is relatively small but still not negligible.

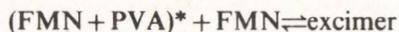
To find an explanation for these phenomena, the interaction of FMN with PVA should be analysed. As we mentioned above, the PVA molecule is a regular chain built up from two different parts. It might be assumed that these can be treated as two types of active centres, with which FMN molecules interact differently. Since the number of these centres with regard to a single FMN molecule changes from $9.2 \cdot 10^4$ to $6.1 \cdot 10^2$ (from C_1 to C_5), in terms of these overall concentrations it is impossible to saturate one type of active PVA centre at any concentration, and therefore the FMN molecules interact with PVA macromolecules equally at high and low concentrations [1]. One possibility remains: the FMN molecules stabilized by PVA chains are present in a local concentration higher than the overall concentration of the solution, similarly to micellar systems [2]. In the formation of excimers the steric factor plays a very important role [6]. Consequently, two factors (the high local concentration and the

specific steric orientation of the FMN molecules attached to the PVA matrix) lead to excimer formation even at comparatively low overall concentration.

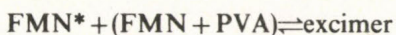
The excimer may be formed by a different mechanism: an FMN molecule connected to the PVA chain is in an excited state and interacts with a molecule in the ground state to form an excimer:



however, it cannot be excluded that the processes



and



also occur.

It further seems possible that FMN photoproducts with the same spectroscopic properties as those of FMN itself likewise take part in excimer formation. Flavin excimers exhibiting a weak fluorescence band at about 570 nm at room temperature have already been found [5]. Our FMN excimers stabilized by PVA have a relatively strong and clearly-defined band shifted to 544 nm, i.e. towards shorter waves. This indicates that our system is energetically very well isolated and the FMN excimer stabilized by PVA is a fairly stable system.

Since the PVA matrix is hydrophilic and FMN molecules should attach to hydrophilic regions [4], our system can be considered a suitable model of biological systems in which the proteins may have hydrophilic regions as well. Therefore, the energetically stable FMN excimer can play an important role in biological reactions, especially in reactions which occur in an electronically excited state.

References

1. K. Bystra, R. Drabent, L. Szubiakowska and B. Smyk, *Spectroscopy Letters* (in press), 1984.
2. K. Csatorday, E. Lehoczki and L. Szalay, *Biochim. Biophys. Acta*, 376, 268, 1975.
3. R. Drabent and H. Grajek, *Biochim. Biophys. Acta*, 758, 98, 1983.
4. R. Drabent and T. Olszewska, *Polymer*, 22, 1655, 1981.
5. R. Foster, in "Molecular Association. Including Molecular Complex". Vol. 2, Academic Press, London—New York—San Francisco, 1979.
6. O. Jelinek, 4th Conference on Luminescence, Conference Digest, Szeged, Hungary, p. 179, 1982.
7. K. Nichimoto, Y. Watanabe and Kunio Yagi, in "Flavins and Flavoproteins", ed. Kunio Yagi and Toshio Yamano, Japan Scientific Societies Press, Tokyo, 1980.
8. D. J. T. Porter, F. Scorbrough, Huey-Sheng Shien and D. Voet, in "Flavins and Flavoproteins", ed. Kunio Yagi and Toshio Yamano, Japan Scientific Societies Press, Tokyo, 1980.
9. W. Schmidt, *Photochem., Photobiol.*, 34, 7, 1981.
10. A. Slifkin, *Charge Transfer Interactions of Biomolecules*, Academic Press, London and New York, 1971.

INVESTIGATION ON COLLOID- AND X_K -CENTRES IN COLOURED NaCl CRYSTALS*

L. MALICKÓ, R. VOSZKA and A. WATTERICH

*Research Laboratory for Crystal Physics of the Hungarian Academy of Sciences
1502 Budapest, Hungary*

Direct transmission electron microscopic investigations were carried out on colloid- (640 nm) and X_K -centres (580 nm) in NaCl crystals. The crystals were checked by optical microscopy as well as by absorption spectroscopy. In samples containing mainly colloids additional reflections could be found in the selected area diffraction patterns. These foreign reflections were attributed to metallic Na particles. The absence of any additional foreign reflection to samples containing mainly X_K -centres indicates that in contrast to the colloids the X_K -centres do not behave like any foreign phase in NaCl.

1. Introduction

It is well known that in additively coloured NaCl crystals by some suitable heat treatment X-centres absorbing at 550 nm and blue colloid centres absorbing at about 640 nm can be produced. These latter centres may also be observed in natural blue rock salt crystals [1].

The views seeking to explain the nature of the X-centres and their relationship with the colloids are contradictory [2, 3]. Accordingly the X-centres may be either very small, non-scattering colloids, or — on the other hand — they might be thought of as point defect agglomerations specially positioned at dislocations. A recent review article referring also to electron microscopic results interprets all bands absorbing between 540 and 650 nm as colloidal centres in NaCl crystals, though with reference to the X-centres the possible role of impurities is also mentioned [4].

In an earlier work it was shown that in extra-pure, OH^- -free NaCl crystals coloured electrolytically or by X-irradiation, X_K -centres absorbing at 580 nm can be produced by F-light illumination at a suitable temperature, and it was shown that this F — X_K centre conversion can be used for information storage [5]. The condition of the F — X_K conversion makes the colloidal nature of the X_K -centres clearly questionable.

By transmission electron microscopy (TEM) using the replica technique a considerable difference was detected between the surface structure of alkali halide crystals containing colloids and the surface of colourless or thermally bleached crystals. In crystals containing colloids, traces of foreign particles between about 20 and 2000 nm could clearly be observed [6–8]. In good correlation with the absorption

* Dedicated to Prof. S. Szalay on his 75th birthday

spectra the colloids in coloured alkali halides were also directly observed in TEM without the appearance of additional reflections of the bcc alkali metals in the diffraction patterns [4, 10–12]. The absence of the expected additional reflections of the alkali metals was explained by the constraint matrix-like fcc structure of the colloids. However, this may be a consequence of the special preparation and TEM investigation techniques used.

The aim of the present work was to investigate whether any difference could be established by direct TEM between the crystals containing dominantly X_K -centres and those containing dominantly large colloids.

2. Experimental

For the investigations extra pure, OH^- -free NaCl single crystals [13] were used. Large cleavage pieces of crystals were heavily coloured either electrolytically or by X-irradiation in order to obtain pronounced differences in their colours and consequently in their microstructure after the subsequent heat- and light treatments carried out as reported earlier [5].

The electrolytic coloration was carried out using a home made apparatus; the crystals were treated in vacuum at about 870 K. For X-irradiation at room temperature a THX-250 deep-therapy apparatus working at 200 kV and 20 mA and yielding a dose rate of about $2 \text{ C} \cdot \text{kg}^{-1} \cdot \text{min}^{-1}$ was used. The bleaching of the F-band was carried out by a monochromator equipped with a xenon lamp. The optical absorption spectra were recorded at room temperature by a Perkin-Elmer 554 or a UV-VIS Specord spectrophotometer.

For comparison various types of large pieces were produced:

- electrolytically coloured, blue (EB) pieces containing relatively large colloids,
- the same as above but thermally bleached, slightly reddish (ER) pieces containing large colloids,
- purple-blue pieces containing X_K -centres, coloured by X-irradiation (XP),
- electrolytically coloured, purple-blue (EP) pieces,
- colourless (CL) pieces for colour and microstructure control.

From the large pieces, microscopic samples of about 1 mm diameter and some 10 μm thickness were cleaved and stuck on copper grids covered with Formvar support films, where they were further thinned by jets of water-ethanol mixtures in order to have single crystalline samples suitable for TEM. Powder samples were prepared in the usual way.

The whole preparation procedure was carried out under optical microscopic control to ensure the homogeneity of the crystals. The samples were then investigated by bright and dark field imaging modes (BF, DF) and selected area diffraction (SAD) in a conventional TESLA BS 500 TEM at 60 kV and beam currents of about 10 μA , at room temperature, without controlling the sample temperature.

Since the samples were prepared in air with water the following possibilities had been considered. Due to some dissolution and recrystallization processes, besides the expected matrix reflections, also traces of matrix reflection rings might appear on the SAD patterns of the single crystalline samples. Further, in the case of samples containing metallic Na one may expect besides the Na reflections the presence of reflections due to different reaction products — sodium oxides, hydroxides and carbonates [11]. However, remembering the extra purity of the matrix crystals used the appearance of any additional foreign reflections actually detects the original presence of reactive metallic Na, in contrast to samples which do not contain colloids.

From the investigations on CL samples a probable accuracy of about $\pm 2\%$ was possible in the evaluation of the SAD patterns. Because of this accuracy and bearing in mind the lattice plane spacings given in the International Table, besides the matrix reflections the presence or absence of the additional 110 and 200 type spots of the bcc Na resulting from different colour centres in the various samples may be expected. Of course, these Na reflections may coincide with certain reflections of the reaction products mentioned. With regard to the irradiation damage caused by the electron beam and manifesting itself in a very high concentration of different defects [14–17] the weak additional reflections can be detected only if the studies are made fast enough on fresh sample regions which are still not too badly damaged.

3. Results and discussion

3.1. Samples containing colloids

In natural blue crystals the so-called “blue” colloids are present [1] causing a typical absorption spectrum with peaks at about 650 nm and 530 nm (the centre structure is not yet known) as shown by curve 1 in Fig. 1. Curves 2 to 6 show that by X-irradiation the colloids are simultaneously converted to F- and X_K -centres. This fact points to the close relationship among the F-, X_K - and colloid centres.

In electrolytically coloured and quenched extra pure NaCl, F-centres are formed. During annealing at about 520 K, first the so-called X-centres appear with an absorption peak at about 550 nm. Further annealing above 520 K leads to the absorption peak at 640 nm being formed due to the colloids (see curve 1 in Fig. 2). After thermal bleaching for one hour at about 720 K the originally blue crystal becomes slightly reddish showing only a very flat, unknown absorption peak at about 740 nm (curve 2 in Fig. 2).

It could be seen from optical microscopic controls that the colour of the large pieces was not homogeneous throughout the entire volume of the pieces. In some regions of a few mm the EB pieces have purple-blue colour, for example, characteristic of the X_K -centres. The EP samples were prepared from these regions. Both in the EB and

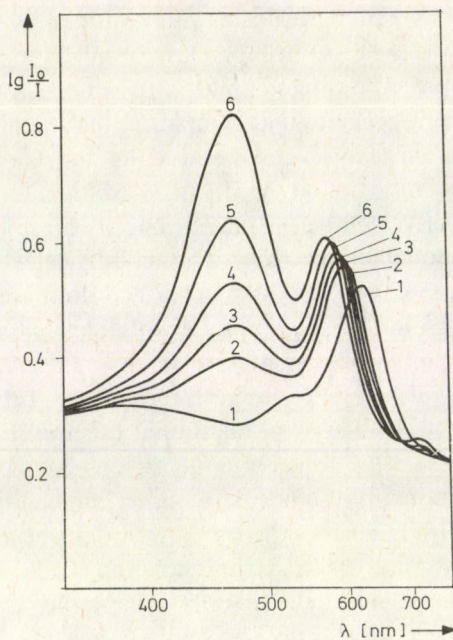


Fig. 1. Absorption spectrum of natural blue NaCl crystal (curve 1) and its change during subsequent X-irradiations of 10, 20, 40, 80 and 160 min (curves 2 to 6)

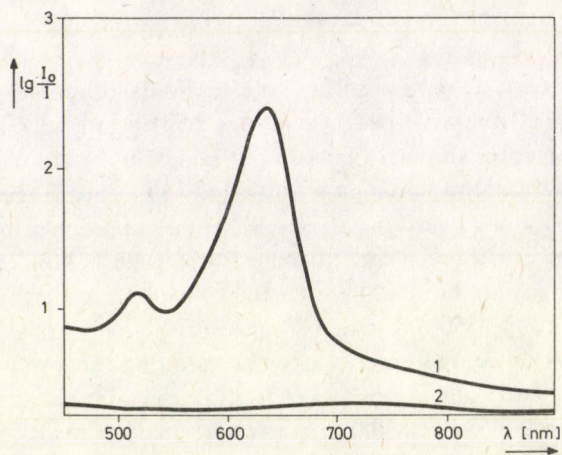


Fig. 2. Absorption spectrum of a small piece of
 — blue NaCl crystal coloured electrolytically (curve 1)
 — slightly reddish NaCl electrolytically coloured and then thermally bleached at 720 K 1 h (curve 2), containing colloids scattering the light

in the ER pieces small scattering and non-homogeneously distributed particles could be observed by ultramicroscopy.

In the single crystalline EB samples the BF images made with $\langle 001 \rangle$ beam vector in TEM show typical dark contrast spots (see parts a and c in Fig. 3) of sizes between about 10 and 300 nm. They are complex absorption and matrix strain contrasts caused by various crystal defects. However, on the basis of such BF images the colloids and other possible defects cannot be distinguished. The DF images made with 200 type matrix reflections (parts d and e of Fig. 3) point only to the presence of defects of partial elongated forms. In the SAD patterns of the single as well as of the polycrystalline EB samples, besides the matrix reflections rather weak additional reflections appeared.

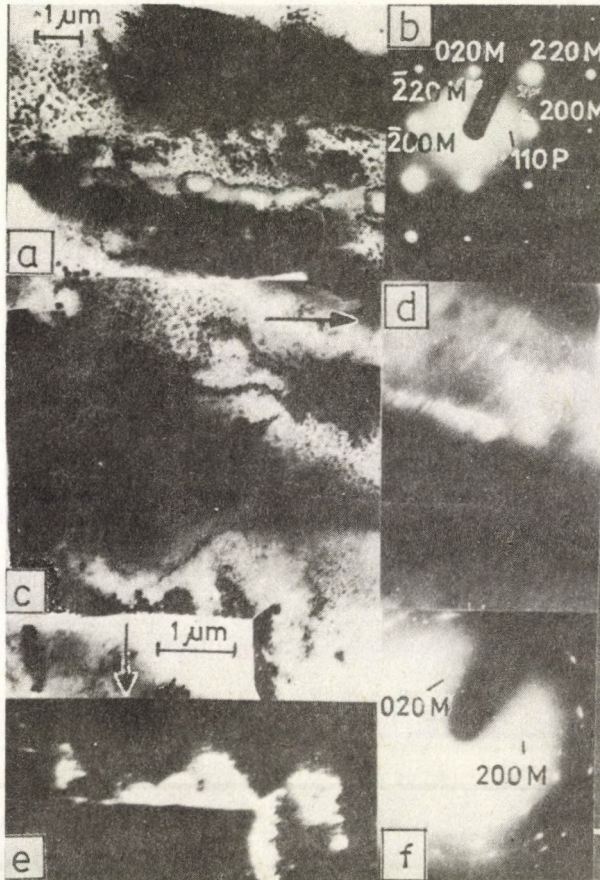


Fig. 3. Bright (a and c) and dark field (d and e) electron micrographs of (001) blue NaCl foil containing colloids. The fresh SAD pattern (b) showing weak additional 110 type reflections of bcc Na besides the [001] oriented matrix reflections. SAD pattern from the same range after considerable electron beam damage (f)

These additional reflections can be attributed to the 110 and 200 type reflections of the metallic bcc Na which naturally cannot be separated from certain reflections of the Na hydroxide and carbonate as possible reaction products. In part b of Fig. 3 for the case of a single crystalline (001) foil the SAD pattern made with the beam vector $\bar{B} = \langle 001 \rangle$ shows, for example, the appearance of weak 110 reflections of Na (see the mark). The SAD pattern taken after the electron irradiation of about 15 min at the same place (part f of Fig. 3) has already become obscured indicating serious damage of the crystal foil. The weak additional reflections cannot be recognized here any more. Because of the weakness of the additional spots and the serious damage to the foils and consequently to their complex SAD patterns good DF images with the additional reflections could not be obtained.

On ER samples the additional reflections mentioned in connection with the EB samples were also found. This is demonstrated in Fig. 4. The BF image of a (001) foil in part a shows also the dark contrast spots. However, both in the fresh (part b) and in the weakly damaged SAD patterns (part c) the 110 type reflections (P) of Na can easily be recognized besides the matrix spots.

These results show that the Na colloids, responsible for the characteristic peak at 640 nm and the unknown peak at 740 nm in the absorption spectra of NaCl, may be linked with the appearance of the additional reflections due to the metallic bcc Na in the TEM SAD patterns.

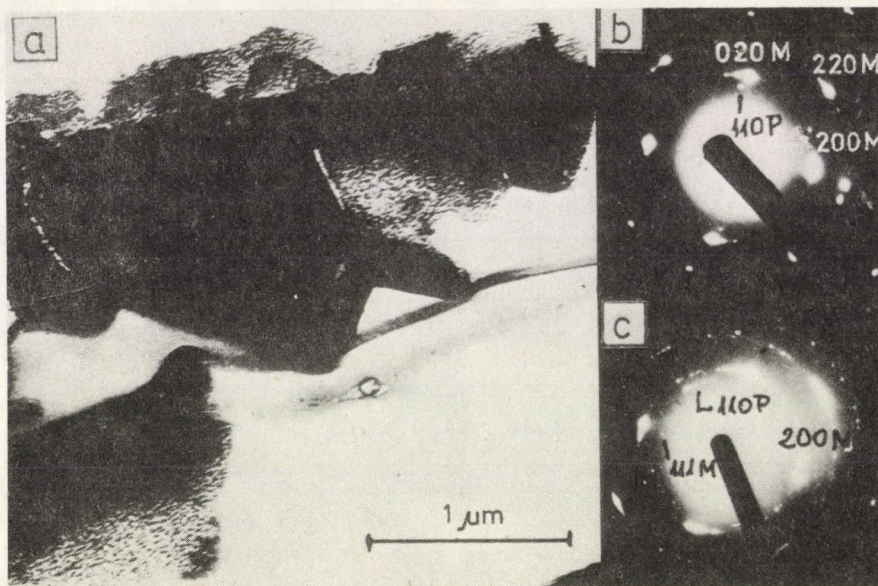


Fig. 4. Bright field electron micrograph (a) of (001) slightly reddish NaCl foil. Both the fresh (b) and the damaged (c) SAD patterns well show, besides the matrix reflections, additional reflections caused by colloids

3.2. Samples containing X_K -centres

The X-ray coloured and treated, purple-blue macroscopic pieces show a typical absorption spectrum with the peak at 580 nm (see curve 1 in Fig. 5) characteristic of the X_K -centres. Curves 2 to 6 demonstrate that by subsequent X-irradiations of 10, 20, 40, 80 and 160 min the X_K -centres can be converted to F-centres.

The spectrum in Fig. 6 was taken on a small macroscopic purple-blue crystal piece used directly for preparing the XP samples. The peak at 580 nm demonstrates the presence of X_K -centres. Judging by investigations using the optical microscope, in contrast to the electrolytically coloured pieces the colour of the X-ray coloured purple-blue crystal pieces seem to be homogeneous and within them no light scattering particles were found.

In the SAD patterns both in the single and the polycrystalline XP samples no additional reflections were found in contrast to the samples containing colloids. For example, part *a* of Fig. 7 is a typical BF image of an (001) XP foil showing here big, dark contrast spots. However, both in the fresh (part *c*) and in the damaged (part *d*) SAD patterns no trace of additional reflections appears. In the DF image (inset *b*) one observes only the usual elongated traces of some defects.

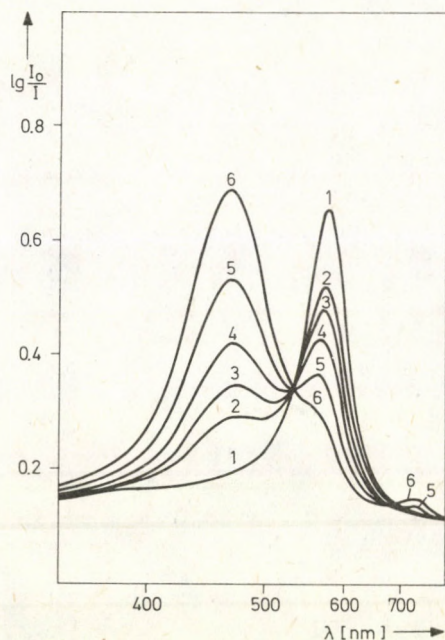


Fig. 5. Absorption spectrum of X-ray coloured, purple-blue NaCl crystal containing X_K -centres (curve 1) and its change during subsequent X-irradiations of 10, 20, 40, 80 and 160 min (curves 2 to 6)

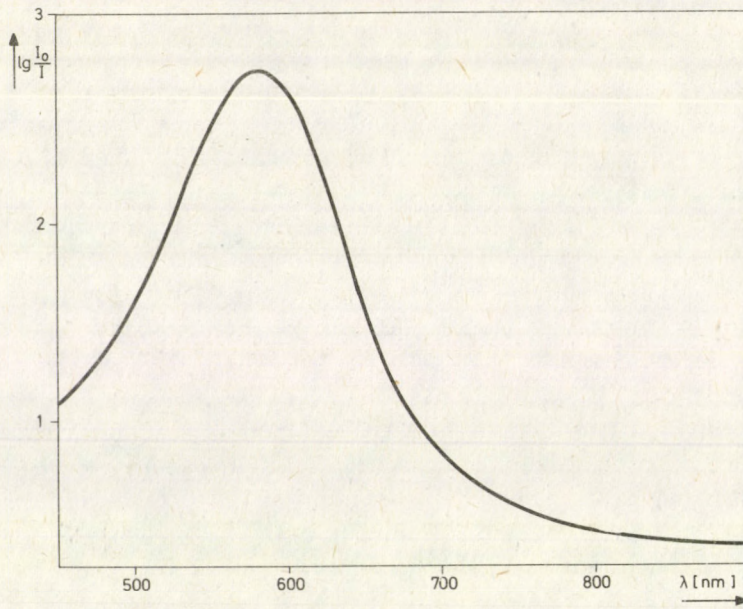


Fig. 6. Absorption spectrum of small piece of X-ray coloured, purple-blue NaCl crystal containing X_K -centres

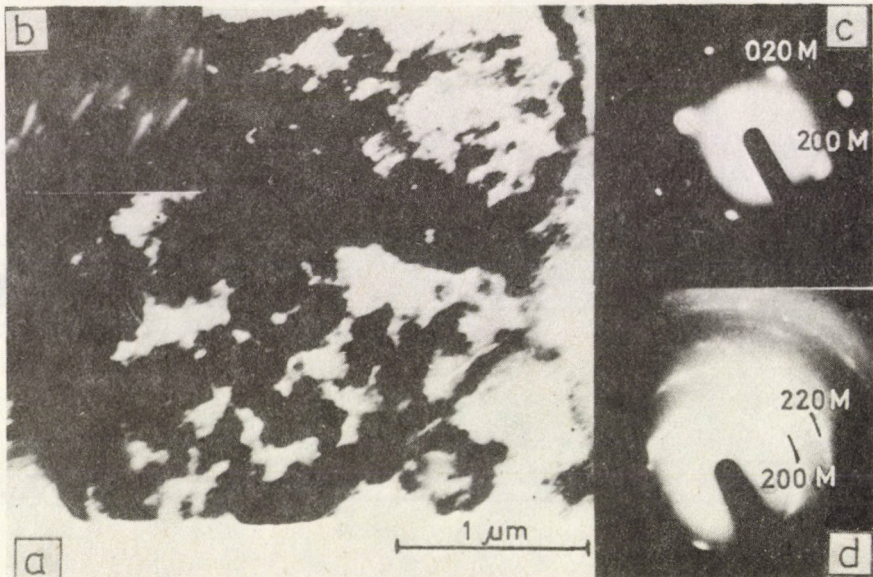


Fig. 7. Bright (a) and dark field (b) electron micrographs of (001) X-ray coloured purple-blue NaCl foil containing X_K -centres. The concerning fresh (c) and damaged (d) SAD patterns have no additional reflection apart from the matrix spots

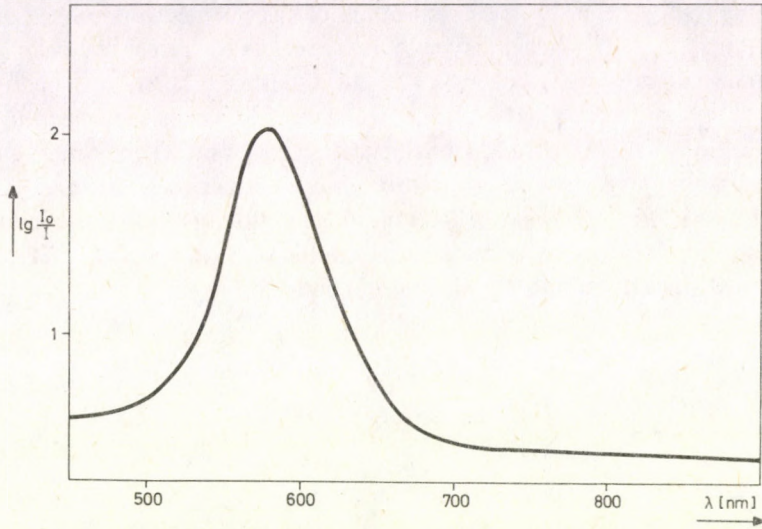


Fig. 8. Absorption spectrum of small purple-blue piece of inhomogeneously coloured blue NaCl crystal, containing X_K -centres

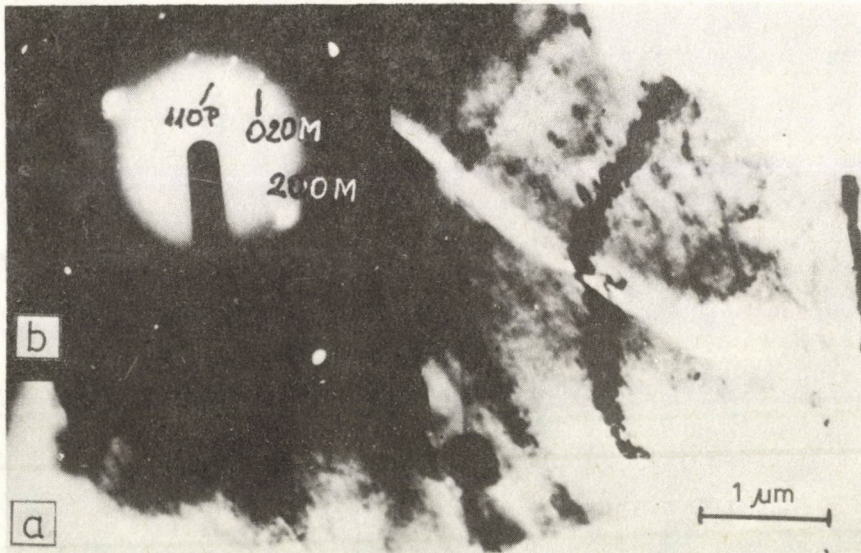


Fig. 9. Bright field electron micrograph (a) of (001) additively coloured purple-blue NaCl foil containing X_K -centres and traces of grain boundaries. The fresh SAD pattern (b) shows weak additional reflections of Na colloids

Figure 8 shows the absorption spectrum of a small macroscopic EP piece from an electrolytically, inhomogeneously coloured large crystal piece. The peak at 580 nm denotes the presence of X_K -centres. The SAD patterns taken on the single and polycrystalline samples originating from this EP crystal piece show generally only the matrix reflections without any additional reflections. However, sometimes — in crystal regions containing large defects, for instance, grain boundaries (as demonstrated by the BF image in Fig. 9a) — the weak reflections of Na colloids (110 P in the inset 9b) may also appear. This feature may be connected with the well known effect of dislocational defects on the nucleation and stabilization of colloids.

3.3. Summary

The results can be summarized as follows. In single crystalline and powder samples originating from electrolytically dark blue coloured NaCl crystals, besides the matrix reflections some additional foreign reflections could be found by direct TEM in the SAD patterns which could be attributed only to the presence of metallic Na particles (the colloids) within the crystals. This should be expected on the basis of the absorption spectra. In contrast, at samples originating from X-ray coloured dark purple-blue crystals no additional foreign reflection could be observed in the SAD patterns. This points to the fact that as opposed to the colloid centres the X_K -centres do not form detectably distinguishable foreign phases in the NaCl matrix. Further, since in our crystals containing X_K -centres no ESR signal could be detected contrary to samples containing colloids the conclusion seems to be feasible that the X_K -centres are not colloidal particles. In good correlation with the ESR and absorption spectroscopic results the differences found by direct TEM investigations between these two types of coloured crystals seem to support the assumption that the X_K -centres may be F-centre agglomerations consisting of more than four F-centres and forming no crystalline foreign phase within the NaCl matrix rather than real colloids.

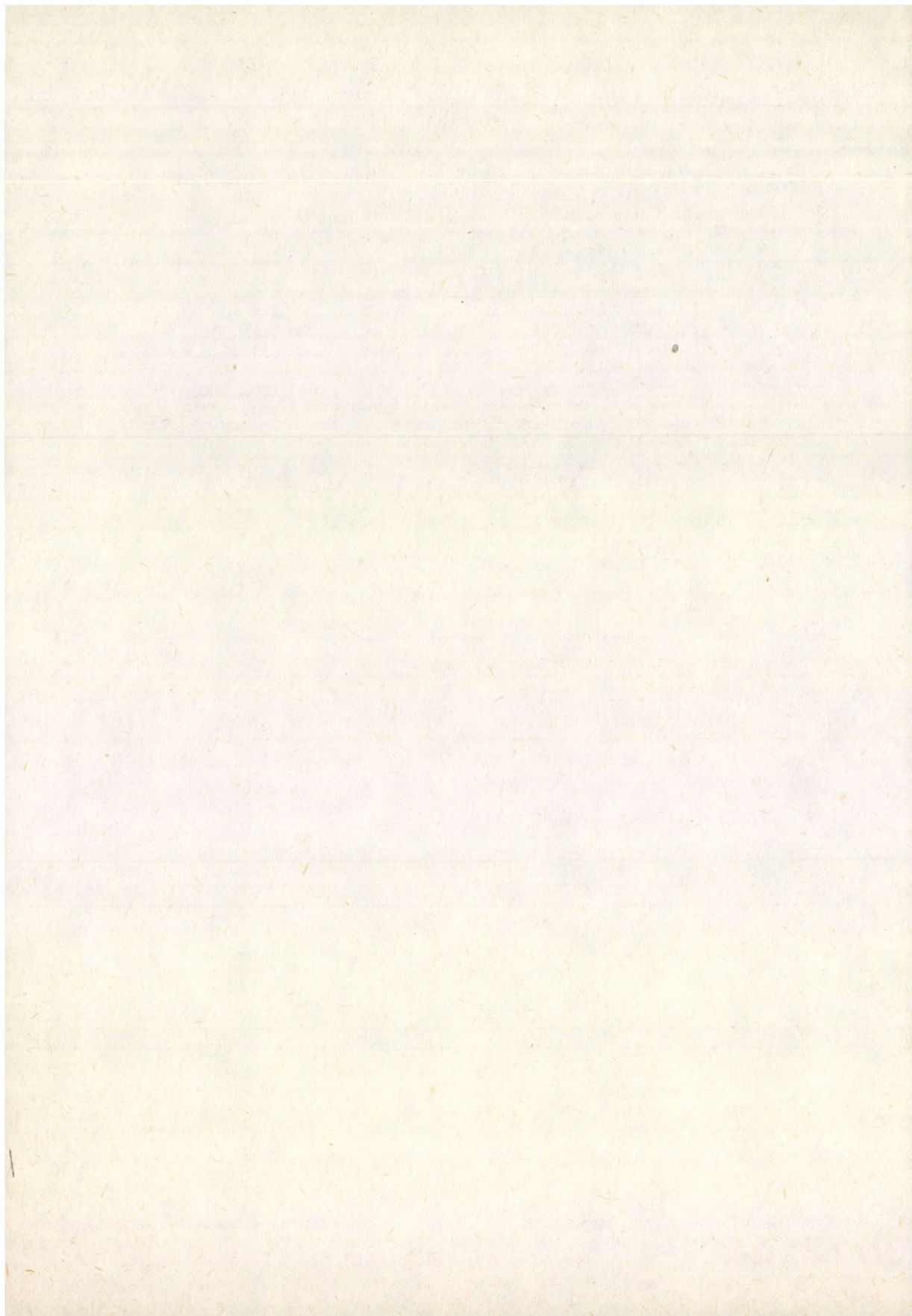
Acknowledgements

The authors wish to thank Dr. M. Krohn for valuable discussion and Mrs. E. Burján, Mrs. K. Farkas, Mrs. M. Kiss and Mrs. S. Tóth for their technical assistance.

This work was supported by the State Office for Technical Development (OMFB).

References

1. Z. Gyulai, *Z. Phys.*, *35*, 411, 1935 b.
2. I. H. Shulman and W. D. Compton, *Colour Centers in Solids*, Pergamon Press, Oxford, 1963.
3. N. A. Tsal and R. L. Didyk, *Phys. Stat. Sol. (b)*, *51*, 891, 1972.
4. A. E. Hughes and S. C. Jain, *Advances in Physics*, *28*, 717, 1979.
5. R. Voszka, Sz. Tóké, P. Kolin and K. Raksányi, *J. de Physique*, *37*, C7-84, 1976.
6. T. Hibi and K. Ishikawa, *J. Phys. Soc. Jap.*, *13*, 709, 1958.
7. T. Hibi and T. Tomiki, *J. Phys. Soc. Jap.*, *14*, 375 and 445, 1959.
8. R. E. Simon and R. L. Sproull, *J. Appl. Phys.*, *31*, 2224, 1960.
9. G. Chassagne, D. Durand, J. Serughetti and L. W. Hobbs, *Phys. Stat. Sol. (a)*, *40*, 629, 1977.
10. L. W. Hobbs, A. E. Hughes and G. Chassagne, *Nature (London)*, *252*, 383, 1974.
11. L. W. Hobbs, in *Surface and Defect Properties of Solids*, Ed. M. W. Roberts and J. M. Thomas. Vol. 4. The Chem. Soc. London, pp. 152-250, 1975.
12. G. Chassagne, D. Durand, J. Serughetti and L. W. Hobbs, *Phys. Stat. Sol. (a)*, *41*, 183, 1977.
13. R. Voszka, K. Raksányi and L. Berkes, *Krist. u. Techn.*, *5*, 409, 1970.
14. T. Hibi and K. Yada, *J. Electronmicroscopy*, *10*, 164, 1961.
15. Z. Morlin and J. Tremmel, *Czechosl. Fiz. J. (B)*, *13*, 216, 1963.
16. J. Heydenreich, *Rev. Roum. Phys.*, *14*, 1253, 1969.
17. L. W. Hobbs, A. E. Hughes and D. Poley, *Proc. R. Soc. London*, *A332*, 167, 1973.



RECENT CONTRIBUTIONS TO PLANNING THERAPEUTIC IRRADIATIONS*

L. BOZÓKY, G. JÓZSEF, GY. REISCHL and G. VARJAS

*National Oncological Institute
Budapest, Hungary*

The computerized treatment planning programs, indispensable for up-to-date irradiation of deep-seated malignancies, must take the influence of ever-greater numbers of physical factors into consideration and they make necessary the specification of ever-more optional factors. For this reason, we have attempted to develop a program also including optimization, on the one hand, and have checked with direct measurements whether the generally used methods in determining dose distribution take the surplus doses (produced by inclined irradiation) correctly into consideration, on the other.

Among the earliest fields of interdisciplinary research works, the cooperation of radiological physicians and radiation physicists is of particular importance. The investigations performed have often led to practical results of great significance and have opened up new vistas in the use of ionizing radiation both in diagnostic and therapeutic applications. A problem dating back half a century and coming to light in these works will be examined, and some new results of our investigations in this province are presented below; we refer here to the planning of irradiations.

One of the current ways to remove malignant tumours is the destruction of the tumour by ionizing radiation by means of a tumour-destroying dose. For over 80 years, side-by-side with special purpose radium sources, X-ray tubes, at a peak voltage of several hundred kV have been used as radiation sources.

With these X-rays of relatively poor penetration power even tumours seated at only 8–10 cm could hardly be reached by beams coming from a single direction. As the dose required for the destruction of the tumour was applied, the body tissues in the path, primarily the skin, suffered heavy irreversible damage.

The problem could be handled by either of two approaches. The first, viz. the application of photon radiations of significantly greater quantum energy, could not be implemented in practice for half a century mainly because of difficulties in the insulation of high voltages. The literature gives an account only of a single piece of X-ray equipment of 1 MV in which the X-ray tube was 10 m long and therefore unfit for routine therapeutic irradiations.

It was not until 1942 that Kerst discovered the principle of circular acceleration: electrons revolving in an annular vacuum tube of not more than 60 cm diameter can be

* Dedicated to Prof. S. Szalay on his 75th birthday

accelerated to an energy of many MeV and either the electrons themselves or the X-rays generated by their collisions can be used for radiotherapy.

These betatron devices, however, were much too expensive and because of their poor dose intensity and other drawbacks did not become widespread in practice. All the more so since, in the last few years, cobalt units charged with ^{60}Co radio-isotope, having parameters more favourable in many respects, have appeared. The 1.25 MeV photon energy is equivalent with the bremsstrahlung of a conventional X-ray machine with about 2500 kV peak voltage.

It should be mentioned here that Hungary has nine cobalt units for therapeutic purposes and one 29 MeV betatron device, but a further ten supervoltage units, in the first place linear accelerators, would be needed; in possession of these, all the old X-ray machines could be scrapped.

The other method to prevent over-irradiation of the tissues surrounding the tumour uses more beams from several different directions, or a moving radiation source rotating around the tumour in such a way that the beam is permanently centred upon the tumour. This technique results in the reduction of the dose upon the skin to half or a third of that applied to the tumour and so there is no risk of the tissues being overexposed.

The aim of the technique can be defined unequivocally: the tumour should be exposed to uniform irradiation as it receives the total irradiation coming from the different directions, while the resultant dose-field around it should drop as abruptly as possible.

The main physical factors influencing the requirements are:

- the energy spectrum of the photon radiation,
- the source – body surface distance,
- the dimensions of the fields of irradiation,
- inhomogeneities in the body (bones, lungs),
- location of the fields,
- directions of the irradiations,
- geometry of the body surfaces under the field,
- dimensions of the wedge filters,
- shape and dimensions of lead blocks shielding the body parts requiring special radiation protection,
- the relative doses delivered to the individual fields.

It goes without saying that the taking into account of the factors listed above, or even a rough estimation of their effects, cannot be done by mental arithmetic. Physicists are required who are familiar with the laws of physics governing the absorption and scattering processes, who are versed in the specialized calculations, and who have adequate knowledge of the relevant equipment, instruments, dosimeters, etc.

Despite these requirements, the physicians involved have no fundamental training in such matters and they cannot even be reasonably expected to acquire them

later, as this could only be done to the detriment of their acquisition of medical knowledge.

At the same time the tasks of the physicians are becoming more tiresome. The drawings of the body cross sections must be completed by the addition of the precise location of the tumour to be irradiated, and the total doses to be delivered, together with their daily fractions.

Now let us return to the problems relating to the field of the physics of treatment planning. Such work used to be done by a physicist who measured the isodose curves belonging to the particular fields, in water or in a tissue-equivalent phantom, at a perpendicular incidence of the beams (Fig. 1) and with the different wedge filters. The data obtained were represented, each separately on a transparent sheet at 1 to 1 scale, and then the sheets were superposed upon the body cross section diagram according to a plan which was deemed to be optimum for graphic summarizing.

Finally after many hours a map-like representation of the resultant dose distribution by means of the isodose curves was obtained. Any allowance for inhomogeneities had, in the majority of cases, to be dispensed with because of lack of time.

A problem that could not be disregarded by any means, was the shifting of the isodose curves coming from incidences not perpendicular to the body surface (Fig. 2). For cobalt units the operation has usually been performed by the method of displacement of the isodose curves, introduced by Garrett and Jones [1]. The gist of the technique is that all points of the isodose curves should be shifted downwards by $2/3$ of the thickness of the air layer between the body surface and the plane perpendicular to the beam axis.

This procedure, though simplified, has rendered possible the objective checking of the methods of irradiations used by the radiologists for long years. The physicians

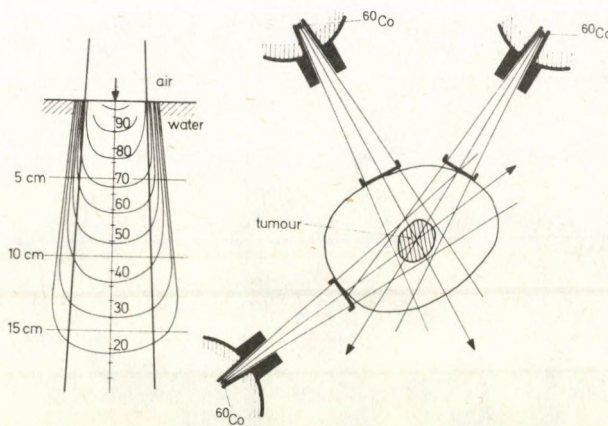


Fig. 1. Isodose curves at perpendicular incidence and cross sectional picture of a three field irradiation

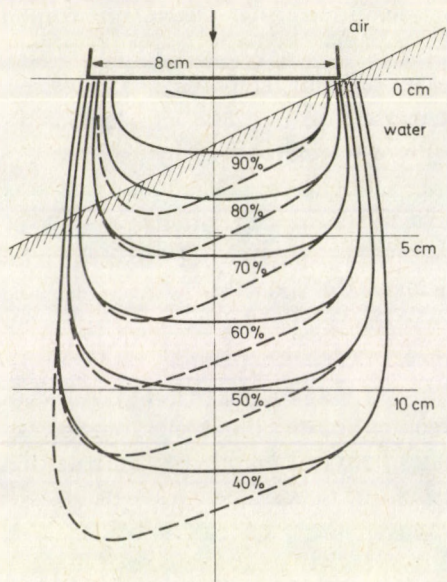


Fig. 2. Isodose curves at inclined incidence, calculated by the Garrett-Jones method [1]

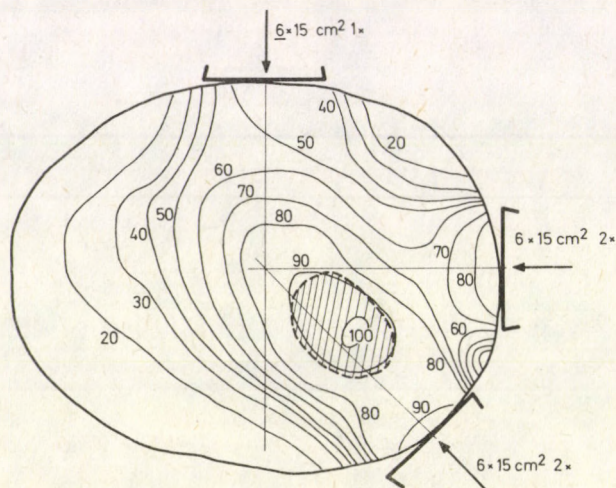


Fig. 3. An acceptable dose distribution chart, calculated using the Extdos program of van de Geijn [2]

were the first to be surprised to see how much the maximum dose sometimes went astray from the tumour and how much better dose distribution could have been obtained even by conventional X-ray irradiations through exact physical calculations.

A quite sudden development has resulted from the entering of computation techniques upon the scene. Though unable to do away with the preparatory work, computers have succeeded in cutting down the time consumed by the calculations themselves (from many hours to a few seconds), while they take all physical factors into consideration.

After an enormous amount of preparatory work we have created in Hungary the National Computerized Treatment Planning Network System in order to take care of the up-to-date computerized irradiation planning on behalf of all cobalt unit radiation centres of the country (4 of them in Budapest plus one each at Debrecen, Miskolc, Szeged, Pécs and Szombathely [2]).

The computation gives the resultant dose distribution chart (Fig. 3) plus the irradiation times. Should the result fail to fulfil the requirements, the input data are modified and another computation performed. Even two or three such computations depending on the practice the planner possesses, might be needed. After all, one cannot be content to believe that the plan in hand is really the best. This is why a program of computations giving optimum dose distribution without trial-and-error guesses and being valid for the given case, would be of primary importance [3].

Investigations attempting the elaboration of optimum computation processes on behalf of treatment planning have long been in progress, yet the problems in connection with them are still far from satisfactory solution. Though the criteria of optimum dose distribution can qualitatively be determined: heavy dose upon the target, slight doses on other parts, and minimum on critical organs — a precise quantitatively optimum definition generally adopted has not yet been created.

Further difficulties preventing the solution of the problems arise from the fact that the criteria can be described mathematically in different ways and therefore comparisons are difficult even among programs based on the same fundamental principles.

The majority of the programs content themselves with the determination of the optimum weighting factors of the fields of irradiation. Some of them add the optimization of the dimensions of the fields and also the wedge angles to this [4, 5, 6].

Our computerized program lends itself to the simultaneous optimization of the weighting factors of several fields, field dimensions, wedge angles, entrance points and directions. The method is based on the principle of the least squares method. The basic procedure is as follows:

After specifying the doses which we desire to deliver to the particular points of the body cross section, the physical parameters of adjustment should be varied until the difference of the squares of the doses actually delivered and those of the required ones are at a minimum. In this way the doses specified can best be approached, by taking all

the points into consideration, by irradiations performed with the parameters obtained as a result of the computation.

Since we wished for the shortest possible computer times and the computations are rather long, the required doses may be specified for a quite restricted number of points. With appropriate specifications the taking into consideration of 70 to 100 points gives fairly good results.

Our optimizing program consists of three parts: the procedure of calculation of the dose distribution, the performance of the calculation of the least squares method and of the program parts for handling the data and results obtained.

General experience gained by our tests so far has shown that the dose distribution can be improved in the first place by variation of the weighting factors, field dimensions and wedge angles. Variation of the entrance points and beam directions are less important.

Among the limitations of our procedure is the primary need to reduce the numbers of points and parameters to be optimized. The taking of 70–100 points and 8–9 parameters into consideration might still require computer times of 3–6 minutes.

The program is suitable for the optimization of maximum 30 MeV electron and bremsstrahlung irradiations and their combination with each other or with cobalt irradiation too.

Naturally, in the course of our experiments with the program we have met the problem — unsolved so far — of the uniform qualitative description of optimum determination. Like other researchers, we have not satisfactorily succeeded in solving the problem.

Computer programs that take into account the effects of physical factors of numbers permanently on the upgrade, require their ever-more exacting checking. Unfortunately, such technical possibilities that would permit the checking of the printed dose distribution cards by direct measurements in phantoms simulating the human body, are unavailable. In view of this the checks must be performed in several steps.

Our present investigations cover the checking of such a factor, not sufficiently discussed so far, namely the direct measurement of the variation of the changes in the deep dose distribution coming from the angles of the body surface. It does not seem that the scattering processes, depending on many conditions, could be corrected by taking a single parameter, namely the thickness of the air layer into consideration such as the Garrett–Jones method does, by shifting the isodose curves by $2/3$ the thickness of the air layer. This is why we have set the target of our work to be the checking and intercomparison of the Garrett–Jones method with the results of our direct measurements [7].

The measurements were performed in the gamma dose field of our Rotacert cobalt unit — developed by us [8] and manufactured by Medicor, Budapest. The source — phantom distance was 60 cm. The inclined water surface was arranged in the water phantom (Chirana, Czechoslovakia) by using an empty plexiglass box of 3 mm

wall thickness, open on the top, immersed in water. The arrangement (Fig. 4) could produce an inclination of $30 \pm 15^\circ$ to the horizontal plane on the water phantom surface.

A PTW micro ionization chamber of 0.1 cm^3 volume was used as a detector. The diameter of the waterproof shell of the ionization chamber was 7 mm.

To measure and record the current of the ionization chamber, we devised an apparatus of high stability and exceptionally short time constant, whose output could

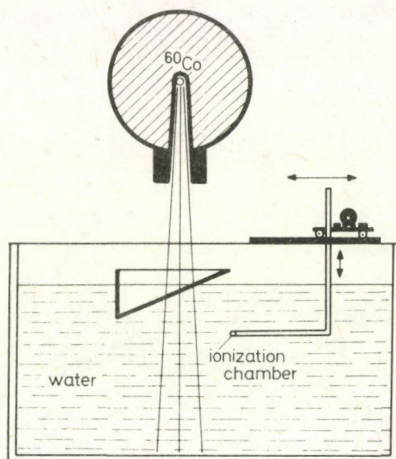


Fig. 4. Experimental equipment constructed for direct measurements of dose distribution in water at inclined incidence of gamma rays of ^{60}Co

operate an XY-printer. The sensitivity of the dosimeter was continuously variable within wide limits. The convenient figure could be read-out and reproduced to high accuracy. The continuous and precise amplification control was of importance for the convenient and prompt norming of the curves recorded by the XY-printer. The curves at scales adapted to the purpose rendered much computation work unnecessary and speeded up the otherwise tedious evaluation work.

The actuating mechanism of the water phantom equally required some transformations to render it adaptable to the special purpose as, in its original condition, it could not be connected to an XY-printer. The devices as manufactured, though fit for remote control and the three-dimensional actuating mechanism permitting the setting of the measuring detector at any place inside the water phantom of $40 \times 40 \times 80 \text{ cm}^3$ volume, but the indication of the position was mechanical and thus analog signals to drive the XY recorder were not convenient. For this reason a position indicator with a potentiometer, whose slide delivered a voltage indicating the location of the detector, necessary for the operation of the XY recorder was applied to each of the three shafts. Thus both dose and isodose curves could be represented true to scale.

The relative errors of the curves drawn by the XY recorder are smaller than ± 0.5 per cent.

We performed measurements on a water phantom with fields of various sizes and inside the fields with various proportions of perpendicular and inclined surfaces. After obtaining diagrams with different parameters, we compared our results with those obtained under identical conditions by the curve shifting method.

Figure 5 illustrates the results of our dose intensity measurements performed with a 9×15 cm field along the median line parallel with the 9 cm side, at 5 and 10 cm

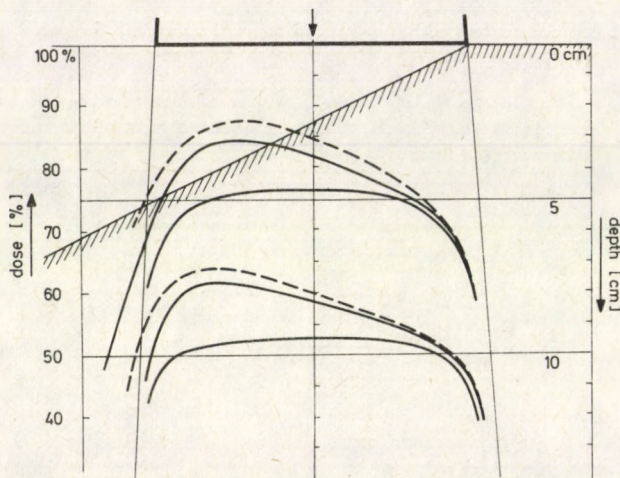


Fig. 5. Dose distribution in water at 5 and 10 cm depth measured (continuous line) and calculated (dotted line)

depths, respectively. The slope of the water surface was 30° downwards. In the same figure the curves calculated by $2/3$ shifts are represented, too. Both results are expressed in terms of percentage of the maximum dose at 5 mm depth below the surface.

The summary of the test results is as follows:

1. The doses obtained by the Garrett-Jones displacement method are greater by 1–5 per cent than the doses found by direct measurements.
2. The differences increase with the thickness of the air layer and the size of the field.
3. The differences depend on the ratios of the perpendicular and inclined surface inside the field.

Based on these findings we are able to state that in most cases, particularly with those involving medium-sized and small fields and slopes, the curve shifting method is affected by errors not greater than 1–2 per cent, and it is thus a simple and convenient technique. With larger field size and greater angles of inclination, however, differences of such importance will be experienced which are difficult to overcome by computations and for the time being, render direct measurement indispensable.

References

1. J. H. Garrett and D. E. Jones, *Brit. J. Radiol.*, 35, 739, 1962.
2. J. van de Geijn, *Computer programs in Biomedicine*, 1, 47, 1970.
3. G. József, *Magyar Onkológia (Hungarian Oncology)*, 26, 171, 1982.
4. C. S. Hope, J. S. Laurie, J. S. Ott and K. E. Halman, *Proc. of the Panel on Role of Computers in Radiotherapy*, IAEA, Vienna, 1968.
5. S. McDonald and P. Rubin, *Biology and Physics*, 3, 307, 1977.
6. A. T. Redpath, B. Vickey and D. H. Wright, *Physics in Medicine and Biology*, 21, 781, 1976.
7. E. W. Webster and K. C. Tsien, *Atlas of Radiation Dose Distribution, Single Field Isodose Charts, Vol. I.*, IAEA Vienna, 1965.
8. L. Bozóky and I. Martos, *Proc. First Int. Congress of Radiation Protection*, Pergamon Press, Oxford, 1968, Vol. II.

PROBLEMS OF MATCHING THE FIELDS IN COBALT TELEETHERAPY*

Z. DÉZSI, T. BORBÉLY, L. MILTÉNYI, E. PINTYE,
D. E. GROSKA and GY. VARGHA

*Department of Radiology, University Medical School
Debrecen, Hungary*

The conditions of field matching were determined using the Gravicert cobalt teletherapy unit. The proper matching of fields was found to be very important in respect of overdosage and underdosage. Undesirable excess dose may cause relapses at the junction of contiguous fields. The results of measurements obtained with the Gravicert unit are presented both graphically and in tables. The optimal amount of field separation should be determined independently for each unit.

A group of malignant diseases such as malignant lymphomas, testicular tumours, etc. necessitates the homogeneous radiation therapy of the entire lymphatic system, but these cannot generally be irradiated in a single treatment field. Gynaecological percutaneous parametric treatment, if it follows intrauterine treatment, also demands the proper matching of the treatment fields. Two aims need to be considered when preparing the treatment plan: to deliver homogeneous doses to a given depth in the spaces between the fields by matching the fields properly, and to avoid undesirable overdosage and underdosage within and between the treatment fields. That is, the contiguous fields should be matched so that no nonirradiated space be left between the fields, which may later become a source of relapse.

The problems of matching opposing fields have been investigated by Faw and Dwight [1] and by Bianciardi et al [2]. Faw and Dwight [1] gave a formula on a geometric basis for the amount of field separation in the case of varying distances between the source skin surfaces. From this formula the distance between the margins of the fields (the gap width) on the skin surface can be calculated. For a more homogeneous dose distribution within the field, it is better to characterize the size of the field by means of a "nominal field" (dosimetric field) which can best be done by means of the 90 per cent decrement line (Debois [3], Dézsi [4]). The (notion of) field size is used in this sense in the present communication, and the abutted adjoining sides are underlined. The decrement lines, at the same time, illustrate the penumbra of the equipment (the field size at any depth) as well [3].

The problems of field matching are of special importance in the case of teletherapy units equipped with an exchangeable collimating system. Because of the

* Dedicated to Prof. S. Szalay on his 75th birthday

limited field sizes the malignant changes very often need to be irradiated through a series of adjacent treatment fields.

Our aim was to develop an appropriate simple method (for use with our own unit) with which the distance between the fields can be determined to ensure a homogeneous dose distribution at the desired depth in the gap between the treatment fields, and to eliminate undesirable overdosage and underdosage.

In clinical radiation therapy the irradiation surface is generally not perpendicular to the direction of irradiation, the light beam indicating that the treatment

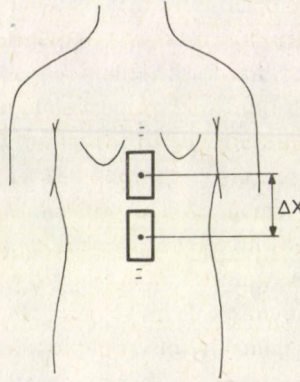


Fig. 1. Position of the fields

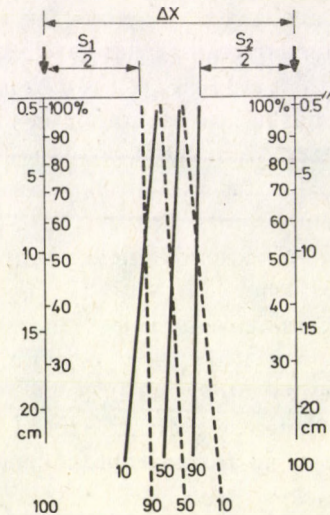


Fig. 2. Notation and the decrement line used in the text

field tends to bulge out at the surface. Thus, the edge of the actual treatment field is not unequivocally defined. Therefore, we think it more expedient to give the distance between the two central axes instead of giving the distance between the edges to define the separation distance between the fields (Fig. 1).

The notation and the decrement line used in the present study are presented in Fig. 2. The value of dose distribution for the gaps between the fields is determined by

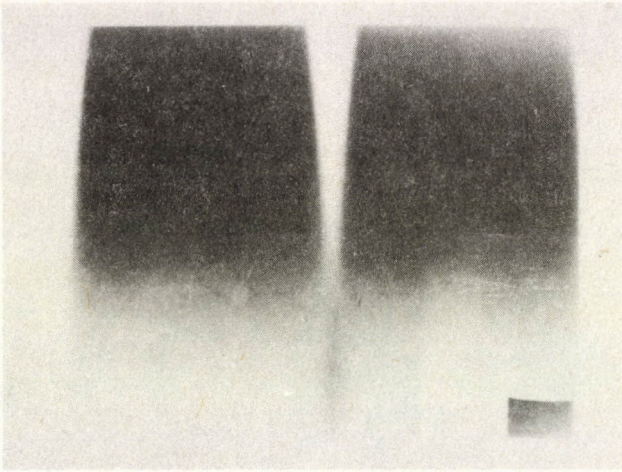


Fig. 3. Density distribution for 10×4 cm fields with penumbra (F) trimmers $\Delta X = 15$ cm (Agfa Gevaert Strukturix D 7 film, Co-60 SSD = 60 cm)

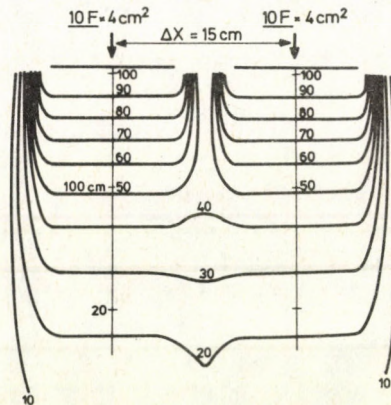


Fig. 3a. Isodose distribution for Fig. 3

the junction isodose distribution. The basic isodose curve applies to perpendicular irradiation; consequently, the problems of field matching were investigated with treatment surfaces perpendicular to the central axis. The correction occurring when irradiation is not perpendicular can be considered by means of the method of "2/3 shift (separation)".

The qualitative study of dose distribution at the junction of contiguous fields was accomplished using Agfa Gevaert Strukturix D 7 films. The films were placed in between 25×30 cm Mix D phantoms of 2–3 cm thickness so that the surface of the film was always parallel to the corresponding edges of the treatment fields and the central axis ran on the surface of the film.

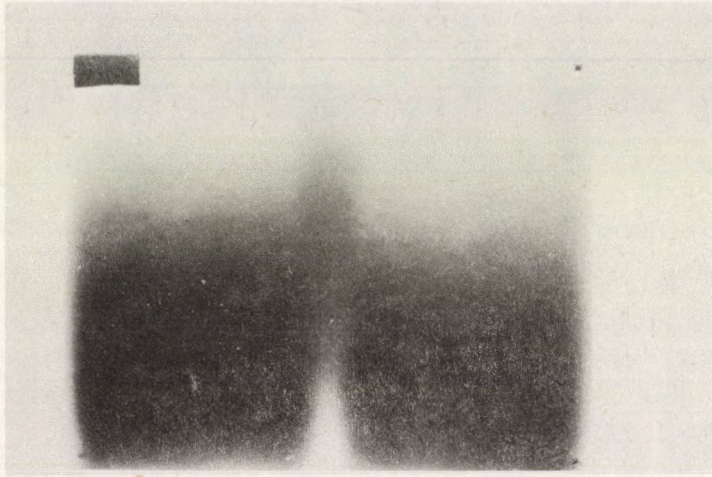


Fig. 4. Density distribution for 10×4 cm fields without penumbra trimmers $\Delta X = 15$ cm

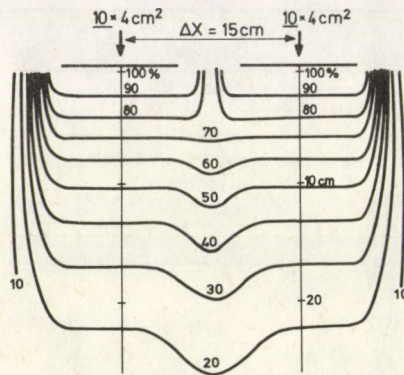


Fig. 4a. Isodose distribution for Fig. 4

Figure 3 illustrates the density distribution obtained for two 10×4 cm fields by using a penumbra trimmer when the spacing of the central axes (ΔX) was 15 cm.

The density distribution obtained for the same fields without using the penumbra trimmer is given in Fig. 4. Comparison of the two figures reflects the obvious function and importance of the penumbra trimmer in field matching.

Figure 5 shows the density distribution obtained for two pairs of opposing fields of 10×4 cm width by using a penumbra trimmer with 15 cm space between the central axes. These figures clearly illustrate the significance of field matching in respect of the resultant dose distribution.

Using the isodose curve one can determine the resultant dose distribution for actual cases so that the doses in the gaps at the depth of interest and on the central axis

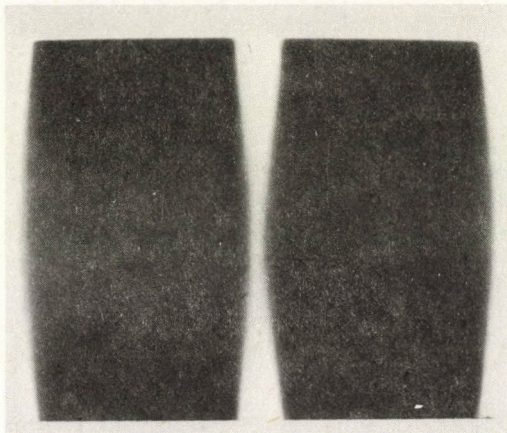


Fig. 5. Density distribution for opposing fields 10×4 cm

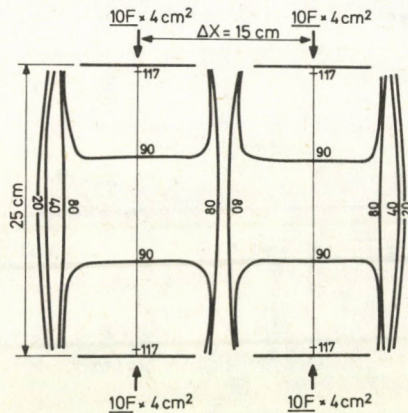
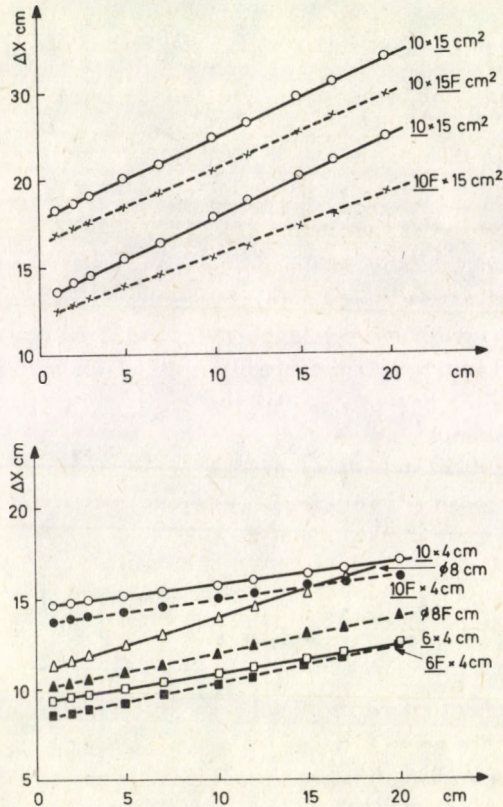


Fig. 5a. Isodose distribution for Fig. 5

at the same depth are equal. The isodose distributions corresponding to the above density distributions are shown in Figs 3a, 4a and 5a. These Figures corroborate our previous statement.

However, because this procedure takes up very much time it is better to define the amount of field separation (matching) graphically or in a tabular form as a function of depth so as to obtain a homogeneous dose for the gaps between the fields. The appropriate separation for two fields was determined using the decrement lines. That distance between the central axes at which the 90 per cent and the 10 per cent decrement lines intersect, i.e. when the dose at the junction is 100 per cent, equal to the dose on the central axis at the same depth, was determined for equal field size combinations (SSD = 60 cm) as a function of depth. With this form of field matching the inhomogeneity of the overlap dose is less than ± 10 per cent.



Figs 6, 7. Separation distance between the central lines as function of the depth, Gravicert SSD = 60 cm, (F with penumbra trimmers)

Table I

Separation distance ΔX (cm) for underlined sides between the central lines of the Gravicert teletherapy unit
SSD = 60 cm*

Depth [cm] Field size [cm × cm]	1	2	3	5	7	10	12	15	17	20
<u>4 × 4</u>	7.2	7.5	7.7	8.2	8.7	9.5	9.9	10.7	11.3	11.9
<u>4F × 44</u>	6.1	6.4	6.6	6.9	7.9	8.4	9.0	9.4	10.0	
<u>6 × 8</u>	9.2	9.4	9.8	10.2	10.7	11.4	11.9	12.6	13.2	13.8
<u>6F × 8</u>	8.5	8.7	9.0	9.5	10.2	10.8	11.4	12.1	12.6	13.5
<u>10 × 4</u>	14.7	14.8	15.0	15.1	15.4	15.7	16.0	16.4	16.7	17.1
<u>10F × 4</u>	13.7	13.9	14.0	14.3	14.5	15.0	15.3	15.7	15.9	16.2
<u>15 × 7</u>	18.3	18.7	19.1	20.0	20.8	22.3	23.1	24.7	25.4	26.8
<u>15F × 7</u>	16.8	17.3	17.6	18.5	19.3	20.5	21.3	22.6	23.5	24.6

F wedge filter

* A more extensive listing may be obtained from the first author

Our results obtained for some fields are shown in Figs 6 and 7 and Table I. The data plotted as a function of depth make up straight lines. It can be seen that the gap between the fields is always wider without a penumbra trimmer than with it, i.e. the proper matching of fields is even more important if no penumbra trimmer is used.

Our studies confirm that it is very important to match the treatment fields properly in order to avoid excessive irradiation and to prevent underdosage. The determination of the required amount of separation should be accomplished separately for each teletherapy unit since the dosimetric systems supplied with the units are not yet standardized.

References

1. F. L. Faw and G. W. Dwight, *Radiology*, 108, 184, 1970.
2. L. Bianciardi, R. Breschi, P. Chiaradia, A. Josi and P. Villa, *Radiology*, 122, 493, 1977.
3. J. M. Debois, *J. Belge. Radiol.*, 49, 200, 1966.
4. Z. Dézsi, *Magyar Radiológia*, 18, 16, 1966 (in Hungarian).

ELECTROVAC SOLUTIONS WITH COMMON SHEARING GEODESIC EIGENRAY*

B. LUKÁCS

*Central Research Institute for Physics
1525 Budapest, Hungary*

The spatially symmetric electrovac problem is investigated in the General Relativity, with common, geodesic and shearing eigenrays. It is shown that all these solutions are Ernst counterparts of the corresponding vacuum solutions.

1. Introduction

The spin coefficient technique has led to many new solutions of the Einstein equation of General Relativity. Without assuming any symmetry, the 4 dimensional Newman–Penrose equations can be solved for geodesic rays, and the Kerr solution is among these solutions, belonging to a special subclass, where the shear of the rays vanishes too [1], [2], [3]. When the space-time possesses a non-null Killing symmetry, the problem is essentially 3-dimensional, and after a decomposition

$$ds^2 = f(dy + \omega_r dx^r)^2 - f^{-1} g_{rs} dx^r dx^s, \quad i = 1, 2, 3 \quad (1.1)$$

it can be reformulated in a 3-dimensional background space or space-time, whose metric tensor is $g_{ik}(x^m)$ [4], [5]. Then the eigenrays play a role analogous to that of the rays in 4 dimensions. (The definition of eigenrays can be found in [4] and [5]; they are projections of rays if the rays are shearfree). The dimensionality of the background space being smaller, more cases can be analytically handled there, in fact, all the classes $\kappa\sigma=0$ have been integrated in vacuum both for stationarity and for space-like symmetry. Since the class $\kappa=\sigma=0$ is known from the 4-dimensional calculation, this means $\sigma\neq\kappa=0$ and $\kappa\neq\sigma=0$ as new solutions. (When $\sigma\neq 0$, the eigenrays do not coincide with the projections of the rays, so, even if they are geodesic, the rays are not.) Unfortunately, none of these new classes contains any generalization of the Kerr metric [6–9].

In the presence of material fields the problem is more complicated, but it is interesting that for stationary, rigidly rotating dust the same $\kappa\sigma=0$ classes have been integrated [10]. With pressure the integration has been successful only for $\kappa=\sigma=0$ [11].

* Dedicated to Prof. S. Szalay on his 75th birthday.

The electrovac case shows some structural similarities with the vacuum problem. Nevertheless, the equations are more complicated, and generally their integration is still not performed. However, there is a special case, i.e. when the gravitational field \mathbf{G} (produced by the decomposition process) and the electromagnetic field \mathbf{H} have common eigenrays, which can be handled in the same way as the vacuum. The condition that the eigenrays of the two fields coincide can be formulated algebraically as [12]

$$(\mathbf{G} \times \mathbf{H})^2 = 0. \quad (1.2)$$

Here \mathbf{G} and \mathbf{H} are defined in a rather complicated way, the actual forms will be discussed in Section 2.

For stationarity the integration was successful in each case when the vacuum equations could be integrated [7], [12], and the class $\kappa = \sigma = 0$ contains the electrified generalization of the Kerr solution [13]. There is a strong tendency to get only the Ernst counterparts of the vacuum solutions, nevertheless, when the strength of the \mathbf{G} field dominates that of the \mathbf{H} field [7], [12].

For space-like symmetry the $\sigma = 0$, $\kappa \neq 0$ solutions are known, containing only Ernst counterparts of the vacuum metrics [9]. So there remains the case $\sigma \neq 0$, $\kappa = 0$ as promising for integration.

Here we show that this class contains also Ernst counterparts only. Having done this, the process of integrating the $\kappa\sigma = 0$, $(\mathbf{G} \times \mathbf{H})^2 = 0$ metrics essentially ends, except producing explicit forms for special line elements, if necessary. Since the Kerr and Kerr–Newman solutions are isolated among the $\kappa\sigma = 0$ metrics, obviously the $\kappa \neq 0$, $\sigma \neq 0$ class should be investigated in order to get asymptotically flat solutions, however, until now constructive methods are not known for handling this class.

2. The field equations for electrovac

Consider the 3+1 decomposition for stationary space-times as in Eq. (1.1). A complex vector field \mathbf{G}

$$\mathbf{G} = \frac{1}{2f} (\nabla f - if^2 \nabla \times \boldsymbol{\omega}) \quad (2.1)$$

can be introduced, instead of the derivatives of f and $\boldsymbol{\omega}$. From the electromagnetic potential A^μ a complex three-vector

$$\mathbf{H} = \frac{1}{\sqrt{|f|}} [\nabla A_0 + i(\nabla \times \mathbf{A} - \boldsymbol{\omega} \times \nabla A_0)f] \quad (2.2)$$

can be constructed, and then the sourcefree Einstein–Maxwell equations contain f , ω , A_0 and \mathbf{A} only in these combinations [12], [14], [15]. In fact, the field equations have the form

$$(\nabla - \mathbf{G})\mathbf{G} = \bar{\mathbf{H}}\mathbf{H} \pm \bar{\mathbf{G}}\mathbf{G}, \quad (2.3a)$$

$$\nabla \times \mathbf{G} = \bar{\mathbf{H}} \times \mathbf{H} \pm \bar{\mathbf{G}} \times \mathbf{G}, \quad (2.3b)$$

$$(\nabla - \mathbf{G})\mathbf{H} = \frac{1}{2}(\mathbf{G} - \bar{\mathbf{G}})\mathbf{H}, \quad (2.3c)$$

$$\nabla \times \mathbf{H} = -\frac{1}{2}(\mathbf{G} + \bar{\mathbf{G}}) \times \mathbf{H}, \quad (2.3d)$$

$$R = -\mathbf{G} \circ \bar{\mathbf{G}} - \bar{\mathbf{G}} \circ \mathbf{G} \pm \mathbf{H} \circ \bar{\mathbf{H}} \pm \bar{\mathbf{H}} \circ \mathbf{H}, \quad (2.3e)$$

where \pm stands for $\text{sgn}(f)$. Here all the tensorial operations are meant with respect to the metric g_{ik} of the background space. Now, Eqs (2.3b, d) are integrability conditions for some scalars B , φ :

$$B_{;i} = \varepsilon_{ikl}(A^{k;1} - \omega^k A_0^{;1})f\sqrt{g}, \quad (2.4)$$

$$\varphi_{;i} = \varepsilon_{ikl}\omega^{k;1}f^2\sqrt{g} + 2(BA_{0;i} - A_0B_{;i}),$$

so one can define two complex scalars [12], [14], [15]

$$\varepsilon = f - \Phi\bar{\Phi} + i\varphi, \quad (2.5)$$

$$\Phi = A_0 + iB,$$

by means of which the remaining of Eqs (2.3) get the form

$$(\text{Re } \varepsilon + \Phi\bar{\Phi})\Delta\varepsilon = (\nabla\varepsilon + 2\bar{\Phi}\nabla\Phi)\nabla\varepsilon,$$

$$(\text{Re } \varepsilon + \Phi\bar{\Phi})\Delta\Phi = (\nabla\varepsilon + 2\bar{\Phi}\nabla\Phi)\nabla\Phi, \quad (2.6)$$

$$R_{ik} = -\frac{1}{2}(\text{Re } \varepsilon + \Phi\bar{\Phi})^{-2} \text{Re} \{ \varepsilon_{;i}\bar{\varepsilon}_{;k} + 2\bar{\Phi}\bar{\Phi}_{;i}\varepsilon_{;k} + \\ + 2\Phi\bar{\Phi}_{;k}\varepsilon_{;i} - 4(\text{Re } \varepsilon)\Phi_{;i}\bar{\Phi}_{;k} \}.$$

The form of these formulae is independent of the sign of $f = K_\mu K^\mu$; the \pm signs in Eqs (2.3) are required because the definition of \mathbf{H} contains a square root.

Eqs (2.6) are called Ernst equations, because they were found first by Ernst for the stationary axisymmetric problem [16]. They remain valid even if there is only one symmetry [14], but for two symmetries the metric in them is flat (in cylindrical coordinates) while now it should be calculated from the last of Eqs (2.6).

Now, it is useful to introduce new field quantities instead of ε and φ as

$$\varepsilon = \frac{\xi - 1}{\xi + 1}, \quad (2.7)$$

$$\Phi = \frac{q}{\xi + 1}.$$

The first two of Eqs (2.6) get the form

$$(\xi \bar{\xi} + q \bar{q} - 1) \Delta \xi = 2(\bar{\xi} \nabla \xi + \bar{q} \nabla q) \nabla \xi, \quad (2.8)$$

$$(\xi \bar{\xi} + q \bar{q} - 1) \Delta q = 2(\bar{\xi} \nabla \xi + \bar{q} \nabla q) \nabla q.$$

Let us assume that, for some reason, $\mathbf{G} = \alpha \mathbf{H}$, and none of them vanishes. This means that

$$q = q(\xi). \quad (2.9)$$

Substituting this into the second of Eqs (2.8) one gets $q_{,\xi\xi} = 0$, i.e.

$$q = C + K(\xi + 1), \quad (2.10)$$

C and K being constant. But the second term yields only a constant in the potential Φ , which can be removed, according to Eqs (2.4-5). Thus there remains

$$q = q_0 = \text{const}. \quad (2.11)$$

and then the first of Eqs (2.8) becomes [12]

$$(\xi \bar{\xi} + q_0 \bar{q}_0 - 1) \Delta \xi = 2 \cdot \bar{\xi} (\nabla \xi)^2. \quad (2.12)$$

If $|q_0| < 1$, the substitution

$$\xi = \sqrt{1 - q_0 \bar{q}_0} \eta \quad (2.13)$$

leads to the vacuum Ernst equation for η . Thus the $\mathbf{G} = \alpha \mathbf{H}$, $|q_0| < 1$ metrics are called the Ernst counterparts of the corresponding vacuum solutions. They can be generated in an almost trivial way from the vacuum metrics, since only f and φ get new expressions, g_{ik} remains unchanged.

If $|q_0| \geq 1$, such a generation is possible, but not from the vacuum solutions. So $|q_0| \geq 1$ metrics are not Ernst counterparts of the vacuum line elements. In fact, for stationarity, some such solutions are explicitly known [7], [12].

The case $|q_0| \geq 1$ is not possible for spacelike symmetry, because then $f = \text{Re } \varepsilon + \Phi \bar{\Phi}$ would not be negative (cf. Eq. (2.7)). So for $f < 0$ all the $\mathbf{G} = \alpha \mathbf{H}$ metrics are Ernst counterparts of vacuum solutions [17].

3. The spin coefficient equations

The complete set of field equations in tensorial form is given in Eq. (2.3). Hence we can proceed as in [5] by introducing a complex basic vector triad. The result is a system of spin coefficient equations (cf. [15]). If the real vector of the triad is chosen a tangent to the eigenray congruence, then one component of \mathbf{G} , G_- , is 0. In contrast to the stationary case, now there are some exceptional cases when eigenrays do not exist [5], [15]. However, here we assume that eigenrays do exist, both for the \mathbf{G} and for the \mathbf{H} fields. After choosing the triad suitably, the spin coefficient ε can be made 0 by permitted triad rotation [5], [15].

According to our fundamental assumption, \mathbf{G} and \mathbf{H} possess common eigenrays, so there exists such a triad gauge that

$$\varepsilon = G_- = H_- = 0 \quad (3.1)$$

and, since in the investigated class the eigenrays are geodesic and shearing,

$$\sigma \neq \kappa = 0. \quad (3.2)$$

Then the nontrivial equations are as follow (cf. [15]):

$$D\rho = -\rho^2 - \sigma\bar{\sigma} - \gamma^2, \quad (3.3a)$$

$$D\sigma = -(\rho + \bar{\rho})\sigma, \quad (3.3b)$$

$$D\tau = -\rho\tau + \bar{\sigma}\bar{\tau} - G_0\bar{G}_- - H_0\bar{H}_-, \quad (3.3c)$$

$$\delta\rho - \bar{\delta}\sigma = 2\sigma\tau - \bar{G}_0G_+ - \bar{H}_0H_+, \quad (3.3d)$$

$$\delta\tau + \bar{\delta}\bar{\tau} = -2\tau\bar{\tau} - \sigma\bar{\sigma} + \rho\bar{\rho} - \gamma^2 - G_+\bar{G}_- - H_+\bar{H}_- \quad (3.3e)$$

$$DG_0 = (-2\bar{\rho} + G_0)G_0 - \gamma^2, \quad (3.3f)$$

$$DH_0 = \left(-2\bar{\rho} + \frac{3}{2}G_0 - \frac{1}{2}\bar{G}_0\right)H_0, \quad (3.3g)$$

$$\delta G_0 - DG_+ = (\bar{\rho} + \bar{G}_0)G_+ + \bar{H}_0H_+, \quad (3.3h)$$

$$\delta H_0 - DH_+ = \left(\bar{\rho} + \frac{1}{2}G_0 + \frac{1}{2}\bar{G}_0\right)H_+ - \frac{1}{2}G_+H_0, \quad (3.3i)$$

$$\bar{\delta}G_0 = \bar{\sigma}G_+ - \bar{G}_-G_0 - \bar{H}_-H_0, \quad (3.3k)$$

$$\bar{\delta}H_0 = \bar{\sigma}H_+ - \frac{1}{2}\bar{G}_-H_0, \quad (3.3l)$$

$$\bar{\delta}G_+ = (\rho - \bar{\rho})G_0 - \tau G_+ - \bar{G}_-G_+ - \bar{H}_-H_+, \quad (3.3m)$$

$$\bar{\delta}H_+ = (\rho - \bar{\rho})H_0 - \left(\tau + \frac{1}{2}\bar{G}_-\right)H_+, \quad (3.3n)$$

where, as a shorthand notation,

$$\gamma^2 = G_0 \bar{G}_0 + H_0 \bar{H}_0. \quad (3.4)$$

If $H_0 = 0$, then, from Eq. (3.31), $H_+ = 0$ too, which is the vacuum case not investigated here (cf. [8]). Thus $H_0 \neq 0$. But then $\gamma^2 \neq 0$, and, from Eq. (3.3f), $G_0 \neq 0$ too.

The differential operators D , δ and $\bar{\delta}$ commute as [5]

$$D\delta - \delta D + \bar{\rho}\delta + \sigma\bar{\delta} = 0, \quad (3.5a)$$

$$\delta\bar{\delta} - \bar{\delta}\delta - \tau\delta + \tau\bar{\delta} + (\rho - \bar{\rho})D = 0. \quad (3.5b)$$

From Eq. (3.3b)

$$D(\sigma/\bar{\sigma}) = 0. \quad (3.6)$$

Such a phase factor can be removed from σ by means of the remaining triad rotations [5], [15], so from here σ is real and positive, and the triad is completely fixed.

4. The proof of the proportionality between \mathbf{G} and \mathbf{H}

The steps that follow here are some amalgam of the calculations in [6], [8] and [12], so it is needless to go into details of the identical steps. First we apply the commutator (3.5a) on $\ln G_0$:

$$\delta(\ln(G_0\sigma)) = G_+ - 2\bar{\tau}, \quad (4.1)$$

just as in the vacuum case [8]. Applying it on $\ln H_0$ the result is

$$\delta(\ln(H_0\sigma)) = \frac{1}{2} G_+ - 2\bar{\tau} + \frac{H_+ G_0}{H_0} \quad (4.2)$$

and then the propagation laws for γ are

$$D\gamma = -(\rho + \bar{\rho})\gamma, \quad (4.3a)$$

$$\delta\gamma^2 = -(2\bar{\tau} + \delta \ln \sigma)\gamma^2 + (G_0 \bar{G}_- + H_0 \bar{H}_-)\sigma. \quad (4.3b)$$

Taking the mixed derivatives of γ^2 one gets

$$\gamma^2(3\bar{\delta}\rho + \bar{\delta}\bar{\rho} + 2\delta\sigma) + \sigma\delta\gamma^2 = 0 \quad (4.4)$$

again as in [6], [8] and [12]. Hence the steps of [6] can be repeated, with the redefinition of δ_{\pm} according to [12] arriving again at

$$\delta\sigma = \delta\gamma = \delta\rho = \bar{\delta}\rho = 0. \quad (4.5)$$

The only nonvanishing component of $\mathbf{G} \times \mathbf{H}$ is

$$X = G_0 H_+ - H_0 G_+. \quad (4.6)$$

Eqs (3.3) yield the propagation laws for X as

$$DX = \frac{3}{2}(-2\bar{\rho} + G_0 - \bar{G}_0)X, \quad (4.7)$$

$$\delta X = -\left(\tau + \frac{3}{2}\bar{G}_-\right)X.$$

From Eqs (3.3d), (4.3b) and (4.5)

$$(\sigma^2 - \gamma^2)\tau = 0, \quad (4.8)$$

$$2\gamma\tau = \bar{G}_0 G_+ + \bar{H}_0 H_+,$$

whence

$$X\bar{X} = \gamma^2(G_+ \bar{G}_- + H_+ \bar{H}_- - 4\tau\bar{\tau}). \quad (4.9)$$

If $\tau = 0$, Eqs (4.8–9) immediately yield $X = 0$. If not, $\sigma^2 = \gamma^2$, and, from the δ -derivative of Eq. (3.3d) one gets

$$\delta\tau = -3\tau^2 + \frac{1}{2}(\rho - \bar{\rho})\sigma. \quad (4.10)$$

Acting on this equation by D ,

$$X\bar{X} + \gamma^2(\sigma^2 + \gamma^2 - \bar{\rho}^2) = 0. \quad (4.11)$$

Hence ρ is real. Now, taking the mixed derivatives of Eqs (4.7):

$$\delta \ln X = \frac{3}{2}G_+ - 7\bar{\tau}. \quad (4.12)$$

Applying now the commutator (3.5b) on $\ln X$, the result is

$$\gamma^2 + \sigma^2 = \rho^2. \quad (4.13)$$

But then, comparing this to Eq. (4.11)

$$X = 0,$$

that is, \mathbf{G} and \mathbf{H} are proportional vectors.

5. The solutions

We showed in Section 2 that in the space-like symmetric case if \mathbf{G} and \mathbf{H} are proportional vectors, then the solution is an Ernst counterpart of the corresponding vacuum solution. The vacuum solutions are given in [8], and there is no reason to explicitly list the counterparts here, the generation process being trivial [12]. As it can

be seen by investigating the vacuum solutions, there are 3 subclasses. The first possesses 3 Killing vectors with the commutation

$$\begin{aligned} [K_1, K_2] &= -2\gamma^0 Q K_3, \\ [K_1, K_3] &= 0, \\ [K_2, K_3] &= 0, \end{aligned} \tag{5.1}$$

where γ^0 and Q are constant parameters of the solution. By redefining the Killing vectors the right hand side coefficient in Eq. (5.1) can be made 1, if it is not 0. Such a symmetry group does not seem to imply obvious physical meaning, except the case $Q=0$, when the vacuum solution is the Kasner Universe.

In the second case there are two commuting space-like Killing vectors. Until now, no physical interpretation has been found for these solutions.

The same is true for the third case, which possesses only one spatial Killing vector, which was originally assumed for the decomposition.

References

1. E. T. Newman and L. Tamburino, *J. Math. Phys.*, **3**, 566, 1962.
2. E. T. Newman, L. Tamburino and T. W. Unti, *J. Math. Phys.*, **4**, 915, 1963.
3. T. W. Unti and R. J. Torrence, *J. Math. Phys.*, **7**, 535, 1966.
4. Z. Perjés, *J. Math. Phys.*, **11**, 3383, 1970.
5. B. Lukács, *Acta Phys. Hung.*, **41**, 137, 1976.
6. J. Kóta and Z. Perjés, *J. Math. Phys.*, **13**, 1695, 1972.
7. J. Kóta, B. Lukács and Z. Perjés, *Proc. 2nd Marcel Grossmann Meeting*, North-Holland, Amsterdam, 1982, p. 203.
8. B. Lukács, *Acta Phys. Slovaca*, **33**, 225, 1983.
9. B. Lukács, *Acta Phys. Hung.*, **54**, 155, 1983.
10. B. Lukács, KFKI-74-87.
11. B. Lukács, E. T. Newman, G. Sparling and J. Winicour, *Gen. Rel. Grav.*, **15**, 567, 1983.
12. B. Lukács, and Z. Perjés, *Gen. Rel. Grav.*, **4**, 161, 1973.
13. E. T. Newman et al., *J. Math. Phys.*, **6**, 918, 1968.
14. Z. Perjés, *Commun. Math. Phys.*, **12**, 275, 1969.
15. B. Lukács, KFKI-73-26.
16. F. J. Ernst, *Phys. Rev.*, **168**, 1415, 1968.
17. There is an exceptional case $(V\xi)^2=0$, when $q_{,\xi\xi}=0$ is not a direct consequence of Eqs (2.8). Nevertheless, in this case eigenrays do not exist (cf. [5] and [15]), so such solutions are not investigated in this paper. Namely, $(V\xi)^2=0$ leads to $\mathbf{G} \cdot \mathbf{G}=0$ (and $\mathbf{H} \cdot \mathbf{H}=0$), which, if eigenrays exist, in a proper triad gauge can be written as $G_0=0$ (and $H_0=0$), and in Section 3 it is shown that the investigated class does not contain such solutions.

NOTES TO CONTRIBUTORS

I. PAPERS will be considered for publication in *Acta Physica Hungarica* only if they have not previously been published or submitted for publication elsewhere. They may be written in English, French, German or Russian.

Papers should be submitted to

Prof. I. Kovács, Editor
Department of Atomic Physics, Technical University
1521 Budapest, Budafoki út 8, Hungary

Papers may be either articles with abstracts or short communications. Both should be as concise as possible, articles in general not exceeding 25 typed pages, short communications 8 typed pages.

II. MANUSCRIPTS

1. Papers should be submitted in three copies.
2. The text of papers must be of high stylistic standard, requiring minor corrections only.
3. Manuscripts should be typed in double spacing on good quality paper, with generous margins.
4. The name of the author(s) and of the institutes where the work was carried out should appear on the first page of the manuscript.
5. Particular care should be taken with mathematical expressions. The following should be clearly distinguished, e.g. by underlining in different colours: special founts (italics, script, bold type, Greek, Gothic, etc.); capital and small letters; subscripts and superscripts, e.g. x^2 , x_3 ; small l and 1 ; zero and capital O ; in expressions written by hand: e and l , n and u , v and ν , etc.
A List of Symbols on a separate sheet should be attached to each paper.
6. References should be numbered serially and listed at the end of the paper in the following form: J. Ise and W. D. Fretter, *Phys. Rev.*, **76**, 933, 1949.
For books, please give the initials and family name of the author(s), title, name of publisher, place and year of publication, e.g.: J. C. Slater, *Quantum Theory of Atomic Structures*, I. McGraw-Hill Book Company, Inc., New York, 1960.
References should be given in the text in the following forms: Heisenberg [5] or [5].
7. Captions to illustrations should be listed on a separate sheet, not inserted in the text.
8. In papers submitted to *Acta Physica* all measures should be expressed in SI units.

III. ILLUSTRATIONS AND TABLES

1. Each paper should be accompanied by three sets of illustrations, one of which must be ready for the blockmaker. The other sets attached to the copies of the manuscript may be rough drawings in pencil or photocopies.
2. Illustrations must not be inserted in the text.
3. All illustrations should be identified in blue pencil by the author's name, abbreviated title of the paper and figure number.
4. Tables should be typed on separate pages and have captions describing their content. Clear wording of column heads is advisable. Tables should be numbered in Roman numerals (I, II, III, etc.).

IV. RETURN OF MATERIAL

Owing to high postage costs, the Editorial Office cannot undertake to return *all* material not accepted for any reason for publication. Of papers to be revised (for not being in conformity with the above Notes or other reasons) only *one* copy will be returned. Material rejected for lack of space or on account of the Referees' opinion will not be returned to authors outside Europe.

Periodicals of the Hungarian Academy of Sciences are obtainable
at the following addresses:

AUSTRALIA

C.B.D. LIBRARY AND SUBSCRIPTION SERVICE
Box 4886, G.P.O., Sydney N.S.W. 2001
COSMOS BOOKSHOP, 145 Ackland Street
St. Kilda (Melbourne), Victoria 3182

AUSTRIA

GLOBUS, Hochstädtplatz 3, 1206 Wien XX

BELGIUM

OFFICE INTERNATIONAL DE LIBRAIRIE
30 Avenue Marnix, 1050 Bruxelles
LIBRAIRIE DU MONDE ENTIER
162 rue du Midi, 1000 Bruxelles

BULGARIA

HEMUS, Bulvar Ruszki 6, Sofia

CANADA

PANNONIA BOOKS, P.O. Box 1017
Postal Station "B", Toronto, Ontario M5T 2T8

CHINA

CNPICOR, Periodical Department, P.O. Box 50
Peking

CZECHOSLOVAKIA

MAD'ARSKÁ KULTURA, Národní třída 22
115 66 Praha
PNS DOVOZ TISKU, Vinohradská 46, Praha 2
PNS DOVOZ TLAČE, Bratislava 2

DENMARK

EJNAR MUNKSGAARD, Norregade 6
1165 Copenhagen K

FEDERAL REPUBLIC OF GERMANY

KUNST UND WISSEN ERICH BIEBER
Postfach 46, 7000 Stuttgart 1

FINLAND

AKATEEMINEN KIRJAKAUPPA, P.O. Box 128 SF-00101
Helsinki 10

FRANCE

DAWSON-FRANCE S. A., B. P. 40, 91121 Palaiseau
EUROPERIODIQUES S. A., 31 Avenue de Versailles, 78170
La Celle St. Cloud
OFFICE INTERNATIONAL DE DOCUMENTATION ET
LIBRAIRIE, 48 rue Gay-Lussac
75240 Paris Cedex 05

GERMAN DEMOCRATIC REPUBLIC

HAUS DER UNGARISCHEN KULTUR
Karl Liebknecht-Straße 9, DDR-102 Berlin
DEUTSCHE POST ZEITUNGSVERTRIEBSAMT Straße der
Pariser Kommüne 3-4, DDR-104 Berlin

GREAT BRITAIN

BLACKWELL'S PERIODICALS DIVISION
Hythe Bridge Street, Oxford OX1 2ET
BUMPUS, HALDANE AND MAXWELL LTD.
Cowper Works, Olney, Bucks MK46 4BN
COLLET'S HOLDINGS LTD., Denington Estate Wellingbo-
rough, Northants NN8 2QT
WM. DAWSON AND SONS LTD., Cannon House Folkstone,
Kent CT19 5EE
H. K. LEWIS AND CO., 136 Gower Street
London WC1E 6BS

GREECE

KOSTARAKIS BROTHERS INTERNATIONAL
BOOKSELLERS, 2 Hippokratous Street, Athens-143

HOLLAND

MEULENHOF-BRUNA B. V., Beulingstraat 2,
Amsterdam
MARTINUS NIJHOFF B.V.
Lange Voorhout 9-11, Den Haag

SWETS SUBSCRIPTION SERVICE

347b Heereweg, Lisse

INDIA

ALLIED PUBLISHING PRIVATE LTD., 13/14
Asaf Ali Road, New Delhi 110001
150 B-6 Mount Road, Madras 600002
INTERNATIONAL BOOK HOUSE PVT. LTD.
Madame Cama Road, Bombay 400039
THE STATE TRADING CORPORATION OF INDIA LTD.,
Books Import Division, Chandralok 36 Janpath, New Delhi
110001

ITALY

INTERSCIENTIA, Via Mazzè 28, 10149 Torino
LIBRERIA COMMISSIONARIA SANSONI, Via Lamarmora 45,
50121 Firenze
SANTO VANASIA, Via M. Macchi 58
20124 Milano
D. E. A., Via Lima 28, 00198 Roma

JAPAN

KINOKUNIYA BOOK-STORE CO. LTD.
17-7 Shinjuku 3 chome, Shinjuku-ku, Tokyo 160-91
MARUZEN COMPANY LTD., Book Department, P.O. Box
5050 Tokyo International, Tokyo 100-31
NAUKA LTD. IMPORT DEPARTMENT
2-30-19 Minami Ikebukuro, Toshima-ku, Tokyo 171

KOREA

CHULPANMUL, Phenjan

NORWAY

TANUM-TIDSKRIFT-SENTRALEN A.S., Karl Johansgatan
41-43, 1000 Oslo

POLAND

WĘGIERSKI INSTYTUT KULTURY, Marszałkowska 80,
00-517 Warszawa
CKP-I W, ul. Towarowa 28, 00-958 Warszawa

ROUMANIA

D. E. P., Bucuresti
ILEXIM, Calea Grivitei 64-66, Bucuresti

SOVIET UNION

SOJUZPECHAT — IMPORT, Moscow
and the post offices in each town
MEZHUNARODNAYA KNIGA, Moscow G-200

SPAIN

DIAZ DE SANTOS, Lagasca 95, Madrid 6

SWEDEN

GUMPERTS UNIVERSITETSBOKHANDL AB
Box 346, 401 25 Göteborg 1

SWITZERLAND

KARGER LIBRI AG, Petersgraben 31, 4011 Basel

USA

EBSCO SUBSCRIPTION SERVICES
P.O. Box 1943, Birmingham, Alabama 35201
F. W. FAXON COMPANY, INC.
15 Southwest Park, Westwood Mass. 02090
READ-MORE PUBLICATIONS, INC.
140 Cedar Street, New York, N. Y. 10006

YUGOSLAVIA

JUGOSLOVENSKA KNJIGA, Terazije 27, Beograd
FORUM, Vojvode Mišića 1, 21000 Novi Sad

Acta Physica Hungarica

VOLUME 58, NUMBERS 3-4, 1985

EDITOR-IN-CHIEF

I. KOVÁCS

EDITORIAL BOARD

**Z. BAY, R. GÁSPÁR, I. GYARMATI, N. KÜRTI,
K. NAGY, L. PÁL, A. SZALAY, P. SZÉPFALUSY, I. TARJÁN,
B. TELEGDI, L. TISZA, E. WIGNER**



Akadémiai Kiadó, Budapest

ACTA PHYS HUNG. APAHAQ 58 (3-4) 157-282 (1985) HU ISSN 0231-4428

ACTA PHYSICA HUNGARICA

A JOURNAL OF THE HUNGARIAN ACADEMY
OF SCIENCES

EDITED BY
I. KOVÁCS

Acta Physica publishes original papers on subjects in physics. Papers are accepted in English, French, German and Russian.

Acta Physica is published in two yearly volumes (4 issues each) by

AKADÉMIAI KIADÓ
Publishing House of the Hungarian Academy of Sciences
H-1054 Budapest, Alkotmány u. 21

Subscription information

Orders should be addressed to

KULTURA Foreign Trading Company
1389 Budapest P.O. Box 149

or to its representatives abroad.

Acta Physica is indexed in *Current Contents*, in *Physics Abstracts* and in *Current Papers in Physics*.

CONTENTS

GENERAL

Spherical functions of the Lorentz group on the hyperboloids. <i>M. Huszár</i>	175
--	-----

ELEMENTARY PARTICLES AND FIELDS

On the initial-value problem of linearized Einstein's equations. <i>A. Mészáros</i>	255
Schwinger model in temporal gauge. <i>J. Balog</i> and <i>P. Hraskó</i>	233

ATOMIC AND MOLECULAR PHYSICS

Dissociation energy of the SrH molecule. <i>V. G. Tulasigeri</i> and <i>V. M. Korwar</i>	157
The ground state of the Heisenberg Hamiltonian in four-spin systems with antiferromagnetic coupling. <i>S. Angelov</i> and <i>I. Mayer</i>	161
Dissociation energies for the electronic ground states of GaF, InF and TlF. <i>R. R. Reddy</i> and <i>T. V. R. Rao</i>	169
Molecular pseudopotential calculations VII. 1. <i>R. Gáspár</i> and <i>I. Tamássy-Lentei</i>	191
Molecular pseudopotential calculations VII. 2. <i>R. Gáspár</i> , <i>I. Tamássy-Lentei</i> and <i>Á. Derecskei-Kovács</i>	195
Molecular symmetry in ab initio calculations. I. <i>F. Bartha</i> , <i>E. Kapuy</i> and <i>C. Kozmutza</i>	219
Molecular symmetry in ab initio calculations. II. <i>F. Bartha</i> and <i>C. Kozmutza</i>	227
An integral representation of the 6j symbol. <i>S. Datta Majumdar</i>	265

CONDENSED MATTER

Geometrical structures of triatomic and tetratomic clusters of Li, Na, K, Cu and Ag atoms. <i>I. László</i> and <i>A. Julg</i>	199
The influence of aggregation phenomena on the yield stress of NaCl(Ca) crystals. <i>J. Sárközi</i> and <i>E. Hartmann</i>	259
Surface of doped NaCl crystals annealed in air. <i>K. Orbán</i> and <i>J. Sárközi</i>	267

ASTROPHYSICS

Does Newton's world model revive? <i>A. Mészáros</i>	187
--	-----

BOOK REVIEWS

217

DISSOCIATION ENERGY OF THE SrH MOLECULE

V. G. TULASIGERI and V. M. KORWAR

Department of Physics, Karnatak University, Dharwad, India

(Received 16 December 1983)

The dissociation energy D_0^0 of the ground state ($X^2\Sigma^+$) of SrH is not yet a settled matter as the range of its variation is from 1.24 to 2.6 eV. These different values of dissociation energy have been determined mainly on the basis of observed predissociation. In the present investigation, a semi-theoretical criterion has been adopted to decide the matter of dissociation energy of SrH by using the Rydberg-Kratzer potential function and RKR method. The dissociation energy is now estimated to be 1.81 ± 0.05 eV.

1. Introduction

The dissociation energy of the SrH molecule is not yet a settled matter for the following reasons. Quoting Grundstrom's dissertation [1], Gaydon [2] gives the dissociation energy (D_0^0) for this molecule to be 2.6 eV. This is obtained on the linear Birge-Sponer extrapolation method with the assumption that the normal state of one of the atoms into which the molecule dissociates, is 1S_0 . But, for such molecules, binding is usually determined by higher atomic electronic states and the extrapolation would not take the usual form. Thus, the true value of dissociation energy is often much lower than that indicated by linear extrapolation.

On the basis of predissociation observed in the molecule, Humphreys and Fredrickson [3] estimate the dissociation energy to be 1.49 eV with dissociation products Sr, ^1S+H , 2S , while More and Cornell [4] with the same dissociation products estimate it at 1.24 eV. However, Gaydon [2] lists a value of 1.75 eV for the dissociation energy on the basis of the atomic state of Sr to be 2D state. Also, he gives an upper limit of 1.66 eV for the dissociation energy on predissociation calculation. Thus, looking into the situation regarding the estimation of the dissociation energy of the SrH molecule, there seems to be some scope for further work on the dissociation energy of SrH. Such an attempt on a semi-theoretical basis has been done in this paper which is briefly described in the following Section.

2. Method of obtaining dissociation energy

It is an established fact that the RKR [5, 6, 7] procedure yields true potential energy curves of diatomic molecules. It is possible, making use of these curves, to compare the true vibrational energy values with the computed results of these on the

basis of some assumed expression of potential energy functions such as Morse [8], Rydberg-Kratzer [5, 9] which is referred to as RK potential, etc. This helps one decide the suitability of the value of D_e (dissociation energy referred to potential minimum). The set of vibrational energy values thus computed which compares most favourably with the RKR results, is taken as the representative set for the molecule and hence, the value of D_e used which generated this set, can be taken as the best value of D_e .

In the present work, the RK potential function proposed by Varma and Jha [10] is taken as the potential function for computing the vibrational energy values. The basis for selecting this potential function may be found in a paper communicated by one of the authors [11] elsewhere.

3. Estimation of dissociation energy

The RK potential function may be expressed as

$$U(r) = -D_e(1 + b\rho) \exp(-b\rho) + D_e \left(\frac{\rho}{r}\right)^2 - D_e, \quad (1)$$

where $\rho = r - r_e$,

$$b = \text{potential parameter, } b = \left\{ \frac{K_e}{D_e} - \frac{2}{r_e^2} \right\}^{1/2}, \quad D_e = \text{dissociation energy.}$$

Table I
Turning points of vibrational motion for the $X^2\Sigma^+$ state of the SrH molecule

State v	Observed $G(v)$ [cm^{-1}]	RKR	
		r_{\min} [nm]	r_{\max} [nm]
0	598.85	0.1992	0.2329
1	1771.05	0.1895	0.2486
2	2909.25	0.1835	0.2607
3	4013.45	0.1789	0.2715
4	5083.65	0.1753	0.2816
5	6119.85	0.1722	0.2913
6	7122.05	0.1695	0.3008
7	8090.25	0.1672	0.3102
8	9024.45	0.1650	0.3196
9	9924.65	0.1631	0.3290
10	10,790.85	0.1614	0.3385
.	.	.	.
.	.	.	.
.	.	.	.
.	.	.	.
.	.	.	.
34	21,379.65 (extrapolated)	0.1189	0.9742

It must be noted here that, for calculating the $U(r)$ value, $2D_e$ must be added to the right hand side of expression (1). This is necessary to bring the minimum of the curves at zero, as suggested by Varma and Jha [10]. In order to calculate the vibrational energy values, the following procedure was adopted. The turning points r_{\min} and r_{\max} for the ground state ($X^2\Sigma^+$) of SrH, have been computed by using the RKR procedure [12, 13, 14]. These are tabulated in columns 2, 3 and 4, respectively, of Table I. These values were then substituted for r in the expression (1) with the assumption that they are the same for the RK potential as for RKR which could yield vibrational energy. These computed values of vibrational energy have been tabulated in columns 3, 4 and 5 of Table II corresponding to D_0^0 's 1.76, 1.81 and 1.85 eV respectively, for various vibrational quantum numbers. As mentioned earlier, the dissociation energy value is around 1.8 eV. That is why we have chosen the three values of dissociation energies mentioned in Table II for generating $G(v)$ values. In the same Table II, percentage deviations of individual calculated $G(v)$ values from their corresponding RKR values are given in parentheses after each calculated value of $G(v)$. The average percentage deviations for different D_0^0 values have also been given in the same Table II. In this Table D_0^0 values are given, but as the RK expression involves D_e

Table II
Comparison of observed and calculated energy values for the $X^2\Sigma^+$ state of the SrH molecule

r [nm]	Observed $G(v)$ [cm^{-1}]	Calculated $G(v)$ [cm^{-1}]			
		$D_0^0 = 1.76$ eV	$D_0^0 = 1.81$ eV	$D_0^0 = 1.86$ eV	
γ_{\max} RKR	0.2329	598.85	601.55(0.4507)	603.11(0.7118)	604.61(0.9622)
	0.2486	1771.05	1770.08(0.0548)	1778.45(0.4177)	1778.50(0.8721)
	0.2607	2909.25	2898.52(0.3689)	2916.61(0.2531)	2934.44(0.8659)
	0.2715	4013.45	3987.72(0.6410)	4018.31(0.1212)	4047.85(0.8570)
	0.2816	5083.65	5038.27(0.8927)	5083.10(0.0108)	5126.45(0.8420)
	0.2913	6119.85	6050.69(1.1301)	6111.41(0.1379)	6170.22(0.8231)
	0.3008	7122.05	7025.54(1.3551)	7103.56(0.2596)	7179.24(0.8030)
	0.3102	8090.25	7963.39(1.5680)	8059.93(0.3748)	8153.72(0.7844)
	0.3196	9024.45	8864.87(1.7683)	8980.95(0.4820)	9093.88(0.7694)
	0.3290	9924.65	9730.59(1.9554)	9867.11(0.5798)	10,000.11(0.7603)
0.3385	10,790.85	10,561.23(2.1279)	10,718.93(0.6665)	10,872.76(0.7591)	
γ_{\min} RKR	0.1992	598.85	593.80(0.8430)	592.47(1.0652)	591.20(1.2768)
	0.1895	1771.05	1758.58(0.7042)	1752.10(1.0701)	1745.94(1.4178)
	0.1835	2909.25	2888.24(0.7221)	2874.99(1.1773)	2862.43(1.6094)
	0.1789	4013.45	3983.53(0.7456)	3962.55(1.2681)	3942.67(1.7636)
	0.1753	5083.65	5045.51(0.7502)	5016.17(1.3273)	4988.38(1.8741)
	0.1722	6119.85	6075.39(0.7264)	6037.25(1.3498)	6001.13(1.9400)
	0.1695	7122.05	7074.43(0.6687)	7027.17(1.3323)	6982.44(1.9602)
	0.1672	8090.25	8043.96(0.5722)	7987.37(1.2717)	7933.86(1.9331)
	0.1650	9024.45	8985.41(0.4326)	8919.36(1.1645)	8856.93(1.8563)
	0.1631	9924.65	9900.33(0.2451)	9824.74(1.0067)	9753.32(1.7264)
0.1614	10,790.85	10,790.39(0.0042)	10,705.21(0.7937)	10,624.75(1.5393)	
Average deviation [%]		0.8512	0.7655	1.5847	

value, appropriate D_e values have been computed and are used for calculating $G(v)$ values. The molecular constants employed in the above calculations have been taken from Huber and Herzberg [15].

4. Results and discussion

On the basis of average percentage deviations worked out, three values of D_0^0 , namely 1.76, 1.81 and 1.86 eV, were selected as representative values. Of the three $G(v)$ sets, the one with $D_0^0 = 1.81$ eV was found to have minimum average percentage deviation. The two sets on either side of this show clearly increased average percentage deviations. Therefore, this particular value of D_0^0 (1.81 ± 0.05 eV) was chosen as the true dissociation energy.

From the results of the three sets of $G(v)$ and average percentage deviations which differ from one another, the value 1.81 eV may be recommended for D_0^0 of SrH. This value is closer to the experimental value 1.75 eV. The present finding supports the earlier work done by one of the authors [11] regarding the suitability of RK potential function for some of the elements of group II A of the periodic table, in particular for SrH. This has been communicated elsewhere.

References

1. B. Grundstrom, Dissertation, Stockholm, 1936.
2. A. G. Gaydon, Dissociation Energies, 3rd ed (London) Chapman and Hall, 1968.
3. R. F. Humphreys and W. R. Fredrickson, Phys. Rev., 50, 542, 1936.
4. K. R. More and S. D. Cornell, Phys. Rev., 53, 806, 1938.
5. R. Rydberg, Z. Phys., 73, 376, 1931.
6. O. Klein, Z. Phys., 76, 226, 1932.
7. A. L. G. Rees, Proc. Phys. Soc., A59, 998, 1947.
8. P. M. Morse, Phys. Rev., 34, 57, 1929.
9. A. Kratzer, Z. Phys., 3, 289, 1920.
10. M. P. Varma and B. L. Jha, Ind. J. Phys., 55B, 164, 1981.
11. V. G. Tulasigeri, to be published, 1985.
12. N. R. Tawde and V. G. Tulasigeri, J. Phys. B 5, 1681, 1972.
13. N. R. Tawde and V. G. Tulasigeri, Acta. Phys. Hung., 38, 299, 1975.
14. N. R. Tawde and V. G. Tulasigeri, Acta Phys. Hung., 50, 103, 1981.
15. K. P. Huber and G. Herzberg, Molecular Spectra and Molecular Structure, Vol. IV, Constants of Diatomic Molecules, Van Nostrand Reinhold, New York, 1979.

THE GROUND STATE OF THE HEISENBERG HAMILTONIAN IN FOUR-SPIN SYSTEMS WITH ANTIFERROMAGNETIC COUPLING

S. ANGELOV

*Institute of General and Inorganic Chemistry, Bulgarian Academy of Sciences
Sofia 1040, Bulgaria*

and

I. MAYER

*Central Research Institute for Chemistry, Hungarian Academy of Sciences
1525 Budapest, Hungary*

(Received 10 January 1984)

The method of spin projection is applied to investigate the ground state of the Heisenberg Hamiltonian for the model of closed and open four-spin chains.

1. Introduction

The phenomenon of antiferromagnetism in insulators is usually rationalized assuming that the spins of the magnetic ions are localized on the corresponding lattice sites and are coupled in such a way as to form two magnetic sublattices. In the absence of an external magnetic field the magnetic moments of the sublattices have to be fully compensated, and each spin is considered to be surrounded by other ones of opposite orientation. Attempts to describe this situation by the so-called Néel function*:

$$\mathcal{F} = \alpha(1)\beta(2)\alpha(3)\beta(4) \dots \alpha(N-1)\beta(N), \quad (1)$$

(where the spins with odd and even indices, respectively, are considered to belong to the two different sublattices) were unsuccessful [1]. The aim of the present communication is to discuss in some detail the problem of the ground state of the antiferromagnets on the example of four-spin systems.

* We consider the case of an even number of spins $s_i = \frac{1}{2}$.

2. Pure singlet wave function and spin correlation functions

As noted by Misurkin and Ovchinnikov [2], a wave function of overall singlet state of the system in question may be obtained from ϑ by applying on it Löwdin's spin projection operator [3, 4]:

$$\Theta_{AF} = \hat{O}_{(S=0)}^S \vartheta = \hat{O}_{(S=0)}^S \alpha(1)\beta(2)\alpha(3)\beta(4) \dots \alpha(N-1)\beta(N). \quad (2)$$

It was also pointed out by Misurkin and Ovchinnikov [2] that there is no meaning to attribute to a given site in the antiferromagnetic crystal a fixed spin orientation ("spin up", α or "spin down", β), only the correlation between the spins belonging to the same or different sublattices is of real significance. Function Θ_{AF} describes a perfect magnetic ordering because it is formed [4, 5] exactly in the "antiferromagnetic" manner that one at first couples all spins α and β , respectively, into two subsystems of maximal multiplicity and then forms from them a resulting singlet. Θ_{AF} is invariant, up to a phase factor, to the simultaneous interchange of all α -s and β -s; therefore it possesses the full translational symmetry of the crystal.

The measure of the ordering degree between the spins located at the sites i and j is given according to [2] by the correlation function $\langle \hat{s}_i \hat{s}_j \rangle$, where the pointed brackets denote expectation values. The perfect long-range ordering described by Θ_{AF} is well reflected by the values of the correlation function we derived:

$$\langle \hat{s}_i \hat{s}_{i+r} \rangle = \begin{cases} -\frac{1}{4} - \frac{1}{N} & (r \text{ odd}), \\ +\frac{1}{4} & (r \text{ even}), \end{cases} \quad (3)$$

which do not depend on the distance between the spins i and $i+r$, but is determined solely by the fact whether i and $i+r$ belong to the same or to different sublattices.

The case of an isolated pair of spins coupled into a singlet is quite specific and must be treated separately. The singlet case is exceptional in the sense that all the three (x, y, z) components of the resulting spin of the pair have simultaneously definite values equal to zero, i.e. the two spins are strictly antiparallel. Accordingly, their correlation function $\langle \hat{s}_1 \hat{s}_2 \rangle$ equals $-3/4$, i.e. has the maximal possible absolute value. This value is in agreement also with Eq. (3). As the situation for two spins in an isolated pair differs principally from that of any other system, it is meaningless, in our opinion, to speak about "molecular antiferromagnetism" for binuclear transition metal complexes [6]. We think that the classification perhaps must not be determined solely by the value of the singlet-triplet separation; one has rather to consider antiferromagnetism as a collective effect, connected with the appearance of sublattices with some long-range magnetic ordering which is established due to an interplay of the short-range exchange interactions.

3. The "antiferromagnetism" of four-spin closed rings

The smallest system which can be treated as a molecular model of a two-sublattice antiferromagnet consists of four spins. For this simplest case one can easily perform analytical and/or numerical investigations facilitating the qualitative understanding of different aspects of the problem. For this reason we shall describe here some of our results obtained for the case of four-spin closed rings.

The exchange interactions we are going to investigate are usually described by the Heisenberg exchange Hamiltonian:

$$\hat{H}_{ex} = -2 \sum_{i < j}^{(n.n.)} J_{ij} \hat{s}_i \hat{s}_j, \quad (4)$$

where one takes into account only the nearest-neighbour (*n. n.*) interactions. The antiferromagnetic character of the coupling means that $J_{ij} < 0$. One may immediately see the intimate connection between the energy of the system and the correlation functions discussed above:

$$E = \langle \hat{H}_{ex} \rangle = -2 \sum_{i < j}^{(n.n.)} J_{ij} \langle \hat{s}_i \hat{s}_j \rangle. \quad (5)$$

Eq. (5) indicates that the energy is essentially a weighted sum of the correlation functions of the nearest-neighbour spins (for which $J_{ij} \neq 0$). The correlation of the distant spins has no influence on the energy. So, the existence of the long-range magnetic order (if any) is only a by-product of the short-range correlations.

Let us now write down explicitly Θ_{AF} for four spins as [3, 4]:

$$\begin{aligned} \Theta_{AF} = \frac{1}{6} \{ & 2[\alpha(1)\beta(2)\alpha(3)\beta(4) + \beta(1)\alpha(2)\beta(3)\alpha(4)] - \\ & - [\beta(1)\alpha(2)\alpha(3)\beta(4) + \alpha(1)\alpha(2)\beta(3)\beta(4) + \\ & + \alpha(1)\beta(2)\beta(3)\alpha(4) + \beta(1)\beta(2)\alpha(3)\alpha(4)] \} \end{aligned} \quad (6)$$

and apply \hat{H}_{ex} on it. (Note that Θ_{AF} is not normalized.) Then one obtains for a closed chain (J_{12} , J_{23} , J_{34} and J_{14} are the non-zero exchange integrals):

$$\begin{aligned} \hat{H}_{ex} \Theta_{AF} = & (J_{12} + J_{23} + J_{34} + J_{14}) \Theta_{AF} - \\ & - \frac{1}{8} (J_{12} + J_{34} - J_{23} - J_{14}) [\alpha(1)\beta(2)\beta(3)\alpha(4) + \\ & + \beta(1)\alpha(2)\alpha(3)\beta(4) - \alpha(1)\alpha(2)\beta(3)\beta(4) - \\ & - \beta(1)\beta(2)\alpha(3)\alpha(4)]. \end{aligned} \quad (7)$$

According to Eq. (7), Θ_{AF} is an eigenfunction of \hat{H}_{ex} if $J_{12} + J_{34} = J_{23} + J_{14}$, i.e. if the

system is a square, a rhombus or a "kite" (see Fig. 1). Such systems may really be considered as the simplest possible models of "molecular" antiferromagnetism*.

It is of meaning to recall here some of our former results of applying the spin projected extended Hartree-Fock (EHF) method to the π -electron structure of cyclobutadiene molecule [4, 7]. In these calculations Θ_{AF} was used as the spin function, while the spatial part of the properly antisymmetrized wave function was built up of

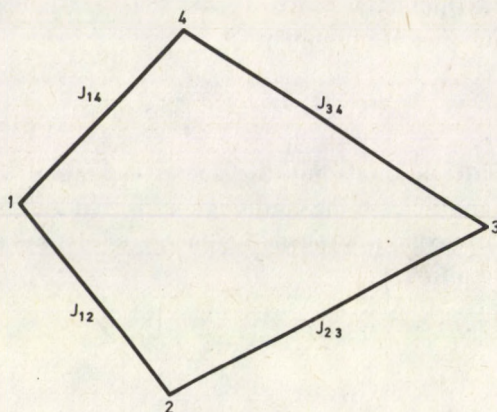


Fig. 1. Symmetric arrangement of four spins for which Θ_{AF} is an eigenfunction of the exchange Hamiltonian ($J_{12} + J_{34} = J_{23} + J_{14}$ is required)

molecular orbitals constructed as appropriately optimized linear combinations of the $2p_z$ carbon atomic orbitals. The Pariser-Parr-Pople (PPP) Hamiltonian — essentially a generalization of the Hubbard Hamiltonian including also two-centre electron-electron repulsion and electron-nuclear attraction terms — was applied. (The interactions were not restricted to the nearest neighbours; for further details see [4] and [7].) It was found that for the configuration of a regular square or for that of a rhombus the EHF wave function became practically identical with the "full CI" wave function (exact ground state solution of the PPP-Hamiltonian): their overlap was different from unity only by $\sim 1.4 \times 10^{-6}$. Owing to the spin coupling, characteristic for Θ_{AF} as discussed above, this observation was considered already in [4] as indication that square cyclo-butadiene, this typical antiaromatic molecule, may be also the simplest possible system of antiferromagnetic character. It was also stressed that this system cannot be described, even qualitatively, by using doubly filled molecular orbitals.

We think it should be of interest to clarify whether one can interrelate these results obtained for square or rhomboidal systems at different levels of sophistication and by using quite different formalisms — the Heisenberg Hamiltonian for localized spins and

* We note that in some circumstances Θ_{AF} remains the eigenfunction of \hat{H}_{ex} even if the exchange interactions along the diagonals are also included in the Heisenberg Hamiltonian.

the EHF method, respectively. (The EHF method is essentially a refined LCAO-MO approach in which the restriction of doubly filled orbitals is removed, but the correct spin properties are ensured.)

The EHF molecular orbitals obtained originally are completely delocalized over the whole system. It is, however, possible to transform them — without changing the many-electron wave function — to some localized orbitals (analogues of Wannier functions) each of which is essentially centred at one of the corners of the square (Fig. 2). The many-electron wave function can then be obtained in the following manner: one attributes spins α and β alternatively to each “Wannier function” and then projects the resulting determinant wave function on the pure singlet state. The “Wannier functions” filled before projection with different spins are not orthogonal to each other; their overlap integral is 0.398. (Note that we are dealing with a π -system in which the interactions are much stronger than between the magnetic orbitals in transition-metal complexes.) The overlap of the “Wannier functions” reflects the presence of ionic terms in the expansion of the wave function in terms of the original atomic orbitals. As we have already analysed in the paper [8], the admixture of such ionic terms is the very essence of the delocalization considered in the framework of Anderson's kinetic

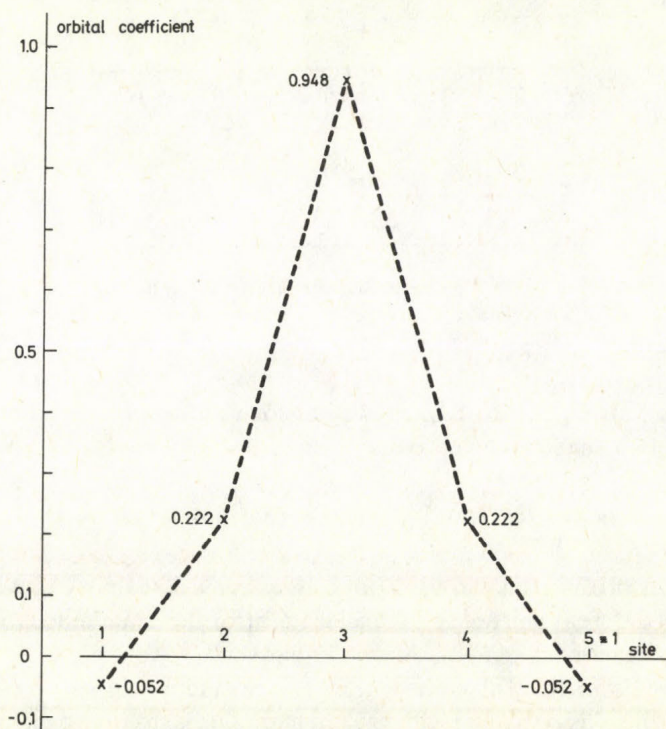


Fig. 2. The Wannier-type localized EHF orbitals for the π -electron system of cyclobutadiene. The LCAO coefficients are indicated.

exchange mechanism leading to the appearance of negative exchange parameters J in the resulting effective exchange Hamiltonian. So we conclude that square cyclobutadiene must really be an "antiferromagnet" rather well described with the Heisenberg Hamiltonian.

4. Open four-spin chain

In general, Θ_{AF} is not an eigenfunction of \hat{H}_{ex} (see [9] for a discussion). This means that for the true ground state of \hat{H}_{ex} the long-range order is reduced as to permit a higher correlation between the nearest neighbour spins. The effect of reduced long-range ordering with respect to that prescribed by Θ_{AF} , which is due to the increase in the short-range correlation, may be observed already for four-spin open-end chain. We have found numerically the eigenvectors of \hat{H}_{ex} for the open chain with $J = J_{12} = J_{23} = J_{34}$ non-zero exchange parameter. Table I displays some of the results obtained for

Table I
Correlation functions^{a)} and energy of some wave functions for an open-end four-spin Heisenberg chain

	Θ_{exact}	Θ_{AF}	Θ_B
$\langle \hat{s}_1 \hat{s}_2 \rangle$	-0.6830	-0.5	-0.75
$\langle \hat{s}_1 \hat{s}_3 \rangle$	0.1830	0.25	0
$\langle \hat{s}_1 \hat{s}_4 \rangle$	-0.2500	-0.5	0
$\langle \hat{s}_2 \hat{s}_3 \rangle$	-0.2500	-0.5	0
E	$-3.232 J $	$-3 J $	$-3 J $

^{a)} The remaining correlation functions are determined by the symmetry

the exact solution Θ_{exact} , for Θ_{AF} as well as for the function Θ_B corresponding to formation of two singlet-coupled pairs 1-2 and 3-4:

$$\Theta_B = \frac{1}{2} [\alpha(1)\beta(2) - \beta(1)\alpha(2)] [\alpha(3)\beta(4) - \beta(3)\alpha(4)]. \quad (8)$$

Θ_B represents in some sense the opposite extreme case than Θ_{AF} considering the correlation of different pairs of spins; accidentally for the given model both functions have the same energy.

The results in the Table show how the correlation of spins 1-2 and 3-4 is increased for Θ_{exact} as compared with Θ_{AF} ; remarkable is the simultaneous decrease of the absolute values of all the other correlation functions (including $\langle \hat{s}_2 \hat{s}_3 \rangle$). For Θ_B spins in the pairs 1-2 and 3-4 are fully correlated while there is no correlation for the

spins in different pairs; this is unfavourable energetically, as far as J_{23} becomes completely disregarded.

The true ground state may be presented as:

$$\Theta_{\text{exact}} = 0.9660 \Theta'_{AF} - 0.2588 \Theta_C. \quad (9)$$

Here Θ'_{AF} is Θ_{AF} renormalized to unity, while

$$\begin{aligned} \Theta_C = \frac{1}{2} [& \beta(1)\alpha(2)\alpha(3)\beta(4) - \alpha(1)\alpha(2)\beta(3)\beta(4) + \\ & + \alpha(1)\beta(2)\beta(3)\alpha(4) - \beta(1)\beta(2)\alpha(3)\alpha(4)] \end{aligned} \quad (10)$$

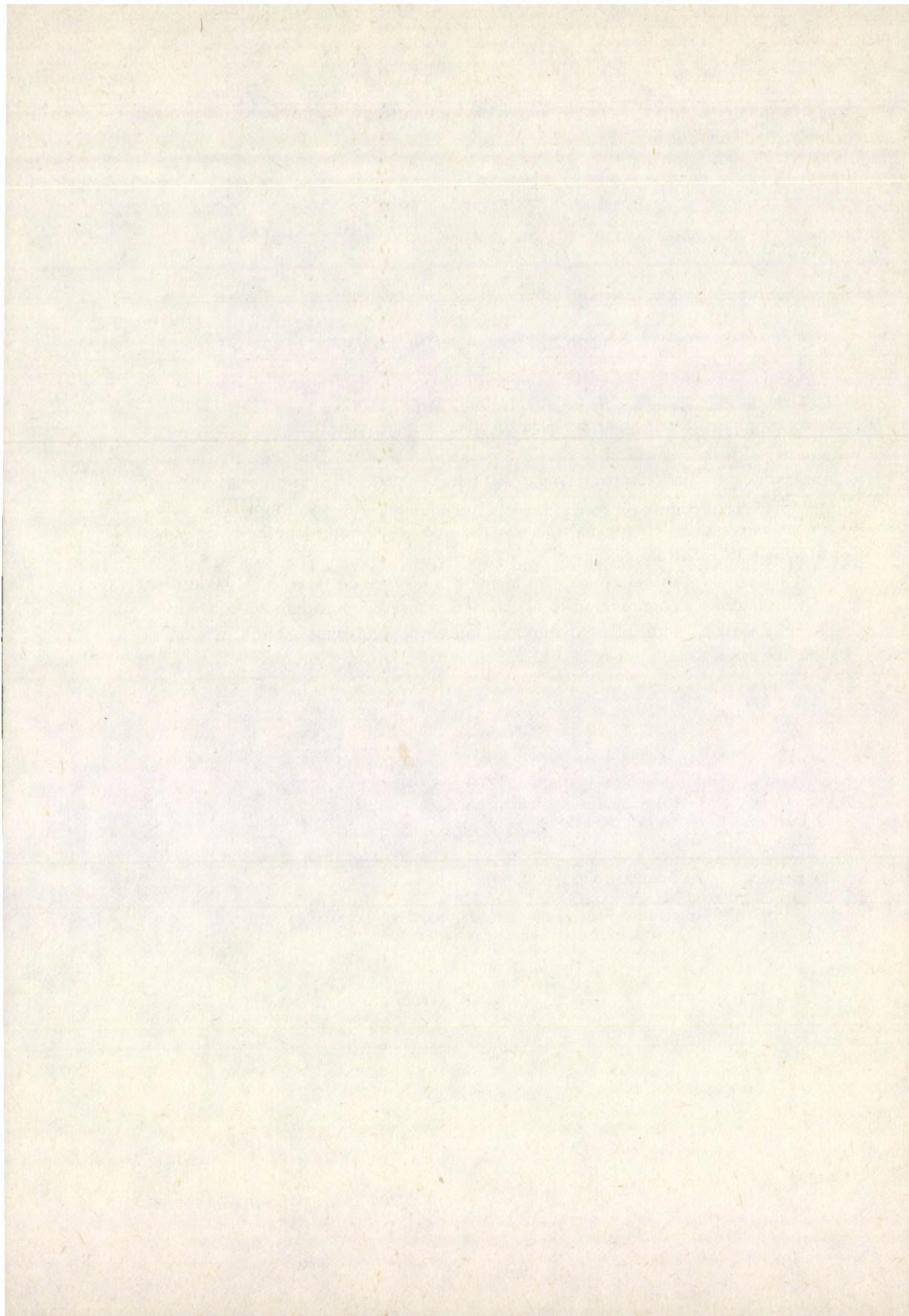
is a superposition of Θ_B with a quite similar function for which spins 2-3 and 1-4 are paired. (Note that Θ_B is not orthogonal to Θ_{AF} but Θ_C is.)

An interesting feature of Θ_{exact} is the increased correlation of the side pairs as compared with the central one. This is a consequence of the fact that a given spin cannot enter more than one local singlet at a time. The large weight of terms with 1-2 and 3-4 singlet coupling in Θ_{exact} is in full agreement with the known molecular geometry of the trans-butadiene molecule, the side C-C bond lengths being much shorter than the central one.

One can suppose that a linear combination of the type Eq. (9) with Θ_{AF} as leading term will describe the ground state of the Heisenberg Hamiltonian of rather large number of systems with different dimensionality, lattice symmetry and number of interacting spins.

References

1. S. V. Vonsovskii, *Magnetism*, Nauka, Moskva, 1971, p. 681.
2. I. A. Misurkin and A. A. Ovchinnikov, *Teor. Eksp. Khim.*, **8**, 291, 1972.
3. P.—O. Löwdin, *Phys. Rev.*, **97**, 1509, 1955.
4. I. Mayer, *Adv. Quantum Chem.*, **12**, 189, 1980.
5. R. Pauncz, *Alternant Molecular Orbital Method*, Saunders, Philadelphia, 1967, p. 35.
6. A. A. Pasynskii, *Inorganica Chim. Acta*, **39**, 91, 1980.
7. I. Mayer, *Acta Phys. Hung.*, **39**, 133, 1975.
8. I. Mayer and S. A. Angelov, *Int. J. Quantum Chem.*, **18**, 783, 1980.
9. I. Mayer and S. A. Angelov, *Solid State Comm.*, **49**, 593, 1984.



DISSOCIATION ENERGIES FOR THE ELECTRONIC GROUND STATES OF GaF, InF and TlF

R. R. REDDY

*Department of Physics, KSRM College of Engineering, Cuddapah
516001, India*

and

T. V. R. RAO

*Department of Physics, University of Constantine, Constantine
Algeria*

(Received 19 January 1984)

The dissociation energies of the diatomic molecules GaF, InF and TlF have been computed by fitting empirical potential functions to the true potential energy curves for the electronic ground states of the molecules. The five parameter Hulbert–Hirschfelder function and Rao and Reddy's modified potential function have been used. The estimated dissociation energies are 9.772 ± 0.288 , 8.571 ± 0.256 and 7.209 ± 0.641 kJ/mol for GaF, InF and TlF, respectively. These values are in good agreement with literature values. The first ionization potentials for these molecules are estimated.

1. Introduction

A special character has been seen in the Group IIIA monohalides. The ground state of all the molecules in the IIIA group is $\pm a^1 \Sigma$ state and the lowest excited state is $a^3 \pi$. The dissociation products in all these molecules are not higher than $M^*(^2P_{3/2})$ and $X^*(2P_{1/2})$ in any of the molecules. The dissociation energy for these molecules from the Birge–Sponer extrapolation method is only 0.7 ± 0.1 eV of the values obtained by thermochemical methods. A special result is obtained from the relation of Somayajulu [1] for the Group IIIA monohalides. Thakur et al [2] thoroughly studied various properties of all these molecules. They state that these molecules are somewhat ionic in nature. The 3-parameter Lippincott potential function has yielded satisfactory estimates of dissociation energies for many diatomic molecules. It gives very low values for these halides [2]. The estimated dissociation energies by the curve fitting method (by 3-parameter Lippincott function) are in great disagreement with other reported values in the literature [3]. Singh et al [4] estimated dissociation energies for some of the Group IIIA monohalides using electronegativity potential function. They did not attempt to calculate the dissociation energies for GaF, InF and TlF molecules.

The work reported in this paper was started with a view to some points. The dissociation energies given in the literature were in disagreement with each other for these molecules. [3]. The 3-parameter Lippincott function fails to lead to the precise dissociation energy [2]. The ionic character for the GaF, InF and TlF molecules is more than 80%. Steele et al [5] reported that the H-H function is the best function of all the potential functions reported in literature. It is proposed to calculate the dissociation energies for GaF, InF and TlF molecules employing H-H function and also to test the utility of Rao and Reddy's modified function [6] to estimate the dissociation energies for these molecules. The molecular constants required for the present work have been taken from Mizushima [7].

2. Empirical potential functions

The empirical potential functions used

(i) the Five-Parameter Hulburt-Hirschfelder function [8] is of the form

where
$$U(r) = D_e [(1 - e^{-x})^2 + cx^3 e^{-2x}(1 + bx)],$$

$$x = \frac{\omega_e}{2(B_e D_e)^{1/2}} \cdot \frac{r - r_e}{r_e},$$

$$c = 1 + a_1 \left(\frac{D_e}{a_0} \right)^{1/2},$$

$$b = 2 - \left[\frac{7}{12} - \frac{D_e a_2}{a_0} \right] / c,$$

$$a_0 = \frac{\omega_e^2}{4B_e}, \quad a_1 = -1 - \frac{\alpha_e \omega_e}{6B_e^2}$$

and

$$a_2 = \frac{5}{4} a_1^2 - \frac{2\omega_e x_e}{3B_e},$$

(ii) Rao and Reddy's modified Hulburt-Hirschfelder function [6] is of the form

where
$$U(r) = D_e [(1 - e^{-x})^2 + cx^3 e^{-2x}(1 + bx)],$$

$$x = (\gamma r_e)^{1/2} \cdot \frac{r - r_e}{r_e},$$

$$\gamma r_e = \frac{\omega_e^2}{4B_e D_e},$$

$$c = 1 - \frac{1}{(\gamma r_e)^{1/2}} - K,$$

$$K = \frac{\alpha_e \omega_e}{6B_e^2(\gamma r_e)^{1/2}},$$

$$b = 2 - \left[\frac{7}{12} - \frac{a_2}{\gamma r_e} \right] / c. \quad (1)$$

The value of a_2 in Eq. (1) is estimated from

$$a_2 = 1 - \frac{\gamma r_e}{2} + \frac{3}{2} K (\gamma r_e)^{1/2} + K \cdot b \cdot \gamma r_e. \quad (2)$$

In Eq. (2), b is considered as universal constant (~ 1.065). The advantage of this function is that the bond energy may be calculated by knowing γ and K only. This method was successfully verified in a number of cases [6, 9–11]. The maximum average error of this modified H–H function is about 2%, as for the original H–H function.

3. Dissociation energy

The potential energy curves for these molecules have been constructed by the method of Lakshman and Rao [12]. These turning points are used in the Hulburt–Hirschfelder's function and for a particular value of D_e , the observed energy values of U are compared with the calculated energy values ($U(r)$). This procedure is repeated for different values of D_e . We will get the best energy values at a particular value of D_e only. This D_e value may be taken as the precise dissociation energy.

4. Results and discussion

Table I displays the turning points (from Lakshman and Rao's method), observed energy values U , energy values obtained from the H–H function for a particular value of D_e (where the percentage deviation is less) and the energy values from Rao and Reddy's method [6]. For GaF, the estimated dissociation energy of 9.772 ± 0.288 KJ/mol agrees with Gaydon's [13] reported value 9.772 ± 0.801 KJ/mol. This result is in good agreement with Huber and Herzberg's [14] value 9.580 KJ/mol and is less than Barrow's [3] value 9.933 KJ/mol. The dissociation energy estimated from the H–H function for InF is 8.571 ± 0.256 KJ/mol. This value is in excellent agreement with Gaydon's [13] value 8.571 ± 0.240 KJ/mol and also with Huber and Herzberg's [14] value 8.411 KJ/mol. The value of D_e from the curve fitting method for TlF is 7.209 ± 0.641 KJ/mol, which is in fair agreement with Barrow's [3] mentioned value 7.609 KJ/mol. These estimated D_e values are significant because these D_e values are evaluated by using the true potential energy curves based on experimental data. The estimated energy values from Rao and Reddy's method [6] are also presented in Table I.

Table I
Results of potential energy calculations for the ground states of GaF, InF and TlF

Molecule	Lakshman and Rao's method r [nm]	U [10^{-16} KJ/mol]	H-H function [10^{-16} KJ/mol]	Rao and Reddy's method [10^{-16} KJ/mol]
GaF ($D_e = 9.772 \pm 0.288$ KJ/mol)	0.1718	0.060	0.060	0.062
	0.1655	0.304	0.309	0.309
	0.1621	0.543	0.546	0.546
	0.1596	0.775	0.775	0.777
	0.1576	0.994	0.999	0.998
	0.1889	0.184	0.181	0.177
	0.1961	0.424	0.424	0.424
	0.2018	0.660	0.663	0.661
	0.2068	0.890	0.895	0.893
Average percentage deviation			0.026	
InF ($D_e = 8.571 \pm 0.256$ KJ/mol)	0.1925	0.052	0.054	0.052
	0.1861	0.262	0.261	0.262
	0.1825	0.467	0.467	0.467
	0.1798	0.668	0.672	0.672
	0.1777	0.865	0.866	0.869
	0.1759	1.058	1.060	1.070
	0.2102	0.157	0.155	0.155
	0.2174	0.365	0.362	0.370
	0.2232	0.568	0.567	0.562
	0.2284	0.767	0.770	0.772
0.2332	0.962	0.970	0.964	
0.2373	1.153	1.148	1.151	
Average percentage deviation			0.032	
TlF ($D_e = 7.209 \pm 0.641$ KJ/mol)	0.2023	0.046	0.046	0.062
	0.1956	0.233	0.249	0.238
	0.1920	0.416	0.416	0.418
	0.1896	0.595	0.628	0.571
	0.2205	0.140	0.140	0.139
	0.2278	0.325	0.330	0.323
	0.2337	0.507	0.509	0.506
0.2373	0.595	0.570	0.629	
Average percentage deviation			0.093	

It is evident from Table I that the modified H-H function also yields satisfactory results but the average error by this function is slightly greater than the original H-H function.

Employing the Hulbert-Hirschfelder function, the ground state dissociation energy of the GaF molecule is estimated as $49.200 \cdot 7 \text{ cm}^{-1}$ (9.772 KJ/mol). Using this value of D_e , the D_e value of GaF^+ (2.403 KJ/mol) and the ionization potential of

gallium as taken from Gaydon [13], the first ionization potential of GaF is evaluated

$$I(\text{GaF}) = I(\text{Ga}) + D_e(\text{GaF}) - D_e(\text{GaF}^+) = \\ = 9.596 + 9.772 - 2.403 = 16.966 \text{ KJ/mol},$$

which is in excellent agreement with the value 16.982 KJ/mol given by Gaydon [10]. Employing the same relation taking all the values from Gaydon [10] except the estimated D_e values for InF and TlF molecules, the ionization potentials for InF and TlF are estimated as 16.950 KJ/mol and 16.037 KJ/mol, respectively. The estimated ionization potential for InF 16.950 KJ/mol is comparable with the value 15.380 ± 0.801 KJ/mol given by Murad et al [15]. The evaluated ionization potential for the TlF molecule is 16.037 KJ/mol, which is less than the value 16.854 KJ/mol by Huber and Herzberg [14].

Acknowledgements

The authors thank Prof. S. V. J. Lakshman for encouragement. One of us (RRR) thanks the CSIR and Dr. C. S. Reddy and the authorities of KSRM College of Engineering, Cuddapah, for providing the necessary facilities.

References

1. G. R. Somayajulu, *J. Chem. Phys.*, **33**, 1541, 1960.
2. S. N. Thakur, R. B. Singh and D. K. Rai, *J. Sci. and Ind. Res.*, **27**, 339, 1968.
3. R. F. Barrow, *Trans. Farad. Soc.*, **56**, 952, 1960.
4. J. Singh, K. P. R. Nair and D. K. Rai *J. Mol. Struct.*, **6**, 328, 1970.
5. D. Steele, E. R. Lippincott and J. T. Vanderslice, *Rev. Mod. Phys.*, **34**, 239, 1962.
6. T. V. Ramakrishna Rao and R. Ramakrishna Reddy, *JQSRT*, **25**, 295, 1981.
7. Mizushima Masataka, *Rotating Diatomic Molecules*, John Wiley, New York, 1975.
8. H. M. Hulburt and J. O. Hirschfelder, *J. Chem. Phys.*, **9**, 61, 1941.
9. R. R. Reddy and T. V. R. Rao, *J. Mol. Struct.*, (Theor. Chem.), **90**, 49, 1982.
10. R. R. Reddy and T. V. R. Rao, *Acta Phys. Pol.* **64A**, 309, 1983.
11. T. V. R. Rao, R. R. Reddy and A. Subbarami Reddy, *J. Mol. Struct.*, (Theor. Chem.), **105**, 249, 1983.
12. S. V. J. Lakshman and T. V. Ramakrishna Rao, *J. Phys.*, **B 4**, 269, 1971.
13. A. G. Gaydon, *Dissociation Energies*, Chapman and Hall, London, 1968.
14. K. P. Huber and G. Herzberg, *Molecular Spectra and Molecular Structure*, Vol. IV, Constants of Diatomic Molecules, Van Nostrand Reinhold, New York, 1979.
15. E. Murad, D. L. Hildenbrand and R. P. Main, *J. Chem. Phys.*, **45**, 263, 1966.

SPHERICAL FUNCTIONS OF THE LORENTZ GROUP ON THE HYPERBOLOIDS

M. HUSZÁR

Central Research Institute for Physics
1525 Budapest, Hungary

(Received 31 January 1984)

By means of suitable coordinate systems spherical functions of the Lorentz group are derived on the double-sheeted, single-sheeted hyperboloids and similarly on the light cone. These form complete orthonormal sets of functions on each hyperboloid as well as on the light cone and transform according to the principal series of unitary representations of the Lorentz group. The spherical functions are given in a basis defined by the two-dimensional momentum $(N_1 + M_2, N_2 - M_1)$ of horospheric translations where \mathbf{N} and \mathbf{M} denote the generators of Lorentz transformations and spatial rotations. It is known that the upper sheet of the double-sheeted hyperboloid is a homogeneous space even under the subgroup $\begin{pmatrix} \alpha & \beta \\ 0 & \alpha^{-1} \end{pmatrix} \in \text{SL}(2, \mathbb{C})$. As a consequence of this the spherical functions have rather simple transformation properties under the Lorentz group.

It was shown a long time ago that matrices of unitary representations of the Lorentz group in horospheric basis take a form simpler than in any other basis provided a suitable parametrization of the group is chosen [1]. The horospheric basis is defined by the eigenvalues of the generators $P_1 = N_1 + M_2, P_2 = N_2 - M_1$, where $\mathbf{M} = (M_1, M_2, M_3)$ and $\mathbf{N} = (N_1, N_2, N_3)$ denote the generators of spatial rotations and boosts, respectively. These are infinitesimal generators of the horospheric subgroup $\begin{pmatrix} 1 & \beta \\ 0 & 1 \end{pmatrix} \in \text{SL}(2, \mathbb{C})$ isomorphic to the Euclidean translation group in two dimensions. Quantities P_1, P_2 are the momenta corresponding to the horospheric translations. Physical meaning of the momenta defined so is that $P_1/p^-, P_2/p^-$ (with the ordinary momentum $p^- = p^0 - p^3$) can be interpreted as the components of the impact parameter [1].

In [1] a suitable parametrization of the $\text{SL}(2, \mathbb{C})$ group has been defined. As mentioned there the $\gamma = 0$ plane is a singular surface of the parametrization of $\begin{pmatrix} \alpha & \beta \\ \gamma & \delta \end{pmatrix} \in \text{SL}(2, \mathbb{C})$ provided the above parametrization is used. The matrices $\begin{pmatrix} \alpha & \beta \\ 0 & \alpha^{-1} \end{pmatrix}$ can be achieved only by a limit process. Note that most global parametrizations of Lie groups have such a singular surface which, however, does not raise difficulties due to its lower dimensionality, i.e. zero measure.

A further property of the above subgroup is that on certain conditions the Lorentz group contracts into this when boosted to a frame moving with the velocity of light.

In what follows the subgroup $\begin{pmatrix} \alpha & \beta \\ 0 & \alpha^{-1} \end{pmatrix}$ is considered for real $\alpha > 0$ values and it is shown that just this subgroup, singular for the $SL(2, C)$ representations, is of some importance for spherical functions on the hyperboloids. It is known that the hyperboloid H_+^1 ($(p^0)^2 - (p^1)^2 - (p^2)^2 - (p^3)^2 = m^2 > 0, p^0 > 0$) is a space homogeneous not only under $SL(2, C)$ but under the subgroup $h = \begin{pmatrix} \alpha & \beta \\ 0 & \alpha^{-1} \end{pmatrix}$ too. Moreover, there is a one-to-one correspondence between h and the points of H_+^1 .

It is a consequence of this that spherical functions of the Lorentz group can be parametrized by the subgroup h , $Y_{\mathbf{P}}^\sigma(p) = Y_{\mathbf{P}}^\sigma(\alpha, \beta)$ where σ labels an irreducible representation and $\mathbf{P} = (P_1, P_2)$ is the horospheric momentum. Spherical functions transform according to irreducible representations of the Lorentz group g ,

$$T_g Y_{\mathbf{P}}^\sigma(p) = Y_{\mathbf{P}}^\sigma(g^{-1}p) = \int d^2 Q D_{\mathbf{Q}\mathbf{P}}^\sigma(g) Y_{\mathbf{Q}}^\sigma(p).$$

However, as mentioned above, to each $g \in SL(2, C)$ an $h = \begin{pmatrix} \alpha & \beta \\ 0 & \alpha^{-1} \end{pmatrix}$ can be found which has the same action on p as g , i.e. $g^{-1}p = h^{-1}p$, therefore, the matrix elements $D_{\mathbf{Q}\mathbf{P}}^\sigma(h)$ are sufficient for determining the transformation properties of spherical functions. The point is, however, that in this case the representation reduces to a δ -function which implies a rather simple transformation of the spherical function,

$$Y_{\mathbf{P}}^\sigma(h^{-1}p) = \int d^2 Q D_{\mathbf{Q}\mathbf{P}}^\sigma(h) Y_{\mathbf{Q}}^\sigma(p) = \alpha^{-2} e^{i\alpha^{-1}\mathbf{P}\beta} Y_{\alpha^{-2}\mathbf{P}}^\sigma(p)$$

with

$$h = \begin{pmatrix} \alpha & \beta \\ 0 & \alpha^{-1} \end{pmatrix}, \quad \alpha > 0, \quad \beta = \beta_1 + i\beta_2, \quad \mathbf{P}\beta = P_1\beta_1 + P_2\beta_2.$$

Actually, this is an addition theorem for spherical functions.

The aim of the present paper is to show that the horospheric basis is of some importance as the spherical functions in this basis have transformation properties simpler than in any other basis considered so far. (Spherical functions of the Lorentz group in several bases can be found in [2], however, this basis is not considered there.)

The situation is similar on the light cone but it is somewhat different on the single-sheeted hyperboloid H_- , $q^2 = -M^2 < 0$ which is not a homogeneous space under the subgroup h but rather splits into two homogeneous spaces according to whether $q^0 - q^3 > 0$ or $q^0 - q^3 < 0$. The plane $q^0 - q^3 = 0$ is a singular surface of the parametrization.

In Section 1 the simultaneous eigenvalue equations of the Casimir operator and those of horospheric momenta are solved on the hyperboloid H_+^1 . Equations for the horospheric momentum imply a two-dimensional plane wave factor common for each hyperboloid and cone. Eigenfunctions are expressed in terms of the Bessel function $K_{i\sigma}$. As a complete set of functions this was found a long time ago [3]. The spherical functions on the cone are expressed by a simple homogeneous function. The situation is somewhat more complicated on the single-sheeted hyperboloid where the Casimir

operator has both discrete and continuous spectra. For a complete set of functions on the single-sheeted hyperboloid both kinds of functions are needed. The eigenfunctions of the discrete spectrum are expressed in terms of Bessel functions of integer index and those of the continuous spectrum are expressed in terms of the Bessel functions $J_{i\sigma}$ and $J_{-i\sigma}$.

1. Spherical functions on the double-sheeted hyperboloid

Consider the hyperboloid $p^2 = p^+ p^- - p^* p = m^2 > 0$, $p^0 > 0$ with $p^+ = p^0 + p^3$, $p^- = p^0 - p^3$, $p = p^1 - ip^2$, $p^* = p^1 + ip^2$. Under $SL(2, C)$ a four-vector transforms as $\hat{p}' = g \hat{p} g^+$ with $\hat{p} = \begin{pmatrix} p^+ & p \\ p^* & p^- \end{pmatrix}$, $g \in SL(2, C)$.

A system of coordinates on the hyperboloid is obtained if we act on the momentum at rest, $(m, 0, 0, 0)$, by $h = \begin{pmatrix} \alpha & \beta \\ 0 & \alpha^{-1} \end{pmatrix}$. Write the subgroup h in the form

$$h = \begin{pmatrix} 1 & z \\ 0 & 1 \end{pmatrix} \begin{pmatrix} l^{1/2} & 0 \\ 0 & l^{-1/2} \end{pmatrix} = \begin{pmatrix} l^{1/2} & z l^{-1/2} \\ 0 & l^{-1/2} \end{pmatrix} \tag{1}$$

$(z = x - iy, -\infty < x, y < \infty, 0 < l < \infty)$

then the parametrization reads

$$\frac{p^+}{m} = l + \frac{|z|^2}{l}, \quad \frac{p^-}{m} = \frac{1}{l}, \tag{2}$$

$$\frac{p}{m} = \frac{z}{l}, \quad \frac{p^*}{m} = \frac{z^*}{l}.$$

The meaning of these parameters is that in the limit of a coordinate system moving with the velocity of light p^- is the Galilean mass [1], therefore, $l = \frac{m}{\mu}$ i.e. l is the ratio of Poincaré and Galilean masses. The parameter z is proportional to the transverse momentum, $p = \mu z$, and it can be identified with Galilean velocity.

The above parametrization has also a simple geometric meaning in the (l, x, y) space. When boosted from the rest frame ($l = 1, x = y = 0$) the particle moves along x_3 -axis until the horosphere passing through the four-momentum $p = p(l, x, y)$ is achieved. Under the subsequent horospheric transformation the particle moves along a straight line perpendicular to the l -axis till the four-momentum p .

Spherical functions satisfy the eigenvalue equation

$$(\mathbf{M}^2 - \mathbf{N}^2) Y^\sigma(l, \mathbf{z}) = -(\sigma^2 + 1) Y^\sigma(l, \mathbf{z}), \tag{3}$$

where σ is a real parameter which labels the principal series of unitary representations.

The Casimir operator can be obtained from the Laplacean

$$\frac{1}{\sqrt{-g}} \partial_\mu \sqrt{-g} g^{\mu\nu} \partial_\nu = -(\mathbf{M}^2 - \mathbf{N}^2), \quad (4)$$

where the metric tensor can be inferred from the line element

$$ds^2 = -\frac{1}{l^2} (dl^2 + dz^* dz).$$

The eigenvalue equation (3) assumes the form

$$\left(\frac{\partial^2}{\partial l^2} - \frac{1}{l} \frac{\partial}{\partial l} + 4 \frac{\partial}{\partial z} \frac{\partial}{\partial z^*} + \frac{\sigma^2 + 1}{l^2} \right) Y^\sigma(l, z) = 0. \quad (5)$$

(The other Casimir operator \mathbf{MN} is identically zero.) The horospheric basis is defined by the eigenvalue equations

$$\begin{aligned} (N_1 + M_2) Y_{\mathbf{P}}^\sigma(l, \mathbf{z}) &= P_1 Y_{\mathbf{P}}^\sigma(l, \mathbf{z}), \\ (N_2 - M_1) Y_{\mathbf{P}}^\sigma(l, \mathbf{z}) &= P_2 Y_{\mathbf{P}}^\sigma(l, \mathbf{z}). \end{aligned} \quad (6)$$

In terms of the parameters (2) these equations can be written as

$$\begin{aligned} i \frac{\partial}{\partial x} Y_{\mathbf{P}}^\sigma(l, \mathbf{z}) &= P_1 Y_{\mathbf{P}}^\sigma(l, \mathbf{z}), \\ i \frac{\partial}{\partial y} Y_{\mathbf{P}}^\sigma(l, \mathbf{z}) &= P_2 Y_{\mathbf{P}}^\sigma(l, \mathbf{z}). \end{aligned} \quad (7)$$

Therefore, the dependence of eigenfunctions on $z = x - iy$ is simply a plane wave factor

$$Y_{\mathbf{P}}^\sigma(l, \mathbf{z}) = \frac{1}{2\pi} e^{-i\mathbf{P}\mathbf{z}} k_{\mathbf{P}}^\sigma(l) \quad (\mathbf{P}\mathbf{z} = xP_1 + yP_2, \quad \mathbf{z} = (x, y)). \quad (8)$$

To solve Eq. (5) let $k_{\mathbf{P}}^\sigma(l) = lK$, $\xi = Pl$ with $P = \sqrt{(P_1)^2 + (P_2)^2}$. Then (5) reduces to

$$\frac{d^2 K}{d\xi^2} + \frac{1}{\xi} \frac{dK}{d\xi} + \left(\frac{\sigma^2}{\xi^2} - 1 \right) K = 0. \quad (9)$$

Two linearly independent solutions of this are $K = I_{\pm i\sigma}(\xi)$, the modified Bessel functions (cf. 7.2.2 (12) of [3]). Since for large ξ these functions behave like $I_{\pm i\sigma} \sim \frac{1}{\sqrt{2\pi\xi}} e^\xi$ the proper linear combination is the third kind modified Bessel function,

$$K_{i\sigma}(\xi) = \frac{i\pi}{2 \operatorname{sh} \pi\sigma} [I_{i\sigma}(\xi) - I_{-i\sigma}(\xi)]. \quad (10)$$

The suitable normalization factor can be derived by several alternative methods, namely, either by direct integration or by the standard method known from the theory of Hermitean differential operators, or by horospheric transformation [4]. The

advantage of the latter one is that the problem of normalization can be circumvented since the inversion formula along with an expansion can be obtained by its use.

By either of these methods the $k_{\mathbf{P}}^{\sigma}(l)$ functions take the form

$$k_{\mathbf{P}}^{\sigma}(l) = \frac{2}{\pi} \sqrt{\frac{\text{sh } \pi \sigma}{\sigma}} l K_{i\sigma}(Pl) \quad (P = \sqrt{(P_1)^2 + (P_2)^2}). \tag{11}$$

With this the spherical functions can be written as

$$Y_{\mathbf{P}}^{\sigma}(l, \mathbf{z}) = \frac{1}{2\pi} e^{-i\mathbf{P}\mathbf{z}} k_{\mathbf{P}}^{\sigma}(l).$$

These are normalized according to

$$\int d\tau_p Y_{\mathbf{P}'}^{\sigma'}(l, \mathbf{z})^* Y_{\mathbf{P}}^{\sigma}(l, \mathbf{z}) = \delta^2(\mathbf{P}' - \mathbf{P}) \frac{1}{\sigma^2} [\delta(\sigma' - \sigma) + \delta(\sigma' + \sigma)], \tag{12}$$

where $d\tau_p$ is the invariant volume element

$$d\tau_p = \frac{du^1 du^2 du^-}{2u^-} = d^2z \frac{dl}{2l^3} = dx dy \frac{dl}{2l^3}$$

with $u^{\mu} = p^{\mu}/m$, the four-velocity. The range of the parameters is $-\infty < x, y < \infty$, $0 < l < \infty$.

Representations labelled by σ and $-\sigma$ are unitary equivalent, the present spherical functions are invariant under the change of the sign of σ ,

$$Y_{\mathbf{P}}^{-\sigma}(l, \mathbf{z}) = Y_{\mathbf{P}}^{\sigma}(l, \mathbf{z}), \tag{13}$$

therefore, it is sufficient to restrict σ to positive values, $0 \leq \sigma < \infty$. Then, in the normalization integral the $\delta(\sigma' + \sigma)$ term can be omitted.

A square integrable function on the hyperboloid can be expanded in terms of spherical functions

$$F(l, \mathbf{z}) = \int_0^{\infty} \sigma^2 d\sigma \int_{-\infty}^{\infty} d^2\mathbf{P} c^{\sigma}(\mathbf{P}) Y_{\mathbf{P}}^{\sigma}(l, \mathbf{z}). \tag{14}$$

The inversion formula is

$$c^{\sigma}(\mathbf{P}) = \int_0^{\infty} \frac{dl}{2l^3} \int_{-\infty}^{\infty} d^2\mathbf{z} F(l, \mathbf{z}) Y_{\mathbf{P}}^{\sigma}(l, \mathbf{z})^*. \tag{15}$$

2. Spherical functions on the cone

A parametrization, analogous to (2), on the upper half of the cone $k^2=0$ is

$$k^+ = \frac{|z|^2}{l}, \quad k^- = \frac{1}{l}, \quad k = \frac{z}{l}, \quad k^* = \frac{z^*}{l}, \quad (16)$$

$$(z = x - iy, \quad -\infty < x, y < \infty, \quad 0 < l < \infty).$$

The spherical functions satisfy again Eq. (3) which takes the form now:

$$\left[\left(l \frac{\partial}{\partial l} \right)^2 - 2l \frac{\partial}{\partial l} + \sigma^2 + 1 \right] y^\sigma(k) = 0. \quad (17)$$

The eigenvalue equations for the horospheric momenta are the same as on the hyperboloid, therefore, the z -dependence is contained again by a plane wave factor. The solution is

$$y_P^\sigma(l, z) = \frac{P^{-i\sigma}}{i\sigma\sqrt{\pi}} l^{1-i\sigma} \frac{1}{2\pi} e^{-iPz}, \quad (18)$$

$$(-\infty < \sigma < \infty, \quad P = \sqrt{(P_1)^2 + (P_2)^2}).$$

These form a complete orthonormal set on the upper cone,

$$\int_0^\infty \frac{dl}{2l^3} \int_{-\infty}^\infty d^2z y_{P'}^{\sigma'}(l, z)^* y_P^\sigma(l, z) = \frac{1}{\sigma^2} \delta(\sigma' - \sigma) \delta^2(\mathbf{P}' - \mathbf{P}). \quad (19)$$

Expansion of a square integrable function on the cone in terms of $y_P^\sigma(l, z)$ is the same as given by Eqs (14) and (15). By the aid of these functions the matrix elements of unitary representations of the subgroup $h = \begin{pmatrix} \alpha & \beta \\ 0 & \alpha^{-1} \end{pmatrix}$ are obtained easily. For this let l, z be the coordinates of a lightlike vector k^μ as given by (16) and parametrize the subgroup h as

$$h = \begin{pmatrix} \alpha & \beta \\ 0 & \alpha^{-1} \end{pmatrix} = \begin{pmatrix} L^{1/2} & ZL^{-1/2} \\ 0 & L^{-1/2} \end{pmatrix}, \quad (20)$$

$$(0 < L < \infty, \quad Z = X - iY, \quad -\infty < X, Y < \infty).$$

Then the coordinates of the transformed vector $k' = h^{-1}k$ are simply

$$l' = \frac{l}{L}, \quad z' = \frac{z - Z}{L}. \quad (21)$$

From this the matrix elements of h can be written as

$$\langle \mathbf{Q} | T_h | \mathbf{P} \rangle = \int d\tau_k y_{\mathbf{Q}}^{\sigma'}(k) * y_{\mathbf{P}}^{\sigma}(h^{-1}k) = \frac{1}{\sigma^2} \delta(\sigma' - \sigma) \delta^2 \left(\mathbf{Q} - \frac{\mathbf{P}}{L} \right) L^{-1} e^{i \frac{\mathbf{PZ}}{L}} \quad (22)$$

with the measure $d\tau_k$ given by (19).

We mention that this simple form of representations can also be obtained from the integral representation for the matrix elements given in [1].

3. Transformation of spherical functions

A vector p on the hyperboloid can be transformed to any other vector on H^{\uparrow}_+ , $p' = g^{-1}p$ with some $g \in \text{SL}(2, \mathbb{C})$. As, however, H^{\uparrow}_+ is a homogeneous space even under h too, there exists an $h = h(p, g)$ which transforms p to p' as well as $g, p' = h^{-1}p$. This h can be given easily. Consider for this

$$h_p = \begin{pmatrix} 1 & p \\ \sqrt{p^-} & \sqrt{p^-} \\ 0 & \sqrt{p^-} \end{pmatrix} \in \text{SL}(2, \mathbb{C}), \quad (p = p^1 - ip^2, p^- = p^0 - p^3)$$

which transforms the vector p at rest $(m, 0, 0, 0)$ to p . Then $h_p \cdot h_p^{-1}$ transforms p to p' , i.e. $p' = h_p \cdot h_p^{-1} p = (h_p h_p^{-1}) p = h^{-1} p$ with

$$h^{-1} = \begin{pmatrix} \sqrt{\frac{p^-}{p'^-}} & \frac{p' - p}{\sqrt{p^- p'^-}} \\ 0 & \sqrt{\frac{p^-}{p'^-}} \end{pmatrix}.$$

Therefore, spherical functions (11) transform under $\text{SL}(2, \mathbb{C})$ as

$$\begin{aligned} T_g Y_{\mathbf{P}}^{\sigma}(p) &= Y_{\mathbf{P}}^{\sigma}(g^{-1}p) = Y_{\mathbf{P}}^{\sigma}(h^{-1}p) = \\ &= \int \sigma'^2 d\sigma' d^2\mathbf{Q} \langle \mathbf{Q} | T_h | \mathbf{P} \rangle Y_{\mathbf{Q}}^{\sigma'}(p) = \frac{1}{L} e^{i \frac{\mathbf{PZ}}{L}} Y_{\frac{\mathbf{P}}{L}}^{\sigma}(p), \end{aligned} \quad (23)$$

$$(g \in \text{SL}(2, \mathbb{C}); \quad h = \begin{pmatrix} 1 & ZL^{-\frac{1}{2}} \\ 0 & L^{-\frac{1}{2}} \end{pmatrix},$$

where the simple form of the matrix elements of T_h as given by (22) has been used.

Denote the coordinates of p by (l, \mathbf{z}) , and $1/L$ by μ ($\mu > 0$) then the transformation rule (23) assumes the form

$$Y_{\mathbf{P}}^{\sigma}(\mu l, \mu(\mathbf{z} - \mathbf{Z})) = \mu e^{i\mu\mathbf{PZ}} Y_{\mu\mathbf{P}}^{\sigma}(l, \mathbf{z}), \quad (24)$$

or alternatively,

$$Y_{\mathbf{P}}^{\sigma}(l', \mathbf{z}') = \frac{l'}{l} e^{-i\mathbf{P}(z' - \frac{l'}{l}z)} Y_{\frac{l'}{l}\mathbf{P}}^{\sigma}(l, \mathbf{z}), \quad (25)$$

where (l', \mathbf{z}') and (l, \mathbf{z}) are the coordinates of two arbitrary four-vectors on the same H_{-}^{\dagger} hyperboloid.

In particular, $Y_{\mathbf{P}}^{\sigma}$ possesses the dilatation property

$$Y_{\mathbf{P}}^{\sigma}(\mu l, \mu \mathbf{z}) = \mu Y_{\mu \mathbf{P}}^{\sigma}(l, \mathbf{z})$$

with any $\mu > 0$ and the translation property

$$Y_{\mathbf{P}}^{\sigma}(l, \mathbf{z} - \mathbf{Z}) = e^{i\mathbf{P}\mathbf{Z}} Y_{\mathbf{P}}^{\sigma}(l, \mathbf{z}).$$

4. Spherical functions on the single-sheeted hyperboloid

Act by the subgroup h as given by (1) on the point $(0, 0, 0, M)$ of the hyperboloid H_{-} ($q^2 = -M^2 < 0$). Then h covers only the half $q^0 - q^3 > 0$ of the hyperboloid. The parametrization of the other half is obtained by acting on $(0, 0, 0, -M)$ with h . The parametrization of the two halves are related by the transformation $q^{\mu} \rightarrow -q^{\mu}$, therefore, the parametrization of the total hyperboloid H_{-} can be written as

$$\frac{q^{+}}{M} = -l + \frac{|z|^2}{l}, \quad \frac{q^{-}}{M} = \frac{1}{l}, \quad \frac{q}{M} = \frac{z}{l}, \quad \frac{q^{*}}{M} = \frac{z^{*}}{l} \quad (26)$$

$$(q^{\pm} = q^0 \pm q^3, \quad q = q^1 - iq^2),$$

where l ranges now from $-\infty$ to ∞ . As, however, $h = \begin{pmatrix} \alpha & \beta \\ 0 & \alpha^{-1} \end{pmatrix}$ cannot change the sign of l , H_{-} is not a homogeneous space under h because the points $q^{-} > 0$ and $q^{-} < 0$ cannot be connected by such transformations. Nevertheless, H_{-} is a homogeneous space under the total $SL(2, \mathbb{C})$, namely, any two points on H_{-} can be transformed into each other by the subsequent action of inversion $\begin{pmatrix} 0 & 1 \\ -1 & 0 \end{pmatrix} \in SL(2, \mathbb{C})$ and $h = \begin{pmatrix} \alpha & \beta \\ 0 & \alpha^{-1} \end{pmatrix}$ (cf. [4] p. 159).

The Casimir operators have the eigenvalues $\mathbf{M}^2 - \mathbf{N}^2 \rightarrow j_0^2 - \sigma^2 - 1$, $\mathbf{M}\mathbf{N} \rightarrow j_0\sigma$. The pseudoscalar Casimir operator $\mathbf{M}\mathbf{N}$ is identically zero as earlier and for its eigenvalues $j_0\sigma = 0$ must hold. For the hyperboloid H_{-}^{\dagger} , $j_0 = 0$ and σ is continuous. In the present case both discrete ($|j_0| = 1, 2, 3, \dots; \sigma = 0$) and continuous spectra ($j_0 = 0, \sigma$ is continuous) of the eigenvalue equation of $\mathbf{M}^2 - \mathbf{N}^2$ are realized [4].

The spherical functions on the single-sheeted hyperboloid satisfy the differential equation

$$(l^2 \frac{\partial^2}{\partial l^2} - l \frac{\partial}{\partial l} - 4l^2 \frac{\partial}{\partial z} \frac{\partial}{\partial z^*} + \sigma^2 + 1 - j_0^2) Y(l, \mathbf{z}) = 0. \tag{27}$$

Discrete spectrum

Substitute in Eq. (27) $\sigma = 0$ and solve the equation. The spherical functions thus obtained take the form

$$Y_{\mathbf{P}}^{j_0}(l, \mathbf{z}) = \frac{1}{2\pi} e^{-i\mathbf{P}\mathbf{z}} j_{\mathbf{P}}^{j_0}(l), \tag{28}$$

with

$$j_{\mathbf{P}}^{j_0}(l) = i^{j_0} \sqrt{\frac{2}{|n|}} |l| J_n(Pl), \tag{29}$$

where $n = j_0 = \pm 1, \pm 2, \dots$; $P = \sqrt{(P_1)^2 + (P_2)^2}$; $J_n(Pl)$ is the Bessel function. These are normalized according to

$$\int_{-\infty}^{\infty} \frac{dl}{2|l|^3} \int_{-\infty}^{\infty} d^2\mathbf{z} Y_{\mathbf{P}'}^{j_0}(l, \mathbf{z})^* Y_{\mathbf{P}}^{j_0}(l, \mathbf{z}) = \frac{1}{n^2} \delta_{|n'|, |n|} \delta^2(\mathbf{P}' - \mathbf{P}) \tag{30}$$

and are symmetric with respect to the change of the sign of j_0 , i.e.

$$Y_{\mathbf{P}}^{j_0}(l, \mathbf{z}) = Y_{\mathbf{P}}^{-j_0}(l, \mathbf{z}).$$

Some further symmetries are stated in the next Section.

Continuous spectrum

Put in Eq. (27) $j_0 = 0$ and separate the two-dimensional plane wave factor as in the previous cases

$$Y_{\mathbf{P}}^{\sigma}(l, \mathbf{z}) = \frac{1}{2\pi} e^{-i\mathbf{P}\mathbf{z}} j_{\mathbf{P}}^{\sigma}(l). \tag{31}$$

Put $j_{\mathbf{P}}^{\sigma}(l) = lJ, \xi = Pl$ then for $J(\xi)$ the differential equation of the Bessel functions

$$\xi^2 \frac{d^2 J}{d\xi^2} + \xi \frac{dJ}{d\xi} + (\xi^2 + \sigma^2) J = 0. \tag{32}$$

is obtained. For $\xi > 0$ $J_{i\sigma}(\xi)$ and for $\xi < 0$ $J_{-i\sigma}(|\xi|)$ solutions are chosen. With these the

normalized solution of the differential equation (32) can be written as

$$j_{\mathbf{P}}^{\sigma}(l) = \frac{1}{\sqrt{\sigma \operatorname{sh} \pi \sigma}} |l| J_{i\sigma}(P|l|) \quad (33)$$

with $\varepsilon = \operatorname{sg} l$, $P = \sqrt{(P_1)^2 + (P_2)^2}$, $-\infty < \sigma < \infty$.

This is obtained by imposing the orthonormality relations (35) and (36). Recalling (13) the spherical functions take the form

$$\mathbf{Y}_{\mathbf{P}}^{\sigma}(l, \mathbf{z}) = \frac{1}{2\pi} e^{-i\mathbf{P}\mathbf{z}} j_{\mathbf{P}}^{\sigma}(l). \quad (34)$$

These are normalized according to

$$\begin{aligned} \int_{-\infty}^{\infty} \frac{dl}{2|l|^3} \int_{-\infty}^{\infty} d^2\mathbf{z} \mathbf{Y}_{\mathbf{P}'}^{\sigma'}(l, \mathbf{z})^* \mathbf{Y}_{\mathbf{P}}^{\sigma}(l, \mathbf{z}) &= \\ &= \frac{1}{\sigma^2} \delta(\sigma' - \sigma) \delta^2(\mathbf{P}' - \mathbf{P}). \end{aligned} \quad (35)$$

It is easy to check that the eigenfunctions of the continuous and discrete spectra are orthogonal to each other,

$$\int d\tau_q \mathbf{Y}_{\mathbf{P}}^{j_0}(l, \mathbf{z})^* \mathbf{Y}_{\mathbf{P}}^{\sigma}(l, \mathbf{z}) = 0, \quad (36)$$

where the volume element is given by Eq. (35).

For the expansion of a square integrable function $F(l, \mathbf{z})$ on H_- both the eigenfunctions of the continuous and discrete spectra are needed,

$$F(l, \mathbf{z}) = \int_{-\infty}^{\infty} \sigma^2 d\sigma \int_{-\infty}^{\infty} d^2\mathbf{P} a^{\sigma}(\mathbf{P}) \mathbf{Y}_{\mathbf{P}}^{\sigma}(l, \mathbf{z}) + \sum_{j_0=1}^{\infty} j_0^2 \int_{-\infty}^{\infty} d^2\mathbf{P} b^{j_0}(\mathbf{P}) \mathbf{Y}_{\mathbf{P}}^{j_0}(l, \mathbf{z}). \quad (37)$$

The inversion formula reads

$$a^{\sigma}(\mathbf{P}) = \int d\tau_q F(l, \mathbf{z}) \mathbf{Y}_{\mathbf{P}}^{\sigma}(l, \mathbf{z})^*, \quad (38)$$

$$b^{j_0}(\mathbf{P}) = \int d\tau_q F(l, \mathbf{z}) \mathbf{Y}_{\mathbf{P}}^{j_0}(l, \mathbf{z})^*.$$

Acting by the subgroup $\begin{pmatrix} \alpha & \beta \\ 0 & \alpha^{-1} \end{pmatrix}$ on $\mathbf{Y}_{\mathbf{P}}^{\sigma}(l, \mathbf{z})$ one finds the addition theorem (24)

to hold in the present case, too:

$$\mathbf{Y}_{\mathbf{P}}^{\sigma}(\mu l, \mu(\mathbf{z} - \mathbf{Z})) = \mu e^{i\mu\mathbf{P}\mathbf{Z}} \mathbf{Y}_{\mu\mathbf{P}}^{\sigma}(l, \mathbf{z}) \quad (\mu > 0)$$

and the same relation for $\mathbf{Y}_{\mathbf{P}}^{j_0}$ of the discrete spectrum. Nevertheless, the subgroup $\begin{pmatrix} \alpha & \beta \\ 0 & \alpha^{-1} \end{pmatrix}$ now does not cover the entire single-sheeted hyperboloid. For this the

inversion $\begin{pmatrix} 0 & 1 \\ -1 & 0 \end{pmatrix} \in \text{SL}(2, \mathbb{C})$ is needed in addition, as mentioned before. Under the action of this element the transformation of spherical functions is not so simple as they transform according to unitary irreducible representations given in [1].

A symmetry property of $Y_{\mathbf{p}}^{\sigma}(l, \mathbf{z})$ is

$$Y_{\mathbf{p}}^{-\sigma}(-l, \mathbf{z}) = Y_{\mathbf{p}}^{\sigma}(l, \mathbf{z}). \quad (39)$$

Another symmetry related to space-time reflection assumes the form

$$Y_{\mathbf{p}}^{\sigma}(-l, \mathbf{z})^* = Y_{-\mathbf{p}}^{\sigma}(l, \mathbf{z}). \quad (40)$$

This relation holds also for $Y_{\mathbf{p}}^{j_0}$.

Finally, it is worth mentioning that the treatment given here is not rigorous in the mathematical sense. It is well known that when continuous basis is used some difficulties arise which are partly the same as those in field theory when plane wave expansion is applied. In a more rigorous treatment the spherical functions given here should be considered as distributions on some infinitely differentiable function space rather than functions in the ordinary sense. This point has been indicated in [1].

References

1. M. Huszár, *J. Math. Phys.*, *14*, 1620, 1973; *Nuovo Cim.*, *31A*, 237, 1976.
2. N. Y. Vilenkin and Y. A. Smorodinsky, *JETP*, *19*, 1209, 1964; N. Y. Vilenkin and L. M. Klesova, *Yad. Fiz.*, *31*, 204, 1980.
3. H. Bateman and A. Erdélyi, *Higher Transcendental Functions*, McGraw-Hill, New York, 1953, Vol. 2, 7. 10. 5 (75).
4. I. M. Gelfand, M. I. Graev and N. Y. Vilenkin, *Generalized Functions*, Vol. 5. Academic Press, New York, 1966.

DOES NEWTON'S WORLD MODEL REVIVE?

A. MÉSZÁROS

*Central Research Institute for Physics
1525 Budapest, Hungary**

(Received 6 March 1984)

Newton's world model may have a physical meaning if the graviton has small non-zero mass and if the observable part of the Universe is the interior of a giant finite body. Both possibilities are in principle allowed.

The oldest and simplest model of the complete physical world is Newton's: the whole Universe is a static, homogeneous and isotropic four-dimensional manifold with the same global and topological properties as Minkowskian space, and the mean matter density is non-zero. (As a matter of fact some ideas relating to such a model had already been formulated by Giordano Bruno.) However, it is well-known that this model conflicts with Newton's and with Einstein's theory of gravitation.

In this paper we show that Newton's world model may have a physical meaning if the graviton has a small non-zero mass m (thus the gravitation here essentially differs from Einstein's gravitation on the scales $\gtrsim 1/m$; $\hbar = c = 1$) and if the observable part of the Universe is the interior of a finite "island". The first possibility cannot be excluded, while the second one even seems to be probable. Thus both possibilities are in principle allowed.

At present, even though it is widely assumed that the complete physical world is described by a Friedmannian model, this model cannot be verified — even in principle — by observations, because the regions beyond the particle horizon are not observable. Therefore extrapolation of the properties of the observable part of the Universe beyond the present particle horizon is questionable. Nevertheless, it is not necessary that this extrapolation be valid. It is not prohibited that there is an edge to matter that will be seen in some future era [1]. Some cosmological considerations even suggest this possibility [2, 3]. If there were an edge beyond the particle horizon, then the observable region could be the interior of a giant body ("island") of size r . This hypothetical body in [3] is known as the M -galaxy. Obviously, r would need to be much bigger than the present Hubble radius.

* Permanent address: Department of Astronomy and Astrophysics, Charles University, 15000 Prague-5, Švédská 8, ČSSR

Here we a priori assume the existence of this island. This then gives rise to the question: What about the exterior of the M -galaxy? Of course, at present this question still seems to be an academic one though its study is not completely without meaning. Any considerations about the complete Universe may be of use with regard to our view of Nature.

The simplest possibility seems to be the following: there is a vacuum in the exterior of the M -galaxy and the space-time is asymptotically flat. Unfortunately, this model is not satisfactory because it conflicts with Mach's principle. (A particle escaping from the M -galaxy would move into flat space, arbitrarily far from all matter, yet its inertial properties would not change, contrary to the idea that inertia is generated by the matter in the Universe; see [4], p. 12.) In view of this, we have to assume the existence of other islands. The characteristic distance between any two islands should be $s \gg r$. The most natural possibility is then obvious: the mean density of these islands and thus of their matter is homogeneous and isotropic on the scale $p \gg s$. Can this matter be static? Obviously, it would be nice to have a static world, i.e. a world of maximum symmetry.

General relativity allows only one reasonable possibility, viz. Einstein's static model, but this no longer seems to be satisfactory since (i) it needs a given density, which leads to instabilities (see [4], p. 14); (ii) it needs a non-zero cosmological term, which conflicts with the identity of gravitation and of standard spin 2 field [5].

The situation essentially changes if the graviton has a small non-zero mass m . (This possibility is not new; see e.g. [6]. In [7] a finite quantum gravity is proposed that needs non-zero mass for the graviton. In any case $1/m$ must be much bigger than the present Hubble radius. We assume $1/m \gtrsim p$). In this case we have a remarkable possibility: Newton's model is in principle allowed.

To show this, consider a manifold that has the same global and topological properties as Minkowskian space. Introducing the unobservable flat background with the metric tensor $\eta^{ij} = \eta_{ij} \equiv \text{diag}(1, -1, -1, -1)$ we obtain the contravariant metric tensor g^{ij} :

$$g^{ij} = \eta^{ij} + f U^{ij}; \quad f = \sqrt{32\pi G}, \quad (1)$$

where U^{ij} is the potential of spin 2 field and G is the gravitational constant (for details see [5]). If the graviton has small non-zero mass m , then Einstein equations are substituted by [7]

$$\begin{aligned} (\square + m^2)U^{ij} - U^{k(i,j)}_{,k} + U^{,ij} + \eta^{ij}U^{km}_{,km} - \eta^{ij}\left(\square + \frac{m^2}{2}\right)U = \frac{f}{2}(T^{ij} + t^{ij}); \\ U \equiv U^{ij}\eta_{ij}; \quad \square \equiv \partial^i\partial_i, \end{aligned} \quad (2)$$

where t^{ij} is the energy-momentum pseudotensor of gravitation and T^{ij} is the usual energy-momentum tensor. For our purpose it is essential that $t^{ij} = 0$ holds for $U^{ij} = \text{const}$. We need to search for a solution with $U^{ij} = \text{const}$, $T^{ij} = \text{const}$. Let us assume that

$$T^{ij} = (p + \rho) V^i V^j - p g^{ij}; \quad p = \text{const.} \geq 0; \quad \rho = \text{const.} > 0; \quad p \leq \frac{\rho}{3} \quad (3)$$

holds, where $V^i \equiv [\sqrt{g^{00}}, 0, 0, 0]$ is the four-velocity, ρ is the density, p is the pressure. In this case we must have

$$m^2 \left(U^{ij} - \frac{1}{2} \eta^{ij} U \right) = \frac{f}{2} T^{ij}. \quad (4)$$

Because $U^{11} = U^{22} = U^{33}$ is fulfilled, we have

$$m^2 \left(U^{00} - \frac{1}{2} U^{00} + \frac{3}{2} U^{11} \right) = \frac{f}{2} (1 + f U^{00}) \rho; \quad U^{ij} = 0 \quad i \neq j; \quad (5)$$

$$m^2 \left(U^{11} + \frac{1}{2} U^{00} - \frac{3}{2} U^{11} \right) = \frac{f}{2} (-1 + f U^{11}) (-p);$$

and hence

$$U^{00} = \frac{f m^2 (\rho + 3p) - f^3 \rho p}{4m^4 - f^2 m^2 (\rho + p) + f^4 \rho p}; \quad (6)$$

$$U^{11} = \frac{f m^2 (\rho - p) + f^3 \rho p}{4m^4 - f^2 m^2 (\rho + p) + f^4 \rho p}.$$

Requiring the fulfilment of the physically obvious conditions $f U^{00} > -1$ and $f U^{11} < 1$, we have the restrictions

$$\rho < \frac{2m^2}{f^2} \quad (7)$$

If these restrictions hold, then in fact we have a "quasi-flat" space-time, i.e. by changing $\bar{x}_0 = \sqrt{g^{00}} x_0$ and $\bar{x}_{1,2,3} = \sqrt{-g^{11}} x_{1,2,3}$ we obtain the Minkowskian space. In other words, in this case the presence of matter changes the time and distances only, but except for this difference the space-time is in fact Minkowskian.

This space-time for very small densities seems to be stable. For this to be apparent, consider a fluctuation on the homogeneous, isotropic and time independent background. Assume that the Jeans approximation is good (see [8], Chapter 9.1). Obviously here in the Poisson equation the substitution $\Delta \rightarrow \Delta - m^2$ must be done. (In other words, Newton's potential is exchanged for Yukawa's.) Except for this difference Jeans' full theory remains unchanged. This says that everywhere the $k^2 \rightarrow k^2 + m^2$ (k is the wave vector) substitution must be done. Thus for the critical Jeans length λ_J we have

$$\frac{f^2}{8} \rho - b^2 \frac{4\pi^2}{\lambda_J^2} - b^2 m^2 = 0, \quad (8)$$

where b is the velocity of sound. If

$$\rho < \frac{8b^2 m^2}{f^2} \quad (9)$$

holds, then there is no critical Jeans length and any fluctuation always behaves like an acoustic wave.

We have arrived at the result: if the graviton has a non-zero mass, then for small densities (see (7) and (9)) a physically reasonable "quasi-flat" manifold may exist. The question posed by the title may be answered positively, i.e. Newton's model may in principle describe the whole physical Universe. Nevertheless, one has to admit that it is not certain that the whole of Nature is described by this model. Indeed, the validity of the Friedmannian model beyond the present particle horizon is questionable and, therefore, it is not necessary that in the whole of Nature the Friedmannian model be valid. On the other hand, it is also not necessary that Nature be described by Newton's model.

Acknowledgement

I would like to thank Dr. B. Lukács and Dr. Á. Sebestyén for valuable discussions.

References

1. M. J. Rees, in *Quantum Gravity 2, A Second Oxford Symp.*, Ed. C. J. Isham, R. Penrose, D. W. Sciama, Clarendon Press, 1981, p. 273.
2. R. Fabbri and F. Melchiorri, *Gen. Rel. Grav.*, *13*, 201, 1981.
3. A. Mészáros, KFKI Report 1983-68, 1983.
4. P. J. E. Peebles, *The Large-Scale Structure of the Universe*, Princeton Univ. Press, 1980.
5. W. Thirring, *Ann. Phys. (N.Y.)* *16*, 96, 1961; S. Weinberg, *Phys. Rev. B*, *138*, 988, 1965; G. Cavalleri and G. Spinelli, *Riv. Nuo. Cim.*, *3*, 1980.
6. V. I. Ogievetsky and I. V. Polubarinov, *Ann. Phys. (N.Y.)*, *35*, 165, 1965.
7. A. Mészáros, to be published.
8. Ya. B. Zeldovich and I. D. Novikov, *Stroyeniye i evoluciya vselenny, Nauka, Moscow*, 1975.

MOLECULAR PSEUDOPOTENTIAL CALCULATIONS

VII.1

EQUILIBRIUM GEOMETRIES, DISSOCIATION ENERGIES, IONIZATION ENERGIES OF THE X_3^+ ($X = \text{Li, Na, K, Rb, Cs}$) TRIATOMIC HOMONUCLEAR ALKALI METAL MOLECULAR IONS

R. GÁSPÁR and I. TAMÁSSY-LENTEI

*Institute of Theoretical Physics, Kossuth Lajos University
4010 Debrecen, Hungary*

(Received 12 March 1984)

The equilibrium geometries, internuclear distances, wave functions and energies for the X_3^+ ($X = \text{Li, Na, K, Rb, Cs}$) triatomic alkali ions, further the dissociation energies for the $X_3^+ \rightarrow X_2 + X^+$ processes and the ionization energies are determined with the pseudopotential method. The calculations were performed using the Hellmann-type analytical potential and one-centre wave functions. The results are compared with the other calculated values available.

In our previous pseudopotential calculations [1(a)], [1(b)], [1(c)], [1(d)], [1(e)], [1(f)] the equilibrium geometries, the electronic structures, the dissociation energies and ionization energies of the X_2 and XY diatomic alkali metal and XH alkali metal hydride molecules, further the X_2H^+ and X_2Y^+ heteronuclear triatomic alkali ions ($X, Y = \text{Li, Na, K, Rb, Cs}$) were investigated theoretically.

Now we intend to present similar results for the X_3^+ homonuclear triatomic alkali molecular ions having two valence electrons.

In our pseudopotential treatment we applied the analytical potential form proposed by Hellmann [2] for the alkali atoms $X = \text{Na, K, Rb, Cs}$ (and the alkali-type ions),

$$V_H = -Z/r + A \exp(-2Kr)/r, \quad (1)$$

where r is the distance from the nucleus of the alkali atoms; $Z = 1, 2, 3, \dots$ for the neutral, singly, doubly, \dots ionized atoms; A and K are parameters determined semi-empirically. Regarding the parameters we refer e.g. to [2], [1(a)], and in the case of the Li atom to [3], [1(d)].

Applying the variational method, the ground state trial wave function of the two-valence electron systems, ψ , was an analytical one-centre function composed from hydrogen-type 1s functions

$$\psi = \psi_{1s}(r_1)\psi_{1s}(r_2), \quad (2)$$

where

$$\psi_{1s}(r) = 2\alpha^{3/2} e^{-\alpha r} \quad (3)$$

and α , further the coordinates of the centre of the one-centre wave function were considered as variational parameters, so the wave function was a floating-type one. The details of the calculations can be found e.g. in [1(a)], [1(b)].

According to the variational procedure, the most stable form for the X_3^+ systems is an equilateral triangle (D_{3h} symmetry) and the centre of the floating-type wave function is in the middle of the triangle, as it can be expected for symmetry reasons. The numerical results for the ground state energies of the X_3^+ ions, E , the wave function parameters, α , the internuclear distances, R , are summarized in Table I.

An important question is the stability of the homonuclear triatomic alkali ions. The calculated data for the dissociation energies, D , regarding the processes $X_3^+ \rightarrow X_2 + X^+$, are to be found also in Table I. As one can see, all of the X_3^+ ions are stable systems, if the pseudopotential method described above is applied.

No experimental information is known for us, therefore we can compare our results with the theoretical values given in the literature.

Table I

Energy values, E ; the best parameter values of the wave functions, α ; the internuclear distances, R , in D_{3h} geometry for alkali triatomic ions X_3^+ ; and the dissociation energies, D , for the $X_3^+ \rightarrow X_2 + X^+$ processes, in atomic units together with other calculated values

X_3^+	$E(X_3^+)$	α	R	R_{calc}	D	D_{calc}
Li_3^+	-0.40179	0.37	6.0	6.18 [5]	0.0288	0.0356 [5]
				5.88 [6]		0.0657 [6]
				5.75 [8]		0.0667 [8]
				5.89 [9]		0.0647 [9]
				5.85 [10]		0.0667 [10]
				6.22 [11]		0.0543 [11]
				5.82 [12]		
				5.67 [13]		
Na_3^+	-0.41310	0.37	5.9	6.23 [7]	0.0360	0.0613 [7]
				6.72 [8]		0.0603 [8]
				6.60 [10]		0.0536 [10]
				6.60 [11]		0.0503 [11]
				6.76 [12]		
				6.54 [13]		
K_3^+	-0.35409	0.32	7.2	7.55 [7]	0.0332	0.0500 [7]
				8.84 [12]		
				8.16 [13]		
Rb_3^+	-0.32485	0.30	7.8		0.0282	
Cs_3^+	-0.30556	0.28	8.4		0.0271	

The diatomic energy values: $E(\text{Li}_2) = -0.37293$, $E(\text{Na}_2) = -0.37705$, $E(\text{K}_2) = -0.32089$, $E(\text{Rb}_2) = -0.29664$, $E(\text{Cs}_2) = -0.27843$ are taken from [4].

Pfeiffer and Ellison [5] applied the DIM (diatomics in molecules) theory for the Li_3^+ .

Ray [6] used the FSGO model for the Li_3^+ ion.

Pickup and Byers Brown [7] calculated the properties of the Na_3^+ , K_3^+ , using a simple model Hamiltonian.

Raffanetti and Ruedenberg [8] made ab initio SCF calculations for the Li_3^+ , Na_3^+ .

Gründler, Friedmann, Nguyen Huu Thong and Schimpf [9] investigated the Li_3^+ by the FSGO method.

Switalski, Huang and Schwartz [10] applied a valence-only electronic structure theory and used flexible Gaussian valence basis functions for the Li_3^+ , Na_3^+ .

Ray and Switalski [11] used a Gaussian based model potential within the FSGO formalism for the Li_3^+ , Na_3^+ .

Eades, Hendewerk, Frey and Dixon [12] performed a SCF level of approximation with contracted Gaussian basis sets for the Li_3^+ , Na_3^+ , K_3^+ .

Flad, Igel, Doly, Stoll and Preuss [13] used in valence-only SCF calculations a combination of pseudopotentials and density functionals for the Li_3^+ , Na_3^+ , K_3^+ .

Our data calculated for the internuclear distances show the same accuracies, as formerly, in the cases of other systems discussed by us. The triatomic internuclear distances are a little larger than the corresponding diatomic ones ($R(\text{Li}_2)=4.90$, $R(\text{Na}_2)=5.06$, $R(\text{K}_2)=6.20$, $R(\text{Rb}_2)=6.64$, $R(\text{Cs}_2)=7.16$).

Every X_3^+ system regarded here is stable with respect to dissociate to $X_2 + X^+$; the dissociation energies are smaller than the other calculated values available, but we can consider the agreement satisfactory.

To determine the ionization energies of the X_3^+ ions we investigated the properties of the X_3^{++} systems in a similar way. Our calculated energies, wave function parameters and internuclear distances are given in Table II.

The predicted ionization energies are reasonable, but experimental or theoretical values for comparison are not available.

The numerical calculations were carried out on the R-30 computer of the University Computer Centre.

Table II

Energy values, E ; the best parameter values of the wave functions, α ; the internuclear distances, R , for alkali triatomic ions X_3^{++} in D_{3h} geometry and the ionization energies of the X_3^+ ions, $I = E(X_3^{++}) - E(X_3^+)$; in atomic units

X_3^{++}	$E(X_3^{++})$	α	R	I
Li_3^{++}	-0.11178	0.34	9.5	0.290
Na_3^{++}	-0.11562	0.36	9.0	0.297
K_3^{++}	-0.10432	0.32	10.05	0.249
Rb_3^{++}	-0.09721	0.30	11.4	0.227
Cs_3^{++}	-0.09301	0.29	12.1	0.212

References

1. R. Gáspár and I. Tamássy-Lentei, *Acta Phys. Hung.*, **33**, 387, 1973 (a); **38**, 3, 1975 (b); **38**, 15, 1975 (c); **40**, 283, 1976 (d); **44**, 191, 1978 (e); **50**, 343, 1981 (f).
2. H. Hellmann, *Acta Physicochim. USSR*, **1**, 913, 1935; **4**, 225, 324, 1936; *J. Chem. Phys.*, **3**, 61, 1935.
3. L. Szász, *Acta Phys. Hung.*, **6**, 307, 1957.
4. R. Gáspár and I. Tamássy-Lentei, *Acta Phys. Chim. Debr.*, **XXIV/IV**, 79, 1981.
5. G. V. Pfeiffer and F. O. Ellison, *J. Chem. Phys.*, **43**, 3405, 1965.
6. N. K. Ray, *J. Chem. Phys.*, **52**, 463, 1970.
7. B. T. Pickup and W. Byers Brown, *Mol. Phys.*, **23**, 1189, 1972.
8. R. C. Raffanetti and K. Ruedenberg, *J. Chem. Phys.*, **59**, 5978, 1973.
9. W. Gründler, R. Friedemann, Nguyen Huu Thong and J. Schimpf, *Z. Anorg. allg. Chem.*, **410**, 287, 1974.
10. J. D. Switalski, J. T. J. Huang and M. E. Schwartz, *J. Chem. Phys.*, **60**, 2252, 1974.
11. N. K. Ray and J. Switalski, *Theor. Chim. Acta (Berl.)*, **41**, 329, 1976.
12. R. A. Eades, M. K. Hendewerk, R. Frey and D. A. Dixon, *J. Chem. Phys.*, **76**, 3075, 1982.
13. J. Flad, G. Igel, M. Dolg, H. Stoll and H. Preuss, *Chem. Phys.*, **75**, 331, 1983.

MOLECULAR PSEUDOPOTENTIAL CALCULATIONS

VII. 2

EQUILIBRIUM GEOMETRIES, DISSOCIATION ENERGIES, IONIZATION ENERGIES OF THE X_3^+ ($X = \text{Cu}, \text{Ag}, \text{Au}$) TRIATOMIC HOMONUCLEAR NOBLE METAL MOLECULAR IONS

R. GÁSPÁR, I. TAMÁSSY-LENTEI and Á. DERECSEKI-KOVÁCS

*Institute of Theoretical Physics, Kossuth Lajos University
4010 Debrecen, Hungary*

(Received 12 March 1984)

The equilibrium geometries, internuclear distances, wave functions and energies for the X_3^+ ($X = \text{Cu}, \text{Ag}, \text{Au}$) triatomic noble metal ions, further the dissociation energies for the $X_3^+ \rightarrow X_2 + X^+$ processes and the ionization energies are determined with the pseudopotential method. The calculations were performed using a modified Hellmann-type pseudopotential (suggested by Ladányi) and one-centre wave functions.

In the first part of this paper [1] we have determined the equilibrium geometries, the internuclear distances, the dissociation energies and ionization energies of the X_3^+ triatomic alkali metal molecular ions ($X = \text{Li}, \text{Na}, \text{K}, \text{Rb}, \text{Cs}$), applying the pseudopotential method and using Hellmann-type pseudopotential [2].

In this part of our paper we extend this investigation to the X_3^+ homonuclear triatomic noble metal molecular ions ($X = \text{Cu}, \text{Ag}, \text{Au}$). The theoretical treatment of these systems is especially interesting, because of the lack of experimental, or theoretical results.

The form of the pseudopotentials for the one-valence electron alkali metal atoms proposed by Hellmann [2] is

$$V_H = -Z/r + A \exp(-2Kr)/r, \quad (1)$$

where A and K are parameters determined semi-empirically.

For the one-valence electron noble metal atoms Ladányi [3] suggested a modified pseudopotential form

$$V_L = -Z/r + A \exp(-2Kr)/r + B \exp(-2\lambda r)/r, \quad (2)$$

where A, K, B, λ are parameters also determined semiempirically. This more flexible function is appropriate to taking into account the effect of the d electrons for the valence electron, considering the $\text{Cu}, \text{Ag}, \text{Au}$ atoms. Regarding the parameters we refer e.g. to [3], [4].

The ground state trial wave function of the two-valence electron systems, ψ , was an analytical one-centre function

$$\psi = \psi_{1s}(r_1)\psi_{1s}(r_2), \quad (3)$$

where

$$\psi_{1s}(r) = 2\alpha^{3/2}e^{-\alpha r} \quad (4)$$

and α , further the coordinates of the centre of the floating-type wave function were considered as variational parameters. Concerning the details of the calculations we refer to [1], [4].

According to the variational procedure, the most stable geometry for the X_3^+ noble metal triatomic systems is, of course, an equilateral triangle (D_{3h} symmetry) and the centre of the wave function is in the middle of this triangle, as it formerly was in the case of the alkali metal triatomic ions.

The numerical results for the ground state energies of the X_3^+ ions, E , the wave function parameters, α , and the internuclear distances, R , are summarized in Table I. The triatomic internuclear distances are a little larger than the corresponding diatomic ones ($R(\text{Cu}_2) = 3.33$, $R(\text{Ag}_2) = 3.28$, $R(\text{Au}_2) = 3.18$).

The calculations show all of the X_3^+ systems to be stable regarding the $X_3^+ \rightarrow X_2 + X^+$ processes. The calculated dissociation energies, D , are listed also in Table I.

Table I

Energy values, E ; the best parameter values of the wave functions, α ; the internuclear distances, R , for noble metal triatomic ions X_3^+ , in D_{3h} geometry and the dissociation energies, D , for the $X_3^+ \rightarrow X_2 + X^+$ processes, in atomic units

X_3^+	$E(X_3^+)$	α	R	D
Cu_3^+	-0.80900	0.57	3.7	0.135
Ag_3^+	-0.77900	0.60	3.4	0.121
Au_3^+	-1.25577	0.67	3.3	0.302

The diatomic energy values: $E(\text{Cu}_2) = -0.67335$, $E(\text{Ag}_2) = -0.65733$, $E(\text{Au}_2) = -0.95336$ are taken from [5]

Table II

Energy values, E ; the best parameter values of the wave functions, α ; the internuclear distances, R , for noble metal triatomic ions X_3^{++} , in D_{3h} geometry and the ionization energies of the X_3^+ ions, $I = E(X_3^{++}) - E(X_3^+)$, in atomic units

X_3^{++}	$E(X_3^{++})$	α	R	I
Cu_3^{++}	-0.23539	0.58	5.0	0.573
Ag_3^{++}	-0.21704	0.58	4.9	0.561
Au_3^{++}	-0.43911	0.71	4.1	0.816

Determining the energies of the X_3^{++} systems one can investigate the ionization energies, too.

The similarly calculated properties of the X_3^{++} systems, energies, wave function parameters and internuclear distances are given in Table II.

The dissociation energies, D , and ionization energies, I , predicted by this approach seem to be reasonable and adequate to our expectation, but no experimental or theoretical values are available for comparison.

References

1. R. Gáspár and I. Tamássy-Lentei, *Acta Phys. Hung.*, 58, 191, 1985.
2. H. Hellmann, *Acta Physicochim. USSR*, 1, 913, 1935; 4, 225, 324, 1936; *J. Chem. Phys.*, 3, 61, 1935.
3. K. Ladányi, *Acta Phys. Hung.*, 5, 361, 1956.
4. R. Gáspár and I. Tamássy-Lentei, *Acta Phys. Hung.*, 33, 387, 1973.
5. R. Gáspár and I. Tamássy-Lentei, *Acta Phys. Chim. Debr.*, XXIV/IV, 79, 1981.

GEOMETRICAL STRUCTURES OF TRIATOMIC AND TETRATOMIC CLUSTERS OF Li, Na, K, Cu AND Ag ATOMS

I. LÁSZLÓ

*Quantum Theory Group, Institute of Physics, Technical University
1521 Budapest, Hungary*

and

A. JULG

*Laboratoire de Chimie Théorique, Université de Provence
13331 Marseille Cedex 3, France*

(Received 13 March 1984)

The geometrical structures of trimers and tetramers of Li, Na, K, Cu and Ag atoms are studied utilizing a semiempirical SCF method. The geometry optimization and the examination of the stability of the clusters have been carried out by a simple method without calculation of the total energy and the results are compared to previous results for Li, Na, K and Cu clusters. The analytical solutions of the secular equations of the examined structures are presented.

1. Introduction

In the last years, rapidly increasing attention has been paid to the investigation of metal clusters. Matrix isolation [1] and molecular beam [2] techniques provide experimental data of small aggregates of metal atoms. Numerous theoretical calculations have been previously reported, local-spin-density (LSD) pseudopotential method [8], CI [9, 10, 15], CNDO/BW [7], LEPS-fit [10], multireference-double-excitation configuration interaction method (MRD-CI) [12], or the same with pseudopotential (PP-MRD-CI) [18], coupled-electron-pair-approximation (CEPA) [12], SCF ab initio methods [11, 13, 14] and SCF with density functional approximation for electronic correlation (SCF-DF) [17]. The predictions regarding the geometrical structure differ significantly from one paper to the other, however, certain trends can be stated. The authors underline the importance of correlation effects and neglecting the correlation in the ab initio SCF methods leads to incorrect results both for the alkali metals [18] and for the Cu clusters [23]. Unfortunately, the consideration of the correlation effects is extremely difficult to carry out, especially for the clusters of a larger number of electrons.

The aim of this article is to demonstrate that a method can be found that is not more complicated than the simple Hückel method, and for all that, it can give good

geometrical structures for the clusters of Li, Na, K, Cu and Ag atoms. In our previous paper [3] we have proposed a semiempirical SCF method applicable to large size metallic aggregates. The previous theoretical descriptions of this method can be found in [4-6]. In the present paper we use the parametrization of [3] and we show that this method is capable of making a comparison between the stabilities of different structures without the calculation of the total energy. To put it more simply we give the analytical solutions of the secular equations of the triatomic and tetratomic structures. We also think that we can indicate some problems that can be clarified with the aid of sophisticated methods. We show for example that the structure of a parallelogram can be more stable than the structure of rhombus. There is no systematic investigation in the literature concerning this problem.

We give a short description of the notation of our method [3] in Section 2. We discuss the triatomic structures in Sections 3 and 4. Tetratomic clusters are studied in Sections 5 and 6. In the first 6 Sections we examine the Li structures only, and in Section 7 we give our results for the structures of Li, Na, K, Cu and Ag atomic clusters and make a comparison with other calculations.

2. Notations

The Hamiltonian matrix L described in our previous paper [3] has the following form

$$L_{pp} = \alpha_p, \quad (1)$$

$$L_{pq} = K f_{pq}(r) - \frac{1}{2} l_{pq}(pp|qq) = \beta_{pq}, \quad (2/a)$$

$$f_{pq}(r) = \left(1 + \rho + \frac{\rho^2}{3} \right) e^{-\rho}, \quad (2/b)$$

$$(pp|qq) = \frac{27.2}{1.26R + r_{pq}(\text{a. u.})}, \quad (2/c)$$

where $\rho = \frac{r}{R} 3.12$, (for R see Eq. (4)), and K is a parameter characteristic of the particular species under study. In the present paper we have used $KR = -7.74$.

$$l_{pq} = \sum_i n_i C_{ip} C_{iq} \quad (3)$$

is the bond order. In the ground states under consideration the n_i values are 0 or 2 depending on whether the i -th orbital is empty or occupied. When the number of electrons is odd and the highest occupied level is not degenerate, $n_i = 1$ for this level. When the highest occupied level is degenerate, the occupation numbers of the

degenerate MOs in the ground state are fractional values to obtain a cluster of neutral charge. For the nearest neighbours we have used a relation between the bond-order and the equilibrium distance:

$$r_{pq} = R \frac{1 + 3.41 l_{pq}}{1 + 5.65 l_{pq}}, \quad (4)$$

where R is a parameter characteristic of the particular species under study. $R = 0.4$ nm, $= 0.48$ nm; $= 0.595$ nm; $= 0.33$ nm; $= 0.37$ nm for the metals Li; Na; K; Cu and Ag, respectively. We have used our method for the determination of the geometrical structures of the clusters of the metals mentioned before. The computational procedure is as follows. From a starting set of distances the matrix L is computed according to Eqs (1) and (2/a-2/c) and it is used to determine the eigenvectors which correspond to the solution for the given geometry. Then the distances are changed according to Eq. (4), so that from the l_{pq} obtained new elements of L can be evaluated. In the structures described in the present paper, the other distances rise from the geometry. Diagonalization is carried out again, and the whole procedure is repeated until two successive matrices L coincide within the considered limit.

3. Determination of the geometrical structures of triatomic clusters

In our model calculation we have used the parametrization of the lithium atom. Clusters investigated in this work are shown in Fig. 1. The four geometries considered of Li_3 clusters are: linear chain, triangle I, triangle II and equilateral triangle. Facilitating the analytical solution of the secular equation, we have used the parameter

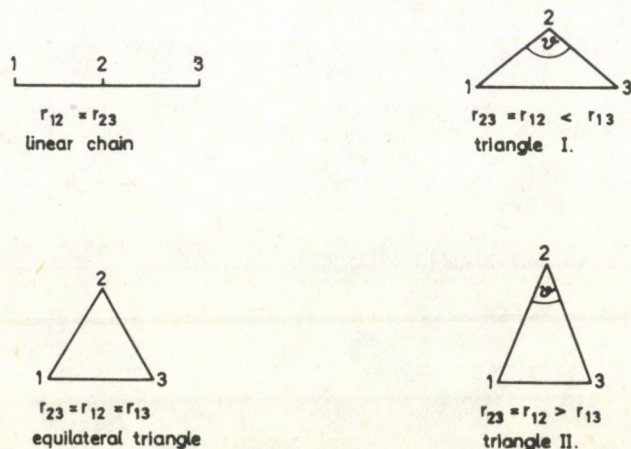


Fig. 1. Geometry of triatomic clusters

λ , where $\beta_{12} = \beta_{23} = \beta$ and $\beta_{13} = \lambda\beta$. The solution of the secular equation is given in the Appendix A. The eigenvalues and the eigenvectors are the following:

$$x_1 = \frac{E_1 - \alpha}{|\beta|} = -\frac{\lambda + \sqrt{\lambda^2 + 8}}{2}, \quad (5)$$

$$C_1 = \frac{1}{\sqrt{4 + \frac{\lambda^2}{2} - \frac{1}{2}\sqrt{\lambda^4 + 8\lambda^2}}} \left(1, -\frac{\lambda}{2} + \frac{\sqrt{\lambda^2 + 8}}{2}, 1 \right), \quad (6)$$

$$x_2 = \frac{E_2 - \alpha}{|\beta|} = \lambda, \quad (7)$$

$$c_2 = \frac{1}{2} (1, 0, -1), \quad (8)$$

$$x_3 = \frac{E_3 - \alpha}{|\beta|} = -\frac{\lambda - \sqrt{\lambda^2 + 8}}{2}, \quad (9)$$

$$C_3 = \frac{1}{\sqrt{4 + \frac{\lambda^2}{2} + \frac{1}{2}\sqrt{\lambda^4 + 8\lambda^2}}} \left(1, -\frac{\lambda}{2} - \frac{\sqrt{\lambda^2 + 8}}{2}, 1 \right), \quad (10)$$

where X_i is calculated from the eigenvalue E_i exploiting the relation $\beta < 0$ of the clusters under study.

Before going into details we make some estimations. Supposing that for the nearest neighbours $|\beta_{ij}| < |\beta_{kl}|$ if $r_{kl} < r_{ij}$ we obtain that:

$$\lambda < 1$$

for the linear chain and the triangle I;

$$\lambda = 1$$

for the equilateral triangle and

$$\lambda > 1$$

for the triangle II.

According to the relations (5) (7) and (9) we obtain

$$x_1 = x_2 < x_3 \quad \text{if} \quad \lambda = -1, \quad (11)$$

$$x_1 < x_2 < x_3 \quad \text{if} \quad -1 < \lambda < 1, \quad (12)$$

$$x_1 < x_2 = x_3 \quad \text{if} \quad \lambda = 1, \quad (13)$$

$$x_1 < x_3 < x_2 \quad \text{if} \quad 1 < \lambda. \quad (14)$$

Thus the occupation numbers n_i are the following:

$$n_1 = 2, \quad n_2 = 1, \quad n_3 = 0 \quad (15)$$

for the linear chain and the triangle I;

$$n_1 = 2, \quad n_2 = 0, 5, \quad n_3 = 0, 5 \quad (16)$$

for the equilateral triangle and

$$n_1 = 2, \quad n_2 = 0, \quad n_3 = 1 \quad (17)$$

for the triangle II.

Using the rough estimation that $\lambda = 1$ for every structure under study the relations (3, 6, 8, 10) and (15–17) yield the bond orders:

$$l_{12} = \frac{2}{3}, \quad l_{13} = \frac{1}{6} \quad (18)$$

for the linear chain and for the triangle I;

$$l_{12} = l_{13} = \frac{1}{2} \quad (19)$$

for the equilateral triangle and

$$l_{12} = \frac{1}{3}, \quad l_{13} = \frac{5}{6} \quad (20)$$

for the triangle II.

Table I shows that the approximation $\lambda = 1$ gives a good geometrical structure. For the Li_3 the qualitative structure depends mainly on the occupation numbers and so the exact value of the λ (i.e. of the β_{pq}) is not very important. Table I shows also the exact values of the parameter λ . Let us take the occupation numbers (2, 1, 0). These are the occupation numbers of the linear chain and the triangle I. Changing the λ , the largest deviation from the exact distance of $r_{12} = 5.17$ a. u. is 0.07 a. u. The deviation from the distance $r_{13} = 6.67$ a. u. is larger, it is in the neighbourhood of 0.88 a. u. We remark here that $l_{13} = 0.075$ and for this bond order the error of the relation (4) is significant as stated in [3].

For the bond order of the equilateral triangle the deviation from the exact distance $r_{12} = r_{13} = 5.35$ a. u. is about 0.08 a. u.

There is a moderate deviation also for the triangle II. That is 0.09 a. u. and 0.05 a. u. from the distances $r_{12} = 5.66$ a. u. and $r_{13} = 5.06$ a. u., respectively. We can explain the moderate deviations by the fact that $l_{13}, l_{12} > 0.3$, and in this domain the relation (4) is a good approximation.

Table II shows the deviations from the exact distances, obtained by changing of 30% of the exact λ . We can see from Table II that the structure of the Li_3 does not depend strongly on the β_{pq} . When there is a larger deviation the corresponding bond order is near zero, where the approximation (4) is uncertain.

Table I

Geometrical structures of triatomic lithium clusters taken as a function of the parameter λ and of the occupation numbers (n_1, n_2, n_3). The distances are in a.u. The exact values are in frames

Type of clusters	λ	Occupation numbers		
		(2, 1, 0)	(2, 0.5, 0.5)	(2, 0, 1)
Linear chain	0.17	$l_{12}=0.706$ $l_{13}=0.030$ $r_{12}=5.16$ $r_{13}=10.32$	$l_{12}=0.529$ $l_{13}=0.397$ $r_{12}=5.31$ $r_{13}=10.62$	$l_{12}=0.353$ $l_{13}=0.765$ $r_{12}=5.56$ $r_{13}=11.12$
Triangle I	0.43	$l_{12}=0.699$ $l_{13}=0.075$ $r_{12}=5.17$ $r_{13}=6.67$	$l_{12}=0.524$ $l_{13}=0.431$ $r_{12}=5.32$ $r_{13}=5.43$	$l_{12}=0.350$ $l_{13}=0.788$ $r_{12}=5.57$ $r_{13}=5.11$
Equilateral triangle	1.00	$l_{12}=2/3$ $l_{13}=1/6$ $r_{12}=5.19$ $r_{13}=6.11$	$l_{12}=0.5$ $l_{13}=0.5$ $r_{12}=5.35$ $r_{13}=5.35$	$l_{12}=1/3$ $l_{13}=5/6$ $r_{12}=5.60$ $r_{13}=5.09$
Triangle II	1.68	$l_{12}=0.608$ $l_{13}=0.255$ $r_{12}=5.24$ $r_{13}=5.79$	$l_{12}=0.456$ $l_{13}=0.566$ $r_{12}=5.40$ $r_{13}=5.28$	$l_{12}=0.304$ $l_{13}=0.878$ $r_{12}=5.66$ $r_{13}=5.06$

Table II

Deviations $|\Delta r_{12}|$ and $|\Delta r_{13}|$ (in a.u.) from the exact distances obtained by changing of 30% of the exact λ in triatomic lithium clusters

	Linear chain	Triangle I	Equilateral triangle	Triangle II
$ \Delta r_{12} $	0.0009	0.006	—	0.03
$ \Delta r_{13} $	0.0018	0.19	—	0.01

4. Stability of the triatomic clusters

4.1. Linear chain

In this cluster $r_{13}=2r_{12}$. Under perturbation this structure changes into the structure of the triangle I. Namely using the bond order ($l_{13}=0.030$) of the linear chain, we obtain $r_{13}=7.12$ a. u. This value is nearer to the $r_{13}=6.67$ a. u. of the triangle I than to the value $r_{13}=10.32$ a. u. of the linear chain.

4.2. Equilateral triangle

Under perturbation this structure changes into the structure of the triangle I or triangle II. (see Table I for $\lambda=1$). This instability is due to the discontinuity of the occupation numbers.

4.3. Triangle I and triangle II

The stability of these structures is verified by the fact that we have obtained these structures using an iterative method described in the previous paragraph.

5. Determination of the geometrical structures of tetratomic clusters

The investigated tetratomic structures are shown in Fig. 2. Five different structures of Li_4 are taken into consideration: linear chain, parallelogram, rhombus, square and the tetrahedron. In order to make the analytical solution of the secular equation easier, we have used the parameters λ, μ and ν where

$$\beta_{12} = \beta_{34} = \beta, \tag{21/a}$$

$$\beta_{23} = \lambda\beta = \gamma, \tag{21/b}$$

$$\beta_{13} = \beta_{24} = \mu\beta = \delta, \tag{21/c}$$

$$\beta_{14} = \nu\beta = \varepsilon, \tag{21/d}$$

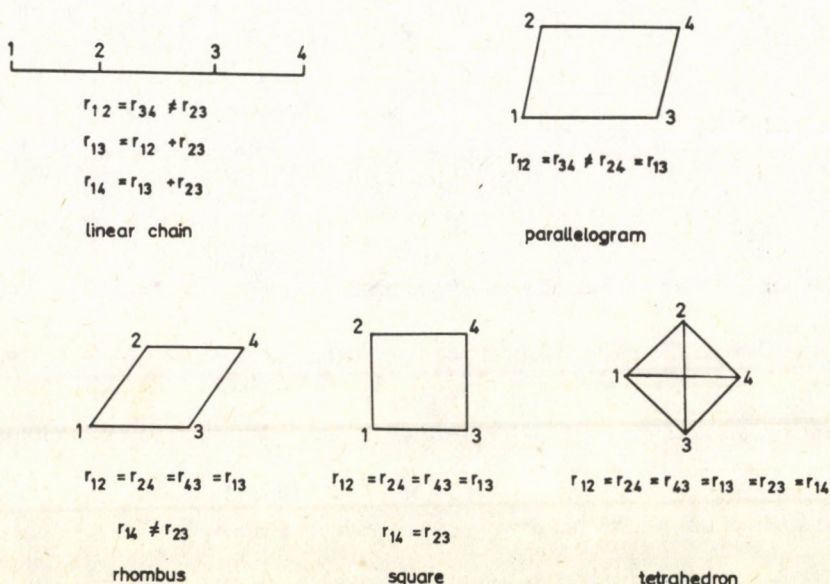


Fig. 2. Geometry of tetratomic clusters

The solution of the secular equation is presented in Appendix B. Introducing the parameters $X_i = \frac{E_i - \alpha}{|\beta|}$ and using the relation $\beta < 0$ we obtain

$$X = -I \frac{\lambda + \nu}{2} - J \frac{\sqrt{(\lambda - \nu)^2 + 4(1 + I\mu)^2}}{2}, \quad (22)$$

where

$$I = 1, \quad J = 1 \quad \text{for } X_1 \text{ and } \bar{C}_1, \quad (23/a)$$

$$I = -1, \quad J = 1 \quad \text{for } X_2 \text{ and } \bar{C}_2, \quad (23/b)$$

$$I = 1, \quad J = -1 \quad \text{for } X_3 \text{ and } \bar{C}_3, \quad (23/c)$$

$$I = -1, \quad J = -1 \quad \text{for } X_4 \text{ and } \bar{C}_4. \quad (23/d)$$

In describing the eigenvectors the following parameters are introduced:

$$U = 1 + I\mu, \quad (24/a)$$

$$V = X + I\nu, \quad (24/b)$$

$$a = -\frac{U}{\sqrt{U^2 + V^2}}, \quad (25)$$

$$b = \frac{V}{\sqrt{U^2 + V^2}} \quad (26)$$

and the eigenvectors may thus be written

$$\bar{C} = \frac{1}{\sqrt{2}}(a, b, b, a) \quad (27)$$

for the vectors \bar{C}_1 and \bar{C}_3 , and

$$\bar{C} = \frac{1}{\sqrt{2}}(a, b, -b, -a) \quad (28)$$

for the vectors \bar{C}_2 and \bar{C}_4 . We have presumed that $\mu \neq 1$.

When $\mu = 1$ and $\lambda \neq \nu$ the \bar{C}_2 has the form

$$\bar{C}_2 = \frac{1}{\sqrt{2}}(-1, 0, 0, 1) \quad (29)$$

and when $\mu = 1$ and $\lambda = \nu$ the states X_2 and X_4 are degenerate. We can choose the following eigenvectors:

$$\bar{C}_2 = \frac{1}{\sqrt{2}}(-1, 0, 0, 1), \quad (30/a)$$

$$\bar{C}_4 = \frac{1}{\sqrt{2}}(0, -1, 1, 0). \quad (30/b)$$

In the other cases the relations (22–28) are valid. The relation (29) is the result of (28) in the limit $\mu \rightarrow 1$ and the relations (30/a) and (30/b) are the limits also of (28) when $\mu \rightarrow 1$ and $(\lambda - \nu) \rightarrow 0$. When $\mu = 1$ and $(\lambda - \nu) \rightarrow 0$ Eqs (28) and (29) give (30/a) and (30/b).

When $\lambda = \nu$ and $\mu \rightarrow 1$ we obtain from (27) and (28) the following eigenvectors:

$$\bar{C}_2 = \frac{1}{2}(1, 1, -1, -1) \quad (31/a)$$

$$\bar{C}_4 = \frac{1}{2}(1, -1, 1, -1) \quad (31/b)$$

The nearest neighbour approximation leads to the following values:

a.) Linear chain:

$$\lambda = 1, \quad \mu = 0, \quad \nu = 0 \quad (32)$$

and

$$n_1 = 2, \quad n_2 = 2, \quad n_3 = 0, \quad n_4 = 0 \quad (33)$$

are the occupation numbers.

b.) Parallelogram:

$$\lambda = 1, \quad \mu = 0, \quad \nu = 0 \quad (34)$$

and

$$n_1 = 2, \quad n_2 = 2, \quad n_3 = 0, \quad n_4 = 0. \quad (35)$$

c.) Rhombus

$$\lambda = 1, \quad \mu = 1, \quad \nu = 0 \quad (36)$$

and

$$n_1 = 2, \quad n_2 = 2, \quad n_3 = 0, \quad n_4 = 0. \quad (37)$$

Regarding also the other interactions, we always have in this structure the relation $\mu = 1$. This relation arises from the geometry

d.) Square:

$$\lambda = 0, \quad \mu = 1, \quad \nu = 0 \quad (38)$$

and

$$n_1 = 2, \quad n_2 = 1, \quad n_3 = 0, \quad n_4 = 1. \quad (39)$$

In this structure the geometry gives the following relations in every calculation: $\mu = 1$ and $\lambda = \nu$. The final geometry does not depend on the values λ and ν , namely the relations (22) and (24/b) give

$$V = -J(1 + I\mu) \quad (40)$$

and in addition the relations (24/a) and (29–30/b) do not contain the parameters λ and ν

e.) Tetrahedron

$$\lambda = 1, \quad \mu = 1, \quad \nu = 1 \quad (41)$$

and

$$n_1 = 2, \quad n_2 = n_3 = n_4 = 2/3. \quad (42)$$

Because of the geometry the parameters λ , μ and ν in (41) are the same as in the exact calculation.

Table III shows the distances obtained using the nearest neighbour approximation, Table IV contains the distances obtained taking every interactions between the atoms (exact values) into account. The results for the square and the tetrahedron are the same in the two Tables according to the geometry as stated above. The nearest neighbour approximation is very good also for the rhombus. For the linear chain the distance r_{12} is practically the same. Our estimation for the distance r_{23} is of 0.27 a. u. smaller than the exact value. In the case of the parallelogram the situation is the same, however, in addition the nearest neighbour approximation gives an excessively large value for the distance r_{13} , namely 7.56 a. u., instead of 7.21 a. u. We can explain this deviation by the fact that $l_{13} \approx 0$, and in this domain the validity of the relation (4) is restricted. For the uncertainty of the distance r_{23} we have the explanation that in the exact calculation the μ is comparable in order of magnitude with the λ , contrary to our supposition (i.e. $\lambda = 1$ and $\mu = 0$).

We remark here that the occupation numbers n_i do not change, using the exact values of λ , μ and ν . We can see that the linear chain, the parallelogram and the

Table III

Geometrical structures (in a.u.) of tetratomic lithium clusters using the nearest neighbour approximation without iterations

Type of clusters	Parameters of β_{pq} (λ, μ, ν)	Occupation numbers (n_1, n_2, n_3, n_4)	Bond orders and distances
Linear chain	(1, 0, 0)	(2, 2, 0, 0)	$l_{12} = 0.894$ $l_{23} = 0.447$ $r_{12} = 5.06$ $r_{23} = 5.41$
Parallelogram	(1, 0, 0)	(2, 2, 0, 0)	$l_{12} = 0.894$ $l_{23} = 0.447$ $l_{13} = 0.0$ $r_{12} = 5.06$ $r_{23} = 5.41$ $r_{13} = 7.56$
Rhombus	(1, 1, 0)	(2, 2, 0, 0)	$l_{12} = 0.485$ $l_{23} = 0.621$ $r_{12} = 5.36$ $r_{23} = 5.23$
Square	(0, 1, 0)	(2, 1, 0, 1)	$l_{12} = 0.5$ $r_{12} = 5.35$
Tetrahedron	(1, 1, 1)	(2, 2/3, 2/3, 2/3)	$l_{12} = 1/3$ $r_{12} = 5.60$

Table IV

Geometrical structures (in a.u.) of tetratomic lithium clusters obtained taking every interaction between the atoms into account. These are called exact values

Type of clusters	Parameters of β_{pq}			Occupation numbers				Bond orders and distances
	λ	μ	ν	n_1	n_2	n_3	n_4	
Linear chain	0.56	0.12	-0.06	2	2	0	0	$l_{12}=0.953$ $l_{23}=0.299$ $l_{13}=0.01$ $l_{14}=-0.299$ $r_{12}=5.03$ $r_{23}=5.68$
Parallelogram	0.55	0.30	0.01	2	2	0	0	$l_{12}=0.956$ $l_{23}=0.283$ $l_{13}=0.023$ $l_{14}=-0.283$ $r_{12}=5.03$ $r_{23}=5.72$ $r_{13}=7.21$
Rhombus	1.17	1.00	-0.14	2	2	0	0	$l_{12}=0.475$ $l_{23}=0.656$ $l_{14}=-0.656$ $r_{12}=5.38$ $r_{23}=5.2$
Square	0.37	1.00	0.37	2	1	0	1	$l_{12}=0.5$ $l_{14}=0.0$ $r_{12}=5.35$
Tetrahedron	1.00	1.00	1.00	2	2/3	2/3	2/3	$l_{12}=1/3$ $r_{12}=5.60$

Table V

Deviations $|\Delta r_{12}|$, $|\Delta r_{23}|$ and $|\Delta r_{13}|$ (in a.u.) from the exact distances obtained by changing of 30% of the exact λ , μ and ν in tetratomic lithium clusters

	Linear chain			Parallelogram			Rhombus	
	λ	μ	ν	λ	μ	ν	λ	μ
$ \Delta r_{12} $	0.01	0.0006	0.002	0.1	0.004	0.0004	0.01	0.001
$ \Delta r_{23} $	0.23	0.0008	0.02	0.3	0.04	0.008	0.02	0.002
$ \Delta r_{13} $				0.2	0.08	0.004		

rhombus have the same occupation numbers. In these structures, however, the constraints of the geometry are significant. In spite of this fact the distances r_{13} and r_{23} of the linear chain are near to the distances r_{12} and r_{23} of the parallelogram. The distances r_{13} are different because of the different constraints.

Table V shows the deviations from the exact distances, obtained by changing of 30% of the exact λ , μ and ν . The distance r_{12} is the least sensitive to the changes of the

parameters. The largest deviation of the r_{12} is 0.02 a. u. for the rhombus. Otherwise the change of the λ brings the largest deviations in the distances. The deviation of the r_{23} is maximum for the parallelogram, with the value 0.3 a. u. In the parallelogram the deviation of the r_{13} has nearly the same value as the r_{23} . We can summarize the results of Table V, by stating that the geometrical structure does not depend very much on the parameters λ , μ , ν . This allows some uncertainty in the selection of the function β_{pq} .

6. The stability of the tetratomic clusters

6.1. Linear chain

Under perturbation this structure changes into the structure of the parallelogram. Namely $r_{13} = 10.71$ a. u. in the linear chain and using the value $l_{13} = 0.01$ of the linear chain in the relation (4) we obtain $r_{13} = 7.41$. This is nearer to the distance $r_{13} = 7.21$ a. u. of the parallelogram than to the distance r_{13} of the linear chain.

6.2. Tetrahedron

Let us suppose that under perturbation one of the interatomic distances of the tetrahedron increases. We can say, without destroying the generality, that the distance r_{14} changes. In this case $\lambda = \mu = 1$ and $\nu \approx 1$ but $\nu < 1$. For the energies X_i we obtain from (22) and (23):

$$X_1 = -\frac{1+\nu}{2} - \frac{\sqrt{(1-\nu)^2 + 16}}{2} < 1, \quad (43/a)$$

$$X_2 = \nu < 1, \quad (43/b)$$

$$X_3 = -\frac{1+\nu}{2} + \frac{\sqrt{(1-\nu)^2 + 16}}{2} > -\frac{1+1}{2} + \frac{4}{2} = 1, \quad (43/c)$$

$$X_4 = 1 \quad (43/d)$$

and thus the occupation numbers have the values:

$$n_1 = 2, \quad n_2 = 2, \quad n_3 = n_4 = 0. \quad (44)$$

When the perturbed distance decreases, we can suppose that the distance r_{23} changes, and we obtain $\mu = \nu = 1$ and $\lambda \approx 1$ but $\lambda > 1$. For the energies we have:

$$X_1 = -\frac{\lambda+1}{2} - \frac{\sqrt{(\lambda-1)^2 + 16}}{2} < 0, \quad (45/a)$$

$$X_2 = \frac{\lambda+1}{2} - \frac{\lambda-1}{2} = 1, \quad (45/b)$$

$$X_3 = -\frac{\lambda+1}{2} + \frac{\sqrt{(\lambda-1)^2+16}}{2} < -\frac{\lambda+1}{2} + \frac{\sqrt{(\lambda-1)^2+2(\lambda-1)\cdot 4+16}}{2} = 1 \quad (45/c)$$

$$X_4 = \frac{\lambda+1}{2} + \frac{\lambda-1}{2} = \lambda > 1 \quad (45/d)$$

and

$$n_1 = 2, \quad n_2 = 0, \quad n_3 = 2, \quad n_4 = 0. \quad (46)$$

Supposing that the perturbation is weak, from (44) we obtain

$$l_{12} = l_{13} = l_{23} = l_{24} = l_{34} = 0.5 \quad \text{and} \quad l_{14} = -0.5. \quad (47)$$

These bond orders correspond to the structure of the rhombus. The relation (46) gives the following bond orders:

$$l_{12} = l_{13} = l_{24} = l_{34} = 0, \quad l_{14} = l_{23} = 1. \quad (48)$$

These describe the dissociation of the tetrahedron Li_4 into two Li_2 molecules.

Consequently, the tetrahedron Li_4 is not stable, it can be transformed into the structure of the rhombus or it can dissociate into two Li_2 molecules.

6.3. Square

When the diagonal r_{23} decreases, the parametrization is as follows: $\lambda = v + \tau$, where v is the exact value and $\mu = 1$, furthermore $\tau \approx 0$ but $\tau > 0$. The expressions for the energies X_i reduce to:

$$X_1 + v = -\frac{\tau}{2} - \frac{\sqrt{\tau^2+16}}{2} < 0, \quad (49/a)$$

$$X_2 + v = 2v < 1.5, \quad (49/b)$$

$$X_3 + v = -\frac{\tau}{2} + \frac{\sqrt{\tau^2+16}}{2} > 1.5, \quad (49/c)$$

$$X_4 + v = 2v + \tau > 2v \quad (49/d)$$

and so

$$n_1 = 2, \quad n_2 = 2, \quad n_3 = 0, \quad n_4 = 0. \quad (50)$$

When $\lambda = v - \tau$, $\mu = 1$ and $\tau \approx 0$ but $\tau > 0$ (i.e. increase of the distance r_{23}) we have:

$$X_1 + v = \frac{\tau}{2} - \frac{\sqrt{\tau^2+16}}{2} < 0, \quad (51/a)$$

$$X_2 + v = 2v < 1.5, \quad (51/b)$$

$$X_3 + v = \frac{\tau}{2} + \frac{\sqrt{\tau^2 + 16}}{2} > 1.5, \quad (51/c)$$

$$X_4 + v = 2v - \tau < 2v \quad (51/d)$$

and so

$$n_1 = 2, \quad n_2 = 0, \quad n_3 = 0, \quad n_4 = 2. \quad (52)$$

The perturbation of the sides of the square can be described with the parameters:

$$\lambda = v \approx 0.37 \text{ (exact value) and } \mu = 1 + \tau \text{ where } \tau \approx 0.$$

Thus

$$X_1 = -\lambda - (1 + \mu) = -2.37 - \tau, \quad (53/a)$$

$$X_2 = \lambda - (1 - \mu) = 0.37 + \tau, \quad (53/b)$$

$$X_3 = -\lambda + (1 + \mu) = 1.63 + \tau, \quad (53/c)$$

$$X_4 = \lambda + (1 - \mu) = 0.37 - \tau \quad (53/d)$$

and when $\tau > 0$ we have

$$n_1 = 2, \quad n_2 = 0, \quad n_3 = 0, \quad n_4 = 2 \quad (54)$$

and when $\tau < 0$ we have

$$n_1 = 2, \quad n_2 = 2, \quad n_3 = 0, \quad n_4 = 0. \quad (55)$$

Supposing that the perturbations are weak, we obtain the following structures. From (50) and (52) we have the bond orders

$$l_{12} = l_{13} = l_{23} = l_{24} = l_{34} = 0.5, \quad l_{14} = -0.5 \quad (56/a)$$

and

$$l_{12} = l_{13} = l_{14} = l_{24} = l_{34} = 0.5, \quad l_{23} = -0.5, \quad (56/b)$$

respectively. These are the structures of the rhombus. From (54) and (55) we obtain the dissociation of the square Li_4 into two Li_2 molecules with the following bond orders:

$$l_{12} = l_{14} = l_{23} = l_{34} = 0, \quad l_{13} = l_{24} = 1 \quad (57/a)$$

and

$$l_{13} = l_{14} = l_{23} = l_{24} = 0, \quad l_{12} = l_{34} = 1. \quad (57/b)$$

For the bond orders in (56/a) and (56/b) we have used the relations of (30/a) and (30/b) and for the bond orders in (57/a) and (57/b) we have used the relations of (31/a) and (31/b).

Consequently, the square Li_4 is not stable, it can be transformed into the structure of the rhombus or it can be dissociated into two Li_2 molecules as the tetrahedron. In any case the bond order $l = 0$ can mean a weak interaction, too, because the function bond order–interatomic distance (4 is not correct in this domain.

6.4. Rhombus

In the structures of the tetrahedron and the square the perturbation destroys the original symmetry and as a consequence it also changes the occupation numbers. Destroying the symmetry of the rhombus, namely changing the value $\lambda=1$, the occupation numbers do not change. We have to use another method to examine the stability of the rhombus. When λ and ν are constants having exact values, we can introduce the functions

$$\beta_{pq} = \beta_{pq}(\mu) \quad (58)$$

and

$$Y = \frac{\beta_{23}(X)}{\beta_{12}(X)} = f(X). \quad (59)$$

The displacement of X by μ_n , where μ_n is the value of μ in the n -th iteration, gives

$$\mu_{n+1} = f(\mu_n) \quad (60)$$

and so

$$1 = f(1), \quad (61)$$

per definition. When the equation $X = f(X)$ can be solved by iteration and the μ is one of the solutions, the following relation holds [24]:

$$\left| \frac{df(X)}{dX} \right|_{X=\mu} < 1. \quad (62)$$

In our case using the values of β_{23} and β_{13} we obtain:

$$\left| \frac{df(X)}{dX} \right|_{X=1} \approx 1.5 > 1. \quad (63)$$

Hence supposing a small perturbation τ for the value $\mu=1$ from (60) we obtain:

$$|f(1+\tau) - f(1)| \approx \left| \frac{df(X)}{dX} \right|_{X=1} \cdot |\tau| \approx 1.5|\tau| > |\tau|. \quad (64)$$

When $\mu_n = 1 + \tau$ the relation (64) means that

$$|\mu_{n+1} - 1| > |\mu_n - 1| \quad (65)$$

that is the structure of the rhombus is not stable.

6.5. Parallelogram

We have obtained this structure by iteration, without any constraint on the parameters λ , μ , ν . Thus the perturbation does not destroy the structure of the parallelogram, and we can say that of the structures linear chain, parallelogram, rhombus, square and tetrahedron, the parallelogram is the most stable structure.

7. Comparisons with other calculations

Table VI–X present the comparisons with other calculations for the clusters of Li, Na, K, Cu and Ag atoms. We have presented also the experimental results for the diatomic clusters. We can see that in general our simple semiempirical method is in no way inferior to the more sophisticated methods in view of geometrical structures. In the methods of Tables VI–X also the correlation energy is taken into consideration in some way. When there is a greater difference between the results obtained by our method and by the other calculations, we can see that the difference for the respective diatomic cluster is of the same order of magnitude and our distance for the diatomic molecule is near to the experimental value. (See for example the tetratomic clusters of K atoms in Table VIII.)

Table VI

Lithium clusters (distances in a.u.)

Cluster Structure	Results
Li ₂	$r_{12} = 5.01$ (LSD[8]: 5.13; CI[10]: 5.169; CNDO/BW[7]: 5.05; SCF ab initio [11]: 5.48; MRD-CI[12]: 5.08; exp [20, 21]: 5.05)
Li ₃ Linear chain	$r_{12} = 5.16$ (CNDO/BW[7]: 5.20)
Li ₃ Triangle I	$r_{12} = 5.17$ (LSD[8]: 5.32; CI[9]: 5.24; CI[10]: 5.3; LEPS[10]: 5.3; CNDO/BW[7]: 5.33) $r_{13} = 6.67$ (LSD[8]: 6.29; CI[9]: 6.11; CI[10]: 6.0; LEPS[10]: 7.2; CNDO/BW[7]: 6.28) $\vartheta = 80^\circ$ (LSD[8]: 72°; CI[9]: 71°; CI[10]: 69°; LEPS[10]: 86°; CNDO/BW[7]: 72°)
Li ₃ Equilateral triangle	$r_{12} = 5.34$ (CNDO/BW[7]: 5.59)
Li ₃ ⁺ Equilateral triangle	$r_{12} = 5.19$ (LSD[8]: 5.59)
Li ₃ Triangle II	$r_{12} = 5.66$ (LSD[8]: 5.83; CI[9]: 5.69; CI[10]: 5.8; LEPS[10]: 6.2) $r_{13} = 5.06$ (LSD[8]: 5.07; CI[9]: 5.16; CI[10]: 5.1; LEPS[10]: 5.3) $\vartheta = 53^\circ$ (LSD[8]: 52; CI[9]: 54°; CI[10]: 52°; LEPS[10]: 51°)
Li ₄ Linear chain	$r_{12} = 5.03$ (SCF ab initio [11]: 5.5) $r_{23} = 5.68$ (SCF ab initio [11]: 7.67)
Li ₄ Parallelogram	$r_{12} = 5.03$ $r_{23} = 5.72$ $r_{13} = 7.21$
Li ₄ Rhombus	$r_{12} = 5.38$ (LSD[8]: 5.8; CEPA[12]: 5.75; MRD-CI[12]: 5.82; CNDO/BW[7]: 5.76) $r_{23} = 5.2$ (LSD[8]: 5.1; CEPA[12]: 5.19; MRD-CI[12]: 5.19; CNDO/BW[7]: 4.91)
Li ₄ Square	$r_{12} = 5.35$ (CNDO/BW[7]: 5.37; MRD-CI[12]: 5.57)
Li ₄ Tetrahedron	$r_{12} = 5.60$ (CNDO/BW[7]: 5.69; MRD-CI[12]: 5.76)

Table VII
Sodium clusters (distances in a.u.)

Cluster Structure	Results
Na ₂	$r_{12} = 6.02$ (LSD[8]: 5.77; CI[15]: 5.86; HF-LD[16]: 5.72; MRD-CI[12]: 5.81; exp [22]: 5.82)
Na ₃ Linear chain	$r_{12} = 6.20$
Na ₃ Triangle I	$r_{12} = 6.20$ (LSD[8]: 6.08; CI[15]: 6.25; HF-LD[16]: 6.1) $r_{13} = 8.00$ (LSD[8]: 8.04; CI[15]: 7.47; HF-LD[16]: 9.1) $\vartheta = 80^\circ$ (LSD[8]: 83; CI[15]: 73; HF-LD[16]: 97)
Na ₃ Equilateral triangle	$r_{12} = 6.41$
Na ₃ ⁺ Equilateral triangle	$r_{12} = 6.23$ (LSD[8]: 6.43)
Na ₃ Triangle II	$r_{12} = 6.80$ (LSD[8]: 6.81; CI[15]: 7.00; HF-LD[16]: 7.15) $r_{13} = 6.08$ (LSD[8]: 5.86; CI[15]: 6.09; HF-LD[16]: 5.7) $\vartheta = 53^\circ$ (LSD[8]: 51°; CI[15]: 51°; HF-LD[16]: 48°)
Na ₄ Linear chain	$r_{12} = 6.04$ $r_{23} = 6.81$
Na ₄ Parallelogram	$r_{12} = 6.04$ $r_{23} = 6.86$ $r_{13} = 8.66$
Na ₄ Rhombus	$r_{12} = 6.45$ (LSD[8]: 6.1; HF-LD[16]: 6.64; MRD-CI[12]: 6.58) $r_{23} = 6.24$ (LSD[8]: 5.7; HF-LD [16]: 5.7; MRD-CI[12]: 5.96)
Na ₄ Square	$r_{12} = 6.41$ (MRD-CI[12]: 6.2)
Na ₄ Tetrahedron	$r_{12} = 6.72$

Table VIII
Potassium clusters (distances in a.u.)

Cluster Structure	Results
K ₂	$r_{12} = 7.46$ (LSD[19]: 7.16; SCF-DF[17]: 7.54; PP-MRD-CI1[18]: 8.2; PP-MRD-CI2[18]: 8.2; PP-MRD-CI3[18]: 7.96; exp [22]: 7.38)
K ₃ Linear chain	$r_{12} = 7.68$
K ₃ Triangle I	$r_{12} = 7.69$ (LSD[19]: 7.49; SCF-DF[17]: 8.22) $r_{13} = 9.92$ (LSD[19]: 8.98; SCF-DF[17]: 14.84) $\vartheta = 80^\circ$ (LSD[19]: 74°; SCF-DF[17]: 129°)
K ₃ Equilateral triangle	$r_{12} = 7.95$
K ₃ ⁺ Equilateral triangle	$r_{12} = 7.72$ (LSD[19]: 7.94)
K ₃ Triangle II	$r_{12} = 8.43$ (LSD[19]: 8.27; SCF-DF[17]: 10.51) $r_{13} = 7.53$ (LSD[19]: 7.23; SCF-DF[17]: 7.53) $\vartheta = 53^\circ$ (LSD[19]: 52°; SCF-DF[17]: 42°)
K ₄ Linear chain	$r_{12} = 7.48$ $r_{23} = 8.44$
K ₄ Parallelogram	$r_{12} = 7.48$ $r_{23} = 8.51$ $r_{13} = 10.73$
K ₄ Rhombus	$r_{12} = 8.00$ (PP-MRD-CI1[18]: 9.27; PP-MRD-CI2[18]: 9.22; PP-MRD-CI3[18]: 8.91) $r_{23} = 7.73$ (PP-MRD-CI1[18]: 8.27; PP-MRD-CI2[18]: 8.23; PP-MRD-CI3[18]: 7.95)
K ₄ Square	$r_{12} = 7.95$ (PP-MRD-CI1[18]: 8.88; PP-MRD-CI2[18]: 8.97; PP-MRD-CI3[18]: 8.67)
K ₄ Tetrahedron	$r_{12} = 8.33$ (PP-MRD-CI1[18]: 9.29; PP-MRD-CI2[18]: 9.37; PP-MRD-CI3[18]: 8.91)

Table IX

Copper clusters (distances in a.u.)

Cluster Structure		Results
Cu ₂		$r_{12} = 4.14$ (SCF ab initio [14]: 4.43; exp [23]: 4.2)
Cu ₃	Linear chain	$r_{12} = 4.26$ (SCF ab initio [13]: 4.77; SCF ab initio [14]: 4.44)
Cu ₃	Triangle I	$r_{12} = 4.26$ (SCF ab initio [13]: 4.72) $r_{13} = 5.5$ (SCF ab initio [13]: 5.5) $\vartheta = 80^\circ$ (SCF ab initio 13: 72°)
Cu ₃	Equilateral triangle	$r_{12} = 4.41$ (SCF ab initio [13]: 4.89; SCF ab initio [14]: 4.55)
Cu ₃ ⁺	Equilateral triangle	$r_{12} = 4.28$
Cu ₃	Triangle II	$r_{12} = 4.67$ (SCF ab initio [13]: 5.29) $r_{13} = 4.18$ (SCF ab initio [13]: 4.61) $\vartheta = 53^\circ$ (SCF ab initio [13]: 52°)
Cu ₄	Linear chain	$r_{12} = 4.15$ $r_{23} = 4.68$
Cu ₄	Parallelogram	$r_{12} = 4.15$ $r_{23} = 4.72$ $r_{13} = 5.95$
Cu ₄	Rhombus	$r_{12} = 4.43$ $r_{23} = 4.29$
Cu ₄	Square	$r_{12} = 4.41$ (SCF ab initio [14]: 4.55)
Cu ₄	Tetrahedron	$r_{12} = 4.62$

Table X

Silver clusters (distances in a.u.)

Cluster Structure		Results
Ag ₂		$r_{12} = 4.64$
Ag ₃	Linear chain	$r_{12} = 4.78$
Ag ₃	Triangle I	$r_{12} = 4.78$ $r_{13} = 6.17$ $\vartheta = 80^\circ$
Ag ₃	Equilateral triangle	$r_{12} = 4.94$
Ag ₃ ⁺	Equilateral triangle	$r_{12} = 4.8$
Ag ₃	Triangle II	$r_{12} = 5.24$ $r_{13} = 4.68$ $\vartheta = 53^\circ$
Ag ₄	Linear chain	$r_{12} = 4.65$ $r_{23} = 5.25$
Ag ₄	Parallelogram	$r_{12} = 4.65$ $r_{23} = 5.29$ $r_{13} = 6.67$
Ag ₄	Rhombus	$r_{12} = 4.97$ $r_{23} = 4.81$
Ag ₄	Square	$r_{12} = 4.94$
Ag ₄	Tetrahedron	$r_{12} = 5.18$

Appendix A

Triatomic structures

The secular equation is the following:

$$\bar{L}C = E\bar{C} \quad (\text{A1})$$

and the determinantal equation has the form

$$\det |\bar{L} - E\bar{I}| = \begin{vmatrix} \alpha - E & \beta & \lambda\beta \\ \beta & \alpha - E & \beta \\ \lambda\beta & \beta & \alpha - E \end{vmatrix} = 0. \quad (\text{A2})$$

Then Eq. (A2) becomes

$$\det |\bar{L} - E\bar{I}| = (\alpha - E - \lambda\beta)[(\alpha - E)^2 + (\alpha - E)\lambda\beta - 2\beta^2] = 0. \quad (\text{A3})$$

From (A3) come the eigenvalues E_i :

$$E_1 = \alpha + \beta \left(\frac{\lambda + \sqrt{\lambda^2 + 8}}{2} \right), \quad (\text{A4})$$

$$E_2 = \alpha - \beta\lambda, \quad (\text{A5})$$

$$E_3 = \alpha + \beta \left(\frac{\lambda - \sqrt{\lambda^2 + 8}}{2} \right). \quad (\text{A6})$$

With the aid of (A4), (A5) and (A6) we obtain from (A1) the eigenvectors in (6) (8) and (10).

Appendix B

Tetratomic structures

The orthogonalized atomic orbitals s_1, s_2, s_3 and s_4 are obtained by the Löwdin procedure [3-6,25], and the non-orthogonalized orbitals are centred on atoms 1, 2, 3 and 4, respectively. Let us introduce the following orthogonalized atomic orbitals:

$$S_1 = \frac{1}{\sqrt{2}}(s_1 + s_4), \quad (\text{B1/a})$$

$$S_2 = \frac{1}{\sqrt{2}}(s_2 + s_3), \quad (\text{B1/b})$$

$$S_3 = \frac{1}{\sqrt{2}}(s_1 - s_4), \quad (\text{B1/c})$$

$$S_4 = \frac{1}{\sqrt{2}}(s_2 - s_3). \quad (\text{B1/d})$$

In this basis the determinantal equation has the form:

$$\det |\bar{L} - E\bar{I}| = \begin{vmatrix} \alpha + \varepsilon - E & \beta + \delta & 0 & 0 \\ \beta + \delta & \alpha + \gamma - E & 0 & 0 \\ 0 & 0 & \alpha - \varepsilon - E & \beta - \delta \\ 0 & 0 & \beta - \delta & \alpha - \varepsilon - E \end{vmatrix} = 0 \quad (\text{B2})$$

and so

$$\det |\bar{L} - E\bar{I}| = \begin{vmatrix} \alpha + \varepsilon - E & \beta + \delta \\ \beta + \delta & \alpha + \gamma - E \end{vmatrix} \cdot \begin{vmatrix} \alpha - \varepsilon - E & \beta - \delta \\ \beta - \delta & \alpha - \varepsilon - E \end{vmatrix} = 0. \quad (\text{B3})$$

From (B3) we obtain the eigenvalues (22) and for the eigenvectors (21/a-31/b) we used the relation (A1). In (22) we have applied the following interpretation of the square root extraction:

$$\sqrt{Z^2} = Z. \quad (\text{B4})$$

References

1. G. A. Thomson and D. M. Lindsay, *J. Chem. Phys.*, **74**, 959, 1981.
2. A. Hermann, E. Schumacher and L. Wöste, *J. Chem. Phys.*, **68**, 2327, 1978.
3. A. Julg, I. László and A. Pellegatti, *Theochem.*, **14**, 393, 1983.
4. A. Julg, In *Growth and Properties of Metal Clusters*, pp. 255, Ed. J. Bourdon, Elsevier Scientific Publishing Company, Amsterdam, 1980.
5. A. Julg, G. Del Re and V. Barone, *Phil. Mag.*, **35**, 517, 1977.
6. G. Del Re, V. Barone, N. Montella and A. Julg, *Surf. Sci.*, **97**, 537, 1980.
7. L. Skála, *Phys. Stat. Sol. (b)*, **107**, 351, 1981.
8. R. Car and J. L. Martins, *Surf. Sci.*, **106**, 280, 1981.
9. W. H. Gerber and E. Schumacher, *J. Chem. Phys.*, **69**, 1692, 1978.
10. J. Kendrick and I. H. Hillier, *Mol. Phys.*, **33**, 635, 1977.
11. F. Martinelli, A. Julg and G. Abbate, *Surf. Sci.*, **59**, 319, 1976.
12. H.-O. Beckmann, J. Koutecký and V. Bonačić-Koutecký, *J. Chem. Phys.*, **73**, 5182, 1980.
13. E. Miyoshi, H. Takewaki and T. Nakauma, *Fourth International Congress of Quantum Chemistry in Uppsala, Sweden, June 14-19, 1982*.
14. C. Bochmann, J. Demuyck and A. Veillard, *Gazz. Chim. Italiana*, **108**, 389, 1978.
15. R. L. Martin and E. R. Davidson, *Mol. Phys.*, **35**, 1713, 1978.
16. J. Flad, H. Stoll and H. Freuss, *J. Chem. Phys.*, **71**, 3042, 1979.
17. H. Stoll, J. Flad, E. Golka and Th. Krüger, *Surf. Sci.*, **106**, 251, 1981.
18. G. Pacchioni, H.-O. Beckmann and J. Koutecký, *Chem. Phys. Lett.*, **87**, 151, 1982.
19. J. L. Martins and R. Car, *Helv. Phys. Acta*, **54**, 262, 1981.
20. P. Kusch and M. M. Hessel, *J. Chem. Phys.*, **67**, 386, 1977.
21. W. C. Stwalley, *J. Chem. Phys.*, **65**, 2038, 1976.
22. K. P. Huber and G. Herzberg, *Constants of Diatomic Molecules*, Van Nostrand, Princeton, 1977.
23. H. Takewaki, E. Miyoshi and T. Nakauma, *J. Chem. Phys.*, **76**, 5073, 1982.
24. A. Ralston and P. Rabinowitz, *A. First Course in Numerical Analysis*, p. 344, McGraw-Hill, New York, 1978.
25. P. O. Löwdin, *J. Chem. Phys.*, **18**, 365, 1950.

MOLECULAR SYMMETRY IN AB INITIO CALCULATIONS. I

THE EFFECT OF THE VARIOUS SYMMETRY OPERATIONS

F. BARTHA

*Department of Theoretical Physics, József Attila University
6720 Szeged, Hungary*

E. KAPUY

*Department of Theoretical Physics, József Attila University
6720 Szeged, Hungary
Quantum Theory Group, Physics Institute, Technical University
1521 Budapest, Hungary*

and

C. KOZMUTZA

*Quantum Theory Group, Physics Institute, Technical University
1521 Budapest, Hungary*

(Received 20 April 1984)

The use of molecular symmetry in ab initio calculations is the subject of a series of papers. The possibility of the treatment of large, related molecules is especially investigated.

In Part I we show that the number of integrals to be calculated is much influenced by the symmetry operations taken into account. Using a fast generation routine the best possible choice of symmetry can be made before the integral evaluation, and so the computational time can be much reduced.

1. Introduction

It is a longstanding goal for theoretical chemists to make calculations on very large systems by accurate methods. Until about 1960 the quantum chemical ab initio methods were used only for atoms or small molecules. The “ab initio” — as is well known — implies the solution of the Schrödinger equation without “significant” approximation, as described in detail in many books (see e.g. [1] and [2]).

The possibility of calculating larger and larger molecules arose in the 70-s and this situation is uniquely inseparable from the presence of computers. Recently, computers have undergone an immense development and this results in the increase of quantum chemical calculations as well: the ab initio methods can now be used for systems with 15–20 atoms with moderate size basis sets. In order to achieve accurate results on *large* systems, however, *extended* basis sets are to be used (i.e. including

polarization functions) and the programs by which the calculations are carried out should be organized *in accordance* with the computers of present time. This latter statement is to be emphasized and one example is given: it is predicted (for the computers of newest type, the so-called vector machines) that the recalculation of integrals in each iteration step for SCF procedure seems to be less time-consuming than their read-in from file [3].

As a consequence, when a program is written which is devoted to making calculations on large systems (i.e. for more than 20 atoms), by using even polarization functions, the following points should be taken into consideration:

- the calculation could be done step by step;
- all possible simplifications ought to be taken into account (i.e. the use of molecular symmetry, the basis set should be shared for similar atoms, etc.);
- the input/output requirements are to be diminished.

The fulfilment of the first requirement makes it possible that *in principle* “any” large system can be treated by “any” extended basis set, independently of the size of the computer (a minimum size is necessary, of course). From the above it follows, that the calculations depend on the program organization: provided it is “perfect” (i.e. requirement 3 is fulfilled), the time requirement of the actual calculations is connected with the “special” features one can use (requirement 2). These latter are the subject of many papers in recent years, including those dealing with the better and better approximation of the gamma function, the use of the shell structure, the various techniques for accelerating the SCF iterations etc. (a review is given in [2]).

In this field the use of molecular symmetry has a very special position in *ab initio* calculations, which could really help much in reducing the necessary computer time in the integral as well as in the SCF procedure (see a series of papers of e.g., [4-8]).

The aim of our work is to treat extended systems by the *ab initio* method. While taking into consideration the three points mentioned above, we will deal with some special features *not* yet investigated by other authors or not in the form we did. We will demonstrate that these time-reducing possibilities are necessary when we would go beyond to-day's limit of *ab initio* calculations. The following problems will be analyzed in a series of papers:

- the use of molecular symmetry in integral evaluation;
- the handling of indices;
- the neglect of zero integrals and their handling;
- the use of symmetry in the SCF calculations;
- the neglect of vanishing integrals when large distances are in the system.

These, and some further features (of smaller importance) will be discussed by demonstrating their effect on actual calculations.

The effect of the number of symmetry operations — a subject debated by several authors — is presented first in this paper.

2. Treatment of the hydrocarbon series

The advantage of using molecular symmetry in quantum chemical calculations is trivial and justified by several works. The way how to take it into consideration, on the other hand, has changed during the years [9]. In this paper we do not point out the different ways of using the molecular symmetry (it has already been discussed [4–8] and even by us [10–11]), here we demonstrate the effect of the number of symmetry operations present.

The higher the symmetry the smaller the number of integrals to be calculated, i.e. which are “unique”. This well-known statement is doubtless, the number of symmetry operations to be taken into account, however, is questionable, as seen from several works. There are evidently three possibilities:

- no use of symmetry;
- making use of 1 or 2 or 3 (but less than all) symmetry operations;
- use of the total symmetry.

All three ideas have followers (see, e.g., [12], [13] and [14], respectively). Now we present our opinion and we support it by the results obtained for a series of hydrocarbons (from C_2H_6 up to C_9H_{20}).

The systems belonging to this series have three symmetry operations, when model geometries are used: the C_nH_{2n+2} molecule is supposed to be a member of the C_{2v} point group when n odd, while that of the D_{3d} point group for n even. The systems of the odd series have, therefore, very similar geometry, with symmetry operations σ , C_2 and i . The molecules from the even series are related to each other through the symmetry operations σ_1 , σ_2 and C_2 . It follows, therefore, that the number of unique integrals (i.e. which are non-redundant by symmetry) will change very similarly within the odd, and even series, respectively.

In a previous paper [10] it was pointed out that an advantageous way for taking into consideration molecular symmetry in the integral evaluation is the grouping of integrals into so-called one-, two-, three- and four-center blocks. This special integral order (not discussed here in detail, see [10]), allows us to determine *in advance*, without any integral evaluation, how the number of integrals to be actually calculated diminishes when molecular symmetry is taken into account. The so-called generation program, which does this work and precedes the integral package makes it possible to obtain information about the effect of the symmetry operations on the expected calculation time. The generation routine is very fast (on an R-55 machine (University of Szeged), it runs less than 3 minutes e.g. for C_9H_{20}). It must be noted that the generation of various-center blocks is *independent* of the basis set.

Let us demonstrate the use of molecular symmetry for the series (possessing three symmetry operations) C_2H_6, \dots, C_9H_{20} . The reduction in integral evaluation when using symmetry can be clearly seen from Table I, where the number of non-redundant two-, three- and four-center blocks are given for this series, including (in parentheses) the redundant ones as well. For a comparison the series C_2H_5, \dots is also given in

Table I
Non-redundant (and redundant) integral groups

Groups	Two-center	Three-center	Four-center
C_2H_6	11 (17)	17 (39)	24 (46)
C_3H_8	20 (35)	52 (113)	99 (231)
C_4H_{10}	31 (60)	102 (262)	281 (720)
C_5H_{12}	45 (91)	195 (485)	650 (1730)
C_6H_{14}	61 (129)	311 (829)	1297 (3548)
C_7H_{16}	80 (173)	490 (1281)	2346 (6509)
C_8H_{18}	101 (224)	700 (1900)	3926 (11024)
C_9H_{20}	125 (281)	993 (2661)	6205 (17546)

Table II
Non-redundant (and redundant) integral groups

Groups	Two-center	Three-center	Four-center
$C_2H_5^-$	13 (8)	21 (14)	21 (14)
$C_3H_7^-$	27 (18)	68 (52)	116 (94)
$C_4H_9^-$	46 (32)	158 (128)	383 (332)
$C_5H_{11}^-$	70 (50)	305 (255)	960 (860)
$C_6H_{13}^-$	99 (72)	523 (446)	202 (1850)
$C_7H_{15}^-$	133 (98)	862 (714)	3801 (3514)
$C_8H_{17}^-$	172 (128)	1228 (1072)	6546 (6104)
$C_9H_{19}^-$	216 (162)	1743 (1533)	10563 (9912)

Table II with similar notations. As to this series, due to the only mirror of plane, the number of non-redundant blocks relative to the redundant ones is not so small as in the case of three symmetry operations.

3. Use of one symmetry operation

Let us see first the effect of the σ operation on the number of blocks to be calculated for the series C_2H_6, \dots, C_9H_{20} . As the effect of the operations C_2 or i , respectively, is very similar, only that of the C_2 is given in Table III: the first figure refers to the σ , while the second one (in parentheses) shows the effect of the C_2 operation. From the results it can be seen that the use of the σ operation is more advantageous than that of the C_2 or i . This conclusion holds for all types of blocks: the difference, on the other hand, does not exceed 12%. From these results it follows that it is worthwhile using more than one symmetry operations. The *order* of them should, however, be well

chosen, as for another series, e.g. the effect of the first symmetry operation can be much larger than that of the next one. In that case it is not sure that the use of the second or third symmetry operation results finally in a decrease of the number of non-redundant blocks: the search for these blocks may be more time-consuming than the calculation of a few redundant integrals.

Table III

Effect of the first (and second) symmetry operation

Groups	Two-center	Three-center	Four-center
C_2H_6	18 (16)	34 (28)	42 (38)
C_3H_8	34 (31)	95 (89)	184 (174)
C_4H_{10}	55 (49)	204 (182)	541 (511)
C_5H_{12}	81 (73)	375 (351)	1265 (1211)
C_6H_{14}	112 (100)	622 (570)	2549 (2445)
C_7H_{16}	148 (133)	959 (901)	4627 (4465)
C_8H_{18}	189 (169)	1400 (1300)	7774 (7514)
C_9H_{20}	235 (211)	1959 (1847)	12306 (11934)

In addition, the results obtained for the series C_2H_6, \dots provide information *in advance* on a related series. See, e.g. the series C_2H_5, \dots similar to the series above. This latter series has only a σ mirror of plane symmetry operation, and the number of non-redundant blocks (relative to the total ones) are really close to those obtained for the C_2H_6, \dots series when using only the σ operation (see Table II and Table III).

4. Use of two symmetry operations

Let us investigate now the effect of two symmetry operations ($\sigma + C_2$ or $\sigma + i$ and $C_2 + i$, respectively). The first pair is given as σ and C_2 , while the second pair is shown as $C_2 + i$ (the latter ones in parentheses) in Table IV. From the results one can see that it is more advantageous to use $C_2 + i$ or $\sigma + C_2$ operations than only one operation. It is also interesting, on the other hand, that these two pairs have the same effect (i.e. the number of blocks remaining to be calculated after their use is the same) as it is shown in Table IV. This implies that the reduction for the series C_2H_6, \dots is indifferent whether the σ and C_2 or σ and i or C_2 and i operations are used: the number of integrals to be calculated are the same in all three cases. From this it follows that the choice of the kind of two symmetry operations is not so important as it was in the case of only one operation.

Table IV
Effect of the first (and second) two symmetry operations

Groups	Two-center	Three-center	Four-center
C ₂ H ₆	6 (7)	11 (17)	16 (18)
	8 (5)	17 (11)	20 (14)
C ₃ H ₈	12 (14)	38 (43)	78 (85)
	15 (11)	44 (37)	88 (75)
C ₄ H ₁₀	20 (24)	80 (102)	238 (260)
	26 (18)	102 (80)	268 (230)
C ₅ H ₁₂	30 (36)	158 (180)	571 (615)
	38 (28)	182 (156)	625 (561)
C ₆ H ₁₄	42 (51)	259 (311)	1166 (1252)
	54 (39)	311 (259)	1270 (1148)
C ₇ H ₁₆	56 (68)	414 (469)	2140 (2281)
	71 (53)	472 (411)	2302 (2119)
C ₈ H ₁₈	72 (88)	600 (700)	3620 (3848)
	92 (68)	700 (600)	3880 (3588)
C ₉ H ₂₀	90 (110)	858 (966)	5765 (6101)
	114 (86)	970 (854)	6137 (5729)

5. Conclusion

We investigate in a series of papers the use of molecular symmetry in ab initio calculations. Special attention is paid to a study of large, related molecules, including also polarization functions into the basis set. In this paper the effect of the number of symmetry operations present has been discussed. It has been pointed out that it is worthwhile studying in advance the effect of the various symmetry operations, as their use influences much the number of integrals to be calculated. From this it follows that the kind as well as the number of symmetry operations should be carefully chosen. It was shown that by a preliminary estimation of the expected effect of the molecular symmetry (i.e. using a fast generation routine) the necessary computer time for the integral evaluation can be reduced.

Acknowledgements

Thanks are due to Zs. Ozoróczy for her help in some calculations. We are very much indebted to Dr. J. Pipek for many valuable discussions.

References

1. E. Kapuy and F. Török, *Quantum Theory of Atoms and Molecules*, Akadémiai Kiadó, Budapest, 1975.
2. P. Čárský and M. Urban, *Lecture Notes in Chemistry*, Springer-Verlag, Berlin, 1980.
3. J. J. Kaufman, P. C. Hariharan and H. E. Popkie, *Int. J. Quant. Chem. Symp.*, 15, 199, 1981.

4. P. D. Dacre, *Chem. Phys. Letters*, *7*, 47, 1970.
5. M. Elder, *Int. J. Quant. Chem.*, *7*, 75, 1973.
6. R. Ahlrichs, *Theoret. Chim. Acta (Berl.)*, *33*, 157, 1974.
7. M. Dupuis, J. Rys and H. F. King, *J. Chem. Phys.*, *65*, 111, 1976.
8. M. Dupuis and H. F. King, *Int. J. Quant. Chem.*, *11*, 613, 1977.
9. C. Kozmutza, *J. Mol. Structure (Theochem)*, (to be published).
10. C. Kozmutza, *Theoret. Chim. Acta (Berl.)*, *60*, 53, 1981.
11. C. Kozmutza and Zs. Ozoróczy, *Chem. Phys. Letters*, (submitted for publication).
12. W. J. Hehre, W. A. Lathan, R. Ditchfield, M. D. Newton and J. A. Pople, *Gaussian 70*, QCPE 236, Indiana University, Bloomington.
13. P. Pulay, *Theoret. Chim. Acta (Berl.)*, *50*, 299, 1979.
14. A. Veillard, IBMOL-4, Version 4, IBM. Res Laboratory, San José, California, 1968.

MOLECULAR SYMMETRY IN AB INITIO CALCULATIONS. II

USE OF LOCAL SYMMETRY IN THE INTEGRAL EVALUATION

F. BARTHA

*Department of Theoretical Physics, József Attila University
6720 Szeged, Hungary*

and

C. KOZMUTZA

*Quantum Theory Group, Physics Institute, Technical University
1521 Budapest, Hungary*

(Received 20 April 1984)

We investigate the use of molecular symmetry in ab initio calculations in a series of papers.

In this paper the effect of symmetry on the number of integrals to be calculated using different basis sets is studied. It is pointed out that this reducing effect strongly depends on the basis set used. When the participation of some groups is rather significant and the symmetry allows, the use of local symmetry can help in reducing the computational time.

1. Introduction

In a series of papers we investigate the role of molecular symmetry in ab initio calculations. Special attention is paid to the reduction of computational time and to the simplification of the integral as well as the SCF procedure by using symmetry operations.

In the first Part of this series [1] we dealt with the effect of the number of symmetry operations taken into account. It was pointed out there that using the symmetry in a so-called generation program, the non-redundant integrals can be "selected" preliminarily, i.e., the redundant ones can be eliminated without significant computational time.

In this paper we study the effect of the molecular symmetry on the number of integrals to be calculated by using different basis sets. The possibility of using local symmetry is also investigated.

2. Various basis sets in use

The quantum chemical methods most widely used are based on the expansion of atomic orbitals as a linear combination of basis functions (LCAO method). The ensemble of these latter functions are referred to as basis set. There are different basis

sets in general use: their difference lies in the exponents, the contraction, the number of functions, etc. The basis functions are usually Slater- or Gaussian-type ones, those of other types (as one-centre expansion, etc.) are less known. The exponents are optimized, while the contraction is important in cases of Gaussian-type functions.

Depending on the number of basis functions there are several types of basis sets: ranging from the minimum set, to double-zeta and extended sets, where these latter (especially in cases of molecules) possess also polarization functions. The name "polarization" is not too felicitous, but commonly used. These functions account for a better description of the electron density distribution in molecules. The presence of polarization functions is equivalent to the inclusion of atomic orbitals with higher azimuthal quantum numbers into the basis set. The importance of a good choice of the basis set for the treatment of molecules by *ab initio* methods is described e.g. in [2], and details are also given e.g. in [3]. Regarding the studies that concern the selection of appropriate basis sets, the following can be stated:

- a) a minimum basis set is adequate for a preliminary estimation of the total energy as well as to obtain an initial vector set for later SCF calculations;
- b) a so-called well-balanced [4] basis set is necessary for a large decrease in the total energy;
- c) the inclusion of polarization functions is essential on the central/heavy atoms for an acceptable description of the molecular geometry, the electron spectra, etc.;
- d) the presence of p-type diffuse functions (generally on the hydrogen) is inevitable when computing electron affinities, polarizabilities, energies of reactions, etc.

It must be added that from the theoretical point of view (in comparison to the above four points where the basis sets are required to be adequate for calculations of experimentally measurable quantities) the largest possible basis sets are topical when one wants to go beyond the Hartree-Fock limit. This implies that for the calculation of correlation energies, e.g. the d- (or of even higher azimuthal quantum numbers) type functions on the heavy atoms as well as the p-type diffuse ones on the hydrogens must be added to the basis set.

It is evident, on the other hand, that the number of integrals (especially that of two-electron integrals) can be drastically decreased by using symmetry. It is not trivial, however, and not yet investigated elsewhere, whether the role of the use of symmetry operations is the same or different when using various basis sets. It was only pointed out by several authors that the number of integrals to be calculated is roughly equal to the original ones divided by the number of symmetry operations. As a consequence, when studying thoroughly the effect of molecular symmetry in the integral evaluation, as we do in this paper, various basis sets are to be investigated.

For this study we have chosen four different basis sets in accordance with the points a)–d) as described above. The four sets are STO-3G [5], 6-31G [6], 6-31G/d [7] and 6-31G/d + p [7]. The references cited are the ones where these sets were introduced.

Closed-shell systems as C_2H_6 , C_3H_8 and C_4H_{10} were investigated by using our method [1, 8]. All of these molecules belong to a symmetry point group with three

symmetry operations. Before studying the effect of symmetry on the number of integrals to be calculated, have a look at the number of integrals for the different groups that occur when computation is carried out for these systems (Table I). Only some interesting results will be pointed out:

- there are certain three-center groups that have the largest number of integrals (and not the four-center ones, as it would have been expected);
- the groups with the largest number of integrals are few, there is only one CCC group, e.g., in C_3H_8 , but some dozens of HHH ones;

Table I
Number of integrals for various groups by different basis sets

	STO-3G	6-31G	6-31G/d	6-31G/d+p
One-centers				
C	120	1035	7260	7260
H	1	6	6	120
Two-centers				
CC	1300	12636	93825	93825
CH	110	1170	4515	14775
HH		43	43	1300
Three-centers				
CCC	3000	30618	232875	232875
CCH	450	5103	22275	60750
CHH	60	756	1800	14625
HHH	6	84	84	3000
Four-centers				
CCCC	1875	19683	151875	151875
CCCH	375	4374	20250	50625
CCHH	75	972	2700	16875
CHHH	15	216	360	5625
HHHH	3	48	48	1875

Table II
Number of integrals when using three symmetry operations

	STO-3G	6-31G	6-31G/d	6-31G/d+p	
C_2H_6	Two-centers	1764	17574	112143	160725
	Three-centers	1476	17514	61254	271125
	Four-centers	648	8712	20808	180000
C_3H_8	Two-centers	3520	35062	224200	318850
	Three-centers	8262	92526	459303	1150125
	Four-centers	3861	49818	149286	901875
C_4H_{10}	Two-centers	6580	65229	430125	572100
	Three-centers	17292	193578	959388	2386500
	Four-centers	14475	180459	659835	2941875

c) the number of integrals of an only group (as follows partly from b)) can dominate the total amount of integrals to be calculated.

This latter statement can be justified by looking at Table II summarizing the total number of integrals for two-, three- and four-center blocks (the one-center ones are less important).

From the results one can see that

- a) for systems like C_2H_6 the only C-C block is responsible for more than 50% of the total number of integrals to be calculated, e.g., by basis set 6-31G/d;
- b) similarly, this percentage is valid for C_3H_8 and its CCC group;
- c) as for C_4H_{10} the CCCC group for basis set 6-31G is not so dominant, and this is also true for the 6-31G/d basis set.

What conclusion could be drawn concerning the various basis sets? The results obtained suggest that

- a) there is no significant problem when using a minimal basis set, as the number of two-electron integrals is not too large, anyway;
- b) when a 6-31G basis set is used, the number of integrals is much increased even in comparison to the next basis 6-31G/d, i.e. the symmetry has a relatively smaller reduction effect than in the case of other basis sets;
- c) owing to the three symmetry operations used, the number of integrals to be calculated is drastically diminished in spite of the presence of polarization function on the carbon atoms in basis 6-31G/d;
- d) it is the number of three- and especially that of the four-centers that increase significantly when basis 6-31G/d + p is used, but these integrals involve mostly s and p type functions and only a few d type ones, therefore their calculation does not require considerable computational time.

From the above it follows that the use of three symmetry operations has the largest effect (among the studied basis sets) on the third basis, i.e. the 6-31G/d. As a consequence, the question arises: what to do when there is no such high symmetry? Here it should be noted that some computer programs are devoted to very effective calculations on molecules with high symmetry, but the same programs do not work successfully for less symmetric systems. Our program is worked out also for the latter case, where local symmetry can be used.

3. Use of local symmetry

The same calculations were carried out by using only the first symmetry operation (a mirror of plane) in order to make a comparison to the case of three symmetry operations. The results are given in Table III. From the results one can see that if only one symmetry operation is taken into account, the necessary computational work increases (as evident) significantly, but the increase is different for the different groups and basis sets. The most important fact is that the participation from the total

number of integrals is the largest for some special groups (containing the heavy atoms). From this it follows that if one can calculate the C-C bond of C_2H_6 , e.g. by using three symmetry operations then the remaining number of integrals is not too high even for an evaluation by using one mirror of plane. A similar conclusion holds for the case of C_3H_8 and its CCC groups. As a consequence, in a related series like C_2H_5-F , C_2H_5-OH , $C_2H_5-NH_2$, etc., the CC group can be treated by using a C_{2v} symmetry even if the total molecular point group has only one symmetry element. This solution helps to avoid the extensive calculations in less symmetric cases. This option is built in into our program named SYCETY [9] with which we are about to perform a series of calculations.

Table III

Number of integrals when using one symmetry operations

		STO-3G	6-31G	6-31G/d	6-31G/d+p
C_2H_6	Two-centers	2 216	22 383	130 332	223 725
	Three-centers	2 952	35 028	122 508	542 250
	Four-centers	1 062	14 364	33 372	303 750
C_3H_8	Two-centers	5 614	56 146	349 888	523 900
	Three-centers	12 816	146 055	656 004	1 939 125
	Four-centers	6 984	90 438	266 154	1 657 500
C_4H_{10}	Two-centers	10 540	104 971	672 385	950 050
	Three-centers	34 584	387 156	1 918 776	4 773 000
	Four-centers	26 295	331 035	1 140 315	5 544 375

Table IV

Number of blocks with the largest number of integrals

	C_2H_6	C_3H_8	C_4H_{10}
One-centers			
C	1	1	1
H	1	1	1
Two-centers			
CC	1	2	4
CH	4	8	12
Three-centers			
CCC	0	1	2
CCH	2	8	18
Four-centers			
CCCC	0	0	1
CCCH	0	3	12
CCHH	6	12	75

Table IV summarizes the number of blocks which contain the largest number of integrals to be calculated for the studied systems. Comparing these figures to those given in Table I it is easy to point out that the necessary computational work can be significantly decreased by using local symmetry for these groups.

Acknowledgements

Thanks are due to Prof. E. Kapuy for many valuable discussions.
The calculations were performed on an R-55 Computer (József Attila University, Szeged, Hungary).

References

1. F. Bartha, E. Kapuy and C. Kozmutza, *Acta Phys. Hung.*, **58**, 219, 1985.
2. E. Kapuy and F. Török, *Quantum Theory of Atoms and Molecules*, Akadémiai Kiadó, Budapest, 1975.
3. P. Cársky and M. Urban, *Lecture Notes in Chemistry*, Springer-Verlag, Berlin, 1980.
4. R. S. Mulliken, *J. Chem. Phys.*, **36**, 3428, 1962.
5. W. J. Hehre, R. F. Stewart and J. A. Pople, *J. Chem. Phys.*, **51**, 2657, 1969.
6. W. J. Hehre, R. Ditchfield and J. A. Pople, *J. Chem. Phys.*, **56**, 2257, 1972.
7. P. C. Hariharan and J. A. Pople, *Theoret. Chim. Acta (Berl.)*, **28**, 213, 1973.
8. C. Kozmutza, *J. Mol. Structure (Theochem)*, (submitted for publication).
9. C. Kozmutza, *Theoret. Chim. Acta (Berl.)*, **60**, 53, 1981.

SCHWINGER MODEL IN TEMPORAL GAUGE

J. BALOG

Roland Eötvös University, Budapest

and

P. HRASKÓ

Central Research Institute for Physics, Budapest

(Received 10 May 1984)

Exact solution of the zero-mass Schwinger model is given in temporal gauge in the presence of arbitrary background charge density. The structure of the Hilbert space is found to be considerably simpler than in Landau gauge. Unitarily implementable c -number gauge transformations are compared with the corresponding transformations in the Landau gauge. The operator solution is extended to the many flavour model and a procedure is suggested for the construction of the physical Hilbert space.

1. Introduction

The Schwinger model has attracted the attention of theoreticians since the time of its invention twenty years ago [1]. During this period much effort has been made to display the content and peculiarities of the model as explicitly as possible. The model permits one to study many intriguing aspects of quantum field theory on an example which, though much simpler than realistic theories, is far from being trivial.

Our study of the model was inspired by the recent results [2], concerning the classification of the family of allowed gauge transformations. Usually this kind of problems is attacked by topological methods [3, 4], but as pointed out in [2] an alternative approach is also possible. According to this latter point of view, the allowed gauge transformations are those which can be unitarily implemented in the Hilbert space. In this method topological considerations are abandoned altogether and they are replaced by purely quantum-mechanical Hilbert-space methods. In [2] unitarily implementable gauge transformations were found to be characterized by a pair of integers and only one of these classes was connected continuously to the identity. The remaining configurations are supposed to be the analogues of the instantons and merons of four-dimensional theories. Remarkably, this classification scheme was obtained in [2] without invoking topological arguments.

The considerations in [2] were confined to Landau gauge and one may wonder whether the classification scheme found in this peculiar gauge survives under other

gauge conditions, too. The question is all the more justified since the arguments in [3, 4] which led to the notion of Θ vacua in four-dimensional non-Abelian gauge theories were based on the temporal ($A_0=0$) gauge. This latter time-independent gauge condition is especially suitable when one is to survey the implications of the topologically non-equivalent configurations on the vacuum while the Landau-gauge condition ($\partial_\mu A^\mu=0$) seems in this respect less natural. Indeed, the gauge functions Λ in the Landau gauge must obey the equation $\square\Lambda=0$. Therefore, they are functions of either x^0+x^1 or x^0-x^1 and, hence, inevitably depend on time contrary to the geometrical picture one usually has in mind. Using temporal gauge, one can avoid this inconvenience.

Both Landau and temporal-gauge conditions fix the vector potential only partially and leave open the possibility of a rich variety of gauge transformations. Following [2], we confine ourselves to c -number gauge transformations. In order to study them in the spirit of [2] we first had to solve the Schwinger model in the temporal gauge. Section 3 will be devoted to the description of this solution which has several new elements with respect to the well-known solution of Lowenstein and Swieca [5] in the Landau gauge. In particular, the characterization of that factor of the Hilbert space where the subsidiary condition acts is substantially simpler in the temporal gauge. The structure of the Hilbert space remains relatively simple even if the number of the distinct fermions exceeds one, therefore, temporal gauge seems more promising for a complete characterization of the Hilbert space of the many-flavour Schwinger model. Our preliminary results in this direction are described in Section 7.

Having obtained the exact solution of the single-flavour model in the $A_0=0$ gauge, it becomes possible to enumerate those gauge transformations which are implementable in the Hilbert space. It turns out that, unlike the case of the Landau gauge, in our solution the allowed gauge transformations do not split into disjoint classes, all of them being continuously connected to the identity.

In the Landau gauge the implementable gauge functions were those whose asymptotic values $\Lambda(\pm\infty)$ at a given moment of time differed from each other in an integer multiple of π . Clearly, only the class in which $\Lambda(\infty)=\Lambda(-\infty)$ is coupled continuously to the identity. In the temporal gauge, on the contrary, the difference of the asymptotic values of the gauge functions is not quantized, therefore, they cannot be characterized by discrete numbers which would play the role of topological quantum numbers.

The reason for this sharp difference in the two gauges can be traced to the fact that while the Hilbert space of the Lowenstein–Swieca solution contains a free zero-mass fermion our solution in the temporal gauge does not involve such a field. Instead, the fermionic character of the field $\psi(x)$ is ensured by means of a gauge-invariant fermionic operator which is constant over space-time. Since in [2] the confinement of $\Lambda(\infty)-\Lambda(-\infty)$ to discrete values came entirely from the condition of implementability of the fermion gauge transformations it is of no surprise that our solution does not lead to such a restriction.

After the completion of this work in preprint form [15] there appeared a paper of Becher [16] which deals with the same problem, however, with different conclusions on the implementability of gauge transformations in the temporal gauge. Becher's solution for the Schwinger model in temporal gauge uses different building-block fields and is entirely different from ours. In his solution the allowed gauge transformations are quantized precisely for the same reason as in the Landau gauge: this solution has a free fermion field among the building blocks.

In Section 6 questions connected with chiral invariance will be discussed. From the point of view of their physical content solutions in the Landau and temporal gauges are completely equivalent. In particular, both of them have degenerate vacua characterized by an angle Θ . The physical interpretation of this degeneracy given by Coleman [6] connects Θ with background charges at large distance. Our solution can be extended so as to include the effect of an arbitrary background charge density and with the aid of this solution the clarification of the connection between Θ and the background charges becomes straightforward.

Our study of the Schwinger model in the temporal gauge remains incomplete since we disregarded Poincaré symmetry, i.e. the requirement of implementation of the Poincaré group in the Hilbert space of the solution. Just as in the case of the Coulomb-gauge, Lorentz transformations under the condition $A_0=0$ involve operator valued gauge transformations. No attempt will be made here to construct the corresponding representation of the Poincaré group.

2. Formulation of the model in temporal gauge

The construction of the Hamiltonian from the Lagrangian

$$\mathcal{L} = \frac{1}{2} (\partial_1 A_0 - \partial_0 A_1)^2 + e j^\mu A_\mu + \mathcal{L}_\psi$$

involves the first class constraints [7]

$$\Pi_0(x) = 0, \quad \partial_1 \Pi_1(x) + e j^0(x) = 0,$$

where Π_μ is the canonical momentum conjugate to A_μ , the physical meaning of Π_1 being the electric field E . The constraints must be appropriately incorporated into the Hamiltonian density

$$\mathcal{H} = \Pi_1 \partial_0 A_1 - \mathcal{L} = \frac{1}{2} \Pi_1^2 + \Pi_1 \partial_1 A_0 - e j^\mu A_\mu + \mathcal{H}_\psi.$$

We will, therefore, work with the extended Hamiltonian

$$H = \int \mathcal{H} dx^1 + \int v_1 \Pi_0 dx^1 + \int v_2 \cdot (\partial_1 \Pi_1 + e j^0) dx^1,$$

where v_1 and v_2 are arbitrary functions of the dynamical variables.

Gauge fixing proceeds as follows. One may simply choose the functions v_i arbitrarily and use the constraints as conditions imposed on the physical states. For example, the choice $v_1 = \frac{1}{2} \lambda \Pi_0 + \partial_1 A_1$, $v_2 = 0$ with $\lambda = \text{const.}$ leads to the family of covariant gauges. Alternatively, one may postulate one or two subsidiary conditions, prescribing zero value for some non gauge-invariant functions of the dynamical variables and adjust v_1 and v_2 so as to ensure the independence of these subsidiary conditions of time. Then one has to introduce new star brackets which permit one to satisfy the subsidiary conditions and the corresponding constraints as operator identities. This is always possible since the subsidiary conditions, owing to their non gauge-invariance, give non-zero Poisson bracket with at least one of the constraints. Those constraints which are not satisfied identically will continue to select the physical subspace of the Hilbert space.

Temporal gauge corresponds to the subsidiary condition $A_0 = 0$. This condition gives non-zero Poisson bracket with Π_0 . Hence, $A_0 = 0$ and $\Pi_0 = 0$ must be satisfied identically. As explained in [7] this amounts to simply omit A_0 and Π_0 from further considerations without altering the Poisson brackets between the remaining variables. The constancy of A_0 in time will be ensured if we put v_1 and v_2 equal to zero, so the Hamiltonian may be written as

$$H = \int dx^1 \left(\frac{1}{2} \Pi_1^2 - e^{j1} A_1 + \mathcal{H}_\psi \right).$$

Now we can formulate those conditions which are imposed on the exact solution in the temporal gauge. One has to find three operator fields $A_1(x)$, $\Pi_1(x)$, $\psi(x)$ which satisfy the following set of equations of motion, equal time commutation relations and subsidiary conditions:

i) equations of motion:

$$\begin{aligned} \dot{\Pi}_1 &= e^{j1}, \\ \dot{A}_1 &= \Pi_1, \\ i\gamma^\mu \partial_\mu \psi &= -e\gamma_1 A_1 \psi, \end{aligned} \quad (2.1)$$

ii) equal-time commutation relations:

$$\begin{aligned} [A_1(x), \Pi_1(x')] &= i\delta(x-x'), \\ \{\psi(x), \psi^+(x')\} &= \delta(x-x'), \\ [A_1(x), A_1(x')] &= [\Pi_1(x), \Pi_1(x')] = \{\psi(x), \psi(x')\} = \\ &= [A_1(x), \psi(x')] = [\pi_1(x), \psi(x')] = 0, \end{aligned} \quad (2.2)$$

iii) subsidiary conditions on the physical state vectors:

$$[\partial_1 \Pi_1(x) + e^{j0}(x)] |\Phi\rangle = 0.$$

In the next Section we will give the solution of this set of equations. In this solution the gauge fixing is incomplete since gauge transformations $A_1 \rightarrow A_1 + \partial_1 \Lambda$ with time-independent Λ are still allowed. A complete gauge fixing would also be possible by imposing the pair of covariant subsidiary conditions $A_\mu = 0$. Curiously enough, this condition expresses the complete absence of any vector potential. If one chooses $v_1 = 0$, $\partial_1 v_2 = \frac{1}{2} \Pi_1 + \partial_1 A_0$ the equations of motion will preserve this subsidiary condition. Now all the constraints and subsidiary conditions are to be satisfied identically, therefore, the Hamiltonian reduces to

$$H = \int dx^1 \left(\frac{1}{2} \Pi_1^2 + \mathcal{H}_\psi \right).$$

In the construction of the star bracket we follow the prescription of Dirac [7], according to which for two arbitrary dynamical quantities ξ and η at a given moment of time the star bracket is given by the formula

$$(\xi, \eta)^* = (\xi, \eta) - \sum_{ss'} \int dx dx' (\xi, w_s(x)) c_{ss'}(x, x') (w_{s'}(x'), \eta),$$

where $(,)$ denotes Poisson-bracket, x and x' stand for x^1 and $x^{1'}$,

$$w_1 = \partial_1 \Pi_1 + ej^0, \quad w_2 = A_1 \tag{2.3}$$

are the pair of nontrivial constraint and subsidiary condition and $c_{ss'}(x, x')$ is defined as an inverse matrix:

$$\sum_s \int dx' c_{ss'}(x, x') (w_{s'}(x'), w_{s''}(x'')) = \delta_{ss''} \delta(x - x').$$

Using (2.3) one easily finds that

$$(\xi, \eta)^* = (\xi, \eta) - \frac{1}{2} \int dx dx' \operatorname{sgn}(x - x') [(\xi, w_1(x)) (w_2(x'), \eta) + (\xi, w_2(x)) (w_1(x'), \eta)].$$

The equations of motion in this gauge are, therefore,

$$\dot{\Pi}_1(x) = (H, \Pi_1(x))^* = ej^1(x) \tag{2.4}$$

and

$$\dot{\psi}(x) = (H, \psi(x))^* = -\gamma^0 \gamma^1 \partial_1 \psi(x) + \frac{ie}{2} \int dx' \operatorname{sgn}(x' - x) \Pi_1(x') \psi(x)$$

which can also be written as

$$i\gamma^\mu \partial_\mu \psi = \frac{e}{2} \int dx' \operatorname{sgn}(x - x') \Pi_1(x') \gamma^0 \psi(x).$$

In calculating $\dot{\Pi}_1$ we used the relation $\int dx' (\mathcal{H}_\psi(x'), j^0) = \partial_1 j^1$ while for ψ the expression $(\psi(x), \psi^+(x')\psi(x')) = i\delta(x-x')\psi(x)$ was employed which is the Poisson bracket analogue of the commutator $[\psi(x), \psi^+(x')\psi(x')] = \delta(x-x')\psi(x)$.

The equation of motion (2.4) and the constraint $w_1=0$ combine into the covariant equation

$$j^\mu = \frac{1}{e} \varepsilon^{\mu\nu} \partial_\nu \Pi_1.$$

The list of the equal-time commutation relations is:

$$[\Pi_1(x), \Pi_1(x')] = -i(\Pi_1(x), \Pi_1(x'))^* = 0,$$

$$[\psi(x), \pi_1(x')] = -i(\psi(x), \Pi_1(x'))^* = \frac{e}{2} \operatorname{sgn}(x-x')\psi(x),$$

$$\{\psi(x), \psi^+(x')\} = \delta(x-x'),$$

$$\{\psi(x), \psi(x')\} = 0.$$

These expressions constitute the set of equations which an exact solution must satisfy under complete gauge fixing $A_\mu=0$. It is seen that though complete gauge fixing reduces the number of variables the Dirac equation becomes nonlocal and afflicted with an ordering problem. We will show in the next Section that when the gauge is only partially fixed no ordering problem arises in the Dirac equation.

3. Solution in the $A_0=0$ gauge

a) Building-block operators

We look for the solution in the form of the Ansatz

$$A_1(x, t) = \frac{e}{\pi} S(x, t) + \frac{1}{e} t \vartheta''(x) + \frac{1}{e} \lambda'(x),$$

$$\Pi_1(x, t) = A_1(x, t) = \frac{e}{\pi} \dot{S}(x, t) + \frac{1}{e} \vartheta''(x),$$

(3.1)

$$\psi(x, t) = Z : e^{ic(x,t)} : b,$$

$$c(x, t) = [S'(x, t) + t\vartheta'(x) + \lambda(x)] - \gamma_5 [\dot{S}(x, t) + \vartheta(x)]$$

which contains three different building-block operator fields S , ϑ and λ . S is a non-covariant free field which has the following explicit expression in terms of its creation and destruction operators:

$$S(x, t) = -i \int_{-\infty}^{\infty} \frac{dk}{\sqrt{4\omega^3}} \{a(k)e^{-i(\omega t - kx)} - a^+(k)e^{i(\omega t - kx)}\}; \quad \omega = \sqrt{k^2 + m^2}.$$

This field obeys the field equation $(\square + m^2)S = 0$, moreover, it is related to the massive boson field operator \tilde{S} of the Landau-gauge solution through the relation

$$\hat{S}(x, t) = -\sqrt{\pi} \tilde{S}(x, t).$$

The time independent fields $\vartheta(x)$ and $\lambda(x)$ are also real, "free" fields in the sense, that they are real linear combinations of their creation and destruction operators. We define their positive and negative "frequency" parts as

$$\langle 0 | \vartheta^-(x) = \langle 0 | \lambda^-(x) = 0,$$

$$\vartheta^+(x) | 0 \rangle = \lambda^+(x) | 0 \rangle = 0,$$

so the usual decomposition

$$\vartheta(x) = \vartheta^+(x) + \vartheta^-(x), \quad \lambda(x) = \lambda^+(x) + \lambda^-(x)$$

obviously holds for them. The explicit expression of these fields will be given in Section 4. In this Section we shall only make use of their commutation relations

$$[\vartheta^+(x), \vartheta^-(y)] = [\lambda^+(x), \lambda^-(y)] = 0, \quad (3.2)$$

$$[\vartheta^+(x), \lambda^-(y)] = \frac{i}{2} g(x-y), \quad (3.3)$$

where

$$g(x) = \frac{\pi}{2} \operatorname{sgn} x \{e^{-m|x|} - 1\}.$$

This function whose physical meaning becomes clear in Section 6 is fixed by the solution but the commutators (3.2) are not uniquely determined, their vanishing is but one possibility. However, the vanishing of the norm of the state $\vartheta^-(x) | 0 \rangle$ which follows from (3.2) is a necessary property of the solution.

The quantity b in ψ is a two-component object

$$b = \begin{pmatrix} b_L \\ b_R \end{pmatrix}$$

whose components are anticommuting unitary operators:

$$b_M b_M^+ = b_M^+ b_M = 1 \quad (3.4)$$

$$\{b_L, b_R\} = \{b_L, b_R^+\} = 0.$$

The commutation relations between b_M and b_M^+ , are the same as those of the so called "bleached" fields [5, 2] of the Landau gauge solution.

Finally, Z is a finite "renormalization" constant which is uniquely determined by the fermion anticommutation relations.* The value of Z will be given in the next subsection.

* For reasons which are not clear to us the analogous constant $Z' = \left(\frac{m'}{\mu}\right)^{1/4}$ (see Appendix) is often omitted from the Landau gauge solution (see e.g. [2]) though its existence is clearly understood.

b) Canonical commutation relations

The commutator function of the S field

$$[S^+(x, t), S^-(y, t')] = \Delta(x - y, t - t')$$

has the integral representation

$$\Delta(x, t) = \int_{-\infty}^{\infty} \frac{dk}{4\omega^3} e^{-i\omega t} e^{ikx}.$$

The function Δ can be expressed in terms of modified Bessel functions but for the calculation of the equal-time commutators it is sufficient to know its derivatives at $t \sim 0$:

$$\begin{aligned} \dot{\Delta}(x, 0) &= \frac{-i\pi}{4} e^{-m(x)}, \\ \ddot{\Delta}(x, 0) &= \frac{1}{4} \ln(m'^2 x^2) + G_1(x^2), \\ \Delta''(x, 0) &= \frac{1}{4} \ln(m'^2 x^2) + \frac{1}{2} + F_1(x^2), \end{aligned} \quad (3.5)$$

where $m' = \frac{1}{2} e^\gamma m$ (γ is Euler's constant), F_1 and G_1 are non-singular functions with the property $F_1(0) = G_1(0) = 0$.

The commutation relations (2.2) can be rewritten as

$$\begin{aligned} [A_1(x, t), A_1(y, t)] &= [\dot{A}_1(x, t), \dot{A}_1(y, t)] = 0, \\ [A_1(x, t), \dot{A}_1(y, t)] &= i\delta(x - y) \end{aligned} \quad (3.6)$$

and

$$[A_1(x, t), c(y, t)] = [\dot{A}_1(x, t), c(y, t)] = 0. \quad (3.7)$$

On the other hand, the equal-time commutation relations between the building-block fields are

$$\begin{aligned} [S(x, t), S(y, t)] &= [\dot{S}(x, t), \dot{S}(y, t)] = 0, \\ [S(x, t), \dot{S}(y, t)] &= if(x - y), \end{aligned} \quad (3.8)$$

and

$$\begin{aligned} [\vartheta(x), \vartheta(y)] &= [\lambda(x), \lambda(y)] = 0, \\ [\vartheta(x), \lambda(y)] &= ig(x - y), \end{aligned} \quad (3.9)$$

where

$$f(x) = -\frac{1}{m^2} g'(x). \quad (3.10)$$

Using (3.8), (3.9) and (3.10) it is easy to verify that (3.6) and (3.7) are satisfied provided

$$m^2 = \frac{e^2}{\pi}.$$

The verification of the fermion anticommutation relations is somewhat more difficult. For example, in order to verify the relation

$$\{\psi_L(x, t), \psi_L^+(y, t)\} = \delta(x, y)$$

we write, using (3.1) and (3.4)

$$\psi_L(x, t)\psi_L^+(y, t) = Z^2 : e^{i[c_L(x, t) - c_L(y, t)]} : e^{[c_L^+(x, t), c_L^-(y, t)]}.$$

Similarly,

$$\psi_L^+(y, t)\psi_L(x, t) = Z^2 : e^{i[c_L(x, t) - c_L(y, t)]} : e^{[c_L^+(y, t), c_L^-(x, t)]}.$$

Now, (3.1), (3.2), (3.3) and (3.5) permits us to calculate the commutator

$$\begin{aligned} [c_L^+(x, t), c_L^-(y, t)] = & -[\dot{A}(x-y, 0) + 2\dot{A}'(x-y, 0) + A''(x-y, 0)] + \\ & + ig(x-y) = -\ln(m'|x-y|) - \frac{i\pi}{2} \operatorname{sgn}(x-y) - \frac{1}{2} F[(x-y)^2], \end{aligned} \quad (3.11)$$

where $F(x^2) = F_1(x^2) + G_1(x^2)$. Writing the first two terms on the r.h.s. of (3.11) as $-\ln\{i[m'(x-y) - i\varepsilon]\}$ we obtain

$$\begin{aligned} \{\psi_L(x, t), \psi_L^+(y, t)\} = & Z^2 e^{-\frac{1}{2} F[(x-y)^2]} : e^{i[c_L(x, t) - c_L(y, t)]} : \\ & \cdot i \left\{ \frac{1}{m'(x-y) - i\varepsilon} + \frac{1}{m'(y-x) - i\varepsilon} \right\} = \delta(x-y) \end{aligned}$$

provided

$$Z = \sqrt{\frac{m'}{2\pi}} e^{\frac{1}{4}}.$$

c) The Dirac equation

The properties of the Δ and g functions lead to the vanishing of the commutator

$$\lim_{\varepsilon^\mu \rightarrow 0} [A_1^+(x + \varepsilon^1, t + \varepsilon^0), c^-(x, t)] = 0.$$

Thus the product $A_1(x, t)\psi(x, t)$ is a well-defined operator, posing no ordering problem. Then due to the relations

$$(\partial_0 - \varepsilon_M \partial_1)c_M = -e\varepsilon_M A_1$$

the Dirac equation holds in its naive form.

d) Currents

The electromagnetic current is defined via the gauge-invariant point-splitting procedure:

$$j_\mu(x, t) = \lim_{\varepsilon \rightarrow 0} \text{Herm} \psi(x + \varepsilon^1, t + \varepsilon^0) \gamma_\mu \exp \left\{ i e \int_{(x, t)}^{(x + \varepsilon^1, t + \varepsilon^0)} A_\alpha(z^1, z^0) dz^\alpha \right\} \psi(x, t).$$

Using this definition, we obtain

$$j_0 = -\frac{1}{\pi} (\mathcal{S}' + \mathcal{G}') \quad j_1 = -\frac{1}{\pi} \ddot{\mathcal{S}}.$$

This current is obviously conserved. The axial current

$$j_\mu^5 = \varepsilon_{\mu\nu} j^\nu$$

is not conserved and we have, instead, the anomaly equation

$$\partial^\mu j_\mu^5 = -\frac{e}{\pi} \dot{A}_1 = \frac{e}{2\pi} \varepsilon^{\mu\nu} F_{\mu\nu}$$

as an operator identity.

The Maxwell equation

$$\ddot{A}_1 + e j_1 = 0$$

holds as an operator equation and the subsidiary condition takes the form

$$A_1' + e j_0 = \frac{1}{e} w(x) \sim 0, \quad (3.12)$$

where $w(x)$ depends on the derivatives of \mathcal{G} :

$$w(x) = \mathcal{G}'''(x) - m^2 \mathcal{G}'(x).$$

4. The physical Hilbert space

Our operator solution is defined on the product space

$$\mathfrak{H} = \mathfrak{H}^{(s)} \otimes \mathfrak{H}^{(w)} \otimes \mathfrak{H}^{(b)}.$$

Here $\mathfrak{H}^{(s)}$ is the canonical Fock space of the S field, whereas the time independent operators \mathcal{G} , λ and the constant operators b_M act in $\mathfrak{H}^{(w)}$ and $\mathfrak{H}^{(b)}$, respectively. We choose the representation for \mathcal{G} and λ which is the simplest one, conforming with (3.2), (3.3), though possibly not the most economic. First we put

$$\mathcal{G}(x) = T_1(x) - T_2(x), \quad \lambda(x) = L_1(x) + L_2(x).$$

Here the fields with subscripts 1 and 2 are commuting independent fields of the same form except that the second one is quantized with indefinite metric. Now (3.2), (3.3) are satisfied if

$$[T_1^+(x), L_1^-(y)] = -[T_2^+(x), L_2^-(y)] = \frac{i}{4} g(x-y).$$

A solution of these relations is given by

$$T_i(x) = -\frac{1}{\sqrt{2}} [S_i'(x, 0) + \sqrt{\pi} \tilde{\eta}_i(x, 0)]$$

$$L_i(x) = \frac{1}{\sqrt{2}} [S_i(x, 0) + \sqrt{\pi} \eta_i(x, 0)].$$

Here S_1 and S_2 are expressed through their own creation and destruction operators in the same way as does S in terms of a and a^+ . The fields η_1 and η_2 are zero-mass scalar fields quantized also with opposite sign. This type of fields is well known from the Landau-gauge solution, however, for completeness we give their explicit representation and the list of some of their properties in the Appendix.

$H^{(w)}$ itself is a product of four Fock spaces:

$$\mathfrak{H}^{(w)} = \mathfrak{H}^{(s_1)} \otimes \mathfrak{H}^{(s_2)} \otimes \mathfrak{H}^{(\eta_1)} \otimes \mathfrak{H}^{(\eta_2)}.$$

It is an indefinite metric space due to the indefiniteness of $\mathfrak{H}^{(s_2)}$, $\mathfrak{H}^{(\eta_2)}$ and $\mathfrak{H}^{(\eta_1)}$. In order to obtain the positive definite physical Hilbert space \mathfrak{H}_{phys} we first define the subspace $\tilde{\mathfrak{H}}^{(w)}$ by the condition

$$w^+(x) | \Phi \rangle = 0 \quad (| \Phi \rangle \in \tilde{\mathfrak{H}}^{(w)}).$$

Actually, due to (3.2) the subsidiary condition is satisfied on $\tilde{\mathfrak{H}}^{(w)}$ in the wider sense

$$\langle \Phi_1 | F[w] | \Phi_2 \rangle = F[0] \langle \Phi_1 | \Phi_2 \rangle$$

for any functional F .

The space $\mathfrak{H}^{(w)}$ is built up from states containing both ϑ and λ type quanta. It is not difficult to show that since w commutes with ϑ but not with λ $\tilde{\mathfrak{H}}^{(w)}$ consists of states

$$| \Phi \rangle = | 0 \rangle_w + \int_{-\infty}^{\infty} f_1(x) dx \vartheta^-(x) | 0 \rangle_w + \int_{-\infty}^{\infty} f_2(x, y) dx dy \vartheta^-(x) \vartheta^-(y) | 0 \rangle_w + \dots$$

constructed from ϑ components alone. Due to (3.2) all terms of this sum except the first one are zero norm states. Since physical observables leave invariant both the positive and zero norm subspaces only the single state $| 0 \rangle_w$ of $\tilde{\mathfrak{H}}^{(w)}$ enters into the physical Hilbert space:

$$\mathfrak{H}_{phys} = \mathfrak{H}^{(s)} \otimes | 0 \rangle_w \otimes \mathfrak{H}^{(b)}.$$

Operators, commuting with $w(x)$, can be restricted to \mathfrak{H}_{phys} :

$$O \rightarrow O_P; \quad O_P = {}_w \langle 0 | O | 0 \rangle_w.$$

Of the building-block fields only λ does not commute with $w(x)$. Therefore, those operators which depend on λ , connect $|0\rangle_w$ with zero norm states and cannot be restricted to $\mathfrak{H}_{\text{phys}}$. Thus, as expected, A_1 and ψ are unphysical quantities. On the contrary, $\Pi_1 = F_{01}$ and j_μ can be restricted to $\mathfrak{H}_{\text{phys}}$ where they have the same form as in the Landau gauge:

$$F_{01(p)} = \frac{e}{\pi} \dot{S} = -\frac{e}{\sqrt{\pi}} \dot{\Sigma},$$

$$j_{0(p)} = -\frac{1}{\pi} \dot{S}' = \frac{1}{\sqrt{\pi}} \dot{\Sigma}',$$

$$j_{1(p)} = -\frac{1}{\pi} \ddot{S} = \frac{1}{\sqrt{\pi}} \ddot{\Sigma}.$$

Turning to the algebra (3.4), we observe that its simplest representation is a two dimensional one given by

$$b_L = ie^{i\theta} \sigma_1, \quad b_R = \sigma_2,$$

where σ_i are the Pauli matrices and θ is an arbitrary angle. These operators are formally gauge invariant but no local gauge invariant observable contains them separately. Local gauge invariant observables depend only on the product $U = b_R^\dagger b_L = e^{i\theta} \sigma_3$ so the algebra of local observables consists only of the two operators $\mathbf{1}$ and U . This algebra is reducible and $\mathfrak{H}^{(b)}$ can be confined to one of the eigenstates of σ_3 which will be denoted by $|\Theta\rangle$:

$$U |\Theta\rangle = e^{i\theta} |\Theta\rangle.$$

Hence,

$$\mathfrak{H}_{\text{phys}} = \mathfrak{H}^{(s)} \otimes |\Theta\rangle$$

and from the point of view of the algebra of observables solutions in the temporal and Landau gauges coincide. This is the expected result.

It is interesting to note that we arrived at the θ -vacuum description directly without the mediation of the discrete set of $|n\rangle$ vacua which necessarily appear when working in the Landau gauge [2]. Obviously we could also introduce a countable infinity of states, representing the algebra (3.4) by infinite matrices. However, unlike the $|n\rangle$ vacua, these states would be invariant with respect to the local gauge transformations. They could support the global gauge and chiral transformations which cannot be represented in the two-dimensional realization of (3.4). As explained at the end of Section 5 there is actually no need to enlarge $\mathfrak{H}^{(b)}$ beyond that given above since the physical consequences of the theory are independent of the realization chosen.

5. Gauge transformations

The field equations (2.1) and commutation relations (2.2) are formally invariant under the time-independent gauge transformations

$$A_1 \rightarrow A_1 + \frac{1}{e} A'(x),$$

$$\psi \rightarrow e^{iA(x)} \psi.$$

In terms of the building-block fields this transformation is accomplished by the displacement of the λ field

$$\lambda(x) \rightarrow \lambda(x) + A(x), \quad (5.1)$$

while all other fields remain unchanged.

Now we consider the question of unitary implementability of (5.1) since, as pointed out in [2], only those gauge transformations are actually allowed which can be implemented in the Hilbert space as unitary transformations.

If a unitary transformation, implementing (5.1), exists then it is given by the expression

$$\mathcal{U}[A] = e^{-\frac{i\pi}{m^2} \int_{-\infty}^{\infty} A(x) w(x) dx}.$$

Under the action of this transformation (5.1) splits into the following transformations:

$$\dot{S}_i \rightarrow \mathcal{U}[A] \dot{S}_i \mathcal{U}^+[A] = \dot{S}_i + \delta \dot{S}_i, \quad S'_i \rightarrow S'_i + \delta S'_i,$$

$$\eta_i \rightarrow \mathcal{U}[A] \eta_i \mathcal{U}^+[A] = \eta_i + \delta \eta_i, \quad \tilde{\eta}_i \rightarrow \tilde{\eta}_i + \delta \tilde{\eta}_i,$$

where

$$\delta S'_i = \delta \tilde{\eta}_i = 0,$$

$$\delta \dot{S}_i = \frac{1}{\sqrt{2} m^2} A''(x),$$

$$\delta \eta_i = \frac{1}{\sqrt{2}\pi} \left[A(x) - \frac{1}{m^2} A''(x) \right].$$

As explained in [2] the transformation $\eta \rightarrow \eta + \delta \eta$ is unitarily implementable if the Fourier transform of $\delta \eta$ at $k=0$ contains at most a $PP\left(\frac{i}{k}\right)$ singularity but no $\delta(k)$ type singularity (or worse). In terms of $A(x)$ this requirement means that $A(x)$ should have finite limits at $x = \pm \infty$ such that

$$A(\infty) = -A(-\infty). \quad (5.2)$$

If $A(x)$ approaches its limits at $x = \pm \infty$ fast enough so that $A''(x)$ is square integrable then [8] the transformation $S \rightarrow S + \delta S$ is also unitarily implementable.

Thus we have found that all local gauge transformations satisfying (5.2) are allowed. In contrast to topological considerations [3, 4] and to what happens in the Landau gauge [2] no quantization of the asymptotic value of A emerges in this gauge.

Since $A = \text{const.}$ does not satisfy (5.2) the global gauge transformations

$$A_1 \rightarrow A_1, \quad \psi \rightarrow e^{i\alpha} \psi$$

are not represented in the Hilbert space. The same is true for the chiral transformations

$$A_1 \rightarrow A_1, \quad \psi \rightarrow e^{i\gamma_5 \alpha_5} \psi,$$

which in terms of the building-block fields correspond to

$$\mathcal{G} \rightarrow \mathcal{G} - \alpha_5.$$

The non-implementability of global transformations is of no surprise since we know that these symmetries are not present in the physical spectrum of the model. In our solution the breakdown of these symmetries takes place already at the level of $\mathfrak{H}^{(b)}$ due to the fact that we have chosen the simplest two-dimensional representation of the algebra (3.4). It is, however, possible to represent (3.4) in an infinite dimensional space $\mathfrak{H}^{(b)}$ whose orthonormal basis vectors are

$$|n_R, n_L\rangle \quad n_R, n_L = 0, \pm 1, \pm 2 \dots$$

and the operators b_L, b_R are defined by

$$b_L |n_R, n_L\rangle = |n_R, n_L + 1\rangle,$$

$$b_R |n_R, n_L\rangle = (-1)^{n_L} |n_R + 1, n_L\rangle.$$

Now the unitary operators $\mathcal{U}(\alpha)$ and $\mathcal{U}_5(\alpha_5)$ defined as

$$\mathcal{U}(\alpha) |n_R, n_L\rangle = e^{i\alpha(n_R + n_L)} |n_R, n_L\rangle,$$

$$\mathcal{U}_5(\alpha_5) |n_R, n_L\rangle = e^{i\alpha_5(n_R - n_L)} |n_R, n_L\rangle$$

represent in $\mathfrak{H} = \mathfrak{H}^{(s)} \otimes \mathfrak{H}^{(w)} \otimes \mathfrak{H}^{(b)}$ the global gauge and chiral transformations:

$$\mathcal{U}(\alpha) b_M \mathcal{U}^\dagger(\alpha) = e^{i\alpha} b_M,$$

$$\mathcal{U}_5(\alpha_5) b_M \mathcal{U}_5^\dagger(\alpha_5) = e^{-i\alpha_5} b_M.$$

However, in order to have an irreducible representation of the algebra of local observables we have to restrict ourselves to the subspace

$$\mathfrak{H}_{\text{phys}}(\Theta) = \mathfrak{H}^{(s)} \otimes |0\rangle_w \otimes |\Theta\rangle,$$

where

$$|\Theta\rangle = \sum_{n_R, n_L} (-1)^{\lfloor \frac{n_L}{2} \rfloor} e^{\frac{i\Theta}{2}(n_R - n_L)} |n_R, n_L\rangle$$

depends on an arbitrary angle Θ . In this way we arrive precisely at the same $\mathfrak{H}_{\text{phys}}(\Theta)$ as in Section 4. The unitary operators $\mathcal{U}(\alpha)$, $\mathcal{U}_5(\alpha_5)$, b_L and b_R cannot be defined separately on $\mathfrak{H}_{\text{phys}}(\Theta)$ but the combination $U = b_R^+ b_L$ acts on $\mathfrak{H}_{\text{phys}}(\Theta)$ as multiplication by the phase factor $e^{i\Theta}$.

6. Solution in the presence of background charges

In temporal gauge it is particularly simple to calculate the response of the one dimensional electron-photon system to the presence of an external static $i_0(x)$ charge density. Inclusion of the corresponding term $ei_0 A_0$ into the Lagrangian density does not alter the field equations and commutation relations. The only change it induces is that the original subsidiary condition (3.12) has to be replaced by

$$\frac{1}{e} w(x) \sim -ei_0(x). \quad (6.1)$$

This modified subsidiary condition is satisfied on the subspace $\mathfrak{H}^{(w)}[i_0]$ whose elements are defined by

$$w^+(x) |\Phi[i_0]\rangle = -\frac{e^2}{2} i_0(x) |\Phi[i_0]\rangle.$$

The subspaces $\mathfrak{H}^{(w)}$ and $\mathfrak{H}^{(w)}[i_0]$ satisfying (3.12) and (6.1), respectively, are connected by the unitary transformation

$$\mathcal{U}[i_0] = e^{i \int_{-\infty}^{\infty} i_0(x) \lambda(x) dx}.$$

Though the gauge-variant operators $\lambda(x)$ cannot be restricted to $\mathfrak{H}^{(w)}[i_0]$ we have for arbitrary functions of $\mathfrak{H}(x)$ the relation

$$\langle \Phi^1[i_0] | F[\mathfrak{H}] | \Phi^2[i_0] \rangle = F[\mathfrak{H}_c] \langle \Phi^1[i_0] | \Phi^2[i_0] \rangle,$$

where

$$\mathfrak{H}_c(x) = \mathcal{U}^+[i_0] \mathfrak{H}(x) \mathcal{U}[i_0] - \mathfrak{H}(x) = - \int_{-\infty}^{\infty} g(x-y) i_0(y) dy. \quad (6.2)$$

In other words, on $\mathfrak{H}_{\text{phys}}[i_0]$ the operator $\mathfrak{H}(x)$ can be replaced by the c-number function $\mathfrak{H}_c(x)$. For example,

$$E(x) = \langle \dot{A}_1(x, t) \rangle = \frac{1}{e} \mathfrak{H}_c''(x) = -\frac{1}{e} \int_{-\infty}^{\infty} g''(x-y) i_0(y) dy.$$

Let us now consider the simple case when point charges of magnitude $\pm q$ are situated at the points $x = \pm L$. Classically a constant electric field of strength q would arise in the interval between the charges. The actual situation is, however, quite different (Fig. 1) since vacuum polarization leads to strong charge shielding, the electric

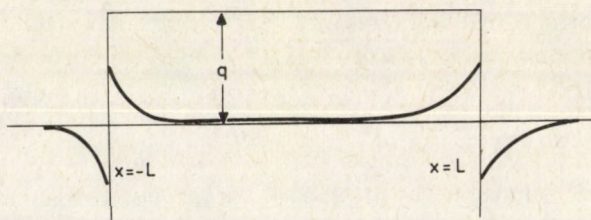


Fig. 1. The electric field between point charges

field of the external charges being completely compensated at a distance larger than $1/m$. Thus constant background field cannot be maintained in the model. As we carry the charges toward infinity the electric field tends rapidly to zero at every point. However, even in the limit $L \rightarrow \infty$ the presence of the charges is still observable. The chiral operator

$$B^-(x) = \frac{1}{2} \bar{\psi}(x) (1 - \gamma_5) \psi(x)$$

takes in \mathfrak{S} the form

$$B^-(x) = \frac{m'}{2\pi} : e^{2i\mathcal{S}(x,t)} : e^{2i\vartheta(x)} b_R^\dagger b_L.$$

Its restriction to $\mathfrak{S}_{\text{phys}}(\Theta)$ is given by

$$B_{(p)}^-(x) = \frac{m'}{2\pi} : e^{2i\mathcal{S}(x,t)} : e^{i\Theta}.$$

According to the rule established above, in the presence of external charges this expression obtains a phase factor:

$$B_{(p)}^-[i_0] = \frac{m'}{2\pi} : e^{2i\mathcal{S}(x,t)} : e^{2i\vartheta_c(x)} e^{i\Theta}.$$

From (6.2) we see that $\vartheta_c \rightarrow -\frac{q\pi}{e}$ as $L \rightarrow \infty$, so the effect of charges at infinity is

expressed in the phase shift $\Theta \rightarrow \Theta - \frac{2\pi}{e} q$ which is in principle an observable effect.

Thus Coleman's explanation [6] of the origin of the parameter Θ given originally for the massive version of the model with incomplete charge shielding is valid also in the massless case: the angle Θ is equal to $2\pi/e$ times the strength of the background electric field which would be present if there were no charge shielding. In both cases physics is periodic in q with period e .

7. Multifermion model

Consider the Lagrangian

$$\mathcal{L} = -\frac{1}{4} F_{\mu\nu} F^{\mu\nu} + \sum_{a=1}^n \bar{\psi}^a i \not{\partial} \psi^a$$

with an $SU_L(n) \otimes SU_R(n)$ "flavour" symmetry. It is straightforward to generalize the temporal gauge solution (3.1) to this theory:

$$A_1 = \sqrt{n} \frac{e}{\pi} S + \frac{1}{\sqrt{n}} \frac{1}{e} t \vartheta'' + \frac{1}{\sqrt{n}} \frac{1}{e} \lambda', \tag{7.1}$$

$$\psi_M^a = Z_n : e^{i c_M^a} : b_M^a,$$

where

$$Z_n = \frac{1}{\sqrt{2\pi}} e^{\frac{1}{4n} (m')^2 \frac{1}{(\mu)^2} (1 - \frac{1}{n})}$$

and

$$c_M^a = \frac{1}{\sqrt{n}} [(S' + t \vartheta' + \lambda) + \varepsilon_M (\dot{S} + \vartheta)] + 2\sqrt{\pi} \sum_{\alpha=1}^{n-1} T_\alpha^a \mu_M^\alpha.$$

Here the massive S field and the time-independent fields ϑ, λ are the same as in the single flavour case except that the mass m is now given by

$$m^2 = n \frac{e^2}{\pi}. \tag{7.2}$$

The η^α fields ($\alpha = 1, \dots, n-1$) are independent zero mass scalar fields (with $s = +1$, see Appendix). The $n \times (n-1)$ matrix T_α^a is chosen to satisfy the relations

$$\begin{aligned} \sum_{\alpha=1}^{n-1} T_\alpha^a T_\alpha^b &= \delta^{ab} - \frac{1}{n}, \\ \sum_{\alpha=1}^n T_\alpha^a &= 0, \\ \sum_{\alpha=1}^n T_\alpha^a T_\alpha^b &= \delta_{\alpha\beta}. \end{aligned} \tag{7.3}$$

Finally, $b_M^a (a = 1, \dots, n; M = L, R)$ are constant anticommuting unitary operators:

$$\begin{aligned} \{b_M^a, b_{M'}^b\} &= 0, \quad (M \neq M' \text{ or } a \neq b), \\ b_M^{+a} b_M^a &= 1. \quad (\text{no summation}) \end{aligned} \tag{7.4}$$

Using (7.2), (7.3) and (7.4) it can be verified that the field equations and the commutation relations are satisfied by the solution (7.1). The subsidiary condition $w \sim 0$ is the same as in the single-flavour case.

Operator solution of the multi-flavour Schwinger model has been given previously in Landau gauge [9] but, owing to the complicated nature of the subsidiary conditions, no satisfactory characterization of the physical Hilbert space has been achieved in that gauge. It is in this respect that temporal gauge seems preferable in spite of the fact that so far we have only partial success in this direction.

The physical (gauge invariant) operators can be restricted to

$$\mathfrak{H}_{\text{phys}} = \mathfrak{H}^{(s)} \otimes [\mathfrak{H}^{(n)}]^{n-1} \otimes \mathfrak{H}^{(b)}$$

since gauge invariant operators are independent of λ and in the absence of external charges \mathcal{Q} can be put equal to zero. However, $\mathfrak{H}_{\text{phys}}$ cannot be accepted as the true physical Hilbert space for the following reasons:

- 1) Due to the indefiniteness of $\mathfrak{H}^{(n)}$ (see Appendix) $\mathfrak{H}_{\text{phys}}$ is not positive definite.
- 2) Physical quantities depend on μ which is an arbitrary mass parameter (infrared cutoff).
- 3) Lorentz invariance is broken.
- 4) The algebra of the constant operators is non-Abelian even in the gauge-invariant sector. Therefore, there is no one-dimensional representation of the algebra and it is not possible to represent the full algebra of observables in a sector of the Hilbert space with a single vacuum.
- 5) Flavour symmetry is broken.

Owing to these difficulties, it is pointless to infer the physical spectrum from the form of $\mathfrak{H}_{\text{phys}}$, asserting, that it consists of one massive and $n-1$ massless free bosons [10, 11]. However, it seems plausible that all difficulties disappear simultaneously in the $\mu \rightarrow 0$ limit. Obviously it would be meaningless to go to this limit in the operator solution but the limit can be performed in the Wightman functions (WF).

Indeed, it can be shown that every WF is proportional to a nonnegative power of μ . Furthermore, the μ independent WF-s are those which are expectation values of Lorentz and $SU_L(n) \otimes SU_R(n)$ invariant operators. The part of these operators which belongs to $\mathfrak{H}^{(b)}$ contains only the combination

$$U_{(n)} = b_R^{+1} \dots b_R^{+n} b_L^1 \dots b_L^n,$$

which can be replaced in the Θ -sector by its eigenvalue $e^{i\Theta}$.

Having defined the WF-s in the $\mu \rightarrow 0$ limit, it becomes possible in principle to reconstruct the physical Hilbert space. We assume that this space is positive definite. However, in this route the explicit information on the structure of the physical states has been lost. Studying the Källén–Lehmann representation of the two-point functions of the theory, one can identify contributions of various $SU_L(n) \otimes SU_R(n)$ nonsinglet massless states, in particular those transforming according to the fundamental representation of $SU_L(n)$ or $SU_R(n)$. All these states are electrically neutral as already envisaged in [9]. The question of whether these contributions correspond to single particle asymptotic states requires further investigation.

We note finally that since flavour symmetry remains exact all fermion bilinears have vanishing vacuum expectation value [12]. The simplest operator which condensates is the $2n$ -fermion operator

$$\Delta_{(n)}(x_1, \dots, x_n) = \frac{1}{(n!)^2} \sum_{\substack{a_1 \dots a_n \\ b_1 \dots b_n}} \varepsilon^{a_1 \dots a_n} \varepsilon^{b_1 \dots b_n} \psi_R^{+a_1}(x_1) \psi_L^{b_1}(x_1) \dots \psi_R^{+a_n}(x_n) \psi_L^{b_n}(x_n).$$

This is an $SU_L(n) \otimes SU_R(n)$ singlet chirally non-invariant operator. Therefore, the order parameter

$$\delta_{(n)} = \langle \Theta | \Delta_{(n)}(x, x, \dots, x) | \Theta \rangle = \left(\frac{m'}{2\pi} \right)^n e^{i\Theta}$$

indicates the breakdown of the anomalous $U_{L-R}(1)$ symmetry. The meaning of Θ is the same as in the single flavour case, i.e. charges at infinity which in the absence of shielding would produce a background electric field E lead to the modified value of the order parameter:

$$\delta_{(n)}(E) = \left(\frac{m'}{2\pi} \right)^n e^{i(\Theta - \frac{2\pi}{e} E)}.$$

Appendix A

Notational conventions

We use the following conventions:

$$g_{00} = -g_{11} = 1,$$

$$\gamma^0 = \begin{pmatrix} 0 & 1 \\ 1 & 0 \end{pmatrix}, \quad \gamma^1 = \begin{pmatrix} 0 & 1 \\ -1 & 0 \end{pmatrix}, \quad \gamma^5 = \begin{pmatrix} -1 & 0 \\ 0 & 1 \end{pmatrix},$$

$$\varepsilon_{01} = \varepsilon^{10} = 1, \quad \varepsilon_{\mu\nu} = -\varepsilon_{\nu\mu}.$$

For massless fields we define the light-cone variables

$$x_M = x^0 + \varepsilon_M x^1, \quad M = L, R,$$

where

$$\varepsilon_L = 1, \quad \varepsilon_R = -1.$$

Then the massless Dirac equation and the massless Klein-Gordon equation have solutions of the form

$$\psi_0 = \begin{pmatrix} \psi_L(x_L) \\ \psi_R(x_R) \end{pmatrix} \quad f = f_L(x_L) + f_R(x_R)$$

with arbitrary functions ψ_M and f_M .

Appendix B

The massless η field

In two dimensions the theory of a free massless scalar field suffers from either the absence of translational invariance [13] or indefinite metric [14]. This is due to infrared difficulties specific to two dimensions.

In our solution we have several massless η -type fields. They are defined in an indefinite metric space and do not break translational invariance [2].

The η field splits into two light-cone components:

$$\eta = \eta_R(x_R) + \eta_L(x_L).$$

The massless pseudoscalar field $\tilde{\eta}$ is related to η by

$$\tilde{\eta} = \eta_R(x_R) - \eta_L(x_L).$$

In terms of creation and destruction operators

$$\eta_M(x_M) = \frac{1}{\sqrt{2\pi}} \int_0^\infty d\omega(k) \{ a_M(k) e^{-ikx_M} + a_M^+(k) e^{ikx_M} \}. \quad (\text{B.1})$$

Here the measure $\int_0^\infty d\omega(k)$ is defined as

$$\int_0^\infty d\omega(k) \cdot f(k) = -\frac{1}{2} \int_0^\infty dk \ln\left(\frac{k}{\mu'}\right) \frac{d}{dk} f(k), \quad (\text{B.2})$$

where μ' is an arbitrary mass parameter.

The commutation relations of a_M and a_M^+ are

$$[a_M(k), a_{M'}^+(k')] = 2sk \delta_{M'M} \delta(k' - k), \quad (\text{B.3})$$

where $s = \pm 1$. The metric is indefinite in both cases since the scalar product

$$\langle f | f \rangle = 2\pi s \int_0^\infty d\omega(k) |f(k)|^2$$

is itself an indefinite expression.

Using (B.1), (B.2) and (B.3) one finds the useful relations

$$[\eta_M^+(x_M), \eta_{M'}^-(y_{M'})] = -\frac{s}{4\pi} \delta_{M'M} \left\{ \ln \mu |x_M - y_M| + \frac{i\pi}{2} \text{sgn}(x_M - y_M) \right\},$$

$$[\eta^+(x), \eta^-(y)] = \frac{-s}{4\pi} \ln \{ -\mu^2(x-y)^2 + i\epsilon(x^0 - y^0) \},$$

where

$$\mu = e^y \mu'.$$

References

1. J. Schwinger, *Phys. Rev.*, *128*, 2425, 1962.
2. A. K. Raina and G. Wanders, *Ann Phys. (N. Y.)*, *132*, 404, 1981.
3. R. Jaçkiw and C. Rebbi, *Phys. Rev. Lett.*, *37*, 172, 1976.
4. C. G. Callan et al., *Phys. Lett.*, *63B*, 334, 1976.
5. J. H. Lowenstein and J. A. Swieca, *Ann. Phys. (N. Y.)*, *68*, 172, 1971.
6. S. Coleman, *Ann. Phys. (N. Y.)*, *101*, 239, 1976.
7. P. A. M. Dirac, *Lectures on Quantum Mechanics*, Belfer Graduate School of Science, Yeshiva University, New York, 1964.
8. Ф. А. Березин, *Метод вторичного квантования*, Наука, Москва, 1965.
9. V. Kurak et al., *Nucl. Phys.*, *B134*, 61, 1978.
10. G. Segre and W. I. Weisberger, *Phys. Rev.*, *D10*, 1976, 1974.
11. H. Minakata, *Phys. Rev.*, *D27*, 395, 1983.
12. S. Coleman, *Commun. Math. Phys.*, *31*, 259, 1973.
13. B. Klaiber, in *Lectures on Theoretical Physics*, Boulder Lectures, 1967, Gordon and Breach, New York, 1968.
14. A. S. Wightman, *Introduction to some Aspects of Quantized Fields*, in "Lecture Notes, Cargese Summer School, 1964", Gordon and Breach, New York, 1964.
15. J. Balog and P. Hráskó, KFKI preprint, KFKI-1983-39.
16. P. Becher, *Ann. Phys. (N. Y.)*, *143*, 223, 1983.

ON THE INITIAL-VALUE PROBLEM OF LINEARIZED EINSTEIN'S EQUATIONS

A. MÉSZÁROS

*Central Research Institute for Physics
1525 Budapest, Hungary**

(Received in revised form 14 June 1984)

It is shown that in the absence of sourceless weak gravitational waves the linearized theory of gravitation is necessarily Lorentz covariant.

It is well-known (see, e.g. [1], Chapter 10) that the investigation of weak (linearized) Einsteinian gravitation is usually done in harmonic systems only. The form of linearized Einstein's equations in an arbitrarily chosen $(x) \equiv (x^0, x^1, x^2, x^3)$ harmonic system is

$$\square h^{ij}(x) = 16\pi \cdot \left(T^{ij}(x) - \frac{1}{2} \eta^{ij} \cdot T(x) \right), \quad T(x) \equiv T^i_i(x), \quad (1)$$

$$h^{ij}(x)_{,j} = \frac{1}{2} h(x)^i, \quad h(x) \equiv h^i_i(x). \quad (2)$$

In this paper the dependence on x denotes the dependence on four x^i coordinates; $T^{ij}(x)$ is the energy-momentum tensor; the index after a comma denotes partial differentiation (e.g. $h^{ij}(x)_{,j} \equiv \frac{\partial h^{ij}(x)}{\partial x^j}$); the system $c = G = 1$ is used, c is the velocity of light and G is the gravitational constant; $\eta^{ij} = \eta_{ij} \equiv \text{diag}(1, -1, -1, -1)$ is the Minkowski's tensor; the indices are moved using the Minkowski's tensor; $\square \equiv \frac{\partial^2}{\partial x^i \partial x_i}$. The ten $h^{ij}(x)$'s are defined by

$$g^{ij}(x) = \eta^{ij} + h^{ij}(x), \quad |h^{ij}(x)| \ll 1, \quad (3)$$

where $g^{ij}(x)$ is the contravariant metric tensor. If $(x) \equiv (x^0, x^1, x^2, x^3)$ is a harmonic system, then the transformed system $(\bar{x}) \equiv (\bar{x}^0, \bar{x}^1, \bar{x}^2, \bar{x}^3)$ is a harmonic one too, if the form of the coordinate transformation is given by

$$\bar{x}^i(x) = x^i + y^i(x), \quad \square y^i(x) = 0, \quad (4)$$

* Permanent address: Department of Astronomy and Astrophysics, Charles University, 15000 Prague-5, Švédská 8, ČSSR

where $y^i(x)$'s are infinitesimal. The relations (1)–(4) in detail are given, e.g. in [1] in Chapters 7.4 and 10.1.

In linearized Einstein's theory the global Lorentz transformations

$$\bar{x}^i(x) = L_j^i \cdot x^j + b^i \quad (5)$$

are allowed too (see, e.g., [2], Box. 18.2), where L_j^i, b^i are constants. Therefore we shall assume that in (4) $y^i(x)$ may be given by

$$y^i(x) = L_j^i \cdot x^j - x^i + b^i, \quad (6)$$

too.

The solutions of wave equations (1) are usually given by the well-known retarded potentials (see, e.g. [2], Chapter 18.4). This paper investigates again the rightfulness of these solutions.

From the theory of wave equation (see, e.g. [3]) it follows that equations (1) have unambiguous solutions if $h^{ij}(x)$ and $h^{ij}(x)_{,k}$ are given on a spacelike hypersurface, which is defined by relation $p(x) = 0$ and is extending to spacelike infinity. In other words the initial-value data $h^{ij}(x)|_{p(x)=0}$ and $h^{ij}(x)_{,k}|_{p(x)=0}$ are given. In this case the wave equations (1) have unambiguous solutions "above" the $p(x) = 0$ hypersurface. (An (x^0, x^1, x^2, x^3) point is "above" the $p(x) = 0$ if $x^0 > x^{*0}$, where x^{*0} is defined by $p(x^{*0}, x^1, x^2, x^3) = 0$. The set of all points "above" gives the "above" part of space-time, i.e. the future Cauchy development of $p(x) = 0$; see, e.g. [4], Chapter 6.5. We may solve the Eq. (1) in the past Cauchy development of $p(x) = 0$, too.) The hypersurface $p(x) = 0$ is usually defined by $p(x) \equiv x^0 - \text{const} = 0$; in this case this hypersurface is the entire three-dimensional space at the time $x^0 = \text{const}$.

Let the $h^{ij}(x)|_{p(x)=0}$ and $h^{ij}(x)_{,k}|_{p(x)=0}$ initial-value data be given, then the solutions of (1) "above" $p(x) = 0$ are given by

$$h^{ij}(x) = {}^I h^{ij}(x) + {}^{II} h^{ij}(x). \quad (7)$$

The ten ${}^I h^{ij}(x)$'s are the solutions of (1) if $h^{ij}(x)|_{p(x)=0} = 0$ and $h^{ij}(x)_{,k}|_{p(x)=0} = 0$ (these are the so-called zero initial-value data); the ten ${}^{II} h^{ij}(x)$'s are the solutions of (1) with $T^{ij}(x) - \frac{1}{2} \eta^{ij} \cdot T(x) = 0$, but $h^{ij}(x)|_{p(x)=0}$ and $h^{ij}(x)_{,k}|_{p(x)=0}$ are non-zero. This decomposition of the solution of the wave equation is explained in [3], Chapter 33. The ten ${}^I h^{ij}(x)$'s are zero if $T^{ij}(x) - \frac{1}{2} \eta^{ij} \cdot T(x) = 0$; the ten ${}^{II} h^{ij}(x)$'s are zero if the initial-value data are zero. The ten ${}^I h^{ij}(x)$'s are the solutions with sources ("the weak gravitational waves having sources"); the ten ${}^{II} h^{ij}(x)$'s are the solutions having no sources ("the sourceless weak gravitational waves"). From the theory of wave equation ([3], Chapter 34.5) it follows that the ten ${}^I h^{ij}(x)$'s are the retarded potentials if $p(x) \equiv x^0 - \text{const} = 0$. Therefore the zero initial-value data are the necessary conditions (1) to have solutions containing retarded potentials only. If $p(x) \equiv x^0 - \text{const} = 0$ is chosen, then the zero initial-value data are sufficient conditions too.

We assume that

$$h^{ij}(x)|_{p(x)=0}=0, \quad h^{ij}(x)_{,k}|_{p(x)=0}=0 \quad (8)$$

is true in an $(x) \equiv (x^0, x^1, x^2, x^3)$ harmonic system. With that we have assumed that there are no sourceless weak gravitational waves in nature. For what other $(\bar{x}) \equiv (\bar{x}^0, \bar{x}^1, \bar{x}^2, \bar{x}^3)$ harmonic systems are the zero initial-value data true? The system $(\bar{x}) \equiv (\bar{x}^0, \bar{x}^1, \bar{x}^2, \bar{x}^3)$ is obtained by transformation (4).

It is obvious; If (\bar{x}) is obtained by the Lorentz transformation (5), then in (\bar{x}) the zero initial-value data are true, too. We search for other systems (\bar{x}) for which the zero initial-value data are fulfilled.

Let

$$\bar{h}^{ij}(\bar{x})|_{\bar{p}(\bar{x})=0}=0, \quad \bar{h}^{ij}(\bar{x})_{,k}|_{\bar{p}(\bar{x})=0}=0 \quad (9)$$

hold. The spacelike hypersurface extending to infinity in the system $(\bar{x}) \equiv (\bar{x}^0, \bar{x}^1, \bar{x}^2, \bar{x}^3)$ is described by $\bar{p}(\bar{x})=0$. Because of

$$\bar{g}^{ij}(\bar{x}) = \eta^{ij} + \bar{h}^{ij}(x), \quad \bar{h}^{ij}(\bar{x}) = h^{ij}(x) + y^i(x)^{,j} + y^j(x)^{,i}, \quad (10)$$

the necessary and sufficient conditions for (9) to hold are

$$(y^i(x)^{,j} + y^j(x)^{,i})|_{p(x)=0}=0, \quad (y^i(x)^{,j} + y^j(x)^{,i})_{,k}|_{p(x)=0}=0. \quad (11)$$

Because of (4), we have

$$\square(y^i(x)^{,j} + y^j(x)^{,i}) = 0. \quad (12)$$

Hence and from (11)

$$y^i(x)^{,j} + y^j(x)^{,i} = 0 \quad (13)$$

follows. It can easily be proved that this is true if and only if

$$y^i(x) = a_j^i \cdot x^j + b^i, \quad a^{ij} = -a^{ji}, \quad (14)$$

where a^{ij} and b^i are infinitesimal constants. (14) give the inhomogeneous infinitesimal Lorentz transformations.

We have arrived at the result that if the zero initial-value data are true in a harmonic system $(x) \equiv (x^0, x^1, x^2, x^3)$, then they remain satisfied in those harmonic systems only which are obtained from $(x) \equiv (x^0, x^1, x^2, x^3)$ by the inhomogeneous Lorentz transformations. The harmonic system $(x) \equiv (x^0, x^1, x^2, x^3)$ and the other harmonic systems, which are obtained from (x) by inhomogeneous Lorentz transformations (5) are called the "harmonic systems with zero initial-value data" — shortly "zero systems". Other harmonic systems are the "non-zero systems". In an arbitrary non-zero system the solutions of (1) contain sourceless weak gravitational waves too, because in this system the initial-value data are non-zero.

Thus we see, if we assume that there are no sourceless weak gravitational waves in nature, then the investigation of linearized gravitation is to be restricted to the zero systems only. The solutions of (1) are given by weak gravitational waves having sources

only in the zero systems. If in a zero system $(x) \equiv (x^0, x^1, x^2, x^3)$ the spacelike hypersurface is $p(x) \equiv x^0 - \text{const.} = 0$, then the solutions of (1) are given by retarded potentials. In a non-zero system in the solutions of (1) there are sourceless weak gravitational waves too, but this mathematical fact is without any physical significance, and it is only the consequence of choosing the coordinate system. Therefore it is rightful to restrict the investigation of linearized gravitation to zero systems. This is equivalent to saying that the theory of weak (linearized) gravitation is Lorentz covariant.

I would like to thank Dr. Á. Sebestyén for illuminating discussions.

References

1. S. Weinberg, *Gravitation and Cosmology*, J. Wiley and Sons, New York, London, Sydney, Toronto, 1972.
2. Ch. W. Misner, K. S. Thorne and J. A. Wheeler, *Gravitation*, W. H. Freeman and Co., San Francisco, 1973.
3. R. Sauer, *Anfangswertprobleme bei partiellen Differentialgleichungen*, Springer-Verlag, Berlin, Göttingen, Heidelberg, 1952.
4. S. W. Hawking and G. F. R. Ellis, *The Large Scale Structure of Space-time*, Cambridge Univ. Press, 1973.

THE INFLUENCE OF AGGREGATION PHENOMENA ON THE YIELD STRESS OF NaCl(Ca) CRYSTALS

J. SÁRKÖZI

*Institute of Physics, Department of Experimental Physics, Technical University
1521 Budapest, Hungary*

and

E. HARTMANN

*Research Laboratory for Crystal Physics, Hungarian Academy of Sciences
1502 Budapest, Hungary*

(Received 14 June 1984)

The aggregation of point defects has been investigated by means of yield stress measurements. The hardening effect of dipoles, dimers and trimers has been discussed in the case of quenched and annealed NaCl crystals, which were doped with CaCl₂ in various concentrations.

1. Introduction

The negatively charged cation vacancies may be associated with cation impurities creating cation vacancy–cation impurity pairs in alkali halide crystals doped with divalent metal impurities [1]. Such pairs, the so-called dipoles interact with the moving dislocations. This elastic interaction significantly increases the yield stress of the crystals, if the impurity concentration is more than $1 \frac{\mu \text{ mol}}{\text{mol}}$ [2–3].

The dipoles may become associated to aggregates especially in annealed and strongly doped crystals. The dipole clustering also results in the hardening of the crystal. The study of the clustering of divalent impurity–cation vacancy pairs in alkali halides has been continuing for over twenty years [4–7].

The aim of this work is to investigate the relation between the dimer kinetics (formation and decay) and the yield stress changes.

2. Experimental

We worked with specially grown, OH⁻-free NaCl(Ca) crystals which practically did not contain other impurities [8]. This fact is of primary importance because unwanted impurities, especially OH⁻, may chemically react with the dopant during the heat treatment and thus make its effect on the yield stress ambiguous.

The Ca concentration of the crystals was estimated by the temperature dependence of the ionic conductivity using standard data for specimens with known Ca concentration.

The yield stresses were measured on an Instron testing machine at room temperature with a strain rate of 10^{-4} s^{-1} .

All crystals were annealed in an inert atmosphere at 600°C for several hours, and cooled down to room temperature at rates of $100^\circ\text{C}/\text{min}$ (quenching) and $0.1^\circ\text{C}/\text{min}$, respectively.

3. Results and discussion

The dependence of the yield stress increment τ_c on the impurity concentration c is given at two different cooling rates in Fig. 1. The yield stress increment is $\tau_c = \tau - \tau_0$, where τ and τ_0 denote the yield stress of the doped and pure crystals, respectively.

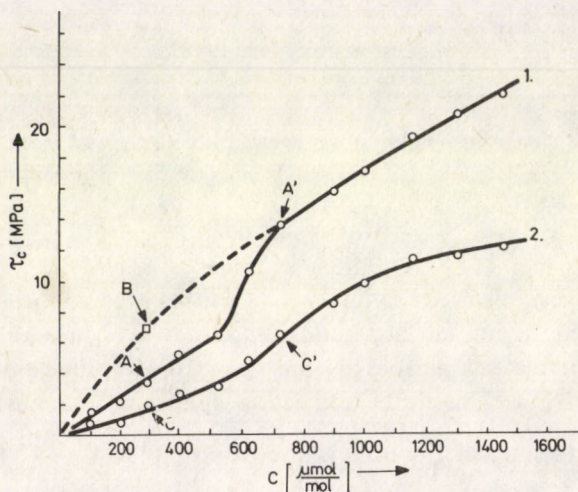


Fig. 1. The dependence of yield stress increment τ_c on the Ca^{2+} -concentration c in NaCl crystals. The samples were quenched from 600°C at the cooling rate: 1. $100^\circ\text{C}/\text{min}$; 2. $0.1^\circ\text{C}/\text{min}$. The dotted line corresponds to the Frank theory for $Z=2$

The significant differences between the curves obtained at high and low cooling rate, respectively, suggest different dipole clustering.

According to the theory of Frank [9] the yield stress increment τ_c is determined by the strong elastic interaction between the moving dislocations and dipole clusters consisting of Z dipoles

$$\tau_c = P \cdot \sqrt{\alpha C_z}, \quad (1)$$

where P and α are constants, C_z is the concentration of dipole clusters.

There is a relationship between the concentration C_z of clusters and the concentration C of divalent impurity cations [9]

$$C = \left(\frac{C_z}{M_z} \right)^{1/z} + Z \cdot C_z, \quad (2)$$

where M_z is the mass cation constant. It was assumed at the derivation of Eq. (2) that one type of dipole clustering predominates, which was shown in the work of Cook and Dryden [4].

The theoretical dependence of the yield stress increment τ_c on the impurity concentration c can be calculated from Eqs (1) and (2) for different Z values. The function for $Z=2$ fits well to our experimental values measured on fast quenched crystals in the high impurity concentration region; below $600 \frac{\mu \text{ mol}}{\text{mol}}$, however, a linear relation exists (Fig. 1, curve 1). On the basis of this result it is suggested that the yield stress increment is determined by dimers in the case of quenched crystals with Ca concentration more than $600 \frac{\mu \text{ mol}}{\text{mol}}$. Below $600 \frac{\mu \text{ mol}}{\text{mol}}$ the yield stress increment is determined by dipoles as it is the case in naturally aged NaCl(Ca) [10]. In the case of slow cooling above $100 \frac{\mu \text{ mol}}{\text{mol}}$ Ca-concentration it is inferred that the aggregates contain three or even more dipoles.

To affirm the above suggestions further experiments were carried out.

The crystals quenched from 600°C had been annealed at 80°C for various periods, then they were quickly cooled to room temperature to freeze in the defect structure developed during the annealing at 80°C .

The dependence of the yield stress increment on the annealing time shows a maximum, if the Ca concentration of the crystals is less than $600 \frac{\mu \text{ mol}}{\text{mol}}$ (Fig. 2).

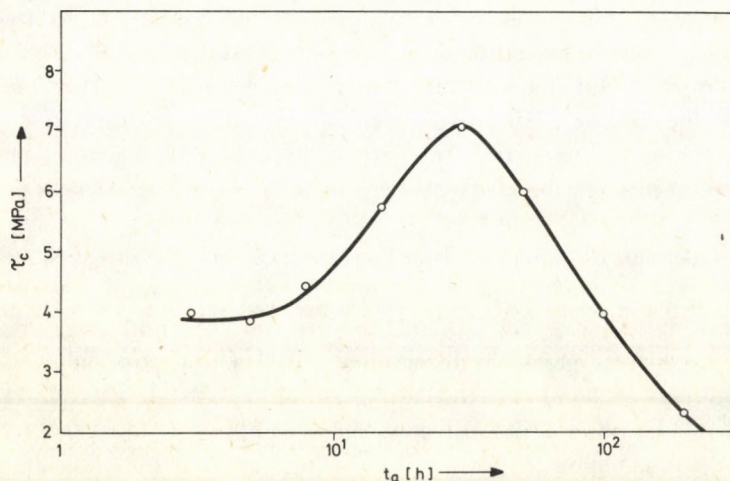


Fig. 2. The dependence of the yield stress increment τ_c on the annealing time t_a for samples of NaCl doped with 3×10^{-4} mol/mol Ca^{2+} . The samples were quenched from 600°C at a cooling rate of $100^\circ\text{C}/\text{min}$. Annealing temperature: 80°C

According to our earlier dielectric loss measurements [11] the dipole concentration decreases with the annealing time due to the formation of dimers and trimers. Therefore it may be assumed that in the first step dimers are formed from single dipoles, and these dimers increase the yield stress of the crystals. At longer annealing times, however, trimers may be formed at the expense of the dimers and the yield stress of the crystals decreases again.

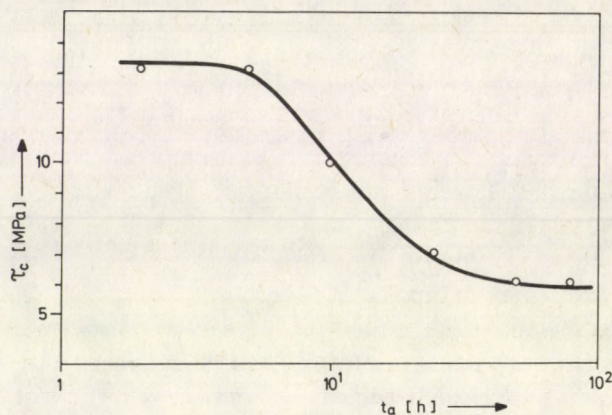


Fig. 3. The dependence of the yield increment τ_c on the annealing time t_a for samples of NaCl doped with 7.2×10^{-4} mol/mol Ca^{2+} . The samples were quenched from 600 °C at a cooling rate of 100 °C/min. Annealing temperature: 80 °C

The processes can also be followed in Fig. 1. During the dimer formation the yield stress increment increases from the value $\tau_c(A)$, which is determined by dipoles, to the value $\tau_c(b)$, which is placed on the curve calculated theoretically from the dimer-dislocation interaction [9], then after a long annealing because of trimer formation it decreases to the value of $\tau_c(C)$. In other words it may be a transition from the *A* state (where the aggregates are mainly dipoles) to the *C* state (where the aggregates are mainly trimers) through the *B* state (where the aggregates are mainly dimers) of the crystals.

The dependence of the yield stress increment on the annealing time in the case of crystals with high impurity concentration (more than $600 \frac{\mu\text{mol}}{\text{mol}} \text{Ca}$) is presented in Fig. 3. The yield stress increment decreases at the transition from the *A'* state (Fig. 1), where the dimers predominate, to the *C'* state of the crystal, where the trimers are predominant. This observation also confirms our above statement that formation of trimers leads to softening.

4. Conclusions

Dipoles can only be obtained by quenching of slightly doped NaCl(Ca) crystals. The yield stress of such crystals increases at annealing by the formation of dimers, but it decreases with the formation of trimers. The dimers seem to be the most effective obstacles to dislocations.

Acknowledgement

The authors are indebted to Dr. R. Voszka for the crystals used in the work.

References

1. A. S. Lidiard, *Handbuch der Physik*, 20, Springer Verlag, Berlin, 1957, p. 246.
2. J. J. Gilman, *J. Appl. Phys.*, 36, 3195, 1965.
3. J. Sárközi and A. A. Predvoditelev, *Kristallografiya*, 24, 622, 1979.
4. J. S. Cook and J. S. Dryden, *Aust. J. Phys.*, 13, 260, 1960.
5. J. S. Cook and J. S. Dryden, *Proc. Phys. Soc.*, 80, 479, 1962.
6. J. S. Cook and J. S. Dryden, *J. Phys. C, Solid St. Phys.*, 14, 1133, 1981.
7. S. W. S. McKeever and E. J. Lilley, *J. Phys. Chem. Solids*, 43, 885, 1982.
8. R. Voszka, I. Tarján, L. Berkes and J. Krajsovsky, *Kristall und Technik*, 1, 423, 1966.
9. W. Frank, *Phys. Stat. Sol.*, 29, 767, 1968.
10. A. A. Urusovskaya, E. V. Darinskaya, R. Voszka and J. Janszky, *Cryst. Res. and Techn.*, 16, 597, 1981.
11. G. Berg, M. Dubiel, J. Sárközi and Cs. Kuti, *Acta Phys. Hung.*, 51, 3, 1981.

SHORT COMMUNICATIONS

AN INTEGRAL REPRESENTATION OF THE $6j$ SYMBOL

S. DATTA MAJUMDAR*

Satyendranath Bose Institute of Physical Sciences
University College of Science, Calcutta 700009, India

(Received 3 April 1984)

The $6j$ symbol is found to have an integral representation of the form [1]

$$\int_0^1 z^{c+d-e}(1-z)^{-a+b+c-d} {}_2F_1'(c-d-e, -a+b-e; -2e; z) \times$$

$$\times {}_2F_1''(-a+c-f, 1-a+c+f; 1-a-b+c+d; z) dz =$$

$$= \left\{ \begin{matrix} a & b & e \\ d & c & f \end{matrix} \right\} (-1)^{c+a+e} \frac{1}{(2e)!} \left[\frac{\Lambda(abe)\Lambda(cde)}{\Lambda(bdf)\Lambda(acf)} \right]^{1/2} \times$$

$$\times (a-c+f)|(b-d+f)|(-a-b+c+d)!, \tag{1}$$

where ${}_2F_1$ denotes the Gauss hypergeometric function,

$$\left\{ \begin{matrix} a & b & e \\ d & c & f \end{matrix} \right\} \text{ is the } 6j \text{ symbol and } \Lambda(abc) =$$

$$= (a+b-c)! (a-b+c)! (-a+b+c)! (a+b+c+1)!. \tag{2}$$

The integral representation opens up the possibility of deriving various expressions for the $6j$ symbol without using the ${}_4F_3(1)$ transformations. A way of doing this which naturally suggests itself is to expand one of the functions ${}_2F_1'$, ${}_2F_1''$ in a power series $\Sigma a_n z^n$ and carry out the integration separately for each power of z . If ${}_2F_1'$ is expanded in a power series then the integration over $z^n {}_2F_1''$ yields a Saalschutzyan ${}_3F_2(1)$ series. Summing this series and using the appropriate values of a , we obtain an expression for the $6j$ in terms of a ${}_4F_3(1)$ series defined only for certain limited ranges of values of the j 's. If, on the other hand, ${}_2F_1''$ is expanded in a power series then the integration over $z^n {}_2F_1'$ yields

* Address: Dr. S. Datta Majumdar, 93/C Regent Estate, Calcutta 700092, India

$$I_r \equiv \int_0^1 z^{r+c+d-e} (1-z)^{-a+b+c-d} {}_2F_1' dz = \frac{(r+c+d-e)! (-a+b+c-d)!}{(r-a+b+2c-e+1)!} \times \\ \times {}_3F_2 \left[\begin{matrix} c-d-e, -a+b-e, r+c+d-e+1; \\ -2e, r-a+b+2c-e+2; \end{matrix} \middle| 1 \right]. \quad (3)$$

The ${}_3F_2(1)$ series occurring here is also Saalschutzhian. The use of the standard expression for its sum gives

$$I_r = \frac{(c-d+e)! (-a+b+e)! (r+c+d+e+1)! (r+c+d-e)!}{(2e)! (r-a+b+c+d+1)! (r+2c+1)!}. \quad (4)$$

Multiplying this by a_r , using Eq. (1) and changing the summation index to $s = a - c + f - r$, we obtain a form of the $6j$ involving a ${}_4F_3(1)$ series which retains its validity for all physical values of the j . The ${}_4F_3(1)$ has the form [2]

$${}_4F_3 \left[\begin{matrix} -a-c-f-1, -b-d-f-1, -a+c-f, b-d-f; \\ -a-d-e-f-1, -2f, -a-d+e-f; \end{matrix} \middle| 1 \right]. \quad (5)$$

Similar results are obtained when both ${}_2F_1'$, ${}_2F_1''$ are subjected to the Euler transformation

$${}_2F_1'(a, b; c; z) = (1-z)^{c-a-b} {}_2F_1'(c-a, c-b; c; z).$$

The integral on the left hand side of (1) has a meaning only if

$$-a+b+c-d \geq 0 \quad (6.1)$$

and

$$-a-b+c+d \geq 0. \quad (6.2)$$

If these conditions are not fulfilled for a given $6j$, they will certainly be fulfilled for an equivalent $6j$ obtained by suitable interchanges of a, b, c, d .

References

1. D. E. Winch, *J. Math. Phys.*, *17*, 1166, 1976.
2. S. D. Majumdar, *Czech. J. Phys. B*, *34* (1984) (in press).

SURFACE OF DOPED NaCl CRYSTALS ANNEALED IN AIR

K. ORBÁN and J. SÁRKÖZI

*Institute of Physics, Department of Experimental Physics, Technical University
1521 Budapest, Hungary*

(Received 30 May 1984)

Introduction and experimental

It has been reported that divalent impurities in NaCl crystals tend to migrate from the volume to the surface during annealing [1–4]. It is generally accepted that impurities present on the surface can play an important role in the crystal properties [5–7]. Several attempts have been made to study the chemical composition of the precipitates by electron microscopy [1–3, 8–11]. On the other hand, relatively few results have been obtained on the surface precipitates of crystals heat treated in air, and in many cases the parameters of the applied heat treatment are not exactly identified. In the present work these observations are extended to the systems NaCl:Ca⁺⁺, NaCl:Mg⁺⁺, NaCl:Ba⁺⁺, NaCl:Sr⁺⁺, NaCl:Pb⁺⁺ and NaCl:Mn⁺⁺, annealed in air, with medium dopant concentrations.

In order to avoid any misleading effects we used specially grown, OH⁻-free NaCl:M⁺⁺ crystals, which contained practically no other impurities [12]. In the studied system the dopant concentration was 1000 mole ppm. The samples were annealed at 500 °C, and quenched at a rate of 10 °C/min in air or in vacuum. The annealing time ranged from 0.5 to 15 h.

The quenched crystals were studied by the gold decoration method [13], and small crystalline grains of the surfaces were investigated directly in a TESLA BS 500 electron microscope by selected area electron diffraction.

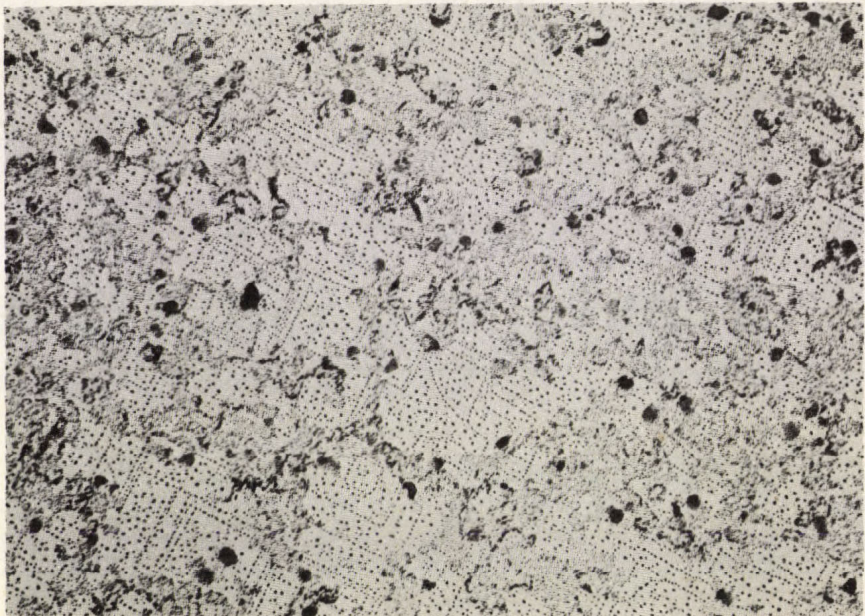
Results and conclusions

The decorated pictures of the tested crystals have shown that essentially different effects are given by the two ways of heat treatment. The shapes and sizes of the surface aggregates fundamentally differ for the two cases. (See for example Figs 1–2).

The chemical composition of the surface layers was studied by electron diffraction. The results are shown in Table I. The annealing time had no significant influence on the composition of these layers, only on their thickness. The detected

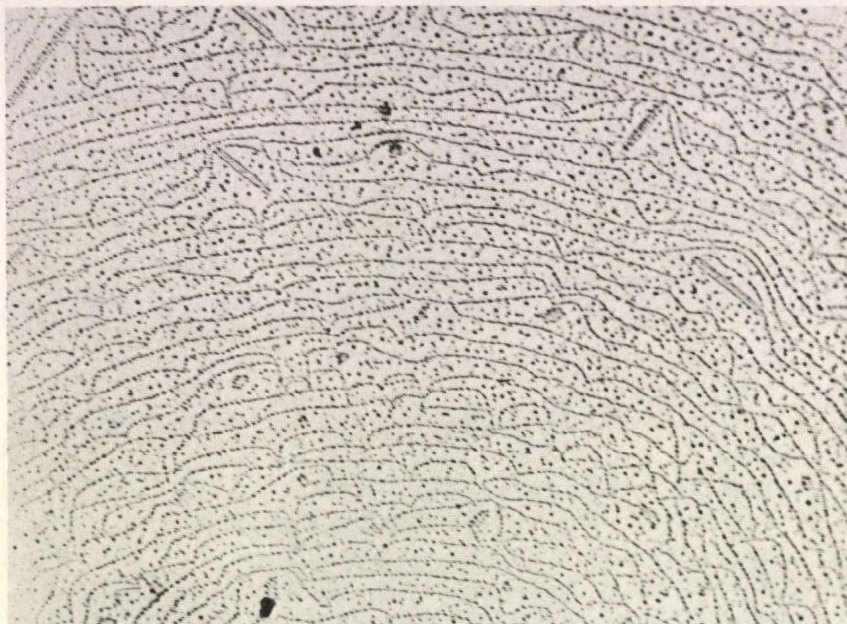


a)



b)

Fig. 1. Electron micrographs of a — NaCl:Mn⁺⁺, heat treated in vacuum,
b — NaCl:Mn⁺⁺, heat treated in air



a)



b)

Fig. 2. Electron micrographs of a - NaCl:Ba⁺⁺, heat treated in vacuum, b - NaCl:Ba⁺⁺, heat treated in air (magnification $\approx 18000X$)

Table I

Compounds detected by electron diffraction on surfaces of crystals annealed in air

Sample	Detected compounds	Unknown compounds
NaCl:Ca ⁺⁺	CaO, CaCl ₂ , CaS	+
NaCl:Sr ⁺⁺	Sr ₄ OCl ₆ , SrS	+
NaCl:Ba ⁺⁺	Ba ₄ OCl ₆ , BaCl ₂	+
NaCl:Mg ⁺⁺	MgO	+
NaCl:Mn ⁺⁺	MnO ₂ , NaMnCl ₃	+
NaCl:Pb ⁺⁺	Pb ₃ O ₄ , PbO, PbCl ₂	+

dopant compounds resisted the electron irradiation much better than the matrix material.

In contrast to the results of other investigations [1–3, 9] in our case a nonhomogeneous layer with varying thickness was formed on the surface of the NaCl crystals during the heat treatment. The inconsistency may be caused by differences in crystal quality, impurity concentrations or by the different annealing procedures.

In every case, unknown, well diffracting crystalline grains could also be found on the surface, not identified as a combination of the dopant, the atmosphere or the matrix material. This indicates that impurities present in the crystal in small amounts tend also to migrate to the surface and react with the atmosphere. This assumption is supported by X-ray emission microprobe analysis.

It should be mentioned that probably some surface formations were not detected because of their small amounts, or because they were not stable enough to resist the electron beam.

The authors wish to express their sincere thanks to Dr. R. Voszka, Head of the Laboratory for Crystal Physics of the Hungarian Academy of Sciences, and his co-workers for supplying the crystals.

References

1. M. J. Yacamán, *Revta max. Fis.*, 20, 91, 1971.
2. M. J. Yacamán, *Phys. Stat. Sol. (b)*, 56, 429, 1973.
3. M. J. Yacamán, A. Gómez and G. A. Bassett, *Thin Solid Films*, 35, 37, 1976.
4. M. J. Yacamán and A. Gómez, *Phil. Mag.*, 32, 13, 1975.
5. J. Budke, *J. Appl. Phys.*, 40, 641, 1969.
6. T. Surek, G. M. Pound and J. P. Hirth, *J. Chem. Phys.*, 55, 5157, 1971.
7. J. Sárközi, A. Tóth, K. Orbán, T. Keszthelyi and P. Kálmán, *Acta Phys. Hung.*, 53, 81, 1982.
8. K. Yagi and G. Honjo, *J. of Phys. Soc. Japan*, 19, 1892, 1964.
9. M. J. Yacamán and E. P. Nieto, *J. of Cryst. Growth*, 7, 259, 1970.
10. M. J. Yacamán, A. Gómez and J. P. Hirth, *Phil. Mag. A*, 39, 709, 1979.
11. I. V. K. Bhagavan Raju, H. Strecker and H. Strunk, *J. de Physique*, C6 41, C6-376, 1980.
12. R. Voszka, I. Tarján, L. Berkes and J. Krajsovsky, *Kristall und Technik*, 1, 423, 1966.
13. M. J. Yacamán and G. A. Bassett, *J. of Appl. Phys.*, 47, 2313, 1976.

BOOK REVIEWS

Phase Transitions — Cargese 1980, Edited by: M. Levy, J.-C. Le Guillou and J. Zinn-Justin Plenum Press, New York and London, 1982

During the past decade spectacular progress has been made in the physics of phase transitions, due mainly to the application of renormalization group (RG) ideas and methods in the theory, which then inspired more extended and more precise measurements. By the end of the seventies the RG methods had been developed to a level that it had become possible to assign error estimates to the results for critical exponents within the framework of RG itself, and to make a meaningful comparison between the RG and the more traditional high temperature series expansion results. While the agreement between these two approaches, and also between theory and experiment proved fairly satisfactory, as longer perturbation series had become available the sharper error estimates started to suggest a slight but persistent discrepancy between the RG and high temperature results. The main point about these slight differences was not the fourth digit of critical exponents, but that they, if confirmed, were threatening to invalidate some of the structural features of the theory, such as hyperscaling, hence the RG itself.

It was with the idea of clarifying the issue and reviewing the state of art both in theory and in experiment that the 1980 Cargese Summer Institute was organized. As a result of excellent timing the school proved to be a real success: new, longer high temperature series had just become available, due to B. Nickel, who also put forward convincing arguments demonstrating that previous error estimates were unrealistically narrow, thereby resolving the discrepancies between the two main theoretical approaches.

This volume is the proceedings of that school. It contains four papers by leading experimentalists (G. Ahlers, D. Beysens, M. R. Moldover, and

J. V. Sengers) on various critical systems (superfluid ^4He , binary mixtures, liquid-gas systems), making a careful comparison between measurements and theory. On the theoretical side, we find a number of papers on the derivation and analysis of high temperature series by G. A. Baker, Jr., W. J. Camp, M. E. Fisher and J. H. Chen, D. S. Gaunt, S. McKenzie and J. J. Rehr; B. Nickel's paper on confluent singularities, reconciling the RG and high temperature series estimates; two lectures on the field theoretical renormalization group technique and its results for critical exponents by E. Brezin and J. Zinn-Justin, respectively; a lecture on polymer solutions by J. des Cloizeaux; one on the promising new technique of Monte Carlo renormalization group by R. H. Swendsen, and finally a paper on critical behaviour in interfaces by D. J. Wallace.

The book is an important document of one of the most recent success-stories in physics and, in view of the significance gained by RG in a number of different fields in physics, the book must be of interest for a much broader audience than those working in statistical physics or in phase transitions.

I. Kondor

Quantum Optics, Experimental Gravitation and Measurement Theory, Proceedings of the NATO Advanced Study Institute "Quantum Optics and Experimental General Relativity" held in Bad Windsheim, Federal Republic of Germany, August 16 to 29, 1981. NATO ASI Series B. Physics, Vol. 94, Edited by Pierre Meystre and Marlan O. Scully, Plenum Press, New York and London, Published in cooperation with NATO Scientific Affairs Division, 1983. XI + 701 pp

The many sided, comprehensive scientific program expressed by the title raises the question whether such a complex program can be covered by

a single conference. The answer is given by the Editors in the Preface as follows:

"At first glance, one might wonder why a meeting should cover these two topics, and a good bit of quantum measurement theory as well, all of which seem to be completely unrelated. The key to what one may call this grand unification lies in the effort, underway in a number of laboratories around the world, to detect gravitational radiation. Present research is pursuing the development of two types of detectors: laser interferometers and resonant bar detectors. Because the signals that one is trying to measure are so weak the quantum mechanical nature of the detectors comes into play".

There are quite many points of contact to Hungary in the book. First of all two chapters (the introductory one: The glorious days of Physics, and the second one of the first part of the book under the heading "Foundations": Review of the Quantum Mechanical Measurement Problem) have been written by E. Wigner. In the former article he remembers his difficulties in choosing a career in his youth in Hungary and he points out the favourable changes experienced since then both in Hungary and throughout the world as regards possibilities to get a post at research institutions in physics: the number of posts available has increased by orders of magnitude.

The second article deals with measurement problems of quantum mechanics, based on fundamental works of E. Schrödinger, W. Heisenberg, P. Jordan and our compatriot J. Neumann.

Another point of contact is represented by frequent references to the "Eötvös-type experiment" in the articles dealing with "the equivalence principle of Einstein".

A most interesting chapter of the book is that of J. A. Wheeler's "Introduction to General Relativity", a very concise yet comprehensive presentation of ideas serving as basis for the entire book. It is worth while to quote here the following introductory lines, summarizing the conceptions and problematics of today in connection with gravity: "Gravity is not a force of foreign origin transmitted through space and time. Gravity is a manifestation of the curvature of spacetime." That is Einstein's account of gravity in brief.

This account, expanded, has two parts: "Space tells mass — right there — how to move. Mass tells space — right there — how to curve".

Let us list here — out of the extremely rich content of the book — a few interesting and very important, fundamental chapters dealing with gravitational theory and measurements, ordered in groups of topics:

Foundations:

M. Hillery and M. O. Scully: On state reduction and Observation in Quantum Optics: Wigner's friends and their amnesia

S. Stenholm: To fathom space and time

Methods of quantum optics:

F. Casagrande and L. A. Lugiato: Fluctuations in quantum optical systems

C. J. Borde: Phase conjugate optics and applications to interferometry and to Laser Gyros

H. Walther: Selected topics of laser spectroscopy of atoms and molecules

Experimental gravitation:

K. S. Thorne: Experimental gravity, gravitational waves and quantum nondemolition: An Introduction

C. O. Alley: Proper time experiments in gravitational fields with atomic clocks, aircraft and laser light pulses

C. O. Alley: Laser ranging to retro-reflectors on the moon as a test of theories of gravity

K. Nordtvedt, Jr.: The meaning of the lunar laser ranging experimental results for gravitational theory

R. W. P. Drever and Colleagues: Gravitational wave detectors using laser interferometers and optical cavities: ideas, principles and prospects

C. M. Caves: Quantum nondemolition measurements

W. G. Unruh: Quantum noise in the interferometer detector

The usefulness of the book is significantly increased by an alphabetical index comprising both authors and themes.

The main task of the book is to deal with processes and phenomena of the gravity field described within the conception of the special relativity theory, to present evidences for the basic theory supported by modern experimental results, as well as the up-to-date results of principle and problems brought about in the course of theoretical developments. Among others we find a treatment of the problem of time variation of g and of the dependence of the eigen-time on the acceleration of the coordinate-system in the space-time continuum, as well as of the basic principles of the existence of gravity waves, and of the detectors built for the observation of them, and of the results of ten years measurements made by a laser mirror placed on the Moon, etc.

In summarizing we can state that the book gives the most recent theoretical and experimental results of investigation of the gravity field and so it is an indispensable basic source book for all physicists dealing with such problems and topics.

Gy. Barta

Relativistic Effects in Atoms, Molecules and Solids Proceedings of a NATO Advanced Study Institute (ASI) held at the University of British Columbia, Vancouver, Canada, August 10–21, 1981. Edited by G. L. Malli. Plenum Press, New York and London, Published in cooperation with NATO Scientific Affairs Division, 1983.

A total of 77 lecturers and students with backgrounds in Chemistry, Physics, Mathematics and various interdisciplinary subjects attended the ASI.

The detailed investigation of the relativistic structure of atoms, molecules and solids would provide an excellent testing ground for the validity and accuracy of the theoretical treatment of the relativistic many-electron systems involving medium and heavy atoms. Such systems are also of interest to the current energy crisis because of their usage for photovoltaic devices, nuclear fuels (UF_6), fusion lasers (Xe_2^+), catalysts for solar energy conversion, etc.

This book contains the main invited lectures and the abstracts (one-page only) of contributed talks.

The main lectures have been as follows: Joseph Sucher, Foundations of the Relativistic Theory of Many-Electron Systems; I. P. Grant, Incidence of Relativistic Effects in Atoms — Formulation of the Relativistic N-Electron Problem — Techniques for Open Shell Calculations for Atoms — Self-Consistency and Numerical Problems; J. P. Desclaux, Numerical Dirac-Fock Calculations for Atoms — Dirac-Fock One-Centre Expansion Method; Peter J. Mohr, Lamb Shift in High-Z Atoms; John H. Detrich and Clemens C. J. Roothaan, Calculation of Relativistic Effects in Atoms and Molecules from the Schrödinger Wave Function; G. L. Malli, Relativistic Self-Consistent-Field Theory for Molecules; D. D. Koelling and A. H. MacDonald, Relativistic Effects in Solids; J. Ladik, J. Cizek and P. K. Mukherjee, Relativistic Hartree-Fock Theories for Molecules and Crystals in a Linear Combination of Atomic Orbitals Form; Cary Y. Yang, Relativistic Scattered-Wave Calculations for Molecules and Clusters in Solids; Yasuyuki Ishikawa and G. L. Malli, Fully Relativistic Effective Core Potentials (FRECP); P. Jeffrey Hay, Electronic Structure of Molecules with Very Heavy Atoms Using Effective Core Potentials; Kenneth S. Pitzer, Electron Structure of Molecules with Very Heavy Atoms Using Effective Core Potentials; Tom Ziegler, Calculation of Bonding Energies by the Hartree-Fock Slater Transition

State Method, Including Relativistic Effects; N. C. Pyper, Relativistic Calculations for Atoms, Molecules and Ionic Solids; Fully Ab-Initio Calculations and the Foundations of Pseudo-Potential and Perturbation Theory Methods; Jaime Keller, The Geometry of Space Time and the Dirac Equation.

The Volume may be interesting for graduate students and scientists working in physics, chemistry, mathematics and on advanced engineering problems.

R. Gáspár

High-Latitude Space Plasma Physics. Edited by Bengt Hultquist and Tor Hagfors, Plenum Press, New York and London, 1983. pp. 543

This volume contains 27 contributions presented at the Nobel Symposium No. 54 on High Latitude Magnetospheric/Ionospheric Plasma Physics, organized in Kiruna, Sweden, March 22–25, 1982 by the Kiruna Geophysical Institute and EISCAT Scientific Association.

The main purpose of the Symposium was to prepare for the intense European research effort in space plasma physics in the mid 1980's, in which the EISCAT facilities and the Swedish satellite Viking are two of the more important constituents. The programme of the Symposium was tied to the physics of those regions of near space where EISCAT and Viking are expected to provide important new observational results. This is rather well covered by the title of the Proceedings.

The presentation is divided in three parts, 1–3, on the Physics of the High Latitude Ionosphere, Solar Wind Influence on the High-Latitude Ionosphere, High Latitude Magnetospheric Physics above a few Thousand Kilometers. This volume explores the physics of the high-latitude ionosphere and how this part of near space is affected by the properties of the solar wind and the interplanetary magnetic field. It also provides extensive coverage of high-latitude magnetospheric physics at altitudes of 1–2 earth radii, the main scientific object of the Viking project.

High-Latitude Space Plasma Physics will be a major source of the latest research for those working in the fields of space physics and astronomy, plasma physics, geophysics and meteorology.

J. Szabó

KASTURI LAL CHOPRA and Inderjeet Kaur: *Thin Film Device Applications*, Plenum Press, New York and London, 1983.

Two-dimensional materials created by the process of condensation of atoms, molecules, or ions, called thin films, have unique properties significantly different from the corresponding bulk materials as a result of their physical dimensions, geometry, nonequilibrium microstructure, and metallurgy. Further, these characteristic features of thin films can be drastically modified to obtain the desired and required physical parameters.

These features have formed the basis of development for a number of extraordinary active and passive thin film device applications in the past two decades. On the one extreme, these applications are in the submicron dimensions in such areas as very large scale integration (VLSI), Josephson junction quantum interference devices, magnetic bubbles, and integrated optics. On the other extreme, large-area thin films are being used as selective coatings for solar thermal conversion, solar cells for photovoltaic conversion, and protection and passivating layers. Indeed, one could hardly find many sophisticated modern optical and electronic devices which do not use thin films in one way or the other.

With the impetus provided by industrial applications, the science and technology of thin films have undergone revolutionary development and are still recognized globally as frontier areas of research and development. Major technical developments in any field of science and technology are invariably accompanied by an explosion of literature in the form of scientific papers, reviews, and books.

The need for a single, concise, and comprehensive textbook on thin film device applications clearly exists and has been felt by graduate students and workers in the field. This monograph presents a concise and coherent study of thin film device applications in such areas as optics, electro-optics, microelectronics, magnetics, quantum engineering, surface engineering, and thermal detection.

What thin films are and how these are prepared and characterized forms the Introduction (Chapter 1). The role of thin films in a wide range of optical and electro-optical applications is described in Chapters 2 and 3. This is followed by the microelectronic and magnetic applications in Chapters 4 and 5. The superconducting properties and quantum tunneling effects of thin films are the basis of a host of quantum engineering applications which are the subject of Chapter 6. Thermal applications of thin films are discussed in Chapter 7. Finally, a whole range of passivating, tribological, decoration,

and biomedical applications form the subject matter of Chapter 8.

The emphasis in all Chapters is placed on giving a brief physical basis and technical description of the devices in a coherent manner. Adequate references are provided for the interested reader to dig deeper into the details of the devices. Both theoretically interesting and commercially viable devices have been covered to inspire the innovative mind. Besides serving as a textbook for graduate students in applied sciences and engineering, it should be a good reference book for scientists and engineers involved in research and development on thin-film-based devices.

A book of this type draws heavily and unhesitatingly from the published works of numerous authors. A concerted effort was made to describe representative examples of applications of thin films from the literature in various areas in a very condensed and brief form.

J. F. Bitó

The Physics of Superionic Conductors and Electrode Materials, Edited by J. W. Perram, Plenum Press, New York and London, 1983

This excellent volume contains the introductory lectures of a 1980 school on superionics. In that school the lectures were followed by a week of exercises in computer simulations, a technique of decisive importance in this subject. As a consequence the book may be useful to anyone starting Monte Carlo or molecular dynamics work on any physical system.

Superionic conductors are crystals of unusually high conductivity, as if the sublattice of one ionic species were molten in them. Whether the above "as if" is a realistic view at their physics, is the heart of the problems tackled in the book. The expansive development of the subject in recent years has been strongly stimulated by economic reasons: energy storage in light-weight batteries is the most important potential application one has in mind.

The first paper by H. Schultz introduces the subject by presenting structural information about superionic conductors and a rough way of guessing conduction mechanisms on the basis of structure. This is followed by the description of a semi-microscopic hopping model by J. H. Harding. The next two lectures by E. R. Smith and J. W. Perram are already important technicalities for computation: details of the evaluation of lattice sums in disordered ionic systems. After some relaxation by Cotterill's nice summary of concepts underlying the idea of sublattice melting, the reader faces the

lectures presenting the two fundamental techniques in computer simulation: molecular dynamics (by A. Rahman and P. Vashista) and Monte Carlo (by D. Adams), both very detailed and useful. The remaining chapters of this nice and useful book contain many applications as well as digressions on minor techniques.

T. G.

Soviet Scientific Reviews, Section A: Physics Reviews, Volume 2, Edited by I. M. Khalatnikov, Harwood Academic Publishers, New York, 1980.

The second volume contains seven review papers, ranging from experimental solid state physics through statistical mechanics to quantum field theory.

The paper by I. P. Krylov on "Macroscopic electrostatics of the intermediate state of pure superconductors" reviews some recently discovered properties of metals containing a mixture of normal and superconducting domains. The properties studied are determined by material characteristics averaged over regions larger than the domain size; that is meant by "macroscopic" in the title. In such properties in the case of high-purity metals a decisive role is played by the scattering of quasi-particles of the normal metal on the domain boundary. Such scattering events are accompanied by electron-hole conversion, as recognized by A. F. Andreev.

In a loosely related paper V. S. Tsoi describes a nice method of studying the scattering of electrons on polished surfaces of high-purity metals. The method uses the focusing action on electrons of a transverse magnetic field, well-known from instruments like a β -spectrometer or a mass spectrometer. In the experiments at hand electrons injected into a metallic sample by a point contact are a few times focussed onto the surface to bounce back each time into the bulk, before being collected by a second point contact. The signal obtained is characteristic of fine local details of electron scattering on the surface.

V. S. Edelman reviewed the "Investigation of electrons localized on liquid helium": an experimentally much-studied system modeling a two-dimensional Coulomb gas. Among the various phenomena so far investigated, the reviewer concentrates on those which are sensitive to the details of the interaction of the electrons with the helium surface and its excitations.

The subject of V. P. Mineev's paper "Topologically stable defects and solitons in ordered media" is the way to generalize the Burgers-circuit character-

ization of defects to the cases of media with a complicated order parameter (e.g. liquid crystals, superfluid ^3He). By means of a method utilizing tools of algebraic topology one can study the stability, intersection, coalescence etc. of defects in cases too complicated to be approached by straightforward geometrical thinking. Mineev, one of the first inventors of the novel method, wrote a useful, readable introduction to these somewhat unusual topics.

In a paper on "Phase transitions in two-dimensional systems with commutative group symmetry" P. B. Wiegmann summarizes his own work, partly based on pioneering research of the untimely deceased V. L. Berezinskii, referring to the phenomena usually called "Kosterlitz-Thouless transitions". The archetype of the problem is the phase transition of the so-called XY model. This model describes at least two physical systems: interacting spins on a two-dimensional lattice freely rotating in the plane, and a thin film of superfluid ^4He . Wiegmann has shown that by means of a duality transform the XY model can be mapped onto an interacting one-dimensional fermion gas. This observation gave rise to a fruitful mutual utilization of known results from both fields.

Two much more remote areas of research are connected to each other in the paper of A. B. Zamolodchikov on "Factorized S matrices and lattice statistical systems". The point is that if in $(1+1)$ -dimensional space-time relativistic L -particle amplitudes are constructed in the form of products of two-particle S-matrices, the expressions obtained for large L correspond to some solvable models of statistical physics (Baxter eight-vertex model, Lieb ice model). These models are exactly solvable in view of an internal symmetry called Z-invariance which works even for irregular lattices; that property assures the existence of an exact solution of the corresponding problem in scattering theory.

Finally, the extensive paper of Bogomol'nyi, Fateev and Lipatev on the "Calculation of high orders of perturbation theory in quantum field theory" is mainly devoted to a steepest-descent method that proved extremely efficient in obtaining exact results about the asymptotic behaviour of high-order terms in a perturbation series. It is interesting to remark that the method is mathematically related to the theory of first-order phase transitions through the physical link of metastable states appearing in both problems.

It would not be easy to find a physicist with deep professional interest towards all topics covered in this volume, however, each paper would find its reader. A useful volume for the physics library.

T. G.

Soviet Scientific Reviews Section C: Mathematical Physics Reviews, Volume 1, Edited by S. P. Novikov, Harwood Academic Publishers, New York, 1980

The purpose of this annual review is a more elaborated presentation for the non-Russian speaking scientific community on the outstanding achievements of Soviet Science. The contents of the first volume of the Mathematical Physics Series as well as the announced contents of the second volume offer a detailed, sometimes pedagogical overview of some fields, where the contribution of the Soviet theoreticians is fully acknowledged. Some of the articles prove useful even for those who follow the Russian literature, because of the homogeneous, unified collection of results otherwise scattered throughout the different journals. Two of the four reviews of the first Volume present accounts of rigorous results from statistical physics. The famous experts of the Moscow State University, R. L. Dobrushin and Ya. G. Sinai communicate results on the limiting Gibbs distribution, which are partially overlapping with the material in the monograph of the latter author published last year by the Publishing House of the Hungarian Academy of Sciences. They outline a general mathematical framework for the renormalization group study of phase transition and pay particular attention to the problem of absence of phase transitions in two dimensional systems. The second review of this type was written by N. N. Bogoliubov Jr., A. M. Kurbatov, D. Ya. Petrina and D. P. Sankovich. They report on an original method for obtaining rigorous results for some Hamiltonian quantum systems by replacing the original Hamiltonian operator by a different one of simpler structure. The procedure has been illustrated on the examples of the BCS model of superconductivity and the Dicke-Haken-Law model from quantum optics.

The other two papers deal with the construction of exact solutions of some non-linear field-theoretical models. The role of such solutions became increasingly important both in the physics of continuous media and in quantum field theory during the last decade. In the first part of the first review paper I. M. Krichever and S. P. Novikov analyze the construction of the so-called finite gap, quasi-periodic solutions of the Korteweg-de Vries non-linear equation. In the second part written by V. G. Drinfeld and Yu. I. Manin the reader will be happy to learn from a detailed description the geometrical construction of topological finite action solutions of the imaginary-time Yang-Mills equations, the instantons. The technique introduced originally by the author has become since then a commonly used tool in the construction of other

solutions of interest like for example the magnetic monopoles, etc.

The review of Academician L. D. Faddeev from the Leningrad Branch of the Steklov Mathematical Institute covers the results obtained by his group in the application of the quantal inverse scattering method to 1+1 dimensional field theoretical models. Their method is a direct generalisation of the recent classical inverse-scattering method discovered in 1967 to the case of quantum systems. The solution of the nonlinear theories is based on an auxiliary linear spectral problem. The paper thoroughly presents the construction of this transfer operator whose matrix elements become operators themselves in the quantum case. The actual problem is the construction of the infinitesimal transfer operator which is illustrated through the examples of the non-linear Schrödinger, the Heisenberg and the sine-Gordon models. The author investigates carefully the relationship of their method to other approaches to 2 dimensional models like the Bethe Ansatz and the Onsager-Baxter method. This review is the clearest introduction to one of the most impressive developments of mathematical physics during the last years.

The book will be extremely useful for theoretical physicists and mathematicians interested in the rigorous treatment of model systems.

A. P.

V. S. LETOKHOV: *Nonlinear Laser Chemistry*. Springer Series in Chemical Physics 22 (Edited by F. P. Schäfer), Springer-Verlag, Berlin-Heidelberg-New York, 1983, XIV + 417 pp., 93 DM

The use of lasers in chemistry is a very promising and exciting development of about the last two decades. Although books and review papers are available on the chemical use of coherent optical radiation, Dr. Letokhov's work is still unique as it deals exclusively with the state-selective excitation of atomic and molecular species. A characteristic of the book is that it is basically built upon the work done at the Institute of Spectroscopy, Academy of Sciences of the U.S.S.R. since 1970.

The book is divided to eight Chapters: 1. Introduction, 2. Selective photoexcitation of atoms and molecules, 3. Multistep selective photoionization of atoms, 4. Selective monomolecular photoprocesses with nonlinear excitation of electronic states, 5. Multiphoton monomolecular photoprocesses in the ground electronic state, 6. Laser photoseparation on an atomic and a molecular level, 7. Selective laser detection of atoms and

molecules, and 8. Laser photochemistry and photo-biochemistry. The text is richly illustrated by drawings, formulae and tables, a section summarizes the symbols and notation used. The bibliographical part contains 622 items grouped separately for each Chapter, plus a list of additional readings running to fifty publications.

The architecture of the book is logical, it leads the reader from the minimum of fundamentals to a full-fledged application to monomolecular decomposition processes. The mathematics applied is simple, lucid and kept to minimum, which contributes greatly to the readability of the book. In the reviewer's opinion it would be difficult to find another text that integrates the elements of spectroscopy with those of chemical kinetics so smoothly and naturally. The spectroscopic motivation is clearly there to see. This is important because to do laser photochemistry and photophysics one needs a thorough knowledge of the atomic and molecular levels, and the molecular dynamics of the quantum system in question. Dr. Letokhov emphasizes the role of infrared lasers in important processes, such as isotope separation and molecular isomerization in the gaseous phase. The separation of isotopes of almost any element out of the periodic system is possible now by coherent optical methods, either in principle or already in practice. Short-lived radioisotopes are no exceptions.

In the last two chapters the author discusses the detection of single atoms by selective multistep photoionization, or of single molecules by a photoionization mass spectrometric technique, the laser photoelectron microscope and wave-corpuscular microscopy. By these latter techniques — the author suggests — it might prove possible to reach resolutions of several Å that may suffice to visualize macromolecules, and to study the molecular photoexcitation dynamics simultaneously. Finally, the subject of photochemistry in biology: photobiochemistry is touched upon, such as the action of very short laser pulses upon the DNA content of viruses and cells.

Dr. Letokhov's truly excellent book is strongly recommended to research workers in laser chemistry, spectroscopy and photochemistry as a good summary of the theoretical background and as an extensive guide to modern literature on the subject. It should then be mentioned that the book's qualities stem from its authenticity and originality, as the author is a leader and foremost authority in laser chemistry.

L. Nemes

L. JARASS, L. HOFFMANN, A. JARASS, G. OBERMAIR: *Wind Energy*, An assessment of the technical and economical potential. A case study for the Federal Republic of Germany, commissioned by the International Energy Agency. Springer-Verlag, Berlin-Heidelberg-New York, 1981, 220 pages, 132 figures, 34 tables ISBN 3-540-10362-7 ISBN 0-387-10362-7

This book contains the results of a study the objectives of which were: analysis of the technical and economic potential of large-scale wind power conversion into electrical power with special attention to complementary power regulation capacity, including storage devices. The analytical methods developed in this study are applied to the Federal Republic of Germany. The report comprises an evaluation of wind data, the optimization and description of technical parameters of wind turbines, description of a simulation model for the integration of wind power in an existing utility grid, an analysis of the fuel saving effect and the capacity displacement capability of wind energy, an assessment of the break-even-costs of wind energy conversion systems, and a discussion of the role and the appropriate size of storage devices.

The main results relative to the FRG may be summarized as follows. The displacement capability depends essentially on the penetration factor, i.e. on the ratio of installed wind energy capacity to total installed capacity. At penetration factors of 5, 10, and 15%, the fuel savings amount to 4.2, 8.8, and 13.9%, resp., while 1.7, 2.6, and 3.2%, resp., are the figures for the displaced conventional plant capacity in the reference case studied. The book presents further detailed data as to the optimum size and kind of energy storage device and related quantities. On the basis of this evaluation, the energy potential of the wind may become comparable to that of hydro power in the FRG.

Z. Szatmáry

L. JARASS: *Strom aus Wind*, Integration einer regenerativen Energiequelle, Springer-Verlag, Berlin-Heidelberg-New York, 1981 140 Seiten, 46 Abbildungen und 10 Tabellen ISBN 3-540-10436-4 ISBN 0-387-10436-4

Schon seit Jahrtausenden und bis zu Beginn dieses Jahrhunderts wurde die kinetische Energie des Windes durch Windmühlen in mechanische Energie umgewandelt. Dann liessen Dampfkraft und Dieselmotoren Windmühlen vorübergehend als überflüssig erscheinen. Ende der 70er Jahre

wurde Windenergie weltweit wieder entdeckt. Eine Reihe von Ländern hat mittlerweile umfangreiche Forschungs-, Entwicklungs- und Markteinführungsprogramme für Windkraftwerke beschlossen. Das technisch nutzbare Potential der Windenergie für die Bundesrepublik Deutschland wurde als 220 TWh/a, d.h. etwa 70% der Bruttostromerzeugung des Jahres 1975 dargestellt. Die Ausnutzung dieses Potentials würde 20 bis 30 Tausend Windkraftanlagen erfordern. Wenn man 10% dessen in einer ersten Ausbaustufe realisiert, ist der Beitrag der Windenergie bereits so gross wie der der Wasserkraft in 1980. Für andere Länder können ähnliche Schätzungen gegeben werden.

Das Buch erörtert zuerst die physikalisch-technischen Grundlagen der Windenergienutzung und die verschiedenen Windkraftanlagentypen. Das Windenergieangebot wird durch meteorologische Schwankungen bedingt. Für die Vergleichsmässigung der Windenergieproduktion wird deshalb immer wieder die Nutzung von Energiespeichern vorgeschlagen. Das Buch betrachtet hydraulische Pumpspeicher und Luftspeicher. Daneben werden auch andere Möglichkeiten wie Schwungradspeicher, Batterien und durch Elektrolyse gewonnener Wasserstoff erwähnt und besprochen. Es wird ein Integrationsmodell aufgestellt um zu untersuchen, wie Windkraftanlagen sich in das Stromversorgungssystem integrieren lassen. Die Nutzbarkeit der Windkraft ist vom Gesichtspunkt der Brennstoff- und Kraftwerkskapazitätsersparungen beurteilt. Bezüglich der Bundesrepublik Deutschland werden Rechenergebnisse angegeben und Massnahmen zur Durchsetzung von Windkraftwerken diskutiert.

Z. Szatmáry

K. M. SALIKNOV, YU. N. MOLIN, R. Z. SAGDEEV and A. L. BUCHACHENKO: *Spin Polarization and Magnetic Effects in Radical Reactions*, Edited by Yu. N. Molin, Akadémiai Kiadó, Budapest, 1984

The discovery of magnetic and spin polarization effects in radical reactions in 1967 has resulted in spectacular progress by the creation of new and rapidly developing research fields on the borderline of magnetic radiospectroscopy and chemical kinetics. The new spectroscopic methods, the chemically induced dynamic nuclear and electron polarization (CIDNP and CIDEPE) have also directed the attention to other new phenomena: the possibility of

controlling the rate of radical reactions by the magnetic interactions, which are weaker by orders of magnitude than the thermal energy, and the magnetic isotope effects in chemical reactions which can substantially surpass any effect based on the atom weight differences of isotopes.

The first work in scientific literature where the spin polarization and magnetic effects are treated on a common viewpoint is the monograph reviewed here. The authors themselves have played a pioneering role in the development of this area. The book summarizes the results of more than 500 original papers in eight chapters on 419 pages with a rich bibliography and a subject index. Besides the common viewpoint, the clear presentation and the rich illustrative material affords good reading of the book. Even a reader not familiar with this field can acquire all important concepts necessary for the understanding of the phenomena CIDNP and CIDEPE as well as the backgrounds of magnetic effects in the first introductory chapter. A deeper insight into the topic can be obtained from the next three chapters, which lay down the necessary physical and mathematical backgrounds. The second chapter contains the theory of radical pairs recombination, where the concept of recombination is used in a generalized meaning, the third chapter treats the theory of magnetic effects in radical reactions and the magnetic isotope effects, while the fourth one gives an account on the theory of CIDNP and CIDEPE spectroscopy. The last four chapters summarize the most important experimental results and conclusions in the fields of chemical kinetics, structural chemistry, molecular physics, magnetobiology and radiospectroscopy. The fifth chapter treats the external field effects observed in radical reactions, the sixth one the magnetic isotope effects, while the seventh and eighth discuss the results obtained by the application of CIDNP and CIDEPE, respectively. A few interesting examples of applications are also presented, e.g. the possibility of field-controlled chemical reactions, applications of magnetic effects to isotope separation, and new ways of interpreting the biological action of magnetic fields.

This book will be indispensable for the specialists who employ CIDNP, CIDEPE and magnetic effects in their investigations, but it can also be recommended to chemists and biologists who may not be active in the field of magnetic radiospectroscopy but can effectively employ the results offered by these methods.

A. Rockenbauer

Cryocrystals, Edited by B. I. Verkin and A. F. Prikhotko, Naukova Dumka Publishers, Kiev, 1983 (in Russian) 527 pp, 269 illus. Price: 7r. 50k.

The book is a critical study on the properties of "basic" simplest molecular solids. This work is the first in the world literature to treat and survey this extensively investigated group of solids on the basis of a unique viewpoint. It is intended for a wide circle of research workers dealing with fundamentals and applications of the physics of molecular solids.

Contents: Part 1. V. G. Manzhelii and M. A. Strzhemechny. Quantum molecular solids. Quantum crystals and solid hydrogen. Hydrogen molecule. Intermolecular potentials. Structures and equilibrium phase diagrams. Equation of state. Thermodynamic properties. Dynamics of solid hydrogens. Kinetic properties. Nuclear magnetic resonance.

Part 2. I. N. Krupskii, V. A. Slusarev and Yu. A. Freiman. Classical molecular solids. General

on N_2 -type solids. Molecular parameters. Molecular interaction potentials. Structure and thermodynamic properties. Theory of orientational motion in N_2 -type solids. Librational motion of molecules in solid oxygen.

Part 3. A. F. Prikhotko, Yu. B. Gaididei, V. M. Loktev and L. I. Shanskii, Elementary excitations in solid oxygen. Spin, electronic and vibrational states of α -oxygen. Exciton-magnon spectra of α -oxygen. Bi-excitons in α -oxygen. Experimental techniques.

Part 4. I. Ya. Fugol and E. V. Savchenko. Excitons in atomic solids. Some physical properties of atomic cryocrystals. Experimental techniques for studying the optic properties. Coherent exciton spectra. Luminescence of self-trapped excitations. Band structure calculations. Scattering of coherent excitons by acoustic phonons. Coexistence of coherent and self-trapped states. Polariton effects and spatial dispersion.

E. F.

Manuscript received by Akadémiai Kiadó: 27 July 1984

Manuscript received by the Printers: 30 June 1984

Date of publication: 20 December 1985

PRINTED IN HUNGARY

Akadémiai Kiadó és Nyomda, Budapest

Acta Technica

Academiae Scientiarum Hungaricae

Editor in Chief:
M. Major



The periodical publishes papers written by Hungarian and foreign scientists dealing with mechanics, material testing, architecture, building technology, highway-, railway- and hydraulic constructions, thermodynamics, mechanical engineering, mechanical technology, metallurgy, electrical engineering, electronics, automation, telecommunication.

Founded 1950
Papers in English
Publication: two volumes annually —
one volume contains four issues
Price per volume: \$44.00; DM 99,—
Size: 17 × 25 cm
ISSN 0001-7035

Order form

to be returned to
KULTURA

Hungarian Foreign Trading Company
P.O. Box 149, H-1389 Budapest, Hungary

- Please enter my/our subscription for
ACTA TECHNICA for one year
- Please enter my/our standing order for
ACTA TECHNICA starting with

Name: _____

Address: _____

Date and signature: _____



Contents of Volume 92, Numbers 1-2

- Lévai, A.*: Gemeinsamkeiten und Gegensätzlichkeiten der Energieträger — Identities and Contrasts between Energy Carriers
- Volkov, E. P.*: Problems in the Calculation of the Concentration of the Injurious Gaseous Impurities of Industrial Pollution Sources — Fragen der Konzentrationsberechnung der aus industriellen Quellen entstehenden schädlichen gasartigen Verunreinigungen
- Csonka P.*: Elliptic Plate with Clamped Edge
- Kerek, A.*: Static and Stability Investigation of Bent Folded Plates — Statische und Stabilitätsuntersuchung der gebogenen Falterke
- Taufik, A. S.*: The Effect of Air or CO₂ Impurity on the Characteristics of Mercury—Argon Discharge at Low Pressure — Die Einwirkung der Schmutzstoffe Luft und Kohlensäure auf die Charakteristiken der Quecksilber—Argon-Entladung bei Niederspannung
- Kerényi, D.*: Analytische Näherungsverfahren zur Berechnung von Wirbelströmen in Metallplatten — Analytic Method for the Approximate Calculation of the Eddy-Current Loss of a Metal Plate Placed into a Magnetic Field
- Kuti, I.*: On the Primal Variational Principles in Linear Elastodynamics — Variationsgrundsätze in der linearen Elastodynamik
- Hédai, L.*: La réduction des oxydes métalliques dans un bain des carbures métalliques chauffé par plasma — Reduction of Metal Oxides in Metal Carbide Fusion Superheated with Plasma — Reduktion von Metalloxyden in einer mit Plasma überhitzten Hartmetallschmelze
- Kolonits, F.*: Flexibility Design of Piping Systems — Entwurf von Rohrleitungssystemen aufgrund der elastischen Formänderungen, Part I
- Hidasi, J.*: Two-Dimensional Subsonic Flow of a Compressible Medium — Ebene Unterschallströmung von kompressiblen Medien
- Almássy, B.—Budavári, S.—Vajna, Z.*: Economically Computerized Calculations for Large-Size Looped Pipe-Networks
- Kolonits, F.*: Flexibility Design of Piping Systems — Entwurf von Rohrleitungssystemen aufgrund der elastischen Formänderungen, Part II
- Károly, Gy.—El-Ghazally, S. A.*: Hydrodynamic Modelling of Power Injection into Melts — Hydrodynamische Modellierung der Pulverinjektion in Schmelzen



Akadémiai Kiadó

Publishing House
of the Hungarian Academy of Sciences
Budapest

Invitation for papers

Manuscripts should be sent to
Acta Technica
H-1051 Budapest
Münnich F. u. 7.
Hungary

NOTES TO CONTRIBUTORS

I. PAPERS will be considered for publication in *Acta Physica Hungarica* only if they have not previously been published or submitted for publication elsewhere. They may be written in English, French, German or Russian.

Papers should be submitted to

Prof. I. Kovács, Editor
Department of Atomic Physics, Technical University
1521 Budapest, Budafoki út 8, Hungary

Papers may be either articles with abstracts or short communications. Both should be as concise as possible, articles in general not exceeding 25 typed pages, short communications 8 typed pages.

II. MANUSCRIPTS

1. Papers should be submitted in three copies.
2. The text of papers must be of high stylistic standard, requiring minor corrections only.
3. Manuscripts should be typed in double spacing on good quality paper, with generous margins.
4. The name of the author(s) and of the institutes where the work was carried out should appear on the first page of the manuscript.
5. Particular care should be taken with mathematical expressions. The following should be clearly distinguished, e.g. by underlining in different colours: special founts (italics, script, bold type, Greek, Gothic, etc.); capital and small letters; subscripts and superscripts, e.g. x^2 , x_3 ; small l and l ; zero and capital O ; in expressions written by hand: e and l , n and u , v and v , etc.
A List of Symbols on a separate sheet should be attached to each paper.
6. References should be numbered serially and listed at the end of the paper in the following form: J. Ise and W. D. Fretter, *Phys. Rev.*, 76, 933, 1949.
For books, please give the initials and family name of the author(s), title, name of publisher, place and year of publication, e.g.: J. C. Slater, *Quantum Theory of Atomic Structures*, I. McGraw-Hill Book Company, Inc., New York, 1960.
References should be given in the text in the following forms: Heisenberg [5] or [5].
7. Captions to illustrations should be listed on a separate sheet, not inserted in the text.
8. In papers submitted to *Acta Physica* all measures should be expressed in SI units.

III. ILLUSTRATIONS AND TABLES

1. Each paper should be accompanied by three sets of illustrations, one of which must be ready for the blockmaker. The other sets attached to the copies of the manuscript may be rough drawings in pencil or photocopies.
2. Illustrations must not be inserted in the text.
3. All illustrations should be identified in blue pencil by the author's name, abbreviated title of the paper and figure number.
4. Tables should be typed on separate pages and have captions describing their content. Clear wording of column heads is advisable. Tables should be numbered in Roman numerals (I, II, III, etc.).

IV. RETURN OF MATERIAL

Owing to high postage costs, the Editorial Office cannot undertake to return *all* material not accepted for any reason for publication. Of papers to be revised (for not being in conformity with the above Notes or other reasons) only *one* copy will be returned. Material rejected for lack of space or on account of the Referees' opinion will not be returned to authors outside Europe.

Periodicals of the Hungarian Academy of Sciences are obtainable
at the following addresses:

AUSTRALIA

C. B. D. LIBRARY AND SUBSCRIPTION SERVICE
Box 4886, G.P.O., Sydney N.S.W. 2001
COSMOS BOOKSHOP, 145 Ackland Street
St. Kilda (Melbourne), Victoria 3182

AUSTRIA

GLOBUS, Höchstädtplatz 3, 1206 Wien XX

BELGIUM

OFFICE INTERNATIONAL DE LIBRAIRIE
30 Avenue Marnix, 1050 Bruxelles
LIBRAIRIE DU MONDE ENTIER
162 rue du Midi, 1000 Bruxelles

BULGARIA

HEMUS, Bulvar Ruszki 6, Sofia

CANADA

PANNONIA BOOKS, P.O. Box 1017
Postal Station "B", Toronto, Ontario M5T 2T8

CHINA

CNPICOR, Periodical Department, P.O. Box 50
Peking

CZECHOSLOVAKIA

MAD'ARSKÁ KULTURA, Národní třída 22
115 66 Praha
PNS DOVOZ TISKU, Vinohradská 46, Praha 2
PNS DOVOZ TLACE, Bratislava 2

DENMARK

EJNAR MUNKSGAARD, Norregade 6
1165 Copenhagen K

FEDERAL REPUBLIC OF GERMANY

KUNST UND WISSEN ERICH BIBER
Postfach 46, 7000 Stuttgart 1

FINLAND

AKATEEMINEN KIRJAKAUPPA, P.O. Box 128 SF-00101
Helsinki 10

FRANCE

DAWSON-FRANCE S. A., B. P. 40, 91121 Palaiseau
EUROPÉRIODIQUES S. A., 31 Avenue de Versailles, 78170
La Celle St. Cloud
OFFICE INTERNATIONAL DE DOCUMENTATION ET
LIBRAIRIE, 48 rue Gay-Lussac
75240 Paris Cedex 05

GERMAN DEMOCRATIC REPUBLIC

HAUS DER UNGARISCHEN KULTUR
Karl Liebknecht-Straße 9, DDR-102 Berlin
DEUTSCHE POST ZEITUNGSVERTRIEBSAMT Straße der
Pariser Kommüne 3-4, DDR-104 Berlin

GREAT BRITAIN

BLACKWELL'S PERIODICALS DIVISION
Hythe Bridge Street, Oxford OX1 2ET
BUMPUS, HALDANE AND MAXWELL LTD.
Cowper Works, Olney, Bucks MK46 4BN
COLLET'S HOLDINGS LTD., Denington Estate Wellingbo-
rough, Northants NN8 2QT
WM. DAWSON AND SONS LTD., Cannon House Folkstone,
Kent CT19 5EE
H. K. LEWIS AND CO., 136 Gower Street
London WC1E 6BS

GREECE

KOSTARAKIS BROTHERS INTERNATIONAL
BOOKSELLERS, 2 Hippokratous Street, Athens-143

HOLLAND

MEULENHOF- BRUNA B. V., Beulingstraat 2,
Amsterdam
MARTINUS NIJHOFF B.V.
Lange Voorhout 9-11, Den Haag

SWETS SUBSCRIPTION SERVICE

347b Heereweg, Lisse

INDIA

ALLIED PUBLISHING PRIVATE LTD., 13/14
Asaf Ali Road, New Delhi 110001
150 B-6 Mount Road, Madras 600002
INTERNATIONAL BOOK HOUSE PVT. LTD.
Madame Cama Road, Bombay 400039
THE STATE TRADING CORPORATION OF INDIA LTD.,
Books Import Division, Chandralok 36 Janpath, New Delhi
110001

ITALY

INTERSCIENTIA, Via Mazzè 28, 10149 Torino
LIBRERIA COMMISSIONARIA SANSONI, Via Lamarmora 45,
50121 Firenze
SANTO VANASIA, Via M. Macchi 58
20124 Milano
D. E. A., Via Lima 28, 00198 Roma

JAPAN

KINOKUNIYA BOOK-STORE CO. LTD.
17-7 Shinjuku 3 chome, Shinjuku-ku, Tokyo 160-91
MARUZEN COMPANY LTD., Book Department, P.O. Box
5050 Tokyo International, Tokyo 100-31
NAUKA LTD. IMPORT DEPARTMENT
2-30-19 Minami Ikebukuro, Toshima-ku, Tokyo 171

KOREA

CHULPANMUL, Phenjan

NORWAY

TANUM-TIDSKRIFT-SENTRALEN A.S., Karl Johansgatan
41-43, 1000 Oslo

POLAND

WĘGIERSKI INSTYTUT KULTURY, Marszałkowska 80,
00-517 Warszawa
CKP-I W, ul. Towarowa 28, 00-958 Warszawa

ROUMANIA

D. E. P., Bucuresti
ILEXIM, Calea Grivitei 64-66, Bucuresti

SOVIET UNION

SOJUZPECHAT — IMPORT, Moscow
and the post offices in each town
MEZHDUNARODNAYA KNIGA, Moscow G-200

SPAIN

DIAZ DE SANTOS, Lagasca 95, Madrid 6

SWEDEN

GUMPERS UNIVERSITETSBOKHANDEL AB
Box 346, 40125 Göteborg 1

SWITZERLAND

KARGER LIBRI AG, Petersgraben 31, 4011 Basel

USA

EBSCO SUBSCRIPTION SERVICES
P.O. Box 1943, Birmingham, Alabama 35201
F. W. FAXON COMPANY, INC.
15 Southwest Park, Westwood Mass. 02090
READ-MORE PUBLICATIONS, INC.
140 Cedar Street, New York, N. Y. 10006

YUGOSLAVIA

JUGOSLOVENSKA KNJIGA, Terazije 27, Beograd
FORUM, Vojvode Mišića 1, 21000 Novi Sad